Space Programs Summary No. 37-29, Volume III

for the period July 1, 1964 to August 31, 1964

The Deep Space Network

JET PROPULSION LABORATORY
CALIFORNIA INSTITUTE OF TECHNOLOGY
PASADENA, CALIFORNIA

September 30, 1964

Space Programs Summary No. 37-29, Volume III

for the period July 1, 1964 to August 31, 1964

The Deep Space Network

JET PROPULSION LABORATORY
CALIFORNIA INSTITUTE OF TECHNOLOGY
PASADENA, CALIFORNIA

September 30, 1964

Preface

The *Space Programs Summary* is a six volume, bimonthly publication designed to report on JPL space exploration programs, and related supporting research and advanced development projects. The subtitles of all volumes of the *Space Programs Summary* are:

Vol. I. The Lunar Program (Confidential)

Vol. II. The Planetary–Interplanetary Program (Confidential)

Vol. III. The Deep Space Network (Unclassified)

Vol. IV. Supporting Research and Advanced Development (Unclassified)

Vol. V. Supporting Research and Advanced Development (Confidential)

Vol. VI. Space Exploration Programs and Space Sciences (Unclassified)

The *Space Programs Summary,* Volume VI consists of an unclassified digest of appropriate material from Volumes I, II, and III and a reprint of the space science instrumentation studies of Volumes I and II.

W. H. Pickering, *Director*
Jet Propulsion Laboratory

Space Programs Summary No. 37-29, Volume III

Prepared under Contract No. NAS 7-100, National Aeronautics & Space Administration

Contents

I. Introduction

The Deep Space Network (DSN) is a precision communication system which is designed to communicate with, and permit control of, spacecraft designed for deep space exploration. The DSN consists of the Deep Space Instrumentation Facility (DSIF), the Space Flight Operations Facility (SFOF), and the DSN Ground Communication System (GCS).

The DSN is a NASA facility, managed by JPL through a contract between NASA and the California Institute of Technology. The Office of Tracking and Data Acquisition is the cognizant NASA office.

It is the policy of the DSN to continuously conduct research and development of new components and systems and to engineer them into the DSN to maintain a state-of-the-art capability.

The DSN has facilities for simultaneously controlling a newly launched spacecraft and a second one already in flight. Within a few months, it will be able to control simultaneously either two newly launched spacecraft plus two in flight, or the operations of four spacecraft in flight at the same time. The DSIF is equipped with 85-ft antennas having gains of 53 db at 2300 Mc and a system temperature of 55°K, making it possible to receive significant data rates at distances as far as the planet Mars. To improve the data rate and distance capability, a 210-ft antenna is under construction at the Goldstone Mars site, and two additional antennas of this size are scheduled for installation at overseas stations.

The DSIF utilizes large antennas, low-noise phase-lock receiving systems, and high-power transmitters located at stations positioned approximately 120 deg around the Earth to track, command, and receive data from deep space probes. Overseas stations are generally operated by personnel of the respective countries. The DSIF stations are:

I.D. No.	Name	Location
11	Goldstone, Pioneer	Goldstone, California
12	Goldstone, Echo	Goldstone, California
13	Goldstone, Venus (R&D)	Goldstone, California
14	Goldstone, Mars (under construction)	Goldstone, California
41	Woomera	Island Lagoon, Australia
42	Canberra (under construction)	Canberra, Australia
51	Johannesburg	Johannesburg, South Africa
59	MTS	Johannesburg, South Africa
61	Madrid (under construction)	Madrid, Spain
71	Spacecraft Monitoring	Cape Kennedy, Florida

The SFOF is located in a three-story building at the Jet Propulsion Laboratory in Pasadena, California, and utilizes operations control consoles, status and operations displays, computers, data processing equipment for analysis of spacecraft performance and space science experiments, and communication facilities to control space flight operations. This control is accomplished by generating trajectories and orbits, and command and control data, from tracking and telemetry data received from the DSIF in near real-time. The SFOF also reduces the telemetry, tracking, command and station performance data recorded by the DSIF into engineering and scientific information for analysis and use by the scientific experimenters and spacecraft engineers.

The DSN Ground Communication System consists of voice, normal and high data rate teletype circuits provided by the NASA World-Wide Communications Network between each overseas station and the SFOF; teletype and voice circuits between the SFOF, Goldstone Stations, and Cape Kennedy; and a microwave link between the SFOF and Goldstone, provided by the DSN.

II. Tracking Station Engineering and Operations

A. Project Engineering

1. Surveyor

Comprehensive tests to verify the interface compatibility of the DSIF and the *Surveyor* command and data console (CDC) ground equipment were conducted over a 4-wk period in June and July. The tests covered telemetry, television, command, and RF systems, and made use of a special ground transponder to simulate the *Surveyor* spacecraft.

In general, RF threshold levels, bit error rates, and television video performance met existing specified standards of performance.

The tests showed that with minor exceptions the CDC/DSIF interface is satisfactory. Some defects remain to be corrected on the CDC, and some minor modifications to the DSIF interface have been recommended.

2. Ranger Block III

DSIF advisor support was given to the following *Ranger 7* flight operations tests:

(1) Spacecraft/DSIF/SFOF compatibility tests.

(2) SFOF/DSIF integration tests.

(3) DSIF training tests.

(4) Operational readiness tests.

The same support was provided for the actual *Ranger 7* mission.

Functional Specification OSE/R3-4-353-A was published and distributed. This publication updated the DSIF RF support commitments to include the specifics of the *Ranger 7* mission.

Technical assistance with testing and coordination and with participation in pre-operation drills was given in preparing the various DSIF Stations for the *Ranger 7* mission.

3. Lunar Orbiter

The interface between DSIF and mission dependent equipment in this project is being studied. No final definition can be made until the Boeing Company freezes equipment design and until a final space flight operations method has been defined. Technical data relevant to the DSIF was supplied to the Lunar Orbiter Project Office and the Boeing Company.

4. Mariner C

The final report on the DSIF/*Mariner C* tests reported in *SPS 37-28* was completed and reviewed. Phasing problems in the ranging and command subsystems were uncovered and are being resolved within the engineering sections affected.

5. Pioneer

Support of the *Pioneer* Solar Probe Project has continued with main interest centering on the definition of both the DIS 910 computer interface and the mission dependent equipment (MDE) panel interface.

Weekly progress reports on the project are now being sent to the DSN office.

6. AMR Spacecraft Monitoring Station, DSIF 71

Project Implementation Document EPD-209 was completed and a final draft submitted for review. Ordering of Goldstone duplicate standard equipment has been started, and the station is scheduled to reach operational status by April 19, 1965.

B. System Integration and Analysis

1. Documentation

The technical writing contractor, Volt Technical Corporation, has been directing the writing effort on Technical Memorandum No. 33-26 to the preparation of Volume II which covers details of the various subsystems. During this reporting period, preliminary drafts have been submitted on the antenna microwave, transmitter, and receiver subsystems, and have been reviewed by JPL personnel. JPL review of Sections I, V, and VI of Volume I is presently in progress. To augment the preparational support to this document, additional JPL engineers have been assigned cognizance to furnish information pertaining to their subsystem and to provide review and evaluation of written drafts concerned with their areas. As an aid to the writing of this document, a flow diagram has been prepared that defines and delineates the functional handling and processes of the written material for Technical Memorandum No. 33-26 to the formal approval of this document.

A rough draft has been prepared and is currently being circulated for comment on the over-all DSIF documentation requirements. The intent of this document is to establish consistent documentation requirements for all organizations supplying the DSIF with equipment.

A Quality Assurance Implementation Plan was recently prepared and published. This plan defines the level and quantity of inspections required for DSIF equipment, and also defines the organization to perform and report on the inspections. Representatives from Division 15 and Division 33 have reviewed the plan and concurred with it.

The functional and detail specifications and the interface definition document for the telemetry and command data handling subsystem were prepared and published. Construction of the prototype unit will begin in the next reporting period.

The System Signal Interface Book was completed and one pre-release copy was given to the Project Manager for reference. Formal publication of the book is being held in abeyance until all information contained therein is verified.

The list assigning reference designations to the major S-band equipment units has been expanded to provide the top assembly drawing number for each of these units.

2. Calibration Standards

Approval was received for implementation of a Primary Standards Laboratory at Goldstone. The initial equipments have been ordered and some have already been received. Once installed and operating, the lab will provide calibration accuracy for certain types of test equipment. Calibration accuracies are traceable to the National Bureau of Standards.

The Collins 960-Mc beacon was sent overseas to the DSIF Stations at Johannesburg and Woomera as a reference calibration standard for checks of the test transponder at those stations. The calibrations were completed, and the equipment is now back at Goldstone ready to be used for a check of the test transponder at the Echo site. The around-the-network circulation of the above test standard will be a continuous procedure.

3. DSIF/Mariner C Tests

Preliminary data reduction of the RF test portion of the DSIF/*Mariner C* tests performed at Goldstone is listed below. These tests were conducted to ascertain the signal levels when loss of carrier lock was reached. These values were determined for the down-link conditions with and without telemetry modulation applied to the spacecraft radio system. Similarly, up-link loss of carrier lock signals was determined; and, finally, two-way loss of carrier lock values was determined with the presence of down-link telemetry modulation.

a. Spacecraft to DSIF (down-link one-way lock).
Test conditions.

(1) Spacecraft power output = 4.7 w/36.7 dbm.

(2) DSIF static phase error = 0 v.

(3) DSIF system noise temperature = 65°K (pointed to collimation tower/Spacecraft Test Facility).

(4) DSIF automatic gain control bandwidth = 0.118 cps.

(5) Carrier suppression when modulation is applied = −4 db.

(6) Telemetry modulation = 33⅓-bits-per-second, phase-shift-keyed, pseudonoise, binary-coded synchronned system.

Test results.

(1) Carrier signal only.

(a) Loss of carrier lock signal values:

DSIF $2B_{Lo}$, cps	Lost-lock signal level, dbm	Theoretical threshold, dbm
48	−162	−163.67
12	−169	−169.67

(b) DSIF residual phase modulation, $|1 - H(s)|$ oscilloscope response, at $2B_L = 12$ cps and −114-dbm input signal level: $\phi_R = \pm 7$-deg peak.

(2) With telemetry modulation applied to spacecraft.

(a) Loss of carrier lock signal values:

DSIF $2B_{Lo}$, cps	Lost-lock signal level, dbm	Theoretical threshold, dbm
48	−163	−163.67
12	−167	−169.67

(b) DSIF residual phase modulation, $|1 - H(s)|$ oscilloscope response, at $2B_L = 12$ cps and −114-dbm input signal level: $\phi_R = \pm 90$-deg peak symmetrical phase modulation resulting in an average phase error of nearly 0 deg due to the phase-shift-keyed/pseudonoise telemetry spectra.

b. DSIF to spacecraft (up-link one-way lock).
Test conditions.

(1) DSIF power output levels = 200 and 500 w, and 1, 5, and 10 kw.

(2) Spacecraft $2B_{Lo} = 20$ cps.

(3) DSIF exciter 3 × VCO frequency = 66,041,046 cps.

(4) Continuous wave signal only.

Test results.

(1) Carrier lost-lock signal level = −150 dbm. (Theoretical = −150.83 dbm, for $2B_{Lo} = 20$ cps and $T_{eff} = 3000$°K).

(2) Spacecraft residual phase modulation, $|1 - H(s)|$ oscilloscope:

DSIF, P_0	200 w	500 w	1 kw	5 kw	10 kw
ϕ_R	±5-deg peak	±5-deg peak	±5-deg peak	±5-deg peak	±6-deg peak

c. Two-way lock.

Test conditions.

(1) Spacecraft power output = 4.7 w.

(2) DSIF system noise temperature = 65°K.

(3) Spacecraft telemetry modulation = 33⅓ bits per second.

(4) DSIF power output = 200 w.

(5) Spacecraft system noise temperature = 3000°K.

Test results.

(1) Carrier lost-lock signal level:

Test condition	1	2
Spacecraft $2B_{Lo}$, cps	20	20
Spacecraft carrier lost-lock level, dbm	−150	−150
DSIF $2B_{Lo}$, cps	48	12
DSIF carrier lost-lock level, dbm	−162	−167

The simulated space loss was achieved by varying the attenuation in series with the test space link. Under Condition 1, lost lock occurred first on the down-link; then both up- and down-link lost lock simultaneously under Condition 2 for these particular ratios of DSIF and spacecraft transmitter power.

(2) DSIF static phase error versus VCO frequencies:

Spacecraft VCO frequency	−200 cps	Nominal	+200 cps
DSIF static phase error, v dc	1.461	0	−1.44
DSIF 3 × VCO receiver frequency, cps	70,155,702	70,156,303	70,156,909
DSIF 3 × VCO exciter frequency, cps	66,040,510	66,041,065	66,041,623

(3) VCO pull-range, two-way lock.

(a) DSIF $2B_{Lo}$ = 12 cps.

(b) DSIF exciter nominal 3 × VCO frequency = 66,041,022 cps.

(c) Below listed frequencies are the DSIF exciter and receiver VCO frequency pull-range limits (from nominal) when two-way lock was lost.

Test conditions	1	2	3
DSIF received carrier level, dbm	−151	−155	−160
Spacecraft received carrier level, dbm	−140	−140	−146
Telemetry modulation	Not applied	Applied	Applied
DSIF receiver 3 × VCO lower frequency, cps	70,156,122	70,156,122	70,156,190
DSIF exciter 3 × VCO lower frequency, cps	66,040,898	66,040,898	66,040,956
DSIF receiver 3 × VCO higher frequency, cps	70,156,367	70,156,367	70,156,292
DSIF exciter 3 × VCO higher frequency, cps	66,041,123	66,041,123	66,041,062
Comments	Spacecraft lost lock first	Spacecraft lost lock first	Spacecraft lost lock on high frequency; both lost lock on low frequency

4. DSIF Receiver AGC Voltage Versus RF Signal Level

The DSIF receiver AGC voltage, which varies as a function of the input carrier signal level, is used to determine the received carrier level from a spacecraft. A typical plot for the various RF loop bandwidths (taken from the DSIF/*Mariner C* tests) is shown in Fig. 1. Many parameters are involved in determining the accuracy of the received signal level from this type of plot. The major parameters are the accuracy of the known levels of inserted signal strength during subsystem calibration, the stability of the receiver AGC loop and its net fixed-gain (amplification and losses), the random phase characteristics of the actual received carrier signal, resolution of the calibrated plot, and the errors in interpolating from

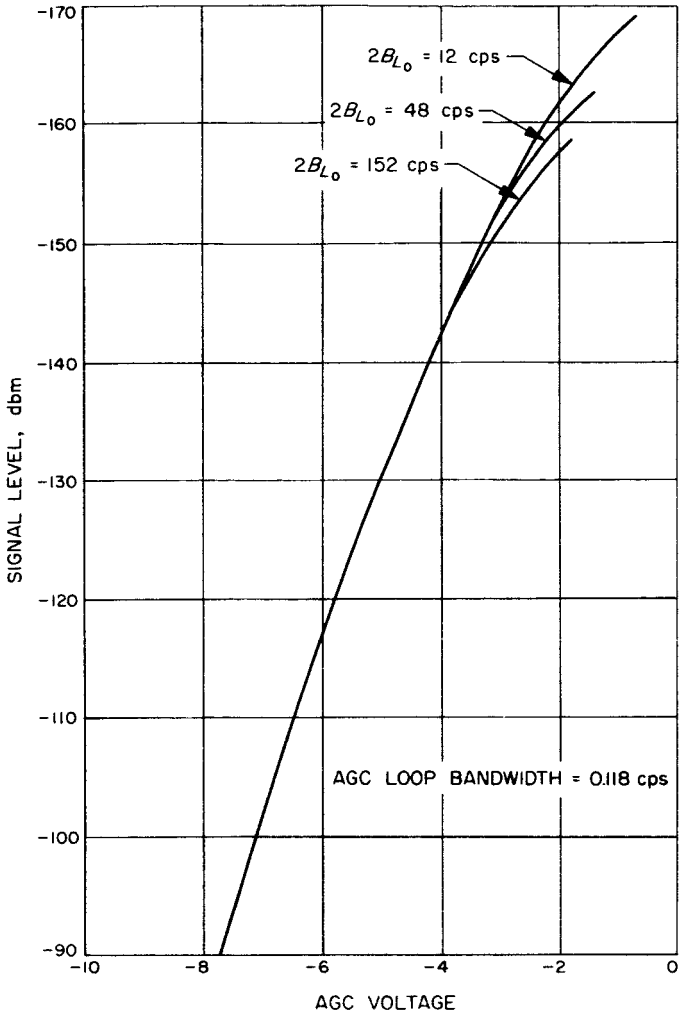

Fig. 1. AGC voltage versus signal level for various loop bandwidths

the calibration curve. System analysis in this area is being prepared to determine the expected accuracy of this method for determining the received signal level.

5. Suitcase Telemetry System

Various components of the Suitcase Telemetry System have been received and are being evaluated. These components are:

(1) Time code receiver Model WWVT, manufactured by Specific Products, a small battery-operated receiver for receiving transmissions from Bureau of Standards WWV.

(2) Master watch navigation chronometer, Hamilton Watch Company.

(3) Pacific Electro Magnetic Co. Model 110, battery-operated portable instrumentation tape recorder to be used for recording the spacecraft telemetry signals.

6. Station Control and Monitor (SCAM) Console

The SCAM Phase I prototype model, fabricated by the Hughes Aircraft Company, Fullerton, has been installed at Goldstone for acceptance testing.

The compilation of the DSIF S-band system parameters for monitoring by the on-site digital instrumentation subsystem (DIS), as a means for assessing the station status and performance during a spacecraft communication mission, is nearing completion as part of the SCAM Phase II Program.

C. Goldstone Operations

The Goldstone Echo and Pioneer sites successfully participated in the *Ranger* 7 mission. After a series of operational readiness and net integration tests, Goldstone was operational for the *Ranger* 7 launch at 16:50:09.8 GMT, July 28, 1964 and, with three tracking periods, completed the mission with video reception from the spacecraft. *Ranger* 7 impacted at 13:25:50.029 GMT, July 31, 1964.

In the interval between *Rangers* 6 and 7, the S-band installation at Pioneer received full support of both stations. Concurrently, the Echo L-band equipment was maintained in operational readiness and, except for a redesign of the wide-band configuration, the system was not materially changed.

1. Equipment

a. Echo site. Although the 2.5-Mc receiver bandpass for *Ranger* 6 was adequate (Ref. 1), attempts were made to increase the bandpass to ensure additional quality and protection. Two systems were assembled, operationally tested, and accepted by mid-July. A nominal bandpass of 4.0 Mc at the 3-db points was achieved and, during the final portion of *Ranger* 7, the bandpass was 3.5 Mc.

Fig. 2 is a block diagram of the modified configuration currently installed at Goldstone. Fig. 3 presents an oscilloscope picture of the accepted bandpass at Echo, while Fig. 4 presents one of the Pioneer configuration. A recently acquired International Telephone and Telegraph (ITT) solid-state distribution amplifier was modified to provide four identical 10.0-Mc wide-band outputs. In this configuration, the system temperature was 124°K, the maser gain was 11.0 db, and the parametric amplifier gain was 20.0 db, with a system bandwidth of approximately 4.0 Mc at the 3-db points. The noise figure remained relatively steady at 11.0 ±1 db during all tests.

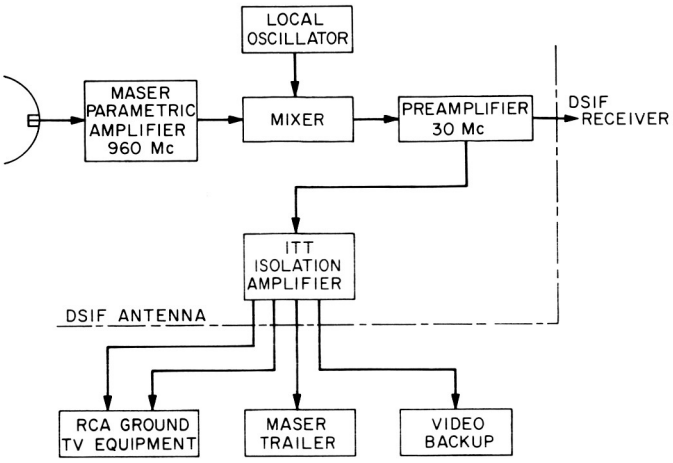

Fig. 2. Receiver front end configuration for *Ranger 7*

Through July, all activity was directed toward the completion of the *Ranger 7* mission. The primary activity was the development of the wider bandpass capability of the L-band antenna-mounted equipment and the interface coupling with the RCA video ground equipment. When it did not conflict with the *Ranger 7* mission, technical support and personnel training was provided to the Pioneer S-band project.

Through August, after the completion of the *Ranger 7* mission, the majority of Echo technical personnel was assigned to full-time support of the S-band project. All cabling to and on the Echo 85-ft antenna was completely rearranged. The hour angle and declination "U" racks and pinion gears were cleaned and lubricated. The power skids were steam-cleaned and repainted where necessary, and an overall general maintenance performed.

The Canberra Cassegrain cone and hyperbola were removed prior to *Ranger 7* and shipped to Australia. The

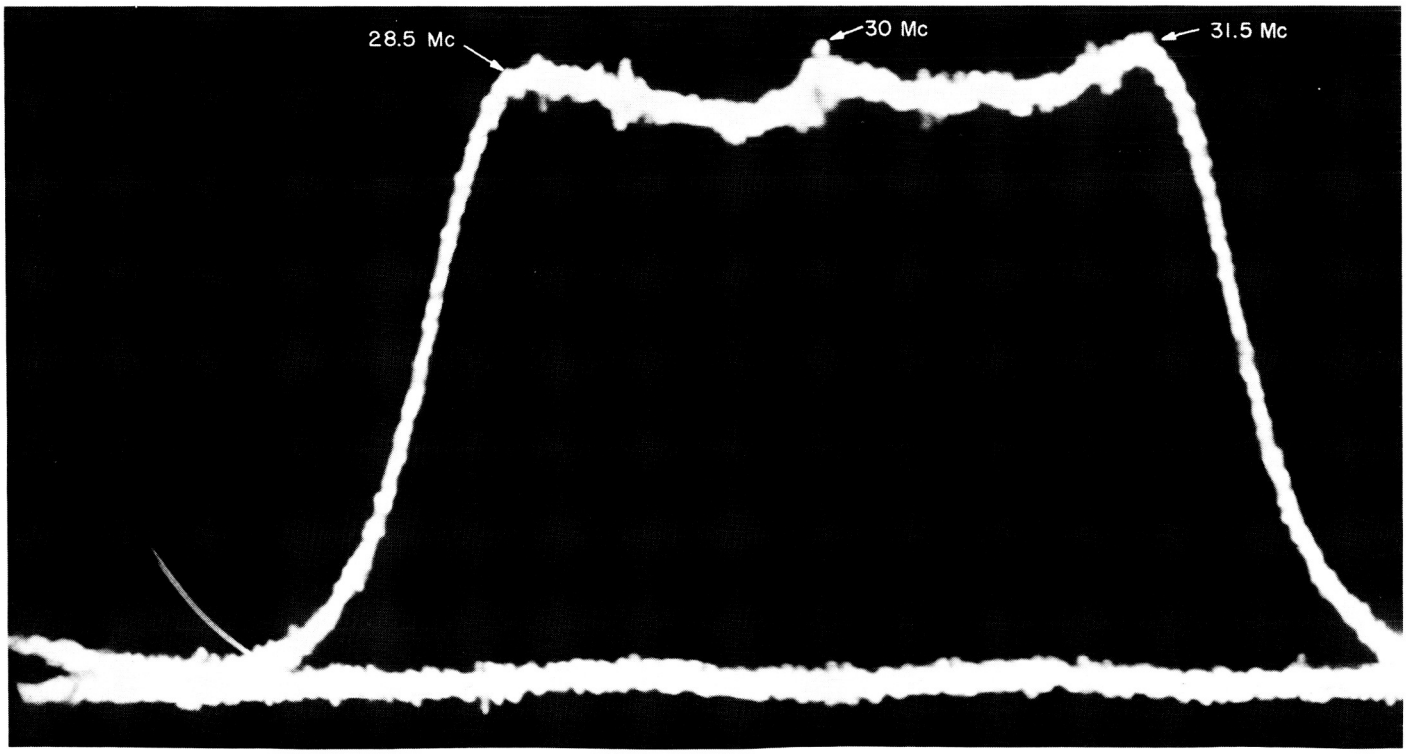

Fig. 3. Oscilloscope pattern of Echo bandpass

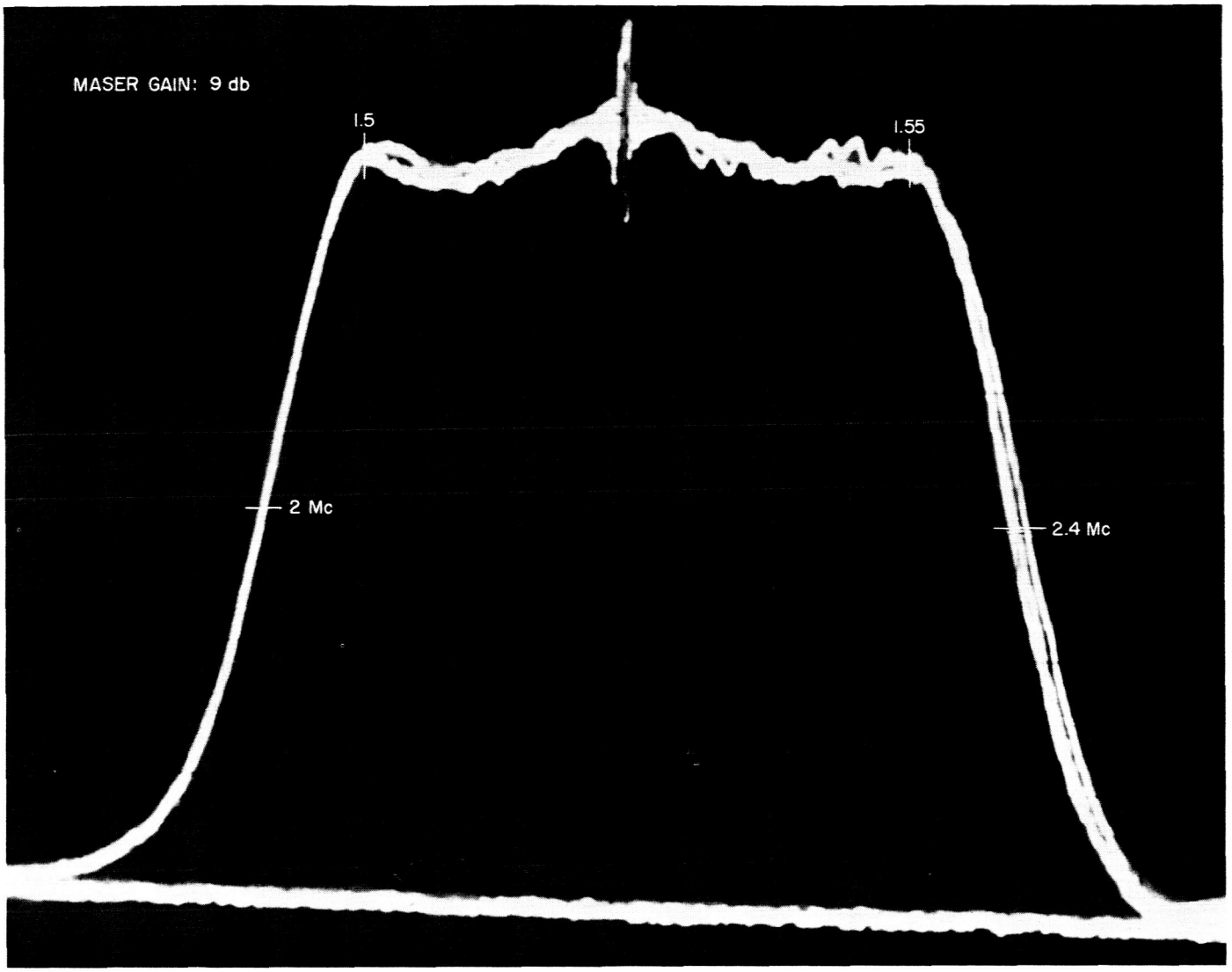

Fig. 4. Oscilloscope pattern of Pioneer bandpass

Madrid Cassegrain cone and hyperbola were installed on the Echo 85-ft antenna for testing. The tests will include near and far field patterns, ellipticities, and null-plain orthogonality alignments. In addition to these tests, a series of star tracks will be performed.

Construction is in progress on the updating and expansion of the station communications facilities. Junction manholes and additional underground conduits are being installed at the Echo site. After award of contract, construction started on an underground 200-pair cable linking Echo site, Pioneer, the Airport, and the Mars site.

b. Pioneer site. Although the Pioneer site was to prepare for and provide a backup tracking facility to the Echo site during the *Ranger* 7 mission, the S-band installation and testing for the DSIF continued. Concurrently, the *Surveyor* Project (Refs. 2 and 3) is progressing through the initial equipment installation and S-band compatibility testing.

During July and August, operation and interface testing of the Pioneer prototype S-band system, installed in the S-band annex, was completed. Currently, the system is being readied to provide the primary control for the *Mariner* 1964 project, and is remaining in its present location until a later date.

Installed in the Manned Space Flight Net (MSFN) annex, the Canberra system has been operationally tested. The installation and testing were performed largely by the Canberra personnel who will install and operate the system at DSIF 42. The system is being prepared for a September shipment.

The new east wing of the enlarged control building is structurally completed. Ultimately, this wing will house the permanent Pioneer S-band installation. Currently the operational test installation of the Madrid system is utilizing the space. The GSDS configuration, established with the original Pioneer system, is being adhered to in this and the Canberra system.

The first SDS digital instrumentation subsystem, operationally and interface tested with the first S-band system, has been shipped to the manufacturer for updating. Upon its return to Pioneer, it will be integrated with the Madrid S-band system.

The L-band system installed in the original control room has been dismantled for temporary storage. Prior to *Ranger* 8 it will be installed in the MSFN wing for tracking backup of the Echo site during *Rangers* 8 and 9.

c. Venus site. Ground testing of the *Mariner* 1964 Cassegrain cone 100-kw transmitter has been completed. The 85-ft Az–El antenna was rigged with the additional cabling and coolant lines to adapt it for handling the *Mariner* 1964 transmitter (Ref. 4 and succeeding issues). Fig. 5 illustrates the interior of the cone from the top. The feedhorn assembly will connect to the top of the waveguide-switch port, shown covered and taped. Operational testing (including interface testing with the common Venus equipment, personnel training, and quick cone change practice) is in progress. The exciter for the *Mariner* 1964 transmitter is under development and fabrication at the Goldstone Research Laboratory.

The Cassegrain cone test elevators in the high-voltage power supply building are completed. Fig. 6 illustrates a cone in position on the elevator for testing, with the ceiling doors open to permit raising the radiating horn above the building roof line.

Fig. 5. Interior of *Mariner* 1964 cone transmitter as seen from the top

Fig. 6. Cone in position on test elevator

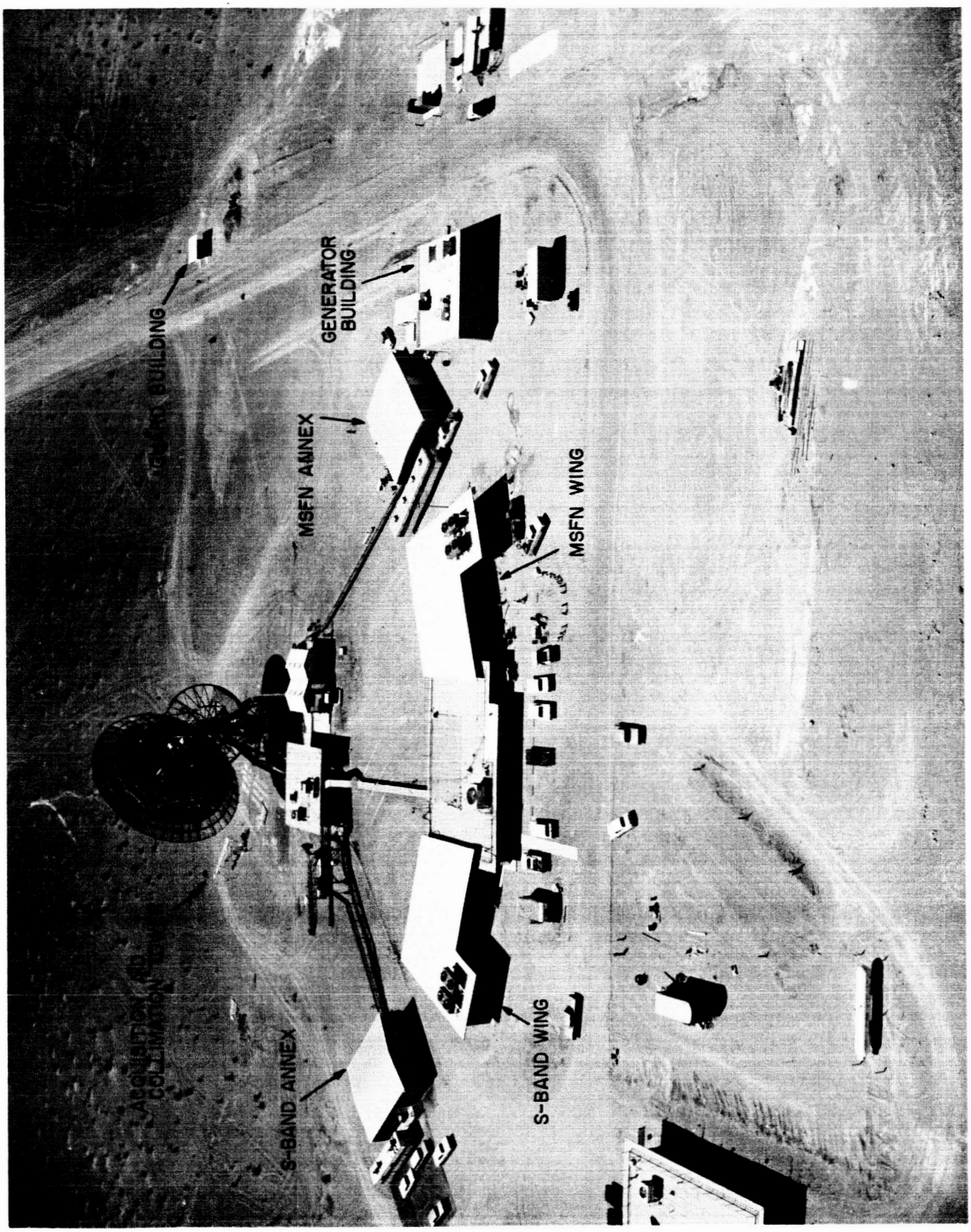

Fig. 7. Aerial view of Pioneer site showing completed buildings (looking south)

2. Construction

The S-band wing and the MSFN wing on the control building at the Pioneer site are essentially completed. The generator building is also completed and in use. The former temporary guard building has been removed, and the new permanent building is now in use. Fig. 7 is an aerial view of the Pioneer site showing the completed buildings.

D. Mark I Ranging Subsystem—Code Components Acquisition and Code Correlation

The Mark I ranging subsystem is being built to equip the DSN with the capability of ranging on spacecraft "turnaround" transponders to distances of 800,000 km. A summary of the basic theory of operation and a brief over-all description of the subsystem were given in Ref. 5. The design and operation of the major functional units were further detailed in subsequent issues of the *SPS*. The present article deals with certain specific aspects of the code-acquisition procedure of the subsystem, for which reference should be made to the sections "Program Unit" and "Acquisition Unit," pp. 11–14 of *SPS 37-23*, Vol. III.

1. Introduction

This article intends to clarify the correlation operation used, in the ranging subsystem and the pertinent S-band radio subsystems, to acquire the individual ranging code components.

In the idealized analysis the actual lengths in bits of the individual code components are ignored; i.e., no account is taken of code component unbalance due to the fact that each contains one more '1" than it does "0's." In the following analyses, component unbalance is included for both the normal-code and the short-code cases.

Throughout this article, as in previous articles, the transmitter code components are designated by lower-case letters. They are x, a, b, c, and cl, all generated in the digital equipment. The receiver code components are designated by upper-case letters. They are X, A, B, and C, generated in the digital equipment, and CL, generated in the RF equipment. (See *SPS 37-21*, Vol. III, pp. 16–17.)

2. Acquisition Program States

The component cl is acquired in the R (Reset) program state by nondigital means, viz., by locking up the receiver clock loop. The components x, a, b, and c are acquired in program states $p3$, $p4$, $p5$, and $p6$, respectively, by digital means. (See *SPS 37-23*, Vol. III, Fig. 5.) Program states $p1$, $p2$, and $p7$ do not directly serve the code-component acquisition purpose.

3. Transmitter Code

The transmitter code can be written, and rewritten, as follows:

$$
\begin{aligned}
&x\,cl + \bar{x}\,[(a\,b + b\,c + b\,c + a\,c) \oplus cl] \\
&\quad = x\,cl + \bar{x}\,[(a\,b + b\,c + a\,c)\,\overline{cl} + (\bar{a}\,\bar{b} + \bar{b}\,\bar{c} + \bar{a}\,\bar{c})\,cl] \\
&\quad = cl\,[x + \bar{x}(a\,\bar{b} + \bar{b}\,\bar{c} + \bar{a}\,\bar{c})] + \overline{cl}\,[\bar{x}(a\,b + b\,c + a\,c)] \\
&\quad = cl\,[x + \bar{a}\,\bar{b} + \bar{b}\,\bar{c} + \bar{a}\,\bar{c}] + \overline{cl}\,[\bar{x}\,a\,b + \bar{x}\,b\,c + \bar{x}\,a\,c]
\end{aligned}
$$

This function can be plotted on a Karnaugh map (Veitch chart), where "true" is indicated by an Arabic "one" (1) and "false" is indicated by its absence (Fig. 8).

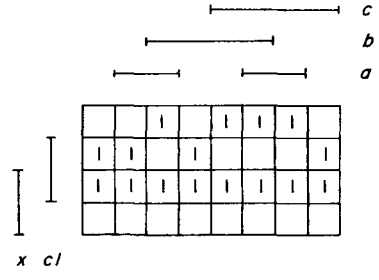

Fig. 8. Transmitter code

4. Receiver Codes

The output of the digital receiver coder is often referred to as the receiver code. For purposes of this article, we shall distinguish between the receiver coder output and the "full" receiver code. The latter is the result of combining the former with the CL (clock) component by the $\oplus$, or *exclusive OR*, operator.

In the following, we shall write down the full receiver code for each acquisition program state and plot it on an appropriate Karnaugh map. For reasons which will appear later, we shall not use the Arabic "one" (1), but rather the Chinese "one" (—) to indicate "true," and its absence to indicate "false."

(a), (b) Reset State. (See Fig. 9.)

Coder output $= 0$

Full code $= 0 \oplus CL$

$= 0\,\overline{CL} + 1\,CL$

$= CL$

Fig. 9. Full receiver code, Reset State

(c), (d) State $p3$. (See Fig. 10.)

Coder output $= \bar{X}\,A$

Full code $= \bar{X}\,A \oplus CL$

$= \bar{X}\,A\,\overline{CL} + (X + \bar{A})\,CL$

$= CL\,[X + \bar{A}] + \overline{CL}\,[\bar{X}\,A]$

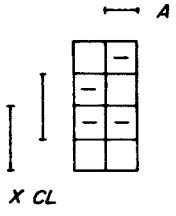

Fig. 10. Full receiver code, States p3 and p4

(e), (f) State $p4$. (See Fig. 11.)

Same as state $p3$.

(g), (h) State $p5$. (See Fig. 12.)

Coder output $= \bar{X}\,B$

Full code $= \bar{X}\,B \oplus CL$

$= CL\,[X + \bar{B}] + \overline{CL}\,[\bar{X}\,B]$

(i), (j) State $p6$. (See Fig. 13.)

Coder output $= \bar{X}\,C$

Full code $= \bar{X}\,C \oplus CL$

$= CL\,[X + \bar{C}] + \overline{CL}\,[\bar{X}\,C]$

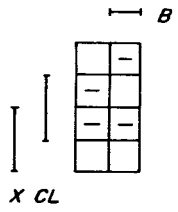

Fig. 11. Full receiver code, State p5

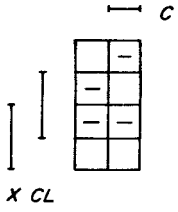

Fig. 12. Full receiver code, State p6

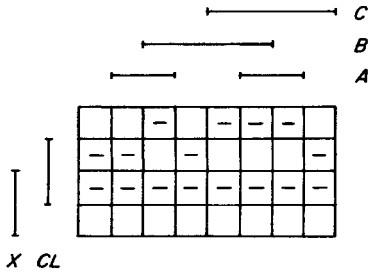

Fig. 13. Full receiver code, State p7

(k) State $p7$. (See Fig. 14.)

Coder output $= \bar{X}\,(A\,B + B\,C + A\,C)$

Full code $= [\bar{X}\,(A\,B + B\,C + A\,C)] \oplus CL$

$= \bar{X}\,(A\,B + B\,C + A\,C)\,\overline{CL}$

$+ [X + (\bar{A} + \bar{B})\,(\bar{B} + \bar{C})\,(\bar{A} + \bar{C})]\,CL$

$= \bar{X}\,(A\,B + B\,C + A\,C)\,\overline{CL}$

$+ (X + \bar{A}\,\bar{B} + \bar{B}\,\bar{C} + \bar{A}\,\bar{C})\,CL$

$= CL\,[X + \bar{A}\,\bar{B} + \bar{B}\,\bar{C} + \bar{A}\,\bar{C}]$

$+ \overline{CL}\,[\bar{X}\,A\,B + \bar{X}\,B\,C + \bar{X}\,A\,C]$

$=$ same as transmitter code.

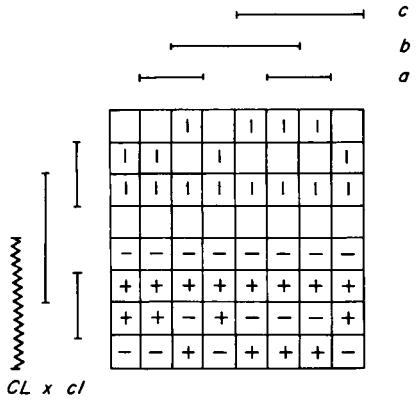

Fig. 14. Code correlation, Reset State, Initial

5. Correlation of Codes

Since we are assuming balanced, random code components, each component of the transmitter code (or receiver code) is entirely independent of each other component of *that* code. Further, each *unacquired* component of the transmitter code is independent of each component of the receiver code and, of course, vice versa. In the Karnaugh maps which follow, then, transmitter and receiver code components are listed *separately* (the latter with a wavy-line designator) when the component is *not* acquired. They are collapsed into *one* (straight-line) designator when the component *is* acquired.

The percentage correlation is derived from the normalized correlation function and reads

$$C = \frac{A - D}{A + D} \times 100\% = \frac{2A - T}{T} \times 100\%$$

where A is the number of agreements (true-true or false-false), D is the number of disagreements (true-false or false-true), and T is the total of A plus D.

Since we use "|" for transmitter code "true" and "–" for receiver code "true," we can readily spot and count agreements by the superposition (+) or absence of these symbols in the following charts. Obviously we can also count disagreements, indicated by "|" for transmitter code true, receiver code false or by "–" for receiver code true, transmitter code false.

6. Correlation Determination for Idealized Codes (Balanced Components)

In this part of this article, the simplifying assumption is made that each of the code components is balanced, i.e., that it contains equal numbers of 1's and 0's. Each square of any one of the following Karnaugh maps has then the same intrinsic probability.

(a) Reset State, Initial (no clock lock). (See Fig. 14.)

Full receiver code = CL

Agreements = 32

Total = 64

Correlation = 0%

(b) Reset State, Final (clock lock). (See Fig. 15.)

Full receiver code = CL

Agreements = 24

Total = 32

Correlation = 50%

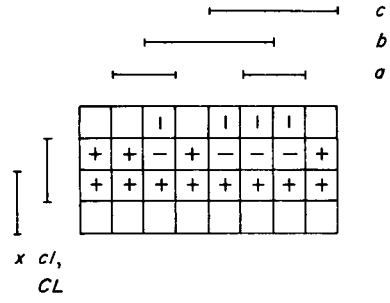

Fig. 15. Code correlation, Reset State, Final

Note: An operational check of the subsystem is often made at this point, switching the (transmitter) code switch from CODE to CLOCK. The transmitter code is then *cl*. (See Fig. 16.)

Full receiver code = CL

Agreements = 2

Total = 2

Correlation = 100%

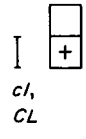

Fig. 16. Clock correlation, Reset State, Final

(c) State $p3$, Initial (x and a not acquired). (See Fig. 17.)

Full receiver code $= CL\,(X + \bar{A}) + \overline{CL}\,(\bar{X}\,A)$

Agreements = 80

Total = 128

Correlation = 25%

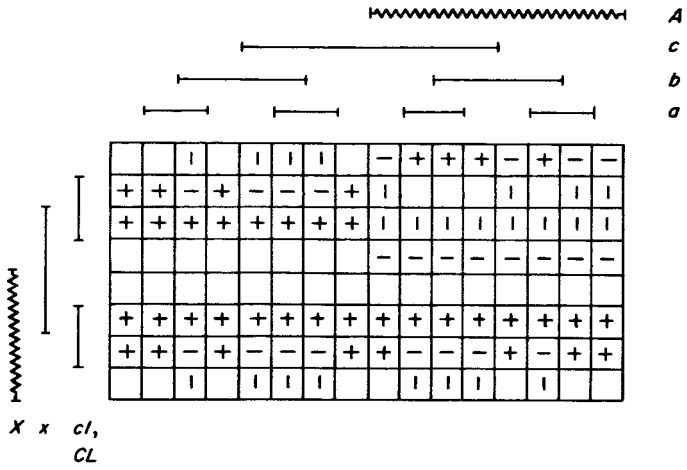

Fig. 17. Code correlation, State p3, Initial

(d) State $p3$, Final (x acquired, a not acquired). (See Fig. 18.)

Full receiver code $= CL\,(X + \bar{A}) + \overline{CL}\,(\bar{X}\,A)$

Agreements = 48

Total = 64

Correlation = 50%

(e) State $p4$, Initial (x acquired, a not acquired). (See Fig. 18.) Same as state $p3$, Final.

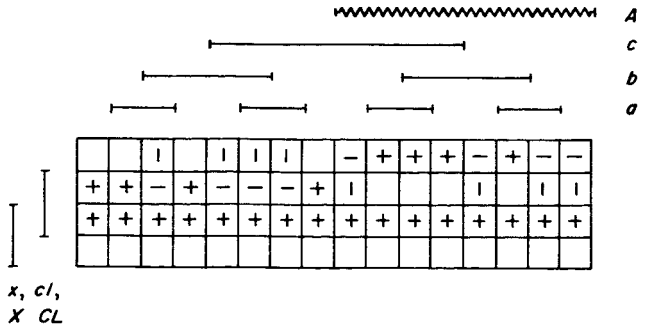

Fig. 18. Code correlation, State p3, Final; State p4, Initial

(f) State $p4$, Final (a acquired). (See Fig. 19.)

Full receiver code $= CL\,(X + \bar{A}) + \overline{CL}\,(\bar{X}\,A)$

Agreements = 28

Total = 32

Correlation = 75%

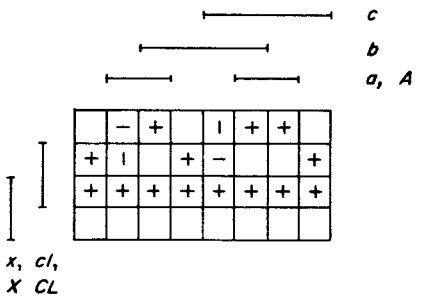

Fig. 19. Code correlation, State p4, Final

(g) State $p5$, Initial (b not acquired). (See Fig. 20.)

Full receiver code $= CL\,(X + \bar{B}) + \overline{CL}\,(\bar{X}\,B)$

Agreements = 48

Total = 64

Correlation = 50%

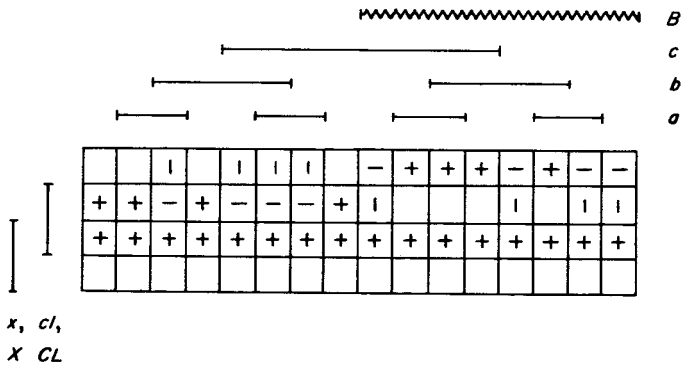

Fig. 20. Code correlation, State p5, Initial

(h) State $p5$, Final (b acquired). (See Fig. 21.)

Full receiver code $= CL\,(X + \bar{B}) + \overline{CL}\,(\bar{X}\,B)$

Agreements = 28

Total = 32

Correlation = 75%

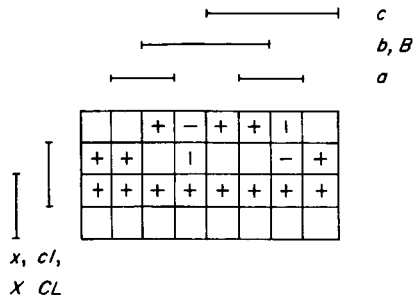

Fig. 21. Code correlation, State p5, Final

(i) State $p6$, Initial (c not acquired). (See Fig. 22.)

Full receiver code $= CL(X + \bar{C}) + \overline{CL}(\bar{X}C)$

Agreements = 48

Total = 64

Correlation = 50%

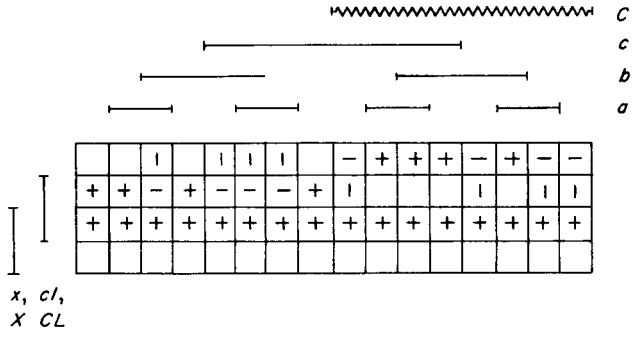

Fig. 22. Code correlation, State p6, Initial

(j) State $p6$, Final (c acquired). (See Fig. 23.)

Full receiver code $= CL(X + \bar{C}) + \overline{CL}(\bar{X}C)$

Agreements = 28

Total = 32

Correlation = 75%

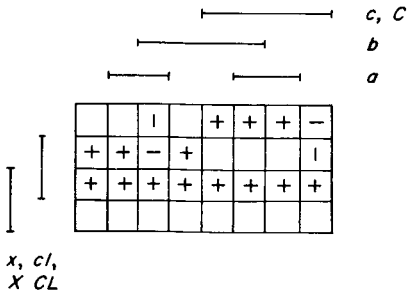

Fig. 23. Code correlation, State p6, Final

(k) State $p7$. (All components acquired.) (See Fig. 24.)

Full receiver code = transmitter code

Agreements = 32

Total = 32

Correlation = 100%

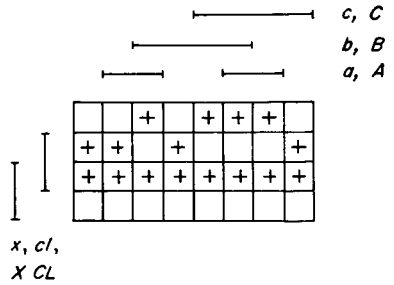

Fig. 24. Code correlation, State p7

7. Correlation Determinations for Actual Normal Code

For the precise correlation determinations, one must take into account the fact of unbalance of all but the clock (cl) code components. Specifically, each square of each applicable Karnaugh map must be weighted with its probability. The probability of each square is the product of its row and column probabilities. These, in turn, are the products of the pertinent probability weights of the constituent binary variables (code components). (See Table 1.)

Table 1. Normal-code components' unbalance

Code component	Total bits	Number of ones	Number of zeros	Probability weight	
				of ones	of zeros
cl, CL	2	1	1	1	1
x, X	11	6	5	1.09	0.91
a, A	31	16	15	1.03	0.97
b, B	63	32	31	1.02	0.98
c, C	127	64	63	1.01	0.99

(a) Reset State, Initial. (See Fig. 14.) The compensating characteristics of this function obviate the need for considering probability weights.

Correlation = 0%

(b) Reset State, Final. (See Fig. 15.) Row probabilities are: 0.91, 0.91, 1.09, 1.09. Column probabilities are:

0.9411, 0.9993, 1.0401, 0.9795, 0.9993, 1.0611, 1.0195, 0.9601.

Agreements = 24.5016

Total = 32

Correlation = 53.14%

(c) State $p3$, Initial. (See Fig. 17.) Row probabilities are: 0.8281, 0.8281, 0.9919, 0.9919, 1.1881, 1.1881, 0.9919, 0.9919. Column probabilities are: 0.9129, 0.9693, 1.0089, 0.9501, 0.9693, 1.0193, 0.9793, 0.9313, 0.9889, 1.0399, 1.0929, 1.0293, 1.0089, 1.0713, 1.0293, 0.9693.

Agreements = 82.0141

Total = 128

Correlation = 28.15%

(d) State $p3$, Final. (See Fig. 18.) Row probabilities are: 0.91, 0.91, 1.09, 1.09. Column probabilities are: 0.9129, 0.9693, 1.0089, 0.9501, 0.9693, 1.0193, 0.9793, 0.9313, 0.9889, 1.0399, 1.0929, 1.0293, 1.0089, 1.0713, 1.0293, 0.9693.

Agreements = 49.4345

Total = 64

Correlation = 54.48%

(e) State $p4$, Initial. (See Fig. 18.) Same as state $p3$, Final.

(f) State $p4$, Final. (See Fig. 19.) Row probabilities are: 0.91, 0.91, 1.09, 1.09. Column probabilities are: 0.9411, 0.9993, 1.0401, 0.9795, 0.9993, 1.0611, 1.0195, 0.9601.

Agreements = 28.3625

Total = 32

Correlation = 77.27%

(g) State $p5$, Initial. (See Fig. 20.) Row probabilities are: 0.91, 0.91, 1.09, 1.09. Column probabilities are: 0.9223, 0.9793, 1.0193, 0.9599, 0.9793, 1.0399, 0.9991, 0.9409, 0.9793, 1.0399, 1.0823, 1.0193, 0.9991, 1.0609, 1.0193, 0.9599.

Agreements = 49.4487

Total = 64

Correlation = 54.53%

(h) State $p5$, Final. (See Fig. 21.) Row probabilities are: 0.91, 0.91, 1.09, 1.09. Column probabilities are: 0.9411, 0.9993, 1.0401, 0.9795, 0.9993, 1.0611, 1.0195, 0.9601.

Agreements = 28.3618

Total = 32

Correlation = 77.26%

(i) State $p6$, Initial. (See Fig. 22.) Row probabilities are: 0.91, 0.91, 1.09, 1.09. Column probabilities are: 0.9317, 0.9893, 1.0297, 0.9697, 0.9893, 1.0505, 1.0093, 0.9505, 0.9697, 1.0297, 1.0717, 1.0093, 0.9893, 1.0505, 1.0093, 0.9505.

Agreements = 49.4444

Total = 64

Correlation = 54.51%

(j) State $p6$, Final. (See Fig. 23.) Row probabilities are: 0.91, 0.91, 1.09, 1.09. Column probabilities are: 0.9411, 0.9993, 1.0401, 0.9795, 0.9993, 1.0611, 1.0195, 0.9601.

Agreements = 28.3596

Total = 32

Correlation = 77.25%

(k) State $p7$. (See Fig. 24.)

Agreements = 32

Total = 32

Correlation = 100%

8. Correlation Determination for Actual Short Code

The same considerations as for the preceding part of this article apply here except that, since two of the code component lengths are different, the probability weights differ as shown in Table 2.

Table 2. Short-code components' unbalance

Code component	Total bits	Number of ones	Number of zeros	Probability weight	
				of ones	of zeros
cl, CL	2	1	1	1	1
x, X	11	6	5	1.09	0.91
a, A	31	16	15	1.03	0.97
b, B	7	4	3	1.14	0.86
c, C	15	8	7	1.07	0.93

The correlations in the course of short-code acquisition are determined, as before, in the following.

(a) Reset State, Initial. (See Fig. 14.) Again there is no need for considering probability weights for this function.

Correlation = 0%

(b) Reset State, Final. (See Fig. 15.) Row probabilities are: 0.91, 0.91, 1.09, 1.09. Column probabilities are: 0.7758, 0.8158, 1.0814, 1.0284, 1.1832, 1.2442, 0.9478, 0.8926.

Agreements = 23.8329

Total = 32

Correlation = 48.96%

(c) State $p3$, Initial. (See Fig. 17.) Row probabilities are: 0.8281, 0.8281, 0.9919, 0.9919, 1.1881, 1.1881, 0.9919, 0.9919. Column probabilities are: 0.7525, 0.7991, 1.0592, 0.9975, 1.1477, 1.2187, 0.9194, 0.8658, 0.9194, 0.9762, 1.2815, 1.2187, 1.0592, 1.1248, 0.8485, 0.7991.

Agreements = 81.1340

Total = 128

Correlation = 26.77%

(d) State $p3$, Final. (See Fig. 18.) Row probabilities are: 0.91, 0.91, 1.09, 1.09. Column probabilities are: 0.7525, 0.7991, 1.0592, 0.9975, 1.1477, 1.2187, 0.9194, 0.8658, 0.9194, 0.9762, 1.2815, 1.2187, 1.0592, 1.1248, 0.8485, 0.7991.

Agreements = 49.4693

Total = 64

Correlation = 54.59%

(e) State $p4$, Initial. (See Fig. 18.) Same as State $p3$, Final.

(f) State $p4$, Final. (See Fig. 19.) Row probabilities are: 0.91, 0.91, 1.09, 1.09. Column probabilities are: 0.7758, 0.8238, 1.0920, 1.0284, 1.1832, 1.2564, 0.9386, 0.8926.

Agreements = 28.3305

Total = 32

Correlation = 77.07%

(g) State $p5$, Initial. (See Fig. 20.) Row probabilities are: 0.91, 0.91, 1.09, 1.09. Column probabilities are: 0.6672, 0.7085, 0.9391, 0.8844, 1.0176, 1.0805, 0.8151, 0.7676, 1.0176, 1.0805, 1.4323, 1.3489, 1.1724, 1.2449, 0.9391, 0.8844.

Agreements = 49.6844

Total = 64

Correlation = 55.26%

(h) State $p5$, Final. (See Fig. 21.) Row probabilities are: 0.91, 0.91, 1.09, 1.09. Column probabilities are: 0.7758, 0.8238, 1.0920, 1.0284, 1.2564, 0.9478, 0.8926.

Agreements = 28.4033

Total = 32

Correlation = 77.52%

(i) State $p6$, Initial. (See Fig. 22.) Row probabilities are: 0.91, 0.91, 1.09, 1.09. Column probabilities are: 0.7215, 0.7661, 1.0156, 0.9564, 1.1004, 1.1684, 0.8815, 0.8301, 0.9551, 1.0142, 1.3443, 1.2660, 1.1004, 1.1684, 0.8815, 0.8301.

Agreements = 49.5619

Total = 64

Correlation = 54.88%

(j) State $p6$, Final. (See Fig. 23.) Row probabilities are: 0.91, 0.91, 1.09, 1.09. Column probabilities are: 0.7758, 0.8238, 1.0920, 1.0284, 1.1832, 1.2564, 0.9478, 0.8926.

Agreements = 28.3880

Total = 32

Correlation = 77.43%

(k) State $p7$. (See Fig. 24.)

Agreements = 32

Total = 32

Correlation = 100%

A summary of correlations is shown in Table 3.

Table 3. Summary of correlations in all program states for idealized, normal, and short codes

Program state	Receiver coder output	Component being acquired	Correlation, %					
			Idealized		Normal code		Short code	
			Initial	Final	Initial	Final	Initial	Final
Reset	0	*cl*	0	50	0	53.14	0	48.96
p1	0	—	50	50	53.14	53.14	48.96	48.96
p2	0	—	50	50	53.14	53.14	48.96	48.96
p3	$\bar{X}A$	*x*	25	50	28.15	54.48	26.77	54.59
p4	$\bar{X}A$	*a*	50	75	54.48	77.27	54.59	77.07
p5	$\bar{X}B$	*b*	50	75	54.53	77.26	55.26	77.52
p6	$\bar{X}C$	*c*	50	75	54.51	77.25	54.88	77.43
p7	$\bar{X}(AB + BC + AC)$	—	100	100	100	100	100	100

E. *Ranger 7* Tracking Data Analysis

1. Introduction

The *Ranger 7* spacecraft was launched with the *Atlas/Agena B* booster system from Cape Kennedy on July 28, 1964. Liftoff occurred at 16:50:07.873[1] Greenwich Mean Time[2] (GMT in hours, minutes, and seconds), and injection into the lunar transfer orbit at 17:20:01.0.[1] The DSIF Stations tracked the spacecraft from shortly after injection until lunar impact, which was recorded at 13:25:50.029[3] on July 31, 1964. Actual station tracking periods, together with nominal view periods, may be seen in Table 4. The ground commands sent to the spacecraft by the DSIF Stations are presented in Table 5.

2. Tracking Performance

DSIF Stations provided continuous angular and doppler tracking data from initial acquisition by DSIF 59 at 17:20:50, July 28, until lunar impact at 13:25:50.029, July 31. In general, the over-all quality of the tracking data was extremely good. Data types used in the Orbit Determination Program (ODP) were angular data taken during the first pass over DSIF 41 and 51, two-way

[1]Liftoff and injection times reported by AMR.

[2]All times referred to will be GMT unless otherwise noted.

[3]Impact time recorded at DSIF 12 does not include signal propagation time correction.

Table 4. Nominal[a] view periods versus actual tracking at DSIF Stations

Date (1964)	DSIF Station	Nominal rise (GMT)	Nominal set (GMT)	Nominal view period	Acquisition by station	Loss of signal by station	Actual view period
July 28	51	17:21:17	17:32:00	$00^h10^m43^s$	17:21:38	17:32:55	$00^h11^m17^s$
↓	59	17:21:17	17:32:00	$00^h10^m43^s$	17:20:50	17:37:53	$00^h17^m03^s$
	41	17:36:54	00:46:21[b]	$07^h09^m27^s$	17:35:24	01:17:00	$07^h41^m36^s$
↓	51	20:42:52	08:28:04[b]	$11^h45^m12^s$	20:45:50	08:54:29	$12^h08^m39^s$
July 29	12	07:11:54	18:36:01	$11^h24^m07^s$	06:44:10	18:45:35	$12^h01^m25^s$
↓	41	14:38:45	01:24:04[b]	$10^h45^m19^s$	14:13:55	01:49:00	$11^h35^m05^s$
↓	51	22:00:10	08:48:32[b]	$10^h48^m22^s$	22:02:45	09:12:03	$11^h09^m18^s$
July 30	12	07:20:28	18:59:03	$11^h38^m35^s$	06:55:30	18:59:49	$12^h04^m19^s$
↓	41	14:59:08	01:31:08[b]	$10^h32^m00^s$	14:36:03	01:59:00	$11^h22^m57^s$
↓	51	22:14:05	08:53:41[b]	$10^h39^m36^s$	22:13:17	09:14:37	$11^h01^m20^s$
July 31	12	07:22:02	13:25:50[c]	$06^h03^m48^s$	07:00:56	13:25:50	$06^h24^m54^s$

[a]Based on 5-deg elevation angle.
[b]Set occurs on next day after rise.
[c]Time of lunar impact.

Table 5. Ground commands sent to *Ranger 7* spacecraft by DSIF Stations

Command[a]	Initiated (date/GMT)	Verified[b] (GMT)	Sent by DSIF Station	Associated T/M event blips recorded at station
RTC-0	7/28/21:15:00	21:15:38	41	N. A.
RTC-0	7/28/21:16:00	21:16:38	41	N. A.
RTC-3	7/28/21:19:00	21:19:38	41	Channel B-20 at 21:19:38
RTC-0	7/29/08:50:00	08:50:39	12	N. A.
RTC-0	7/29/08:52:00	08:52:39	12	N. A.
SC-1	7/29/08:54:00	08:54:40	12	Channel B-20 at 08:54:41
SC-2	7/29/08:56:00	08:56:41	12	Channel B-20 at 08:56:42
SC-3	7/29/08:58:00	08:58:41	12	Channel B-20 at 08:58:42
RTC-0	7/29/09:36:00	09:36:38	12	N. A.
RTC-0	7/29/09:38:00	09:38:39	12	N. A.
RTC-3	7/29/09:40:00	09:40:39	12	Channel B-20 at 09:40:41
RTC-4	7/29/10:00:00	10:00:38	12	Channel B-20 at 10:00:40
RTC-0	7/29/11:21:00	11:21:38	12	N. A.
RTC-0	7/29/11:23:00	11:23:39	12	N. A.
RTC-3	7/29/11:25:00	11:25:39	12	Channel B-20 at 11:25:43
RTC-0	7/31/11:15:30	11:16:08	12	N. A.
RTC-0	7/31/11:17:30	11:18:09	12	N. A.
SC-4	7/31/11:19:30	11:20:10	12	Channel B-20 at 11:20:13
SC-5	7/31/11:21:30	11:22:10	12	Channel B-20 at 11:22:12
SC-6	7/31/11:23:30	11:24:10	12	Channel B-20 at 11:24:13
RTC-0	7/31/11:51:00	11:51:38	12	N. A.
RTC-0	7/31/11:53:00	11:53:39	12	N. A.
RTC-8	7/31/11:55:00	11:55:38	12	Channel B-20 at 11:55:54
RTC-6	7/31/12:52:08	12:25:47	12	Channel B-20 at 12:25:54

[a]The commands are defined as follows:

RTC-0 Clear spacecraft command subsystem.

RTC-3 Antenna switchover.

RTC-4 Initiate midcourse maneuver sequence.

RTC-6 Initiate terminal maneuver sequence.

RTC-8 Maneuver override (used prior to RTC-6 because no terminal maneuver was necessary, but CC&S commands to the TV subsystem for both turn-on and switching to full power were desired).

SC-1 Midcourse maneuver roll duration.

SC-2 Midcourse maneuver pitch duration.

SC-3 Midcourse maneuver velocity increment.

SC-4 Terminal maneuver first pitch duration.

SC-5 Terminal maneuver yaw duration.

SC-6 Terminal maneuver second pitch duration.

[b]Verified by ground station read-write-verify (RWV) system.

doppler taken during the first pass over DSIF 59, and two-way doppler taken during all passes over DSIF 12, 41, and 51. A summary of the data used in the ODP, together with the data statistics, is given in Table 6. The relative quality of tracking data taken during each pass and at each station may be obtained by comparing the standard deviations, the root-mean-squares, and the first moments of the data as listed in the table. As can be seen, in general each orbit represents an improvement over the previous orbit with respect to the data statistics. Exceptions to this pattern are more indicative of the particular selection criteria used in the (exceptional) orbit, for instance, DACO XB, than of the addition to the orbit of poorer quality data.

In general, DSIF Station operations were effectively implemented. For instance, after first pass over DSIF Stations 59, 51, and 41, the spacecraft was in two-way lock at all times and a minimum of good data was lost during station transfers. During first pass over DSIF 59, 51, and 41, however, several difficulties were encountered. Although both DSIF 51 and 59 acquired the spacecraft quite soon after injection, neither was very successful in obtaining good two-way data during the pass. Both stations were unable to maintain their receivers in continuous lock, with DSIF 59 particularly evidencing trouble in locating and following the spacecraft. Moreover, both DSIF 51 and 59 indicated certain data as being good with their data condition code, when in fact the data was unusable. From the period 17:28:41 to 17:29:06, DSIF 51 and 59 reported good two-way data, a clearly impossible situation. At this time the problems appear to be at least partially due to the high angular rates encountered during the pass.

During the first pass transfer from DSIF 51 to DSIF 41, a gap occurred from 17:35:11 until 17:38:02 in which neither station had the spacecraft in two-way lock. When DSIF 41 acquired two-way lock at 17:38:02, it was unable to obtain good two-way doppler until 17:54:02. This problem appears to be due to a wrong connection in the mechanical system at DSIF 41; no further trouble was encountered after the correct connections were made at approximately 17:53:00.

During the remainder of the mission two minor problems arose at DSIF 41. On occasion 100- or 200-cycle dropouts occurred in the doppler when the last two digits of the doppler were zero. This was evidently a

Table 6. Summary of DSIF tracking data used in *Ranger 7* spacecraft orbit computations

Orbit ID	DSIF Station	Data	Beginning time (date/GMT)	Ending time (date/GMT)	Number of points	Standard deviation[a]	Root mean squared (rms)[a]	First moment[a]
Predict orbit (XA)	59	CC3	7/28/17:22:28	7/28/17:28:53	8	0.2930	0.3490	−0.1900
	41	HA	7/28/17:40:02	7/28/17:51:02	10	0.0221	0.0460	−0.0404
	41	Dec	7/28/17:40:02	7/28/17:51:02	10	0.0071	0.0191	−0.0177
	51	CC3	7/28/17:22:28	7/28/17:30:43	6	0.7600	0.7890	−0.2140
	51	HA	7/28/17:21:56	7/28/17:30:16	22	0.0523	0.1960	0.1890
	51	Dec	7/28/17:21:56	7/28/17:30:16	21	0.0217	0.0460	0.0405
Injection conditions evaluation orbit (XA)	59	CC3	7/28/17:22:28	7/28/17:28:53	8	0.4290	0.4810	0.2180
	41	CC3	7/28/17:54:32	7/28/18:38:32	43	0.0382	0.0387	−0.0065
	41	HA	7/28/17:40:02	7/28/18:39:02	55	0.0115	0.0962	−0.0955
	41	Dec	7/28/17:40:02	7/28/18:39:02	55	0.0078	0.0332	−0.0323
	51	CC3	7/28/17:29:03	7/28/17:30:43	6	0.7580	0.3010	2.9100
	51	HA	7/28/17:21:56	7/28/17:30:16	21	0.0152	0.0981	0.0970
	51	Dec	7/28/17:21:56	7/28/17:30:16	21	0.0242	0.0513	0.0452
Preliminary pre-midcourse orbit (XA)	59	CC3	7/28/17:22:28	7/28/17:28:53	8	0.2940	0.2940	0.0143
	41	CC3	7/28/17:54:32	7/28/19:51:32	110	0.0127	0.0129	0.0020
Data consistency orbit (XB)	59	CC3	7/28/17:22:38	7/28/17:25:43	6	0.3400	0.3430	−0.0428
	41	CC3	7/28/17:54:32	7/29/00:04:32	263	0.0200	0.0201	0.0017
	51	CC3	7/28/17:28:58	7/29/01:26:32	126	0.0508	0.0527	0.0140
Nominal maneuver orbit (XA)	59	CC3	7/28/17:22:38,	7/28/17:25:43	5	0.1990	0.1990	−0.0088
	41	CC3	7/28/17:54:32	7/29/00:04:32	267	0.0127	0.0129	0.0021
	51	CC3	7/28/17:28:58	7/28/17:30:43	2	0.0273	0.0920	0.0879
	51	CC3	7/28/21:57:32	7/29/03:10:32	228	0.0110	0.0111	−0.0012
Last pre-midcourse orbit (XA)	59	CC3	7/28/17:22:38	7/28/17:25:43	6	0.3310	0.3320	0.0083
	12	CC3	7/29/07:11:32	7/29/08:16:32	66	0.0082	0.0084	0.0019
	41	CC3	7/28/17:54:32	7/29/00:04:32	267	0.0121	0.0121	−0.0001
	51	CC3	7/28/17:28:58	7/28/17:30:43	2	0.0215	0.2300	0.2290
	51	CC3	7/28/21:57:32	7/29/06:59:32	418	0.0106	0.0170	−0.0013
First post-midcourse orbit (XA)	12	CC3	7/29/10:41:32	7/29/18:41:32	471	0.0175	0.0175	−0.0006
	41	CC3	7/29/18:44:32	7/29/19:00:32	16	0.0158	0.0172	0.0067
Second post-midcourse orbit[b] (XA)	12	CC3	7/29/10:41:32	7/29/18:41:32	470	0.0115	0.0115	−0.0002
	41	CC3	7/29/18:44:32	7/30/01:40:32	392	0.0193	0.0193	0.0003
	51	CC3	7/30/01:52:32	7/30/06:46:32	263	0.0158	0.0159	−0.0014
Third post-midcourse orbit[b] (XA)	12	CC3	7/29/10:41:32	7/29/17:50:32	372	0.0090	0.0090	0.0010
	12	CC3	7/30/08:23:32	7/30/17:55:32	563	0.0089	0.0089	−0.0002
	41	CC3	7/29/18:46:32	7/30/00:23:32	295	0.0176	0.0176	0.0014
	41	CC3	7/30/19:01:32	7/30/22:26:32	201	0.0240	0.0241	−0.0015
	51	CC3	7/30/01:52:32	7/30/06:46:32	256	0.0140	0.0140	0.0002
Fourth post-midcourse orbit[b] X(D)	12	CC3	7/29/11:31:32	7/29/17:50:32	341	0.0086	0.0086	0.0010
	12	CC3	7/30/08:23:32	7/30/17:56:32	564	0.0089	0.0089	−0.0001
	41	CC3	7/29/18:46:32	7/30/00:23:32	295	0.0176	0.0177	0.0013
	41	CC3	7/30/19:01:32	7/30/23:39:32	264	0.0239	0.0240	−0.0010
	51	CC3	7/30/01:52:32	7/30/06:46:32	256	0.0140	0.0140	0.0005
	51	CC3	7/30/23:44:32	7/31/06:50:32	365	0.0180	0.0180	−0.0006

[a]Units are cycles for doppler and degrees for angles.
[b]For brevity some small data samples have been omitted.

Table 6. Summary of DSIF tracking data used in *Ranger 7* spacecraft orbit computations (Cont'd)

Orbit ID	DSIF Station	Data	Beginning time (date/GMT)	Ending time (date/GMT)	Number of points	Standard deviation[a]	Root mean squared (rms)[a]	First moment[a]
Fifth post-midcourse orbit[b] X(D)	12	CC3	7/29/11:37:02	7/29/17:43:02	38	0.0032	0.0032	0.0004
	12	CC3	7/30/08:25:02	7/30/17:48:02	58	0.0016	0.0016	0.0001
	12	CC3	7/31/08:20:32	7/31/10:59:32	151	0.0092	0.0092	0.0000
	41	CC3	7/29/18:51:02	7/30/00:17:02	36	0.0083	0.0085	0.0017
	41	CC3	7/30/19:06:02	7/30/23:35:32	29	0.0071	0.0071	0.0005
	51	CC3	7/30/01:53:32	7/30/06:46:32	31	0.0056	0.0056	−0.0001
	51	CC3	7/30/23:54:02	7/31/07:14:32	64	0.0114	0.0115	−0.0017

[a] Units are cycles for doppler and degrees for angles.

[b] For brevity some small data samples have been omitted.

purely mechanical problem in one of the counters. During third pass a gradual reduction in signal strength occurred, dropping from about −119 dbm at the beginning of the pass to about −126 dbm at the end of the pass. At present, this problem appears to have been caused by a marginal power supply at DSIF 41.

3. Pre-Midcourse Phase

a. Angular tracking. Preliminary analysis of the angular tracking data from DSIF Stations 41 and 51 indicates that the present correction polynomials used to describe the systematic angular pointing error are not adequate. This is evidenced by both the large biases and standard deviations encountered in the angular data from DSIF 41 and 51. The corrections used for *Ranger 7* were derived primarily from a series of horizon-to-horizon optical star tracks conducted at DSIF 41 and 51 in 1961–62. These correction polynomials attempt to remove optical pointing error, but past missions indicate they do not remove total pointing error. The situation is further complicated by the recent L- and S-band conversion work at DSIF 41 and 51. This work has caused the correction coefficients to be even less adequate in removing pointing errors as is shown by recent star tracks conducted at DSIF 41 and 51 after the L- and S-band conversion.

b. Doppler tracking. As noted, very little good doppler was obtained until about 17:54 when DSIF 41 began receiving good two-way doppler. DSIF 41 continued to transmit in the two-way mode until 21:56:02, at which time DSIF 51 assumed the transmitting assignment and kept it until 23:09:02. It was transferred at that time to DSIF 41, which retained it until the end of its pass at 00:14:02. DSIF 51 then transmitted from this time until 07:09:02 at which time DSIF 12 began transmitting, obtaining approximately 3 hr of good two-way doppler before midcourse maneuver.

4. Midcourse Maneuver Phase

Midcourse motor burn was initiated at approximately 10:27:09 and was cut off at about 10:27:58. Total doppler shift was on the order of −183 cycles. During this phase, DSIF 12 took 1-sec doppler samples.

5. Post-Midcourse Phase

For post-midcourse orbit computations, only two-way doppler from DSIF 12, 41, and 51 was used. The over-all quality of this data was excellent, as may be seen by inspecting the residuals[4] from post-midcourse passes over DSIF 41, 51, and 12. At 11:00:02, July 31, DSIF 12 stopped using the atomic frequency standard and began using the voltage controlled oscillator (VCO). One can obtain a good estimate of the relative stability and ensuing reduction of noise of the atomic frequency standard as compared to the voltage controlled oscillator by noticing the large increase in the magnitude of the residuals after 11:00:02. At 12:25:18 DSIF 12 changed from 1-min doppler samples to 10-sec doppler samples, which accounts for the very large increase in the magnitude of the residuals after 12:25:18.

[4] The term "residual" is defined as the ODP computed value minus the observed value.

References

1. "Receiver Modifications," *SPS 37-25,* Vol. III, pp. 5–6, Jet Propulsion Laboratory, Pasadena, California, January 31, 1964.

2. "*Surveyor* Project," *SPS 37-27,* Vol. III, p. 9, Jet Propulsion Laboratory, Pasadena, California, May 31, 1964.

3. "*Surveyor* Project," *SPS 37-28,* Vol. III, p. 13, Jet Propulsion Laboratory, Pasadena, California, July 31, 1964.

4. "*Mariner* C 100-kw Transmitter," *SPS 37-25,* Vol. III, pp. 18–19, Jet Propulsion Laboratory, Pasadena, California, January 31, 1964.

5. "Mark I Ranging Subsystem," *SPS 37-20,* Vol. III, pp. 12–15, Jet Propulsion Laboratory, Pasadena, California, March 31, 1963.

III. Space Flight Operations Facility

A. Display Systems

1. Closed Circuit TV System

The closed circuit TV display system within the SFOF has been designed fundamentally to increase the effectiveness and efficiency of space flight operations themselves. The 95 closed circuit TV cameras and the 212 closed circuit TV monitors are used specifically to provide 3 distinct capabilities.

The first of these capabilities is to permit remote viewing of display boards and devices. The second is to serve as a prime display of manually generated information required for simultaneous viewing in several separate areas. The third is to facilitate operational control by means of area surveillance.

In all cases the principal function performed is that of simplifying personnel traffic and action required to collect and receive information.

In its present configuration the closed circuit TV system affords two general means of TV viewing: (1) by console monitors which are 14-in. TV tubes placed in the operational consoles, permitting a nominal viewing distance of from 2 to 3 ft (Fig. 1); (2) by banks of 23-in. TV monitor tubes mounted as wall displays (Fig. 2).

The prime value of closed circuit TV (i.e., its ability to display most any type or format of information without a change to the system) also forms its most serious operational limitation. A continuing effort is required in the SFOF to assure that televised displays are, in fact, readable by human beings.

Where TV is used to relay to remote points a fixed display or display format, such as a chalk board with magnetic letters or the typing of a teletype machine, no serious problems ensue. The lighting, camera lenses, and character sizes are all controlled to present a display that is indeed readable. On the other hand, where the copy

Fig. 1. Typical console TV installation

or display material which is being televised is readily changeable (for example typewritten or handwritten material) the problem is more complex. To minimize this problem, it has been necessary to extend considerable training to personnel using the closed circuit TV system to assure its continuing value.

The prime criterion for TV viewing is the angular height and width of characters or detail. Thus, viewing distance controls the character size and this, together with screen size, controls the screen information density. Therefore, a wide disparity exists in the information density upon a screen designed to be viewed by a group of people as opposed to a screen designed for individual viewing.

If information to be distributed by TV must appear simultaneously on both group and individual monitors, it is apparent that the lower density of information required for group viewing must be a controlling factor in the design of the original material.

In actual space flight operations, as well as operational tests conducted in the SFOF to date, an increasing desire to elevate the information density now in use has been in evidence. The obvious conclusion is to locate TV screens closer to the individuals who wish to view them.

This is not, however, the complete answer although study is presently being given to the possibility of relocating the banks of wall monitors so that smaller groups

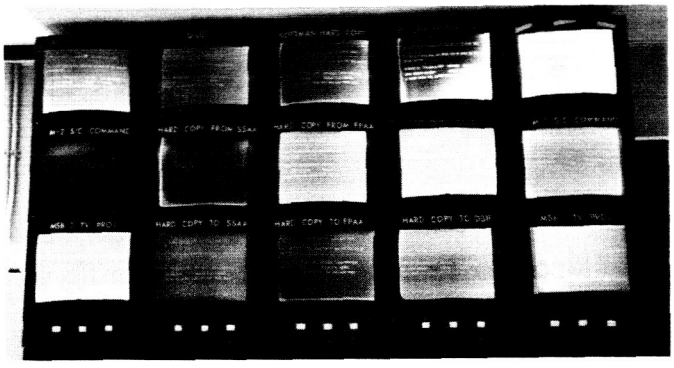

Fig. 2. Typical wall-mounted TV installation

of them may be arranged throughout an area to permit closer viewing. The nature of TV presents a limit to this screen information density which is unfortunately much less than that of the film displays with which most personnel are familiar. The fact that a TV picture actually consists of a number of raster lines or substantially horizontal and parallel, but not contiguous, slices of the original image is the basic problem.

For pictorial images the space missing between lines is unnoticeable (Fig. 3). At optimum viewing distances, the human eye effectively integrates the lines it sees into an apparently continuous picture.

The effect of slicing alpha numeric characters is such that if eight or less of these lines is used to formulate a character, the human eye may be able to resolve the image but cannot reliably identify all alpha numeric characters

Fig. 3. TV pictorial image viewed from line-fusion distance

so presented (Fig. 4). Reliable readability requires that each character be composed of at least 9 such elements and optimally, 15 (Fig. 5). This requirement is independent of both viewing distance and screen size and forms the maximum density of alpha numeric information which may be presented effectively by means of TV.

To obviate these difficulties within the SFOF, particular care has been taken to design original fixed displays with the particular viewing positions in mind to maintain the optimum condition.

Where changeable material is presented, as in the case of the hard copy TV cameras illustrated in Fig. 6(a), special frames have been designed which force the use of precisely the correct size of original copy [Fig. 6(b)]. Forms have been designed (Fig. 7) which are lightly printed with blocks visible to the naked eye but which are not "picked up" by the TV camera. These blocks indicate the correct size and spacing for characters.

2. Spacecraft SFOF Functional Model System

The spacecraft model system, located in the spacecraft performance analysis area of the SFOF, has been provided to assist cognizant personnel in evaluating performance and/or planning corrective maneuvers to be executed by the spacecraft.

The system (Fig. 8) provides a means of simulating the spacecraft and its motions in celestial environment. The

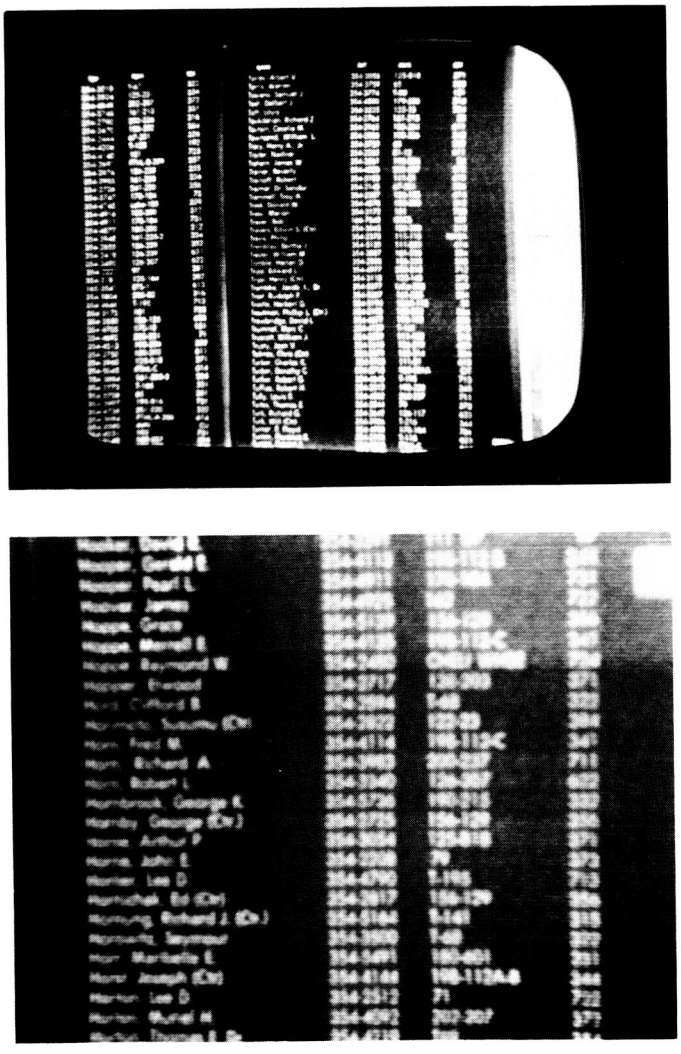

Fig. 4. TV images devoting seven raster lines per character

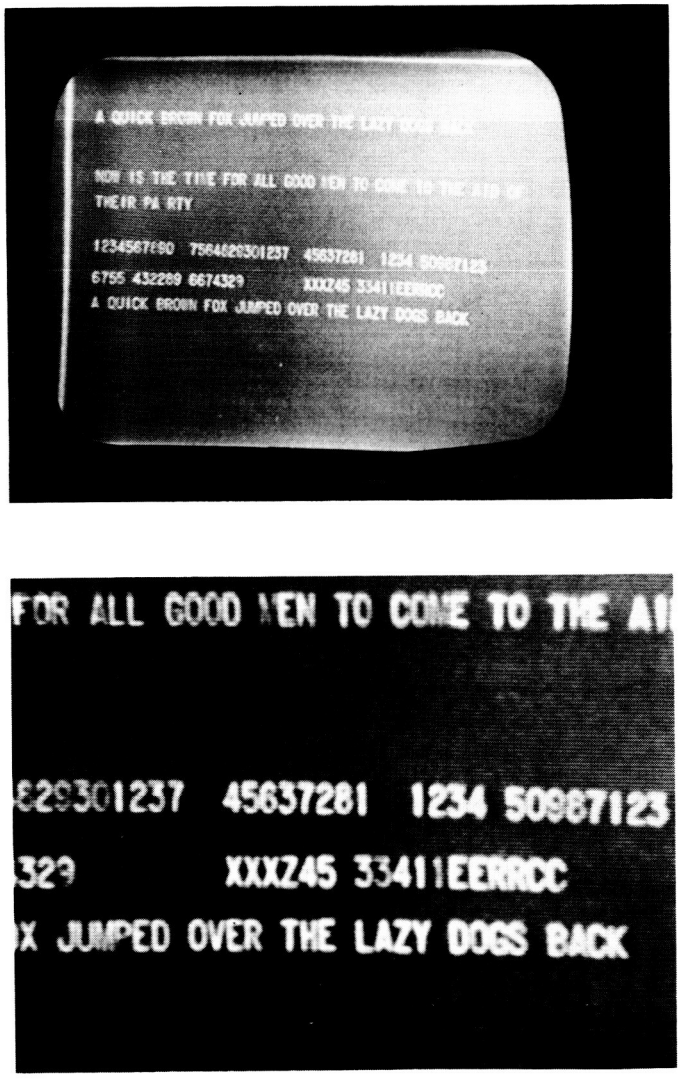

Fig. 5. TV images devoting ten scan lines per character

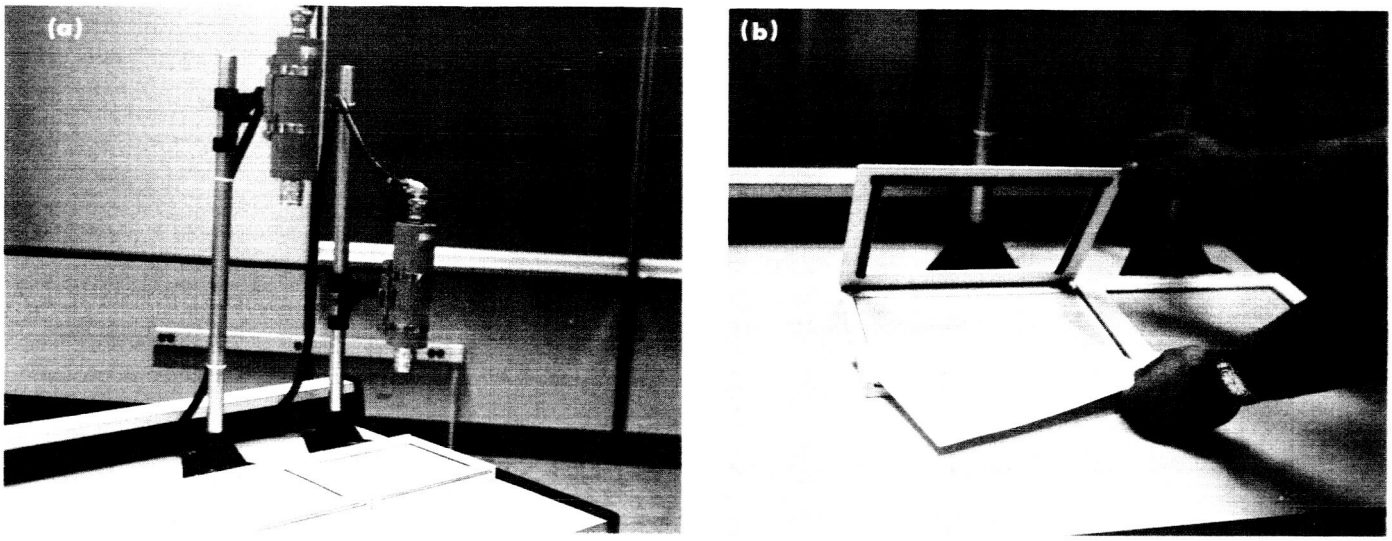

Fig. 6. Hard copy TV cameras and special frames

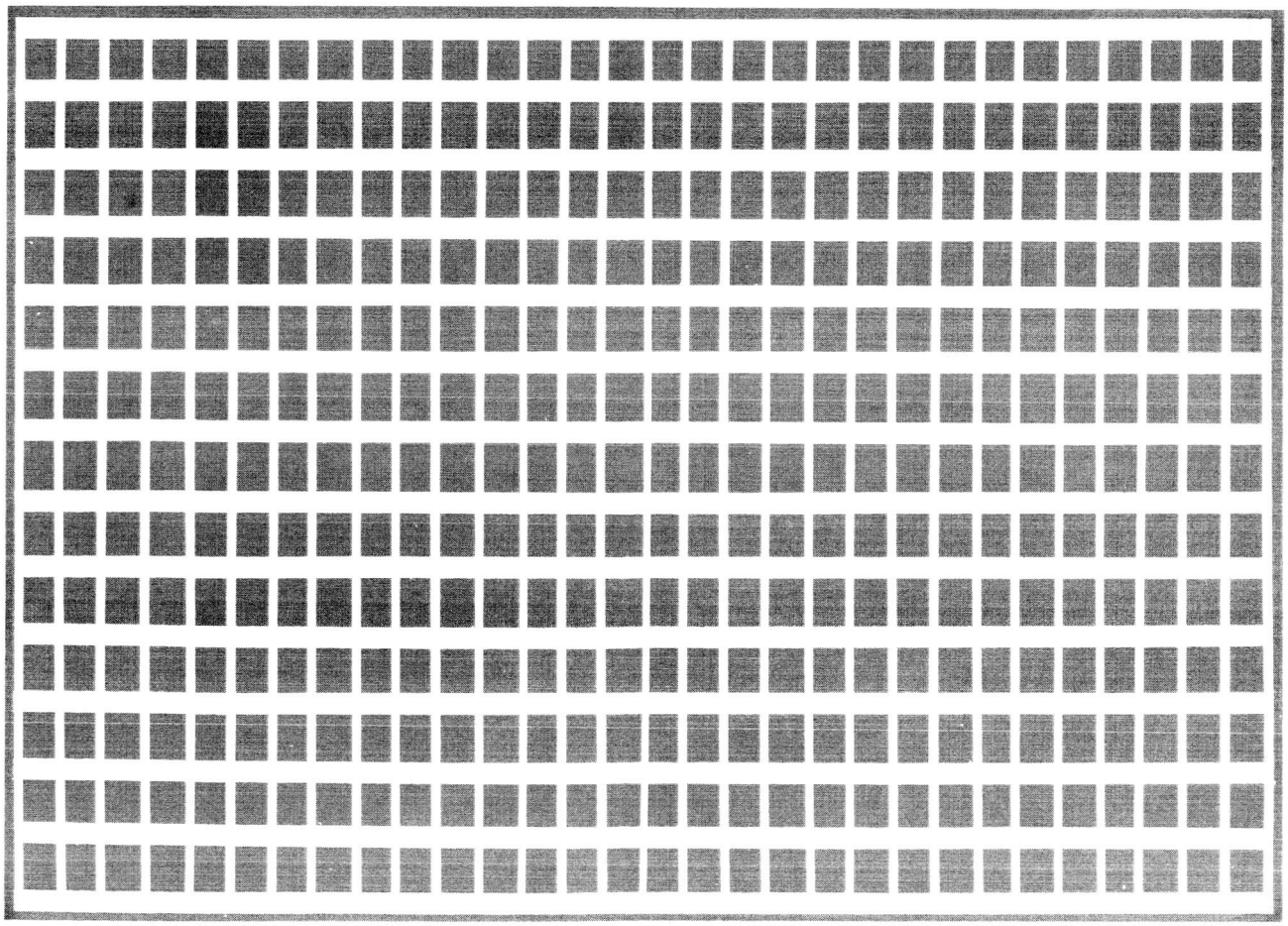

TO USE: PRINT ONE LETTER IN EACH BLOCK. FILL THE WHOLE BLOCK.
TYPING: IGNORE BLOCKS. USE CAPS ONLY, STAY INSIDE BORDER

Fig. 7. Hard copy makeup forms

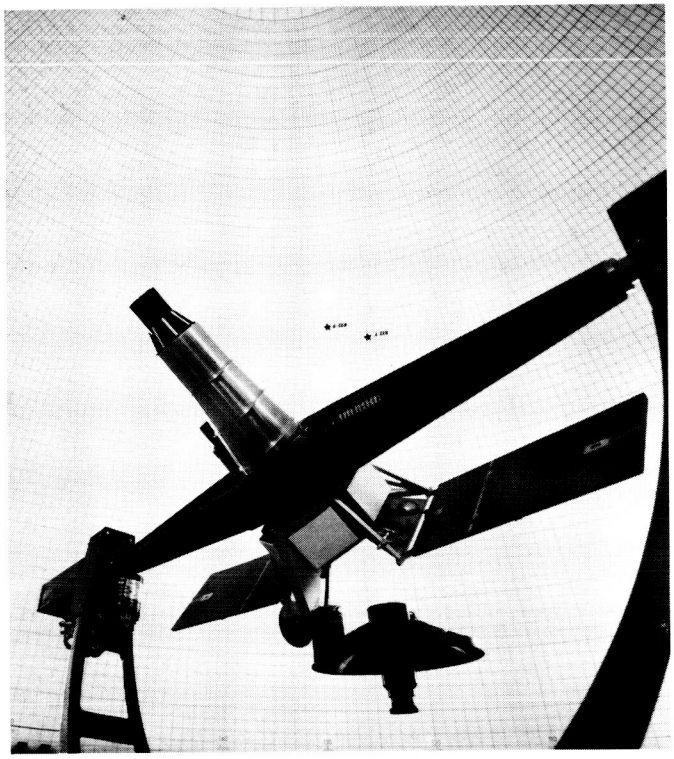

Fig. 8. Spacecraft model system

system consists of four basic components: the hemispherical enclosure, the active model and gimbal assembly, the computer/control console, and a power supply rack.

The interior surface of the 17½-ft hemisphere is marked with azimuth and elevation lines which correspond to a spacecraft-centered coordinate system defined by the ecliptic plane and the direction of the vernal equinox.

In this coordinate system the pertinent stellar bodies are located at fixed positions on the hemisphere while the positions of the solar bodies are a function of the particular trajectory and are available from the computer trajectory program. The northern and southern ecliptic hemispheres are represented in different colors, and thus the full environment of the spacecraft is illustrated.

The *Ranger* spacecraft model is mounted on a three-degrees-of-freedom gimbal assembly at the center of the hemisphere. The model contains small optical projectors which illuminate the interior surface of the hemisphere with scaled representations of the spacecraft sensors fields of view. The *Ranger* model is removable and can be replaced by models representing other spacecraft (i.e., *Mariner* or *Surveyor*).

Fig. 9. Control console

The automated gimbal assembly is driven from the control console shown in Fig. 9. This console contains the equipment necessary to place the model in any required initial attitude, and then to duplicate the attitude motions of the spacecraft in space. As the spacecraft refers to no coordinate system other than its own, the console contains a small analog computer which provides the conversion from the input commands, in body-centered coordinates to gimbal-referenced motion. The conversion requires the dynamic solution of three simultaneous differential equations.

The system can be used to visually analyze a spacecraft maneuver prior to actually performing the maneuver. The projected view fields provide the operator with a continuous illustration of what the spacecraft should sense with its various sensors during the course of its flight.

B. A Model for Systems Reliability Analysis

During this reporting period an analytical model for predicting the operational reliability of the DSN ground support system was constructed. The model assumes a single-thread system with repair. Redundancy is considered to the extent that a failed item of equipment may be replaced by an available equivalent standby in lieu

of repairing the failed item. The model considers only equipment reliability; human factors considerations are excluded.

The basic element of the model is an operation, O, about which these assumptions are made:

(1) Associated with O are certain given equipments $E_1, \cdots, E_q$ with repair times $r_1, \cdots, r_q$ and mean-times-between-failure $m_1, \cdots, m_q$.

(2) Every equipment is in a failed state, an operable state, or in a "turned off" state.

(3) Given O, there is a fixed number $t \geqq 0$ such that O is completed if and only if $E_1, \cdots, E_q$ are concurrently operable for an interval of time of length, t.

(4) There is an interval of concern $[0, T]$ such that $T \geqq t$ and O cannot begin prior to 0 and for success, O must be completed at or before T. At 0 nothing is known of the history of any equipment.

(5) If, while O is in progress, an equipment E_i fails, O must cease. Immediately after E_i fails, repair is begun. Repair is not interrupted. After repair is accomplished (time r_i after failure) O recommences from its beginning.

(6) All equipment failures are mutually independent.

(7) All equipment failures are exponentially distributed.

(8) After repair (or replacement) of a failed equipment (except that the time is later), all conditions relevant to the accomplishment of O are the same as they were at the beginning of the first attempt to accomplish O.

The following are definitions:

(1) S = the event that O is completed at or before T.

(2) A^0 = the event that all equipments are operable at time 0.

(3) $T(O)$ = the time actually required (including repairs and unsuccessful attempts) to accomplish O.

(4) $Y_1 = \{i : T - r_i < t\}$

(5) $Y_2 = \{1, \cdots, q\} - Y_1$

Then,

$$P(S) = \sum_{i \in Y_2} \int_0^{r_i} P(T(O) \leqq T - \tau) \frac{1}{r_i} d\tau + \sum_{i \in Y_1} \int_0^{T-t} P(T(O) \leqq T - \tau) \frac{1}{r_i} d\tau + P(T(O) \leqq T) \prod_{i=1}^{q} \left(\frac{m_i}{m_i + r_i} \right). \quad (1)$$

Let

$$\Lambda = \sum_{i=1}^{q} \frac{1}{m_i}.$$

$P(T(O) \leqq X)$ is calculated for the case in which $t > 0$.

Let

$$Z(1, X, n) = \left\{ (j(1), \cdots j(n)) : X - \sum_{i=1}^{n} r_{j(i)} \geqq (n+1)t \right\}$$

$$Z(2, X, n) = \left\{ (j(1), \cdots j(n)) : X - \sum_{i=1}^{n} r_{j(i)} < (n+1)t \right\}$$

Clearly

$$Z(1, X, n) \cap Z(2, X, n) = \phi$$

and $Z(1, X, n) \cup Z(2, X, n)$ has q^n elements. Then

$$P(T(O) \leqq X) = e^{-\Lambda t}(1 + Q)$$

where,

$$Q = \sum_{n-1}^{\infty} \left\{ \sum_{j \in Z(2, X, n)} \sum_{K=0}^{n-1} \left[\binom{n}{K} (-1)^K \frac{1}{\prod_{i=1}^{n} m_{j(i)}} \times \int_{u_n} \cdots \int_{u_{K+1}} \int_{u_K} \cdots \int_{u_1} \times \exp\left[-\Lambda \left(\sum_{i=1}^{n} \chi_i \right) \right] d\chi_1 \cdots d\chi_n \right] + \sum_{n=1}^{\infty} \sum_{j \in Z(1, X, n)} \left[\frac{1}{\prod_{i=1}^{n} m_{j(i)}} \left(\frac{1}{\Lambda} (1 - e^{-\Lambda t}) \right)^n \right] \right\} \quad (2)$$

where

$$u_1 = \left[t, X - \sum_{i=1}^{n} r_{j(i)} + t(1-K) - \sum_{i=2}^{n} \chi_i \right)$$

$$\vdots$$

$$u_K = \left[t, X - \sum_{i=1}^{n} r_{j(i)} + t(1-K) - \sum_{i=K+1}^{n} \chi_i \right)$$

$$u_{K+1} = \left[0, X - \sum_{i=1}^{n} r_{j(i)} - Kt - \sum_{i=K+2}^{n} \chi_i \right)$$

$$\vdots$$

$$u_n = \left[0, X - \sum_{i=1}^{n} r_{j(i)} - Kt \right)$$

for

$$X - \sum_{i=1}^{n} r_{j(i)} + t(1-K) > t$$

and j ranges over all n-tuples of integers drawn from $1, \cdots, q$ and $j(i)$ is the ith component of j. Otherwise, the multiple integral has value zero.

For the case $t = 0$, without loss of generality, assume $r_1, \cdots, r_a \leqq T$ and $r_{a+1}, \cdots, r_q > T$. Then

$$P(T(O) \leqq T) = \prod_{i=1}^{q} \left(\frac{m_i}{m_i + r_i} \right) + a - \sum_{i=1}^{a} \left(\frac{m_i}{m_i + r_i} \right) + T \sum_{i=a+1}^{q} \frac{1}{r_i} \tag{3}$$

In this case ($t = 0$) O is accomplished successfully if, and only if, at some instant in $[0, T]$ $E_1, \cdots, E_q$ are simultaneously operable.

The previous situation is generalized such that we have operations $O_1, \cdots, O_M$ and an interval of concern $[0, T_M]$ such that O_1 cannot begin prior to 0 and for success O_M must be complete at or before T_M. Further, O_i must be completed before O_{i+1} can begin. It may be required that between the completion of O_i and the beginning of O_{i+1} there must elapse an interval $\bar{t}_i$. Assume such an interval $\bar{t}_i$ always exists and is such that $\bar{t}_i \geqq 0$. Let the equipments used in O_i be $E_1^i, \cdots, E_{q_i}^i$ with repair times $r_{i1}, \cdots, r_{iq_i}$ and mean-times-to-failure $m_{i1}, \cdots, m_{iq_i}$. Let $M = 2$. Let $T_1 \epsilon [0, T_2]$ be the time at which O_1 is completed. If $E_1^2, \cdots, E_{q_2}^2$ are the equipments used in O_2 let $E_1^2, \cdots, E_{\bar{q}}^2$ be those such that for $j \leqq \bar{q}$, E_j^2 is not used in O_1 or $r_{2j} \leqq \bar{t}_1$ and if $j > \bar{q}$ then E_j^2 is used in O_1 and $r_{2j} > \bar{t}_1$. Let S = the event that O_2 is complete at or before T_2. Then

$$P(S) = C^{(1)} + \sum_{i=1}^{q_1} C_i^{(2)} + \sum_{i=1}^{\bar{q}} C_i^{(3)} + \sum_{j=1}^{\bar{q}} \sum_{i=1}^{q_1} C_{ij}^{(4)} + \sum_{i=\bar{q}+1}^{q_2} C_i^{(5)} + \sum_{j=\bar{q}+1}^{q_2} \sum_{i=1}^{q_1} C_{ij}^{(6)} \tag{4}$$

where

$$C^{(1)} = \int_{t_1}^{T_2 - t_2 - \bar{t}_1} P(T(O_2) \leqq T_2 - T_1 - \bar{t}_1) \cdot P'(T(O_1) = T_1)\, dT \cdot P(A_1) P(A_2) \tag{5}$$

$$C_i^{(2)} = \int_{t_1}^{T_2 - t_2 - \bar{t}_1} P(T(O_2) \leqq T_2 - \bar{t}_1 - T_1) \times \left[\int_0^{r_{1i}} P'(T(O_1) = T_1 - \tau_1) \frac{1}{r_{1i}} d\tau_1 \right] dT_1 P(A_2) \tag{6}$$

$$C_i^{(3)} = \int_{t_1}^{T_2 - t_2 - \bar{t}_1} P'(T(O_1) = T_1) \left[\int_0^{r_{2i}} P(T(O_2) \leqq T_2 - \bar{t}_1 - T_1 - \tau_2) \frac{1}{r_{2i}} d\tau_2 \right] dT_1 P(A_1) \tag{7}$$

$$C_{ij}^{(4)} = \int_{t_1}^{T_2 - t_2 - \bar{t}_1} \int_0^{r_{1i}} \int_0^{r_{2j}} P(T(O_2) \leqq T_2 - \bar{t}_1 - T_1 - \tau_2) \times P'(T(O_1) = T_1 - \tau_1) \frac{1}{r_{1i}} \frac{1}{r_{2j}} d\tau_1 d\tau_2 dT_1 \tag{8}$$

$$C_i^{(5)} = \int_{t_1}^{T_2 - t_2 - \bar{t}_1} P'(T(O_1) = T_1) \left[\int_0^{\bar{t}_1} P(T(O_2) \leqq T_2 - \bar{t}_1 - T_1 - \tau_2) \frac{1}{m_{2i}} e^{(-1/m_{2i})\tau_2} d\tau_2 \right] dT_1 P(A_1) \tag{9}$$

$$C_{ij}^{(6)} = \int_{t_1}^{T_2 - t_2 - \bar{t}_1} \int_0^{r_{1i}} \int_0^{\bar{t}_1} P(T(O_2) \leqq T_2 - \bar{t}_1 - T_1 - \tau_2) \times P'(T(O_1) = T_1 - \tau_1) \frac{1}{r_{1i}} \cdot \frac{1}{m_{2j}} e^{(-1/m_{2j})\tau_2} d\tau_1 d\tau_2 dT_1 \tag{10}$$

where

$$P'(T(O_1) = T_1 + \tau) = \frac{dP(T(O_1) \leqq T_1 + \tau)}{dT_1}$$

$$\frac{dQ}{dT_1} = \sum_{n=1}^{\infty} \sum_{j \epsilon Z(2,X,n)} \sum_{K=0}^{n-1} \binom{n}{K} (-1)^K \frac{1}{\prod_{i=1}^{n} mj(i)} \times \frac{\left(X - \sum_{i=1}^{n} r_{j(i)} - (K+1)t\right)^{n-1}}{(n-1)!}$$

If $t_1 = 0$ then

$$C^{(1)} = P(T(O_2) \leqq T_2 - \bar{t}_1) P(A_1) P(A_2) \tag{11}$$

$$C_i^{(2)} = \int_0^{r_{1i}} P(T(O_2) \leqq T_2 - \bar{t}_1 - \tau_1) \frac{1}{r_{1i}} d\tau_1 P(A_2) \tag{12}$$

$$C_i^{(3)} = \int_0^{r_{2i}} P(T(O_2) \leqq T_2 - \bar{t}_1 - \tau_1) \frac{1}{r_{2i}} d\tau_2 \cdot P(A_1) \tag{13}$$

$$C_{ij}^{(4)} = \int_0^{r_{1i}} \int_0^{r_{2j}} P(T(O_2) \leqq T_2 - \bar{t}_1 - \tau_1 - \tau_2) \times \frac{1}{r_{1i}} \frac{1}{r_{2j}} d\tau_1 d\tau_2 \tag{14}$$

$$C_i^{(5)} = \int_0^{\bar{t}_1} P(T(O_2) \leqq T_2 - \bar{t}_1 - \tau_2) \times \frac{1}{m_{2i}} e^{(-1/m_{2i})\tau_2} d\tau_2 \cdot P(A_1) \tag{15}$$

$$C_{ij}^{(6)} = \int_0^{r_{1i}} \int_0^{\bar{t}_1} P(T(O_2) \leqq T_2 - \bar{t}_1 - \tau_1 - \tau_2) \times \frac{1}{r_{1i}} \frac{1}{m_{2j}} e^{(-1/m_{2j})\tau_2} d\tau_1 d\tau_2 \tag{16}$$

where

$$P(A_1) = \prod_{i=1}^{q_1} \left(\frac{m_{1i}}{m_{1i} + r_{1i}}\right), \quad P(A_2) = \prod_{i=1}^{q_2} \left(\frac{m_{2i}}{m_{2i} + r_{2i}}\right)$$

In the case of M operations $O_1, \cdots, O_M$ to be done in $[0, T_M]$ let A_1 = the event that $E_1^1, \cdots, E_q^1$, are operable at 0; let A_2 = the event that $E_1^2, \cdots, E_{q_2}^2$ are operable at $T_1 + \bar{t}_1, \cdots$, let A_M = the event that $E_1^M, \cdots, E_{q_M}^M$ are operable at $T_{M-1} + \bar{t}_{M-1}$. Then $P(A_1), \cdots, P(A_M)$ are time independent. The expressions for

$$P(S/A_1 \cap \cdots \cap A_M)$$

will be exhibited. From this, the expression for

$$P(S/A_{i_1}^c \cap \cdots \cap A_{i_s}^c \cap A_{i_{s+1}} \cdots \cap A_{i_M})$$

etc., can be deduced. Then

$$\frac{P(S/\bigcap_{i=1}^{M} A_i)}{\prod_{i=1}^{M} P(A_i)} = \int_{X_1} P'(T(O_1) = T_1 \int_{X_2} P'(T(O_2) = T_2 - T_1 - \bar{t}_1) \cdots \int_{X_{M-2}} P'(T(O_{M-2}) = T_{M-2} - T_{M-3} - \bar{t}_{M-3}) \int_{X_{M-1}} P'(T(O_{M-1}) = T_{M-1} - T_{M-2} - \bar{t}_{M-2}) P(T(O_M) \leqq T_M - T_{M-1} - \bar{t}_{M-1}) dT_{M-1} \cdots dT_1 \tag{17}$$

where

$$X_1 = \left[t_1, T_M - \sum_{i=2}^{M} t_i - \sum_{i=1}^{M-1} \bar{t}_i\right]$$

$$X_2 = \left[T_1 + \bar{t}_1 + t_2, T_M - \sum_{i=3}^{M} t_i - \sum_{i=2}^{M-1} \bar{t}_i\right]$$

$$\vdots$$

$$X_j = \left[T_{j-1} + \bar{t}_{j-1} + t_j, T_M - \sum_{i=j+1}^{M} t_i - \sum_{i=j}^{M-1} \bar{t}_i\right]$$

$$\vdots$$

$$X_{M-1} = [T_{M-2} + \bar{t}_{M-2} + t_{M-1}, T_M - \bar{t}_{M-1} - t_M]$$

C. *Surveyor* On-Site Telemetry and Command Data Handling System Modifications

System design of the modifications to the *Surveyor* telemetry and command data handling system was completed during this reporting period. The purpose of the modifications was to integrate the on-site data processing (OSDP) subsystem into the *Surveyor* telemetry and command data handling system. The modifications establish a compatible interface between existing *Surveyor* equipment and the OSDP subsystem; they enable the *Surveyor* equipment to function within the expanded data handling configuration and to output telemetry data directly onto the high-speed data line (HSDL) in the event the OSDP subsystem is unavailable.

A functional block diagram of the *Surveyor* on-site telemetry and command data handling system is shown in Fig. 10. The system consists of the DSN on-site data processing subsystem, the command and data handling console (CDC), the buffering equipment necessary to establish a compatible electrical interface between the CDC and the OSDP subsystem, the communications signal converting equipment necessary to establish a compatible electrical interface between the CDC and the operational communications system and the control, switching, patching and input–output equipment necessary to integrate the CDC and the OSDP subsystem into an operational entity.

The CDC is part of the existing *Surveyor* telemetry and command data handling system. Those functional items added to the system are briefly described here.

The communications signal converter incorporates the electronic circuitry necessary to accept telemetry data and clocking signals from points internal to the CDC and output a serial telemetry bit stream and bit clocking signals to the HSDL modem. The communications signal converter outputs data to the HSDL modem at constant gapless rates. The output is continuous and uninterrupted to allow the "receive end" to maintain synchronism.

The telemetry and command buffer incorporates the registers, address decode logic, line drivers and other electronic circuitry required to accept telemetry and command confirmation data from points internal to the CDC and outputs the data in word parallel form to a computer in the OSDP subsystem. The buffer is connected to the parallel input–output channel of an OSDP subsystem computer.

The registers which store telemetry and command confirmation data are serviced by the computer on an interrupt basis. When a register is loaded and ready for interrogation, an appropriate interrupt signal is sent to the computer from the buffer. Upon receiving an interrupt, the computer interrogates the appropriate register within the allowable holding time.

The buffer utilizes three interrupt channels to the computer: when the telemetry register may be interrogated by the computer; when the command confirmation register may be interrogated by the computer; and when indicating the beginning of a new telemetry data frame.

The input–output equipment shown in Fig. 10 consists of two input–output typewriters, two paper (Mylar) tape readers, two paper (Mylar) tape punches, two spoolers and the associated control units and computer couplers. Reader 1, Punch 1 and Spooler 1 comprise a physically integrated input–output equipment group. Reader 2, Punch 2 and Spooler 2 comprise a second physically integrated input–output group. The tape reader control units and the input–output typewriter and tape punch couplers incorporate the address decoding logic and other electronic circuitry required for control and synchronization of the respective input–output devices.

The manual controls and switching unit incorporates switches, circuits, control devices, indicators, etc. necessary to perform these switching and control functions:

(1) Selection of one configuration which interconnects tape readers to tape reader control units and tape punches to the punch coupler chassis. Each configuration permits the performance of a particular combination of simultaneous input–output functions.

(2) Connection of either input–output typewriter to either typewriter coupler chassis. At any time the two input–output typewriters are on-line through the *W* and *Y* buffers, respectively.

(3) Connection of either tape punch to the punch coupler chassis associated with the computer *Y* buffer. Only one punch is on-line at any time.

(4) Generation of an interrupt signal for each input–output typewriter. The interrupt signal instructs the computer to call for an input–output typewriter

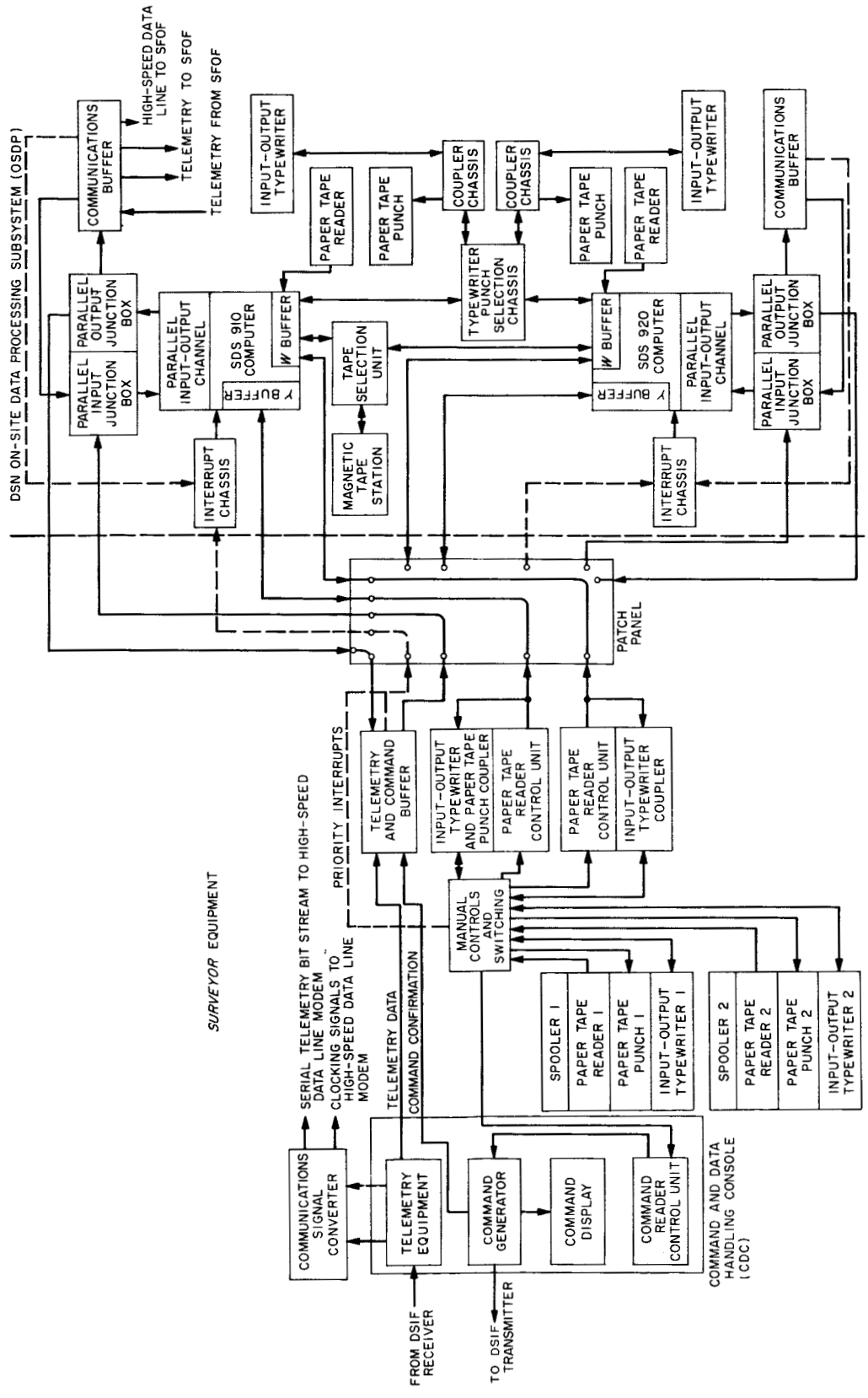

Fig. 10. Surveyor on-site telemetry and command data handling system functional block diagram

input. This is required any time the operator must input data to the computer for program control or the selection of a data processing mode.

The SDS 910 computer is nominally to be used to perform all *Surveyor* telemetry and command data processing. In the event the SDS 910 is unavailable, the SDS 920 may be used for *Surveyor* telemetry and command data handling. The switchover from the SDS 910 to the SDS 920 will be accomplished by means of a patch panel, located at the CDC, and designed to permit switchover in 30 sec or less.

IV. Communications Engineering Developments

A. S-Band Implementation for DSIF

1. TWM for DSIF

a. Summary. Traveling wave maser/closed cycle refrigerator (TWM/CCR) subassemblies are now installed and operating at the Pioneer, Woomera, and Johannesburg Stations. The Canberra and Madrid units are nearly complete and will soon be ready for shipment.

The prototype CCR in the Venus site planetary radar receiver maser was modified in April to use the new Slo-Syn (gearless) drive crosshead. Since then the refrigerator has been in continuous operation for 2750 hr.

b. Woomera installation. The Woomera TWM/CCR installation and checkout was completed on July 20, 1964. At that time the CCR had 304 hr of run time on the antenna. Two normal cooldown cycles had been performed.

Performance tests were made on the antenna at Woomera with the TWM output connected directly to the monitor receiver. Figs. 1 through 5 show recordings or reduced results from recordings made during tests at Woomera.

The following is a summary of system performance based on the Woomera test data:

(1) *Maser gain.* Can be operated at 33- to 37-db gain depending on adjustment of CCR.

(2) *Maser gain stability.*

Gain jitter: 0.1 db (max) peak-to-peak (10 sec).

Long-term gain drift: 0.5 db (max) in 10 hr.

Gain versus antenna position: 0.5 db peak-to-peak (max) for any position.

(3) *System temperature.*

Antenna–maser–monitor receiver: 42°K.

N_2 load–maser–monitor receiver: 100°K.

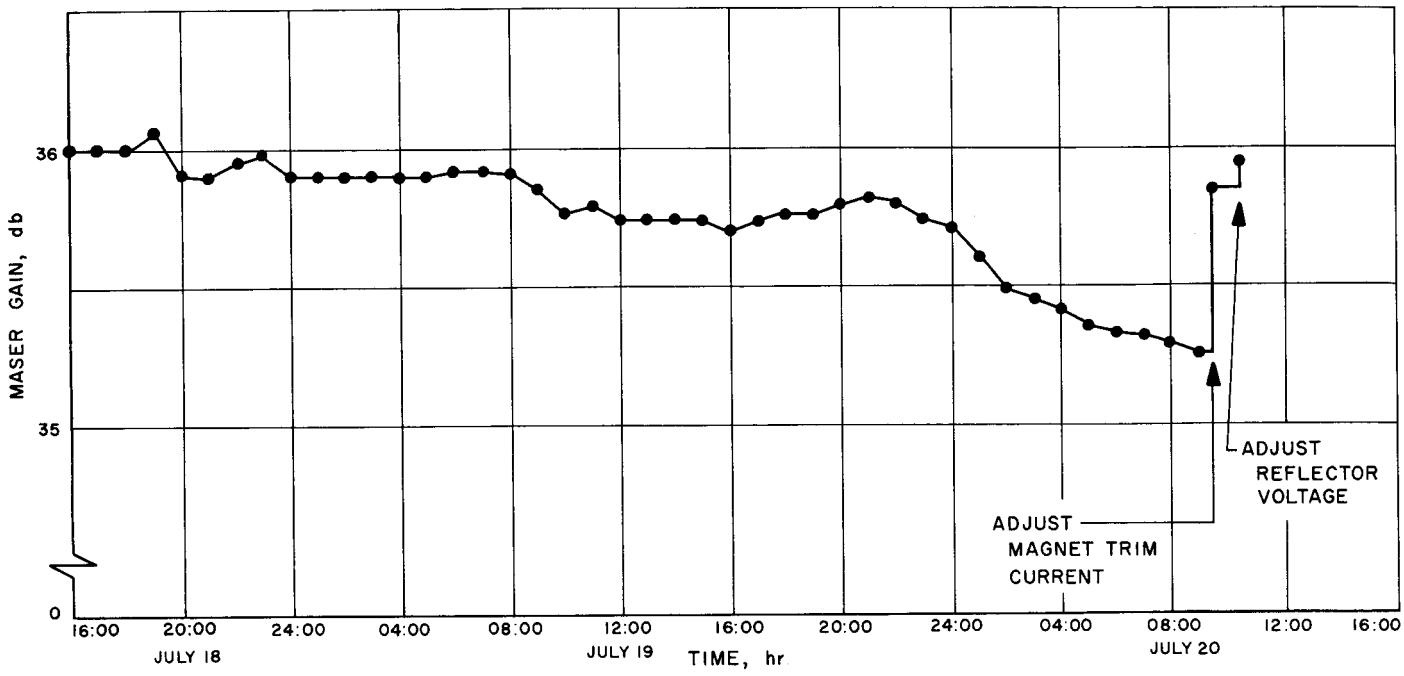

Fig. 1. Gain versus time (41 hr)

Laboratory data for the 2295-Mc TWM/CCR are shown in Table 1; some of this data can be compared with the field performance.

2. Acquisition Aid for DSIF

As a part of the DSIF S-Band Implementation Project, an S-band acquisition aid (SAA) has been developed for the 85-ft antennas. Performance tests of the first system at the Goldstone Pioneer site were reported in the previous issues; this system is being prepared for shipment to the Canberra, Australia, DSIF Station. Installation of the second and third systems at Woomera, Australia, and Johannesburg, South Africa, has been completed; these systems are presently being checked out and calibrated. Documentation of the SAA system is approximately 70% complete.

Table 1. Laboratory performance of TWM

Maser gain at:	
2285 Mc	37 db
2295 Mc	35 db
2305 Mc	32 db
Bandwidth (instantaneous):	
3 db	16 Mc
1 db	10 Mc
Input VSWR at:	
2285 Mc	1.3
2295 Mc	1.15
2305 Mc	1.1
Output VSWR at:	
2285 Mc	1.2
2295 Mc	Below 1.1
2305 Mc	Below 1.1
Maser gain versus pump power:	
0 db below maximum pump power	34.5-db gain
4 db below maximum pump power	35-db gain
9 db below maximum pump power	34-db gain
Maser equivalent input temperature	10°K
Maser gain stability:	
Versus time	
10 sec	0.04 db peak-to-peak
10 min	0.1 db peak-to-peak
Versus position (moving 180 deg)	0.6 db peak-to-peak

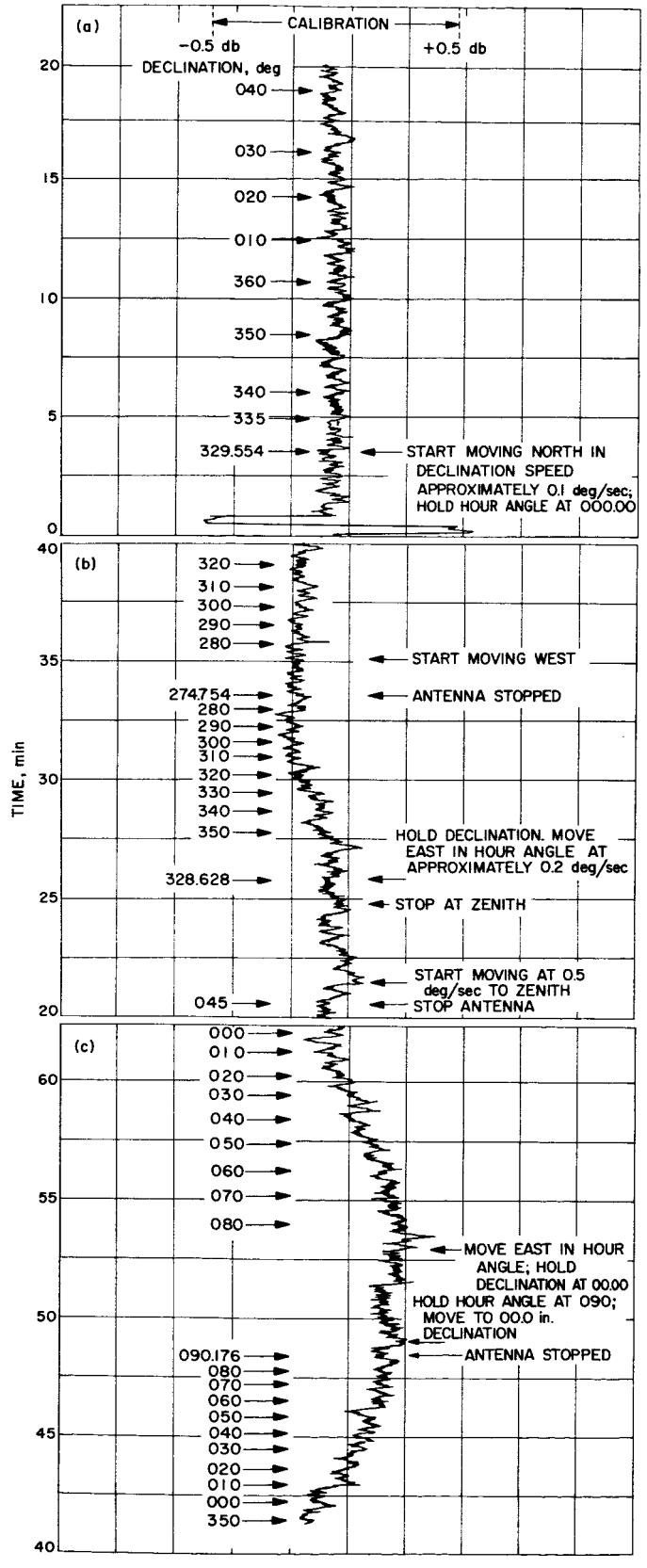

Fig. 2. Gain versus antenna position

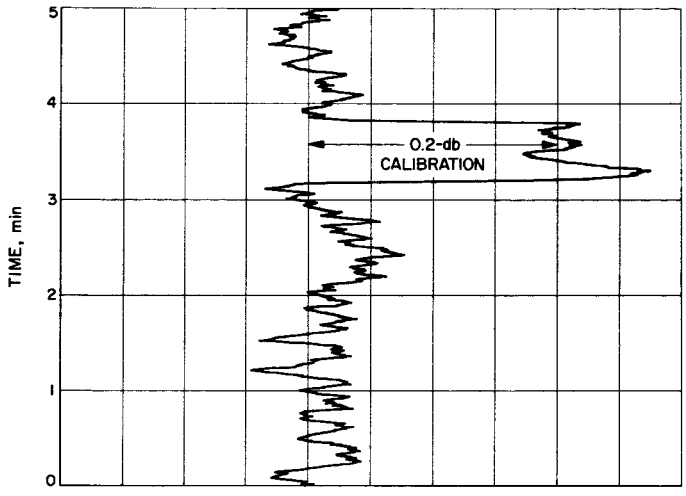

Fig. 3. Short-term gain stability, normal operation

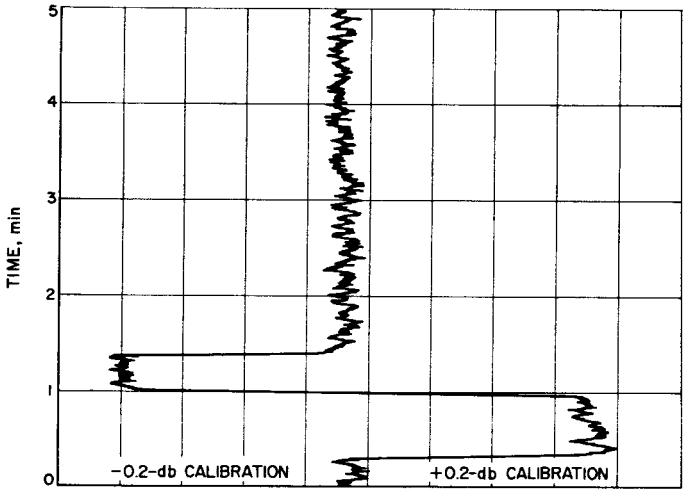

Fig. 4. Short-term gain stability, JT return to atmosphere

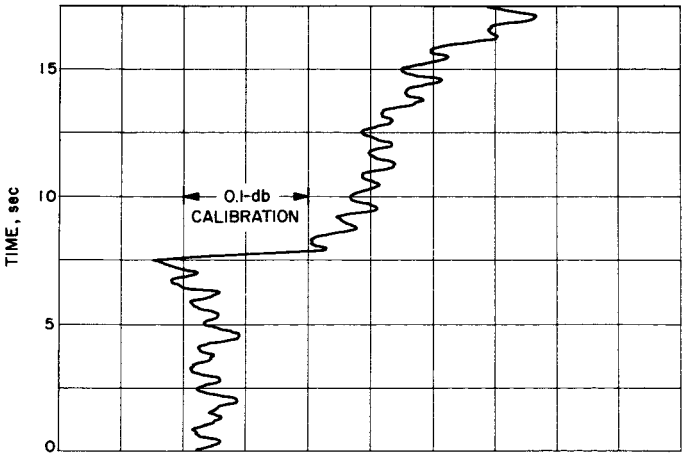

Fig. 5. Short-term gain stability, no minimum time constant

B. Ground Instrumentation for *Mariner C* Occultation Measurements

The *Mariner C* occultation experiment places unique demands on the measurement capabilities of the DSIF. The most important data occurs in an interval of time of about 1 min prior to occultation by the planet Mars. It is possible that the ground received signal at this time will be very close to the receiver threshold. In order to investigate the merits of alternative configurations for the measurements, a simulator has been constructed. The simulator has been used recently at the Goldstone Pioneer site; however, the experimental results have not yet been reduced.

The *Mariner C* occultation experiment will attempt to measure the perturbations, which are produced by the refractive index of the Martian atmosphere, on the radio signal received at DSIF Stations. The effects to be measured are perturbations of the received signal doppler frequency and perturbations on the received signal amplitude due to Fresnel diffraction phenomena. Since both these phenomena are time functions of short duration, it will not be possible to integrate in the manner normally used in tracking operations. If all the negative tolerances in the communications system obtain, operation will be very close to threshold. The precision of measurements made close to threshold is severely compromised by the presence of noise. This takes the form of random power fluctuations in measurement of received signal strength and of intermittent loss of lock which causes gain or loss of cycles in doppler count. A simulator has been constructed to investigate the achievable performance of several different alternative receiver configurations. This simulator uses a synchronous motor to drive a cam which varies an attenuator as a function of time. The attenuation output as a function of time is presented in Fig. 6. It was originally planned to use the simulator to drive the transmitter exciter VCO and also to produce a phase modulation on the input signal. In testing the motor driven variable attenuator with the transponder in the control room, it was found that the leakage of the transponder was well above threshold. The transponder was then placed in the declination wheel house and used to drive the test transmitter. The test transmitter was then attenuated through the driven variable attenuator, and the signal from the attenuator was injected through a directional coupler into the maser.

The data taken in this configuration has not yet been evaluated.

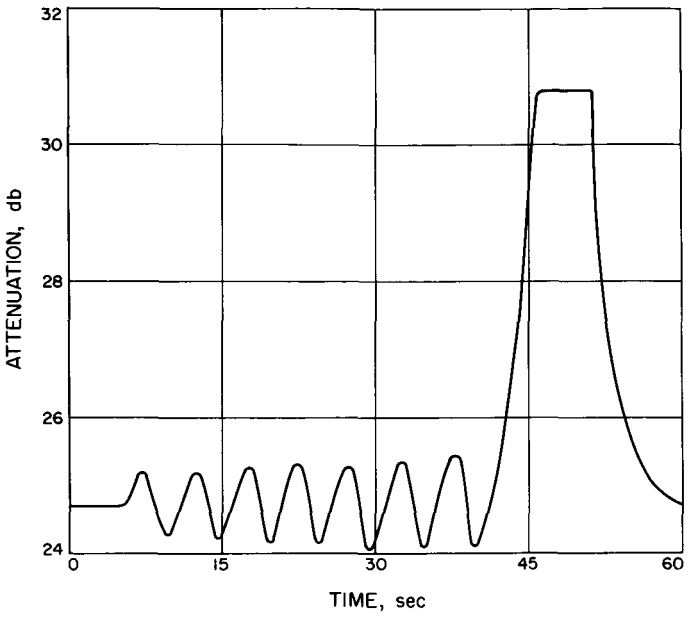

Fig. 6. Attenuation versus time for simulator

C. *Mariner C* Transmitter Development

1. 100-kw Transmitter

a. Introduction. A ground transmitter power of 100 kw continuous wave (CW) will be required for the *Mariner C* Project under certain operating conditions. The complete transmitter program to meet this requirement consists of a 100-kw klystron amplifier subassembly, a ground test and checkout facility, and specialized controls for this installation.

b. Klystron amplifier subassembly. The amplifier subassembly which was delivered during the last reporting period (Ref. 1) has been installed on the cone cart in the ground test facility, and ground tests are in progress.(The amplifier subassembly is shown in the ground test facility in Sect. II, Fig. 6 of this volume.)The interface between the original 2388-Mc system (Ref. 2) and the *Mariner C* subassembly has been checked, and all controls and interlocks are operating correctly.

Amplifier 2 (Ref. 3, Fig. 1, p. 50) was operated with no difficulty at 100-kw CW into the RF water load at 2388 Mc. With 100-kw forward power into the water

load, the reflected power was 300 w. This is a voltage standing wave ratio (VSWR) of 1:1.11 for this portion of the waveguide run—well within design limits of 1:1.22. The amplifier will be returned to 2115 Mc and retested.

The klystron for Amplifier 1 was returned to the manufacturer to have the collector replaced prior to any operating time on the klystron. This became necessary when incorrect manufacturing techniques were discovered during the tests on another klystron. The klystron has been corrected, tested, and returned to JPL. It will be installed in the *Mariner C* subassembly, Amplifier 1, and operated during the next reporting period.

c. Ground test and checkout facility. In order to safely test the amplifier subassembly with full power out of the feedhorn in the ground test facility, it is necessary to raise the complete feed cone assembly so that the horn will project above the roof. In order to accomplish this, two hydraulic hoists have been installed in the ground test and checkout facility. With the installation of these hoists, facilities are now available for checkout, maintenance, and storage of two Cassegrain feed cone assemblies. Fig. 7 shows the west hoist in a partially raised position.

d. Specialized controls. A waveguide switch control and amplifier status panel has been designed, fabricated, and installed in the test facility monitor cabinet (Fig. 8). The lines and squares on the panel will light to indicate:

(1) Exciter in operation.

(2) To which amplifier the exciter is connected.

(3) To which amplifier the control cables and high-voltage cables are connected.

(4) Whether the connected amplifier is radiating into the RF water load or out the antenna feedhorn.

The two key switches operate the RF waveguide switch. When the "SAFE SW." is operated, the output of the amplifier to which the control and high-voltage cables are connected will be directed into the RF water load. The "POSITION SW." is used to direct the output of either Amplifier 1 or Amplifier 2 into the antenna feedhorn. The operation of the "SAFE SW." will over-ride the "POSITION SW." to assure safe operation of the connected amplifier for test and maintenance.

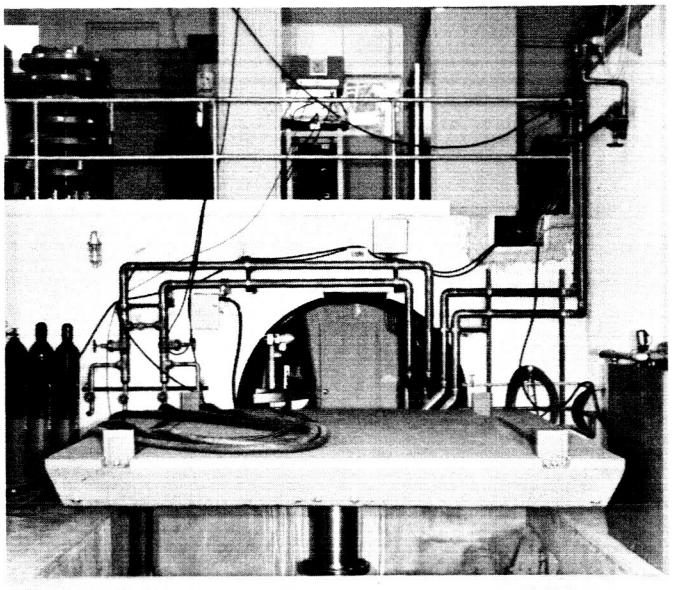

Fig. 7. Cone hoist partially raised

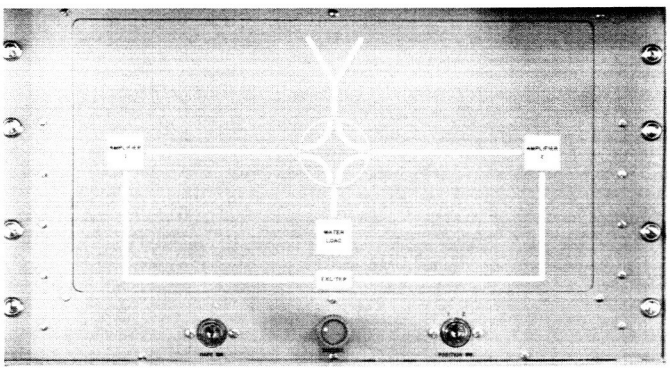

Fig. 8. Switch control and amplifier status panel

References

1. "*Mariner* C 100-kw Transmitter," *SPS 37-28*, Vol. III, pp. 43–45, Jet Propulsion Laboratory, Pasadena, California, July 31, 1964.

2. "*Mariner* C 100-kw Transmitter," *SPS 37-25*, Vol. III, pp. 18–19, Jet Propulsion Laboratory, Pasadena, California, January 31, 1964.

3. "*Mariner* C 100-kw Transmitter," *SPS 37-27*, Vol. III, pp. 50–52, Jet Propulsion Laboratory, Pasadena, California, May 31, 1964.

V. Communications Research and Development

A. Ground Antennas

1. Precision Drive System for 30-ft Antenna

The installation of a new precision servo drive system on the 30-ft antenna located at the Goldstone Venus site was reported in Ref. 1. The design, assembly, and installation were done by JPL using commercially available components; the work was accomplished according to the schedule in Ref. 1. The primary objective of the new drive system was to provide very precise steering over a wide speed range; this objective will provide versatile performance for test aircraft or satellite to astronomical target tracking over a range of frequencies from S-band to 20 to 30 Gc.

The precision servo drive system installation was completed on June 22 ,1964, according to the schedule, Ref. 1, to meet the readiness requirements for the experimental measurements of the 20- to 24-Gc radiation from the planet Venus. After a short period of checkout and testing, the 30-ft antenna was committed to the preparations for the experiment on June 24, 1964. The experiment whose scientific purpose was to determine the water content of the Venus atmosphere was successfully conducted on a daily basis during the scheduled period of June 29 through July 20, 1964.

Figs. 1 through 7 present a pictorial review of the project.

The performance of the antenna and servo drive system was very good during the entire experiment. The availability record of the drive system for the daily 12-hr data runs was perfect except for a down period of about 4 hr resulting from wetting an electrical connector during steam cleaning of the antenna.

Comprehensive experimental measurements of pointing accuracy performance have not yet been conducted; however, repeated calibrated measurements of the error signal during the Venus experiment indicate that the 3-σ tracking error on either axis for wind velocities less than 22 mph is well within the ± 0.006 deg in the modification design specification. By repeated RF boresighting on the radiation from Venus, it was established that the absolute steering of the beam to within a tenth of the 0.1-deg beamwidth was well within the system capability.

The measured low-speed axis rate is 0.25 deg/sec on both axes. The specified rates in high speed were 3 deg/sec in elevation and 5 deg/sec in azimuth. Corresponding

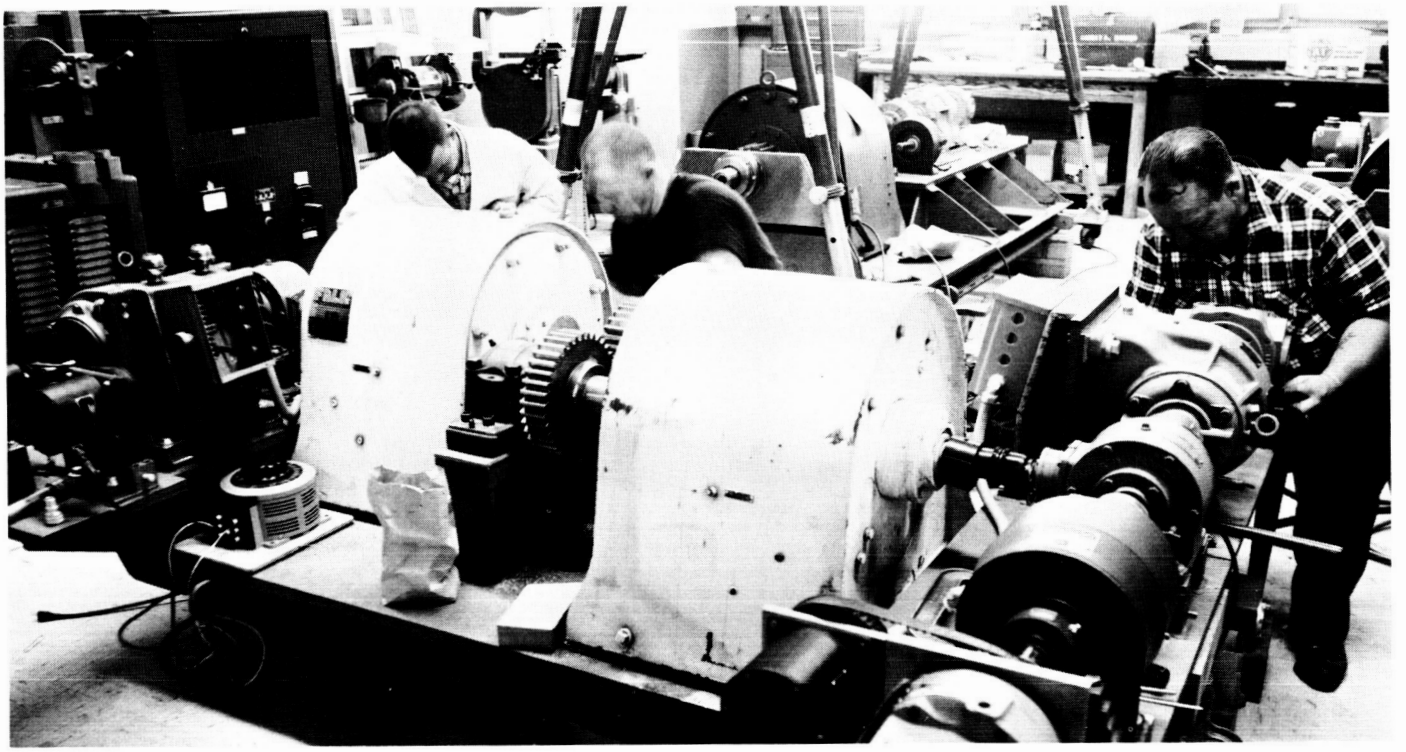

Fig. 1. Assembly of drive skids, elevation skid in foreground

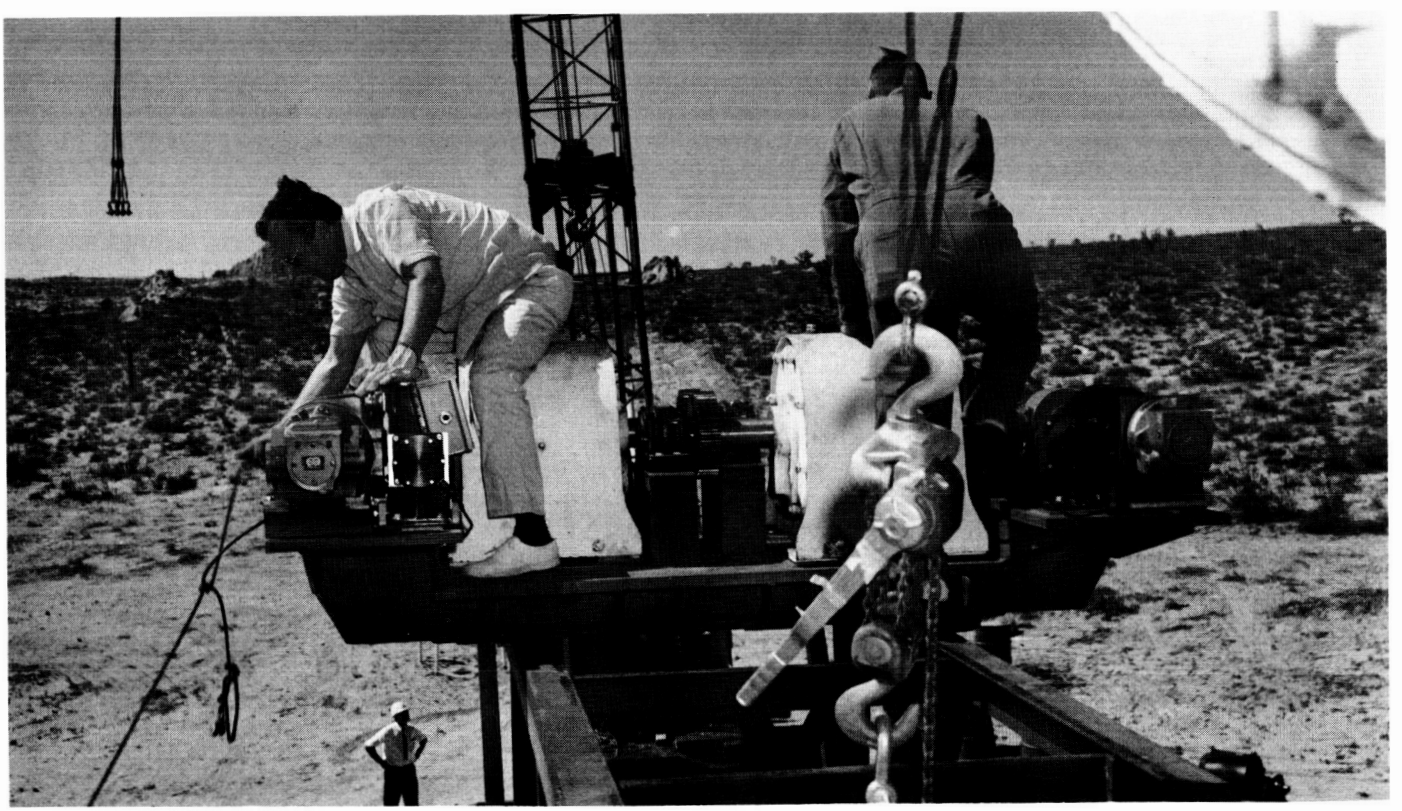

Fig. 2. Preparations for sliding elevation drive skid into installation position on antenna

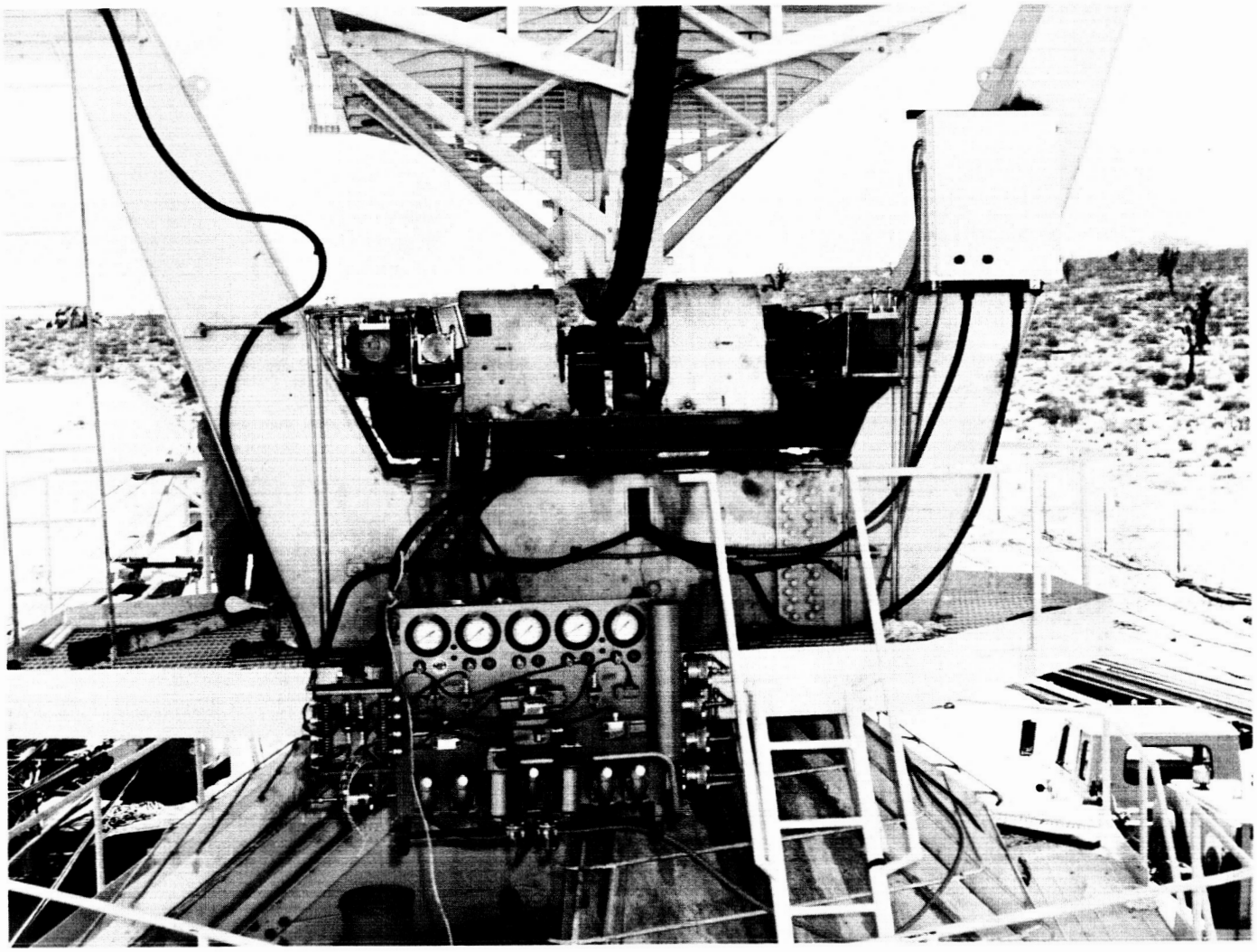

Fig. 3. Elevation drive skid and hydraulic panel installation

measured rates are 2.7 and 4.4 deg/sec. The full specified rates should be obtainable through minor changes in servo valve characteristics and/or pressure level changes.

2. *Antenna Instrumentation*

A transportable instrumentation system is being developed for use in research and development testing of the structural and mechanical properties of large ground antennas. It has been used in a measurement program on the 85-ft antenna at the Goldstone Venus site; it will be used extensively during the alignment and testing of the 210-ft-diameter Advanced Antenna System (AAS). A detailed description of the instrumentation system is given in Ref. 2; progress reports have been made in subsequent issues.

A second simplified transportable instrumentation facility is being prepared to provide recording of some data required continuously from the early stages of the on-site construction in the AAS Project. It will be used initially for measurements of the concrete pedestal structure related to the hydrostatic azimuth bearing installation, and subsequently for the initial performance testing of the bearing.

A data reduction program is being developed for reducing data obtained with the transportable instrumentation system on the 85-ft Az–El antenna. The reduced data will give the surface waviness of the reflector panels and the dead-load deflection characteristics of the antenna. Some results of the dead-load deflection measurements are reported in this *SPS*.

Fig. 4. Installation of one of the azimuth drive skids

Table 1 gives the results of one extensometer test run on the 85-ft Az–El antenna (Ref. 3, Fig. 1, p. 54). The first column is data with only scale-factor (SF) corrections applied. The scale-factor correction is derived from

Table 1. Extensometer data[a]

Elevation angle, deg	Channel 11		Channel 12	
	Data correction for SF and zero shift	Temperature correction data	Data correction for SF and zero shift	Temperature correction data
90	0.0000	0.0000	0.0000	0.0000
75	−0.0048	−0.0071	−0.0017	−0.0029
60	0.0047	0.0010	0.0224	0.0201
45	0.0227	0.0188	0.0607	0.0582
30	0.0546	0.0527	0.0967	0.0971
15	0.0914	0.0893	0.1172	0.1174
0	0.1207	0.1197	0.1182	0.1205
15	0.1025	0.1015	0.1285	0.1302
30	0.0743	0.0718	0.1202	0.1214
45	0.0449	0.0437	0.1056	0.1064
60	0.0149	0.0130	0.0726	0.0722
75	−0.0032	−0.0038	0.0311	0.0323
90	−0.0132	−0.0138	−0.0166	−0.0162

[a] Azimuth = 260 deg; no pol. sign indicates "+." Reading is in inches.

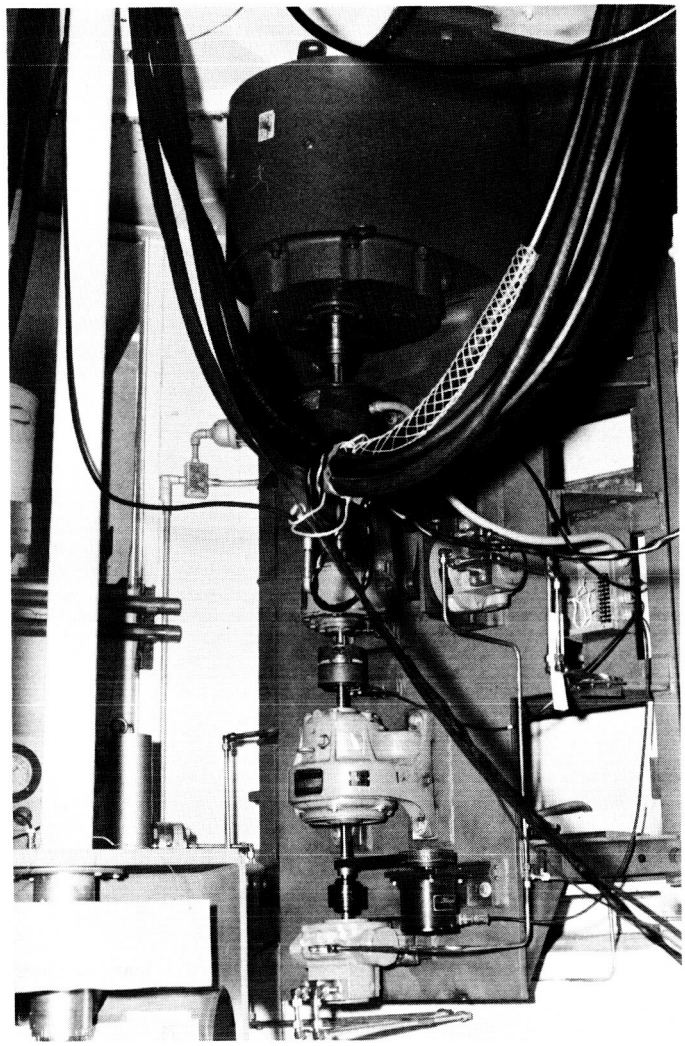

Fig. 5. Azimuth drive skid installed. Gage on azimuth hydraulic panel visible lower left

±¼-in. calibrations with the proper zero-shift corrections. The second column includes temperature correction. The temperature correction is derived from sampling the wire span temperature. Fig. 8 shows the location of the extensometers for the data in Table 1. These tests were run in January/February of this year, and are being compared with similar tests run on the same antenna structure in August of 1963; the results of these tests are reported in Ref. 4.

The significant features of this recent test series are that wire-span temperature correction data were obtained, and the data reduction and plotting are being handled by a computer. Fig. 9 shows plots of the extensometer data showing the effect of temperature compensation on the reduced data.

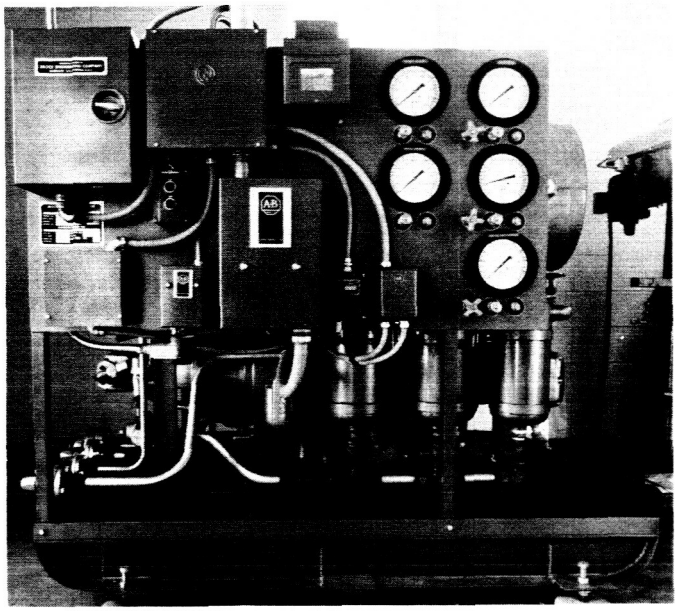

Fig. 6. Hydraulic supply unit installed in hydromechanical building

Fig. 7. Left to right: shared steering computer control panel, servo operator's control panel, and servo electronic racks

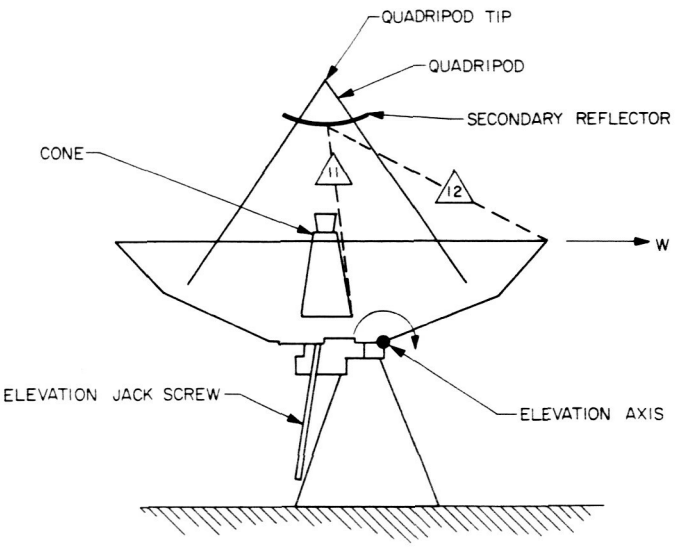

Fig. 8. Extensometer positions for data in Table 1

3. *Radio Calibration Techniques: Simultaneous Lobing Radiometric Tracking System*

a. Summary. The S-band systems for the DSIF 85-ft and future 210-ft antennas will use simultaneous lobing angle tracking feed systems. A radiometer which could be used with the tracking feed would be a useful device for angle pointing and gain calibrations of the antenna system using radio star sources.

An X-band laboratory model of a simultaneous lobing radiometer receiver channel has been constructed (Ref. 5).

The intermediate frequency (IF) and direct current components of the demonstration system were recently operated at the Echo site of the Goldstone Tracking Station using the 85-ft antenna and the L-band receiver system. The results of this experiment, which demonstrated the feasibility of the system, can be found in Refs. 6 and 7.

b. Recent work. The results of the experiments at the Echo site on the night of April 30 to May 1, 1964 (Refs. 6 and 7) were obtained by using a 30-Mc IF system compatible with the L-band and L- and S-band systems. To be compatible with the DSIF S-band system, an IF frequency of either 10 or 50 Mc must be employed. This modification was incorporated into the X-band bench setup described in Ref. 5. The correlation detectors have been redesigned to improve their conversion efficiency

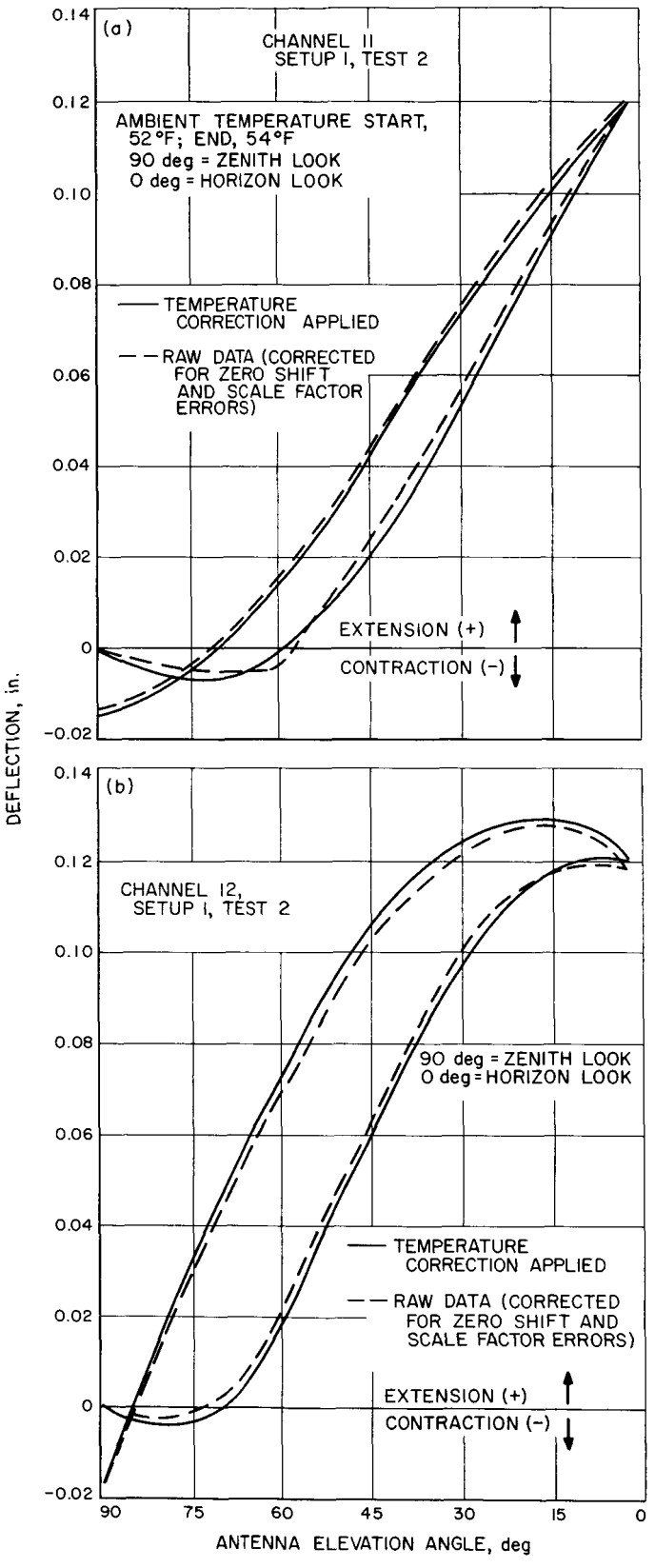

Fig. 9. 85-ft antenna structural deflections

(Fig. 10). This unit exhibits a total RF, IF (and dc null drift of about 0.3 mv for a 45-min period (Fig. 11). When the results of this null drift test are coupled with the peak output from the detector (approx ±0.8 v) and a typical error channel antenna pattern of the DSIF 85-ft antenna S-band monopulse system (Fig. 12), it is seen that the null drift rate corresponds to a boresight drift rate of about 75×10^{-6} deg/hr based on the slope of the antenna pattern. This amount is much less than is resolvable by the servo encoders (2×10^{-3} deg). It is proposed to operate the IF and dc components of this unit at the Pioneer site of the Goldstone Tracking Station using the 85-ft antenna and the S-band receiver system as soon as antenna time is available. The components were chosen so that operation is possible at either 10 or 50 Mc intermediate frequency.

c. Discussion. It is of interest to investigate the dispersive effect of unequal path lengths in the reference and error channels of the system. Letting the voltages arriving at the broad-band correlator be denoted by V_R and V_E, we have

$$V_R = A$$
$$V_E = B \angle\theta$$

where θ is the angle denoting the phase angle between V_R and V_E.

Upon entering the correlator, a sum and difference are taken

$$V_1 = k(V_R + V_E) = k(A + B\cos\theta + jB\sin\theta)$$
$$V_2 = k(V_R - V_E) = k(A - B\cos\theta - jB\sin\theta)$$

These signals are then detected in two square law detectors:

$$V_{1dc} = k^2(A + B\cos\theta)^2 + k^2(B\sin\theta)^2$$
$$= k^2A^2 + 2k^2AB\cos\theta + k^2B^2\cos^2\theta + k^2B^2\sin^2\theta$$
$$V_{2dc} = k^2(A - B\cos\theta)^2 + k^2(B\sin\theta)^2$$
$$= k^2A^2 - 2k^2AB\cos\theta + k^2B^2\cos^2\theta + k^2B^2\sin^2\theta$$

The difference of these two dc voltages is then taken in a dc differential amplifier

$$V_{dc} = V_{1dc} - V_{2dc} = 4k^2AB\cos\theta$$

Setting the gain constant, $4k^2$, equal to 1 we get the normalized control voltage being sent to the servo system of the antenna as

$$V_{dc} = AB\cos\theta \quad \text{v/rad/sec}$$

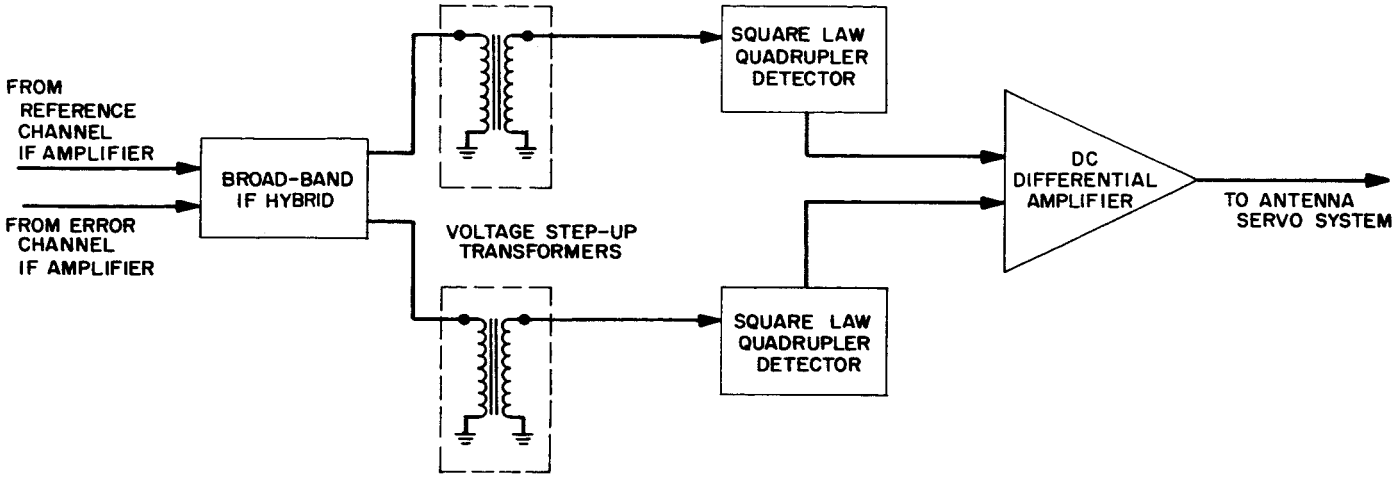

Fig. 10. Block diagram of broad-band correlation detector

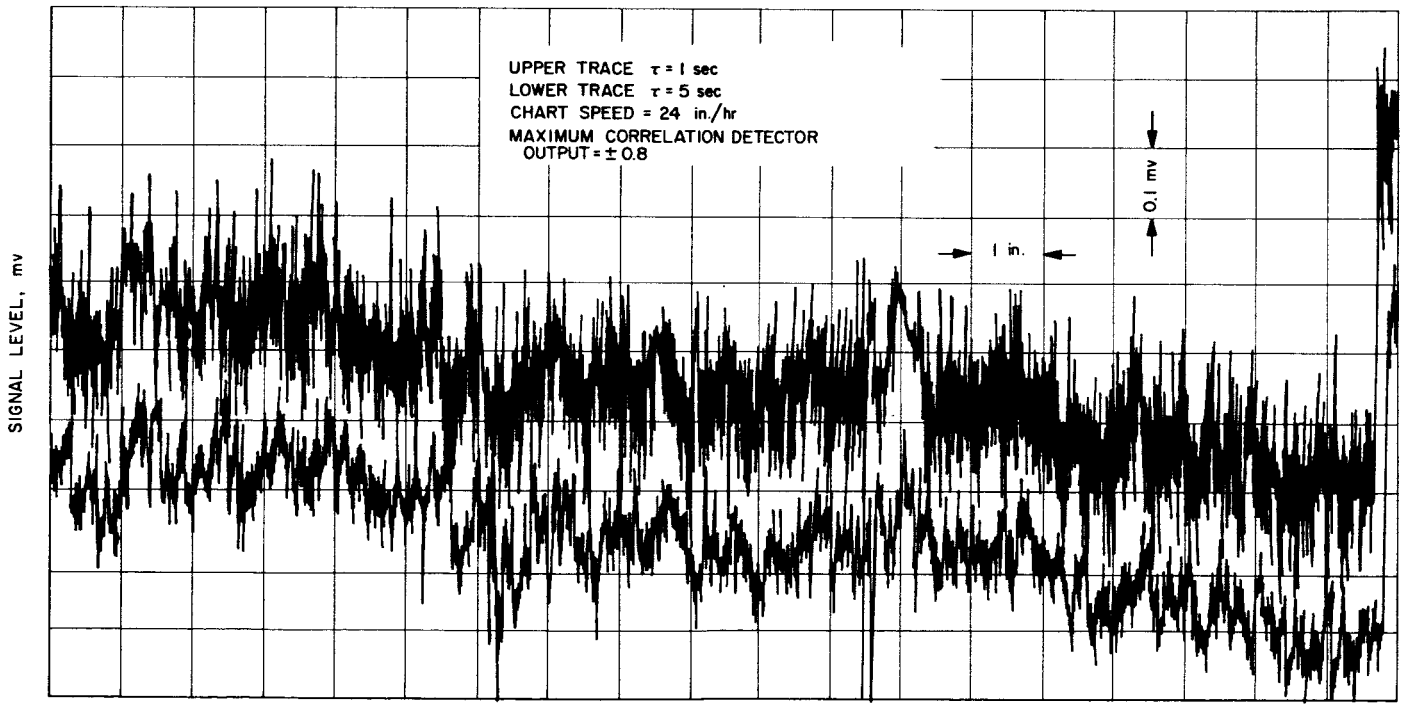

Fig. 11. Null drift of correlation detector

Integrating this result over the bandwidth of the system then gives the total control voltage being sent to the servo system of the antenna. For comparison purposes, this integration will be conducted for a system that is assumed to be nondispersive, and for a system that is dispersive.

Case 1. Nondispersive system assumptions.

(1) Uniform spectral density over the bandwidth of the system.

(2) Phase shift constant over bandwidth.

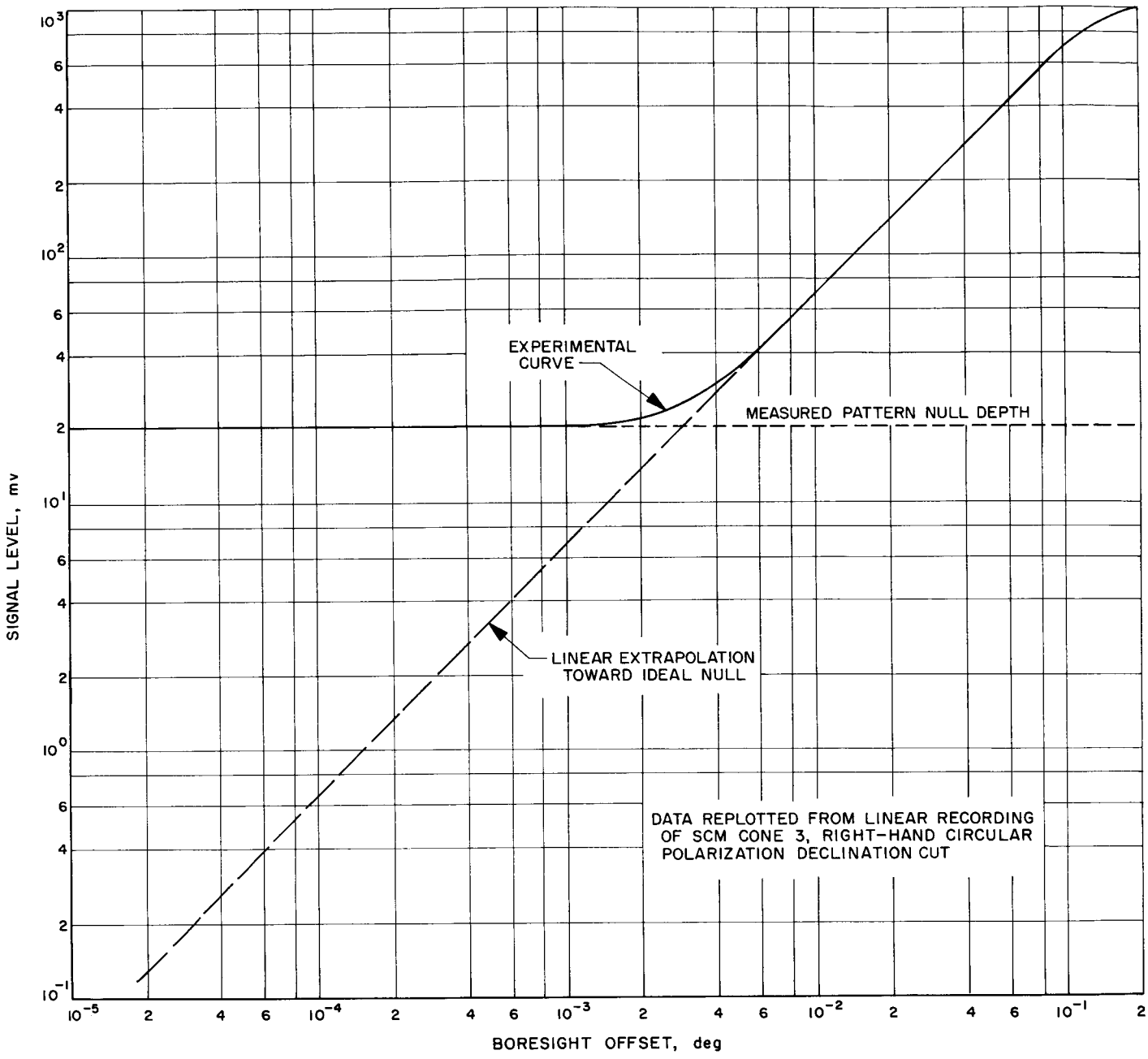

Fig. 12. Normalized error channel antenna pattern

Define:

(1) $V_{dc\,ND}$ = nondispersive dc output voltage.

(2) θ_0 = phase difference between voltage components at center frequency ω_0.

(3) ω_L = lower edge of passband.

(4) ω_H = upper edge of passband.

(5) $BW = \omega_H - \omega_L$.

Then

$$V_{dc\,ND} = \int_{\omega_L}^{\omega_H} AB \cos\theta_0 \, d\omega$$

$$= (AB \cos\theta_0)\,\omega \Big|_{\omega_L}^{\omega_H}$$

$$= (AB \cos\theta_0)\,(\omega_H - \omega_L)$$

$$= (AB \cos\theta_0)\,(BW)$$

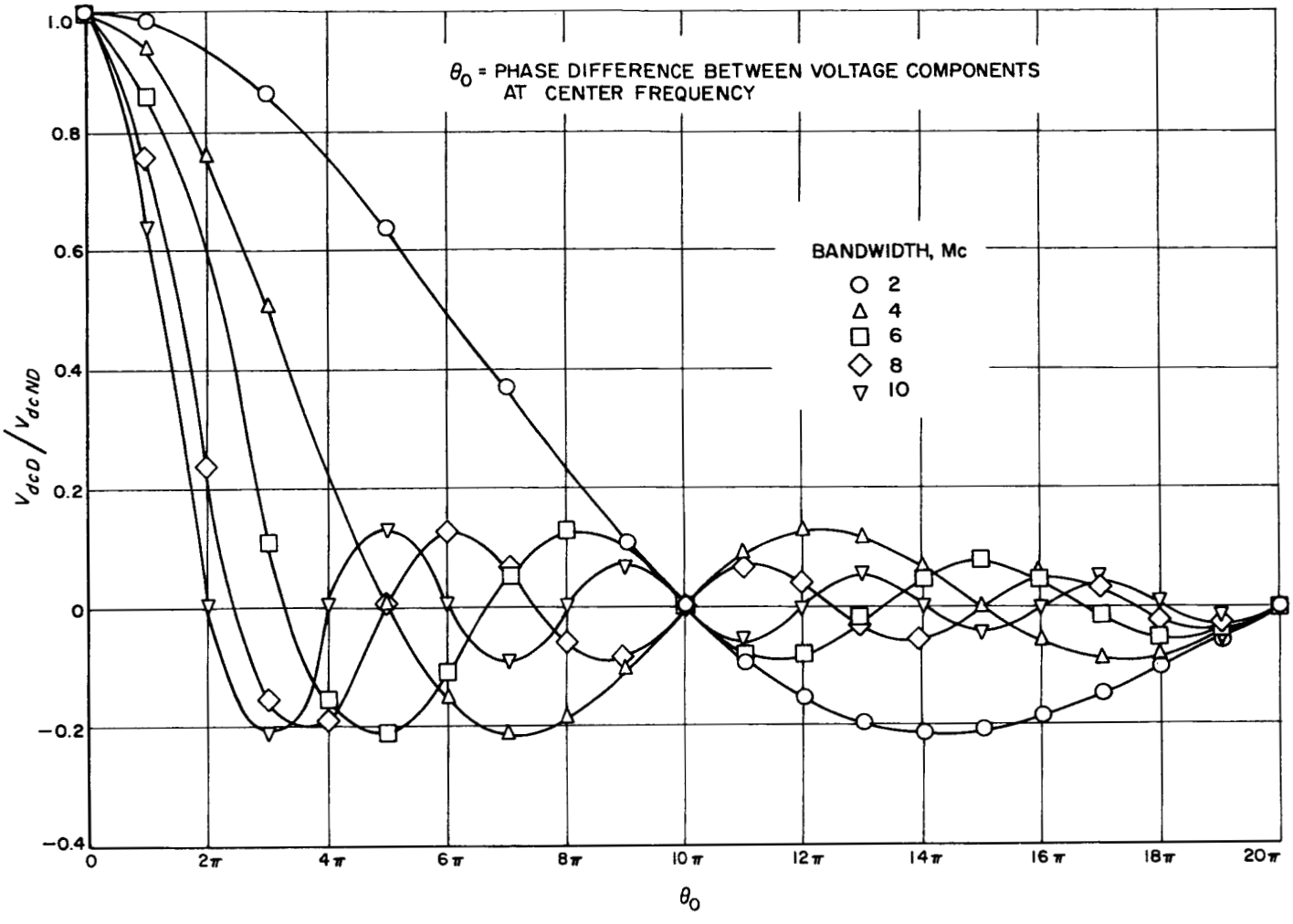

Fig. 13. Ratio of dc servo control voltage derived from a dispersive system to that derived from a nondispersive system for f_0 = 10 Mc and *BW* as a parameter

It should be pointed out that ΔL in the above expression is an effective differential line length. That is, it is assumed that any amplifiers, filter, etc. in the signal lines can be replaced with equivalent zero delay components in a series with lengths of transmission lines.

This last formulation for V_{dcD}/V_{dcND} points out the important fact that any degradation of the system due to dispersion is not a function of the center frequency of the system.

4. 85-ft Antenna Reflector Deformations of the Reflector Structure from Gravity Loads

a. Summary. The progress of the design and development of antenna reflector structures should be markedly advanced with the introduction of the three-dimensional structural computing programs. The formulations and assumptions of the 7094 STAIR Program (Ref. 8) are satisfied closely by the conditions of nearly all of the joints of a reflector structure. Structural data of the Venus site 85-ft Az-El antenna were inputted in the STAIR Program; the results in terms of deformations of the panel supporting joints are presented as analyzed by an RMS Program (Ref. 9). The calculated results can be compared with experimental field data for validation of the design techniques used in the 210-ft AAS design and for optimization of precision antenna reflectors for operation at increasing RF frequencies.

b. Recent work. The structural data of one-half of the reflector structure of the 85-ft Az–El antenna were inputted in the STAIR Program. (The structure is symmetrical about the vertical cutting plane through the vertex

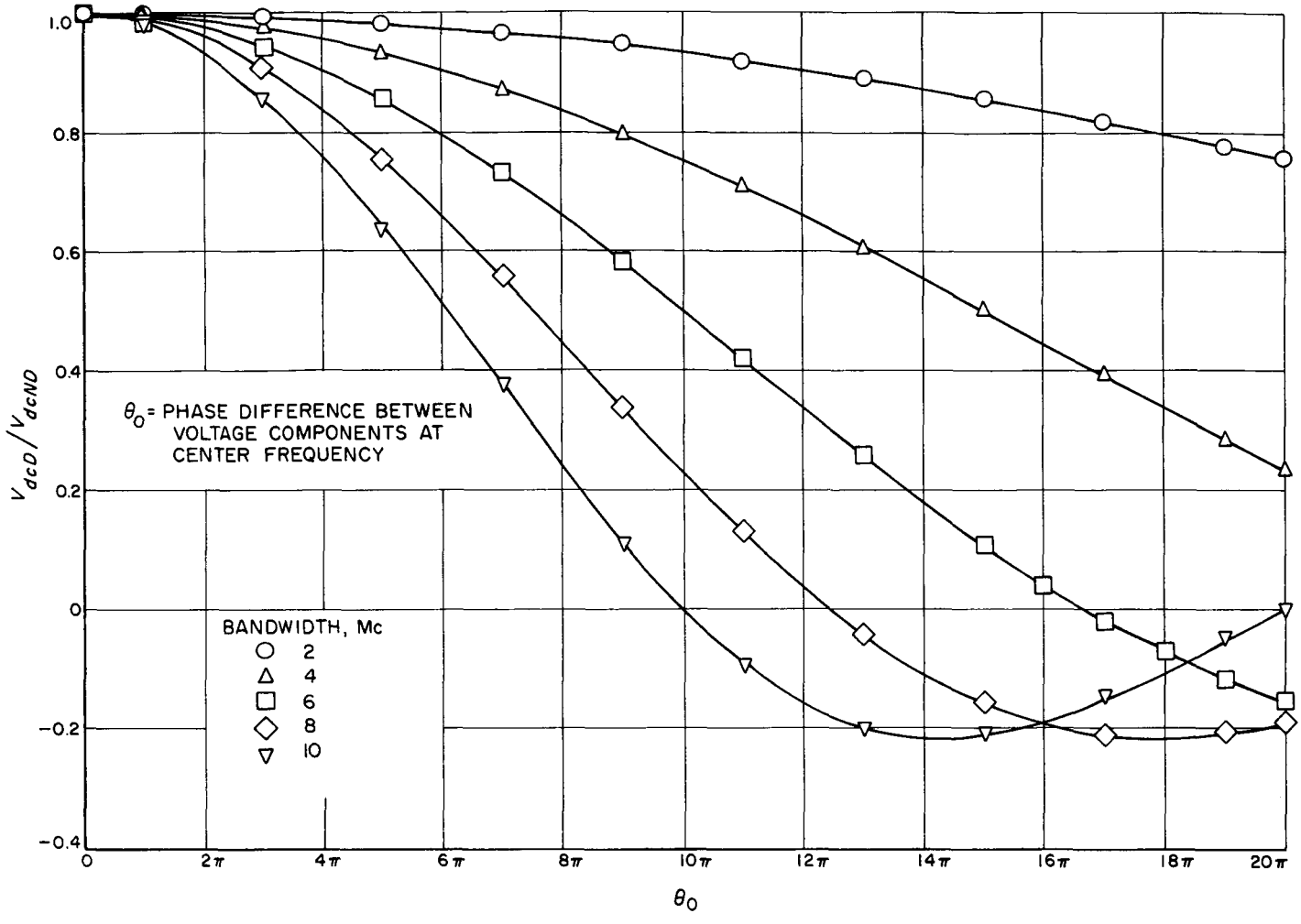

Fig. 14. Ratio of dc servo control voltage derived from a dispersive system to that derived from a nondispersive system for f_0 = 50 Mc and *BW* as a parameter

of the paraboloid and at right angles to the elevation axis.)

The STAIR was programmed to compute the gravity *off–on* load cases from the zenith and the horizon look positions. The deformation data from these two positions can then be manipulated to compute the deformations of the joints relative to the elevation angle where the reflector panels were initially set to the true paraboloid shape.

Fig. 15 shows a 90-deg rotated view of the right half of the antenna as one looks into the face of the reflector; the joint numbers shown were those actually used in the STAIR computations. A total of 399 joints was inputted; this resulted in an equivalent solution by the computer of a 1197 by 1197 matrix.

The deformation data as outputted by the computing program are in the form of three orthogonal components of the displacement vector. Fig. 16 shows the plot of the gravity *off–on* zenith look position deformations reduced to normal errors to the best fitted paraboloid with the original focal length. The plus errors are joint deformations measured toward the focal point from the best fitted paraboloid. Fig. 17 shows the horizontal look gravity *off–on* deformations.

The normal errors were reduced from the three-component format by the best fitting RMS Computing Program (Ref. 10). Table 2 shows the resulting rms values for deformations in terms of ½ path length errors from the best fitted paraboloid with the original focal length for the four cases computed. The rms values refer only to the structural joints or the panel supporting points.

Case 2. Dispersive system assumptions.

(1) Uniform spectral density over the bandwidth of the system.

(2) The dispersion is a linear function of frequency. This would be the case if all the dispersion were due to unequal line lengths in the two channels.

Define:

(1) $V_{dc\,D}$ = dispersive dc output voltage.

(2–5) Same as for nondispersive case.

(6) $\omega_0 = \frac{1}{2}(\omega_H + \omega_L)$.

Then

$$V_{dc\,D} = \int_{\omega_L}^{\omega_H} AB \cos \frac{\omega}{\omega_0} \theta_0 \, d\omega$$

$$= AB \left(\frac{\omega_0}{\theta_0}\right) \sin \frac{\omega}{\omega_0} \theta_0 \Bigg|_{\omega_L}^{\omega_H}$$

$$= AB \left(\frac{\omega_0}{\theta_0}\right) \left[\sin \frac{\omega_H}{\omega_0} \theta_0 - \sin \frac{\omega_L}{\omega_0} \theta_0 \right]$$

from the definitions

$$\omega_H = \omega_0 + \frac{BW}{2}$$

$$\omega_L = \omega_0 - \frac{BW}{2}$$

Substituting these quantities into the above expression for $V_{dc\,D}$, we get

$$V_{dc\,D} = AB \left(\frac{\omega_0}{\theta_0}\right) \left[\sin \left(1 + \frac{BW}{2\omega_0}\right) \theta_0 - \sin \left(1 - \frac{BW}{2\omega_0}\right) \theta_0 \right]$$

$$= AB \left(\frac{\omega_0}{\theta_0}\right) \left[\sin \theta_0 \cos \frac{BW}{2\omega_0} \theta_0 + \cos \theta_0 \sin \frac{BW}{2\omega_0} \theta_0 - \sin \theta_0 \cos \frac{BW}{2\omega_0} \theta_0 + \cos \theta_0 \sin \frac{BW}{2\omega_0} \theta_0 \right]$$

$$= AB \left(\frac{\omega_0}{\theta_0}\right) \left(2 \cos \theta_0 \sin \frac{BW}{2\omega_0} \theta_0 \right)$$

Taking the ratio of the output in the dispersive case to the output in the nondispersive case, we get

$$\frac{V_{dc\,D}}{V_{dc\,ND}} = \frac{AB \left(\frac{\omega_0}{\theta_0}\right) \left(2 \cos \theta_0 \sin \frac{BW}{2\omega_0} \theta_0 \right)}{AB \, (\cos \theta_0) \, (BW)}$$

$$= \frac{2\omega_0 \sin \frac{BW}{2\omega_0} \theta_0}{\theta_0 \, (BW)}$$

Redefining BW in terms of cycles rather than in terms of radians, we get

$$\frac{V_{dc\,D}}{V_{dc\,ND}} = \frac{2f_0 \sin \frac{BW}{2f_0} \theta_0}{\theta_0 \, (BW)}$$

where

$$f_0 = \frac{\omega_0}{2\pi}$$

$$BW = f_H - f_L$$

The function $V_{dc\,D}/V_{dc\,ND}$ is shown plotted in Fig. 13 with $f_0 = 10$ Mc and BW as a parameter, and in Fig. 14 with $f_0 = 50$ Mc and BW as a parameter.

If it is assumed that the velocity of propagation in the two channels is equal, we can write

$$v_0 = f_0 \lambda_0$$

and

$$\theta_0 = \frac{\Delta L}{\lambda_0} (2\pi)$$

$$= \frac{f_0 \Delta L}{v_0} (2\pi)$$

where ΔL is the differential line length between the two signal paths.

Substituting this expression for θ_0 into the expression for $V_{dc\,D}/V_{dc\,ND}$ we get

$$\frac{V_{dc\,D}}{V_{dc\,ND}} = \frac{\sin \frac{\pi BW}{v_0} \Delta L}{\frac{\pi BW}{v_0} \Delta L}$$

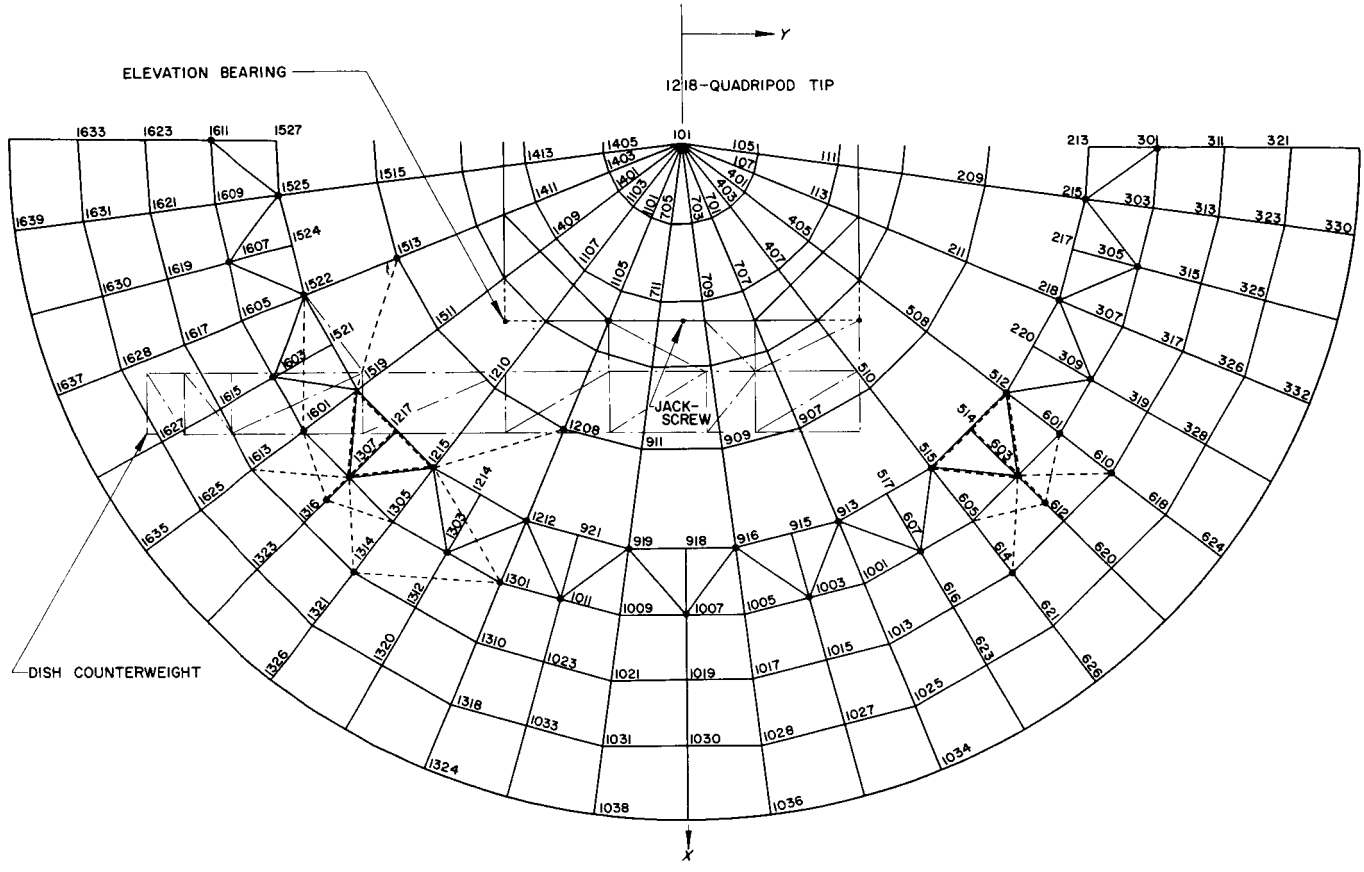

Fig. 15. 85-ft Az–El antenna surface panel joint numbers

Table 2. Resulting rms values for deformations

Case No.	Reflector position	RMS ½ path length, in.
1	Zenith look gravity *off–on*	0.046
2	Horizon look gravity *off–on*	0.018
3	Horizon look panels set at 45-deg elevation	0.037
4	Horizon look panels set at zenith look	0.060

Cases 3 and 4 are of practical interest because the gravity forces are *on* at all times and the panels (RF reflective paraboloid) are set to a paraboloid shape at a predetermined elevation angle. In order to compute Case 3, the gravity force inputted in the STAIR Program is (1 − coz 45 deg) × 1.0 g in the Y-direction subtracted from coz 45 deg × 1.0 g in the Z-direction. To compute Case 4 where the panels are set at zenith look, the zenith look gravity *off–on* deformations are algebraically subtracted from the horizontal look gravity *off–on* deformations. In all cases the distortions are vectorially added before the paraboloid is best fitted.

The above method of calculating Case 4 results from the fact that, at zenith look where the panels are set to zero error, the horizontal force component is equal to zero and the zenith force is the maximum. Rotation in elevation angle of 90 deg to the horizontal look changes the direction of gravity relative to the reflector by 90 deg, resulting in the addition of the full horizontal look deformations to the opposite sign deformations of the zenith look. (The gravity force producing the zenith look deflection reduces to zero from full value as the reflector is pointed at the horizon.)

c. Discussion. Inspection of Fig. 16 deformations shows correlation to the structural tie existing from the reflector structure to the counterweight at joint 1314 (Fig. 18). Removal or transfer of this tie should obviously reduce the deformations about this joint.

The normal displacements at joints 1036 and 1038 show that the tip of the reflector moves upward 0.041 and 0.202 in., respectively, to the best fitted paraboloid. This

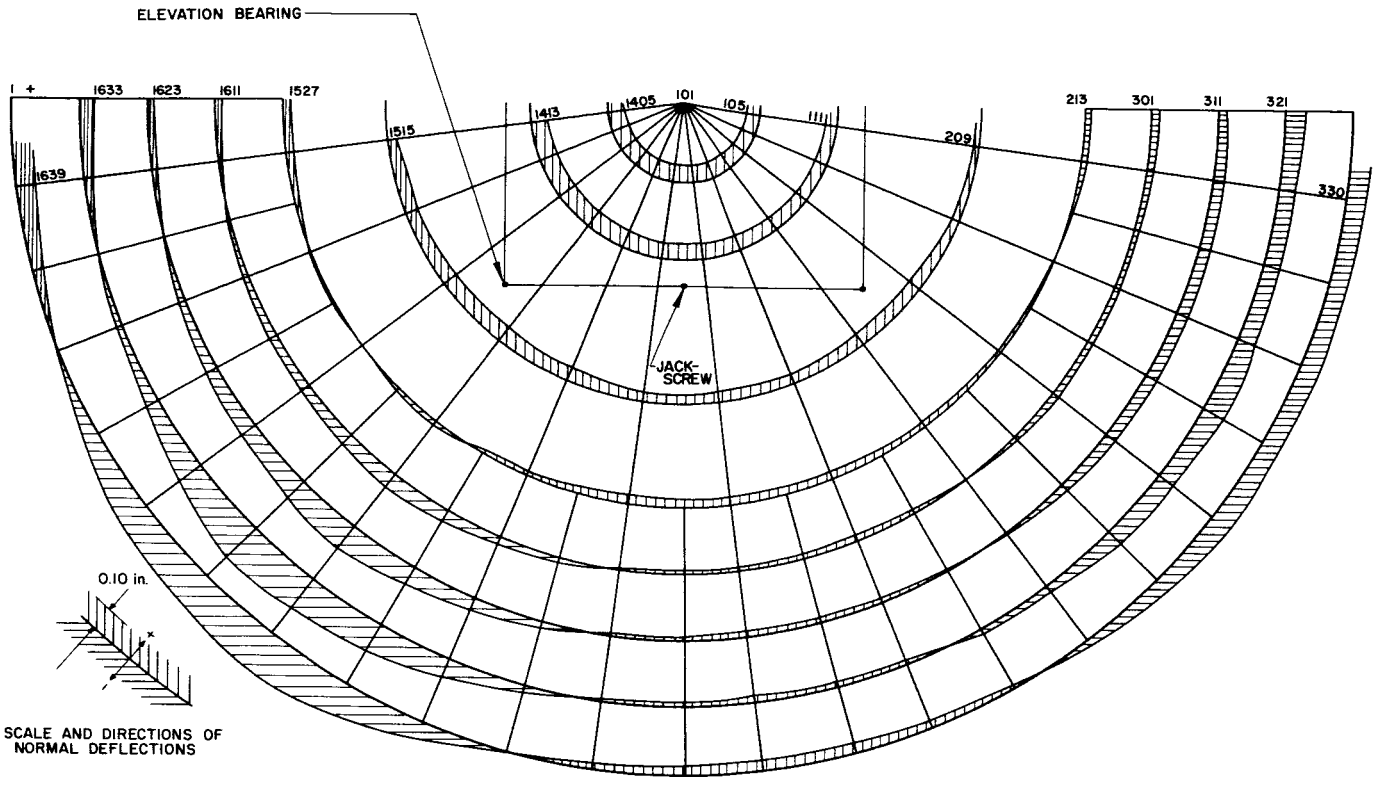

Fig. 16. Normal deflections from best fitted paraboloid: zenith look gravity *off—on*

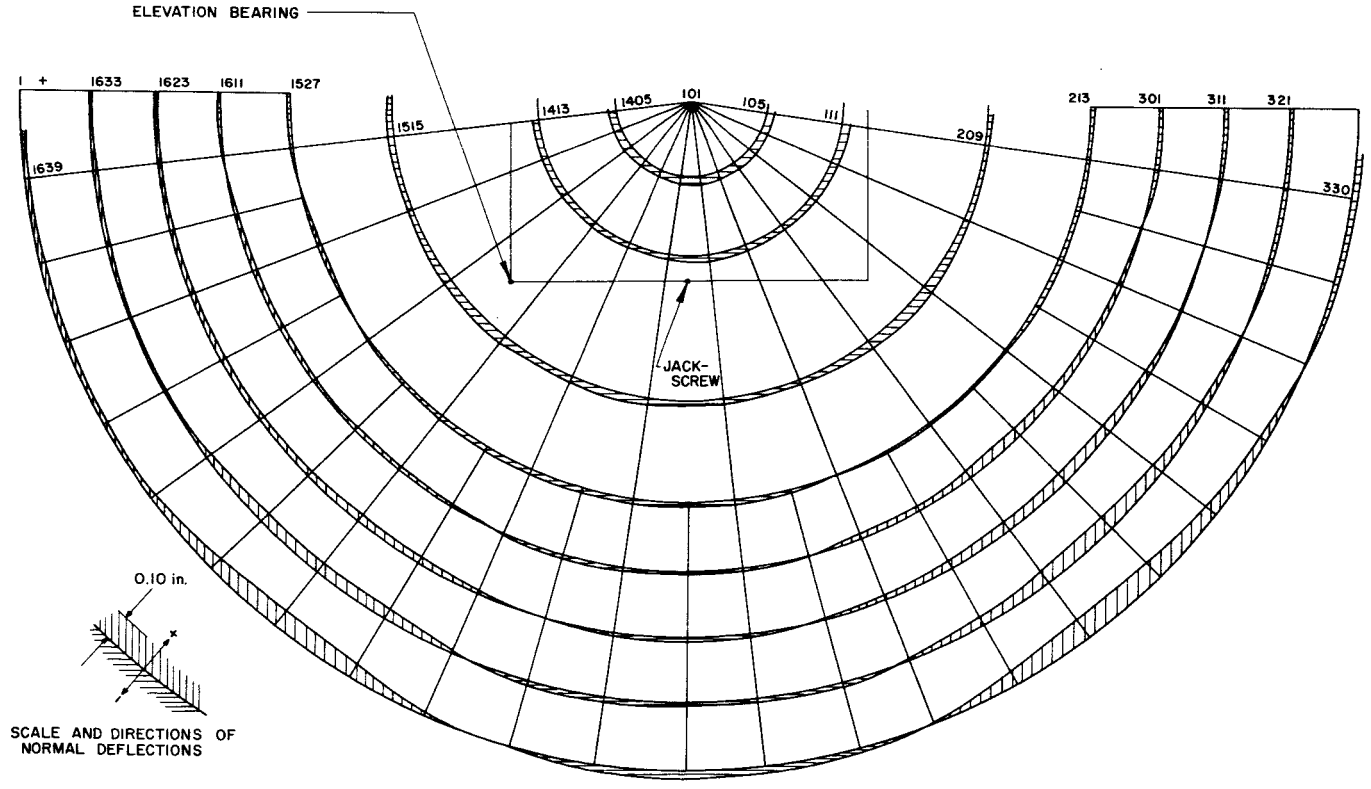

Fig. 17. Normal deflections from best fitted paraboloid: horizontal look gravity *off—on*

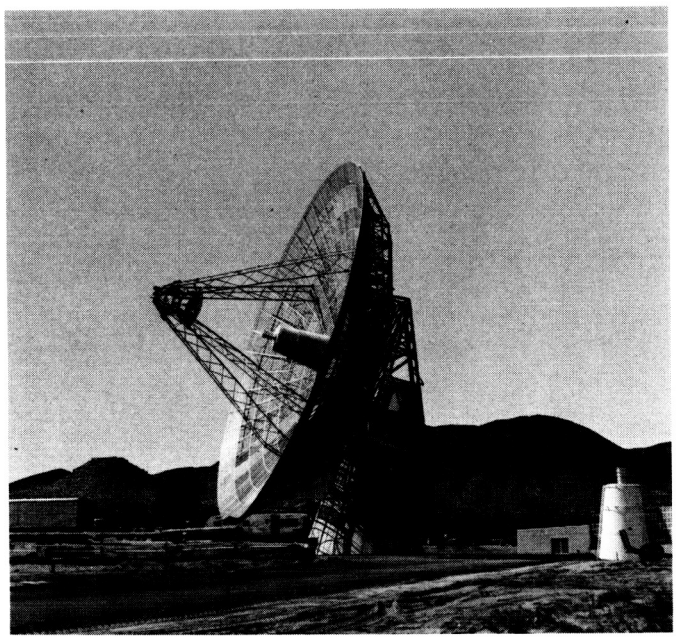

Fig. 18. 85-ft Az–El antenna

is contrary to the normal expectations of the edge deflections and is the result of the structure acting as a three-dimensional body. The removal of the above-mentioned tie will influence the distortions of these joints 1036 and 1038. This upward deformation is checked by measurement data from extensometers 8 and 9, as reported in Ref. 10.

The normal distortions (as pictured by Figs. 16 and 17 for Cases 1 and 2) for gravity *off–on* loads are of importance in the design of reflector structures. Closeness to symmetry of these deflections results in a better fit with a paraboloid. If the paraboloid is allowed to change in focal length, an even closer fit resulting in a better reflective surface can be made. At the present time, the RMS Program does not vary the focal length in the best fitting computations. Since the loads for Cases 1 and 2 are at right angles to each other and act on symmetrical structures, changes in the structures should be optimized so as to result in symmetrical deflecting structures for increased RF efficiencies.

A comparison study is under investigation of the 85-ft Az–El deformations from the change in direction of the gravity forces as computed by the STAIR Program and as measured by extensometers during field tests. (See Sect. V-A-2 of this report for preliminary discussion of extensometer data.)

B. S-Band Lunar/Planetary Radar Project

1. Venus Site Experimental Activities

a. Summary. Experimental operations activity at the Venus site for the period April 20 to June 20, 1964 was reported in Ref. 11. During the present reporting period, the planetary radar system was used to continue the ranging, mapping, synchronous receiver, continuous wave (CW) spectrum receiver, and total spectrum experiments on the planet Venus. Additionally, ranging experiments were performed on the Moon, thermal radiation studies (black body) were made on Venus, and radio star tracking was done on Hercules and Cygnus A. Table 3 is a summary of the activities of the Venus site during the period June 20 to August 20, 1964.

The 30-ft Az–El antenna was used for radiometric measurements of Venus in the region of 20 to 24 Gc. Inasmuch as one of the water vapor absorption bands lies in this region (approximately 22.4 Gc), it was hoped that the received energy would show a dip in the appropriate region. The results of the experiment are not yet available.

The 30-ft Az–El antenna was also used for validating the performance calculated for the 210-ft antenna planned for the Advanced Antenna System (AAS). A ½-scale model Cassegrain feed system has been built and installed on the 30-ft dish, and pattern and gain measurements are being made at the appropriate scale frequencies.

Table 3. Summary of Venus site radar experimental activity (June 20 through August 19)[a]

Experiment	Hours
Primary experiments	
Planetary radar	413
Lunar radar	9
Secondary experiments	
Venus thermal radiation	9
Radio star track	14
Testing, calibration, construction, maintenance (scheduled)	844
Downtime (equipment failure, includes unscheduled maintenance)	120
Holidays	31
Total	1440

[a] Effective August 1, 1964, Venus site reverted to a nonoperating status while equipment modification is completed.

The 100-kw transmitter, the traveling wave maser, and the digital subsystems were the major contributors to "downtime" during the period, with an aggregate of 120 hr out-of-service time. The receiver, servo system, and 85-ft antenna performed without failure.

Continuous observation of Venus was terminated on August 1, 1964. The "round-the-clock" operation of the site was also discontinued on that date. Effective August 3, 1964, the Venus site has been engaged in a modify/rebuild/improve program carried out on a one-shift basis during the day.

b. Current experiments. During the period June 21 to August 1, 1964, the following radar experiments were made with the planet Venus: ranging, mapping, synchronous (coherent) receiver, circularly polarized CW spectrum (normal polarization), circularly polarized CW spectrum (cross polarization), total spectrum (normal polarization), total spectrum (cross polarization), and linearly polarized CW spectrum (normal polarization). Additionally, thermal radiation measurements at 2.4 Gc were made.

Lunar ranging was performed in a continuing effort to refine the ephemeris; radio star tracking continued for use in evaluation of any boresight changes on the 85-ft Az–El antenna.

The schedule for the period June through October at the Venus site is shown in Fig. 19. Note that essentially three programs are in progress. This multi-project activity is part of the continuing effort to improve manpower and equipment utilization.

Ranging experiment. The ranging experiment uses the "511" PN coders to biphase modulate both the transmitter exciter and the receiver local oscillator. During the receive cycle, the Mod III stored program controller (SPC) shifts the receiver coder left and right one digit period each second, thus enabling a comparison to be made between the signal strengths in the two adjacent range gates. For closed loop ranging, the Mod III SPC shifts the receiver coder until the range is such that the signal strength in two adjacent range gates is equal.

Mapping experiment. The mapping experiment also uses the "511" PN coders to biphase modulate the transmitter exciter. However, the received signal is processed by the PB-250 computer and an associated 9-channel correlator to obtain signal strength and spectra in each of the 9 adjacent range gates. These range gates have a depth of approximately 11.5N mi, where N may be any

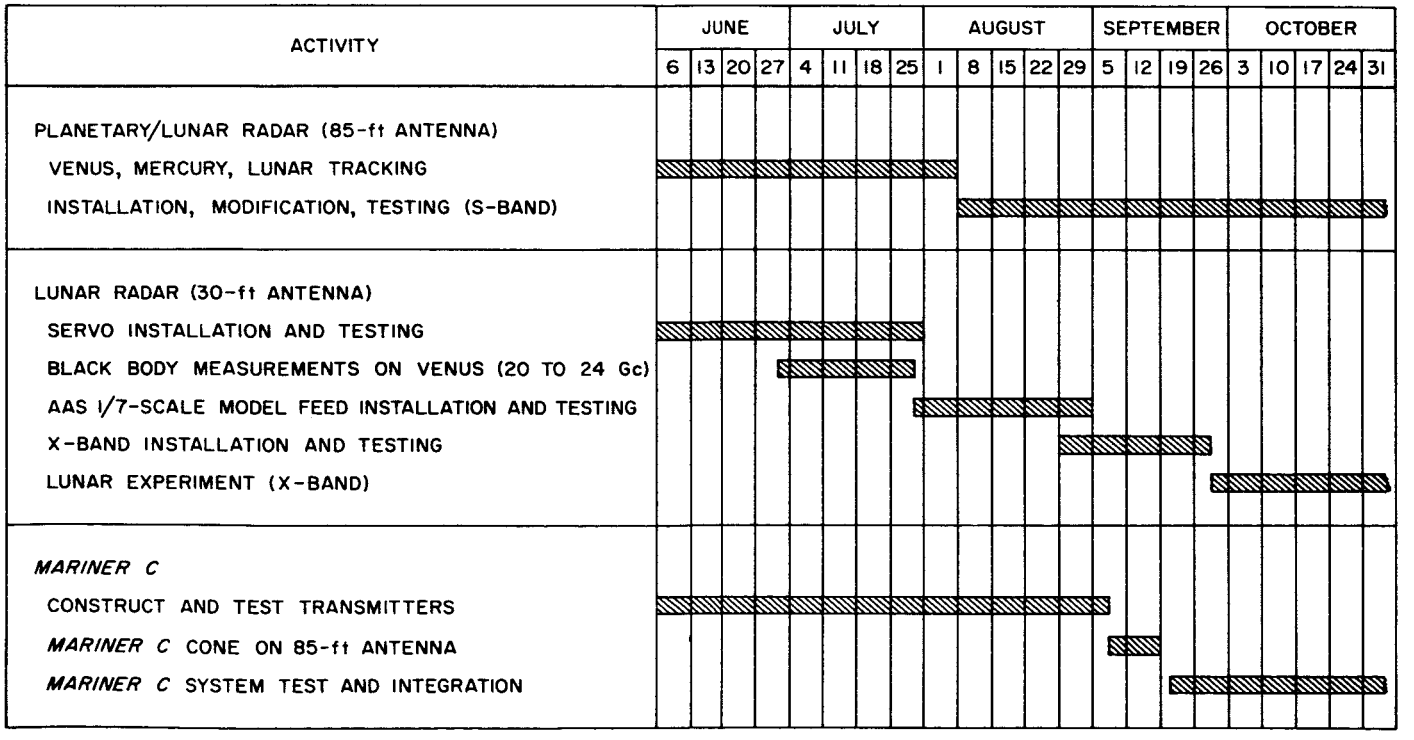

Fig. 19. Venus site activity schedule

integer. At the conclusion of the receive cycle, the 9 signal strengths are typed out by the PB-250 computer, which will also, on command, present the information in a graph of signal power versus frequency, with the graph centered on the nominal receive frequency (transmit frequency corrected for doppler shift due to relative velocity between Earth and Venus).

Synchronous receiver experiment. When operating in the synchronous receiver mode, the frequency of the first mixing oscillator is controlled by the output from the tracking filter, rather than from a precomputed punched tape. However, the local oscillator frequency so obtained is compared with the precomputed frequency, and the difference is punched onto teletype tape for use in correction of the ephemeris.

CW spectrum experiment. During the CW spectrum experiment, the transmitter exciter is unmodulated and a very pure carrier is transmitted. The received signal, after being passed through a filter and analog-to-digital converter, is recorded onto magnetic tape for later spectrum analysis by the IBM 7094 computer on the Laboratory.

When operating in the circularly polarized mode, "normal" polarization is when right-hand circular is transmitted and left-hand circular is received. For the "cross" polarization mode, both transmission and reception are right-hand circular.

When operating in the linearly polarized mode, "normal" polarization is when the same polarity is used for both transmission and reception. Due to the availability on the 85-ft Az–El antenna of a polarization rotator, transmission and reception of other than purely vertically or purely horizontally polarized plane waves are also possible.

Total spectrum. Although similar in operation, the total spectrum experiment differs from the CW spectrum experiment in that signal processing is accomplished by the PB-250 computer and the associated 9-channel correlator operating in a special mode. Signal strengths are computed and typed out by the PB-250, while spectra plots are prepared on the *X–Y* recorder on demand.

Data outputs from the above experiments are: (1) CW spectrum is recorded on magnetic tape for analysis on the Laboratory; (2) mapping and total spectrum are processed by the PB-250 computer and the 9-channel correlator, and signal strength printouts and spectra are prepared after each complete transmit-receive cycle. Additionally, at the end of the experiment period, the cumulative results of computation are punched onto paper tape for later detailed evaluation on the Laboratory; (3) planetary ranging results are compiled minute-by-minute and punched out on paper tape as a permanent record. Quick look/verify results are also put onto the strip chart recorder (analogs of signal strength, left/right channel strengths, coder offset change, etc.), the printer (same data as punched), and the *X–Y* plotter (signal strength/coder offset change during search and lockup). Data available on punched tape is transferred to IBM punched cards for further processing; (4) synchronous receiver data outputs are doppler error and third local oscillator frequency, and are punched onto teletype tape. Additionally, during all the above experiments, certain data is punched onto teletype tape and made available along with the experiment results.

c. Subsystem performance.

100-kw transmitter (operation). The transmitter for this reporting period has operated at approximately 12 hr/day at an average power output of 100 kw, with the exception of the voice-bounce experiment when the average power output was 80 kw with peak outputs of 120 kw. The total operating hours for this reporting period were approximately 496 hr, while the total lost time due to failures of the transmitter was 50 hr. The major portion of this lost time was due to:

(1) Loss of a cooling water hose in the high-voltage rectifier.

(2) Failure of the Energy System's klystron filament power supply.

(3) Shorting of the high-voltage cable between the antenna teepee and the power supply building.

(4) Shorting of some of the crowbar modules.

The total lost time due to all other failures of the system and interlock kick-offs was less than 3 hr.

During the 5 days that Venus was too close to the Sun for tracking purposes, klytron tube Serial No. 1 was removed and replaced with Serial No. 3 with the intended purpose of obtaining increased output power for the voice-bounce experiment, but after 45 hr of operation the tube was outgassing too badly and was removed and returned to Varian for bakeout. Serial No. 1 was reinstalled, and operated satisfactorily at 100 kw.

100-kw transmitter (modifications). A new panel was installed in the exciter for switching of the inputs from

the ranging equipment to the phase modulator and keyer for easy switching to all different modes of experiment operations.

The carriage and hoist in the power supply vault are now complete and ready for installation of the new solid-state rectifier.

The hydraulic hoists in the cone storage and testing area were completed and are being used in conjunction with the testing of the *Mariner C* cone and 100-kw transmitters.

The crowbar trigger auxiliary power supply (UD65-8) was modified by splitting the series load resistance in the rectifier bridge in an effort to reduce the diode failures due to the reflected current surges.

The heat exchanger (UD40) panel was modified with push-to-test lamp sockets in order to better check the different interlocks of the heat exchanger system.

Receiver. During the period June 20 to August 1, 1964, the Mod IV reeciver operated without failure while being used in all experiments performed during that period.

The receiver was returned to its normal configuration after completion of the voice-bounce experiment (Ref. 11) and performed satisfactorily until discontinuance of tracking operations on August 1, 1964. During the period August 1 to 19, 1964, the Mod IV receiver underwent an extensive replace/rebuild program to simplify its operation and further improve its stability and reliability.

Maser. The Venus site 2388-Mc traveling wave maser continued to operate as a test bed for DSIF equipment evaluation. The new crosshead drive (slow-speed synchronous motor) has operated 2887 hr with no maintenance. The crosshead was inspected at this time and the only wear evident was on the cam follower roller bearings. Further evaluation has to be made on the bearings, but it is felt that 1500 hr should be the time period set for replacement.

Gas tube calibration remained at 25.5°K; system temperatures and maser gain were as follows: $G_m = 41.5$ db, $T_{sa} = 31$°K, $T_{sh} = 28$°K, $T_{sn} = 99.5$°K. Tracking and communications (extraterrestrial) receiver noise contribution was checked and averaged out to be 0.46°K ($T_r/G_m = 0.46$°K). Downtime totaled 62 hr due to a leak in one of the flexible helium lines at the elevation axis. The system had to be shut down, the lines repaired, and the system cooled down again. The 12.83-Gc pump klystron was also replaced but did not contribute to any downtime. At present, all rack equipment is being checked and recalibrated where necessary.

85-ft antenna. During this reporting period, the operation of the servo system was normal with no major failures or difficulties. The joints between the panels of the antenna surface were taped and a worn portion of the surface was repainted. Other maintenance included the steam cleaning of the inside of the base structure, the elevation hydraulic cylinders, and the alidade.

A recheck of the linear feed polarization gave the following results: When receiving on "A" arm, a polarizer setting of 90 or 270 deg gives vertical polarization. A setting of 0 or 180 deg gives horizontal polarization. The settings are reversed for "B" arm.

Currently, new cable trays are being installed on the dish structure and the cables are being rearranged. A new water system is also being installed to bring distilled, deionized cooling water up to the transmitter. The system will allow water to be piped not only to the normal position of the transmitter on the alidade, but will also provide for transmitter cooling when it is located in the feed cone.

Digital equipment. No new digital equipment was installed at the Venus site during the period from the last report until the termination of tracking operations on August 1. During this tracking period, all digital equipment performed in a satisfactory manner.

The SDS 910 computer was used with the antenna pointing program to drive the 30-ft antenna during the July millimeter (20 to 24 Gc) radiometer experiment on Venus. The program was operated in both the ephemeris drive and sideral drive with rate offset modes. Operation in both these modes was satisfactory. Since the completion of the radiometer experiment, the SDS 910 computer has been used to drive the 30-ft antenna with constant rates while making pattern measurements. The location of the computer in the loop between the servo operator and antenna has been very useful not only in normal tracking but also in moving the antenna to desired positions and supplying desired rates for tests and measurements.

Since the termination of tracking operations, six new unregulated power supplies have been installed to replace regulated power supplies in the Mod III SPC. The new power supplies are of a higher power rating and are assembled into two panels which match the Computer

Control Company Type RP-10 power supplies. The new power supplies are individually metered and fused in both the primary and the secondary.

A 10-channel multiplexed Adage analog-to-digital converter (ADC) is presently being installed in the Mod III SPC. The Adage ADC will be used with three Ballantine Model 320A true rms voltmeters and three Philbrick Model P-65 operational amplifiers. All of this equipment has been installed in a rack next to the Mod III SPC auxiliary rack. The purpose of this new equipment is to provide a square law detector of more than 30-db dynamic range. Previous planetary and lunar ranging experiments have used one Ballantine and a single-channel ADC. This has been sufficient in the past because the signal-to-noise ratio never exceeded 10 db. It is expected that future lunar ranging experiments will operate at a signal-to-noise ratio in excess of 10 db.

Programs are presently being written which will allow both the Mod III SPC and the SDS 910 computer to expand polynomial curve fits to the angle, range, and doppler ephemerides. These polynomials will be supplied by the computer group on the Laboratory and computed on an IBM 7094. The outputs of the Mod III SPC and the SDS 910 computer will be punched paper tape, which can be used by the existing equipment.

An addition to the SDS 910 is now in the planning stage which will allow this computer to point both the 85- and 30-ft antennas simultaneously. The system design calls for each antenna to have an operating console so that operation of the antennas will be completely independent.

d. Work on 30-ft antenna: mm wave operations and 1/4-scale AAS preparations.

30-ft antenna site facilities modifications and tests (scheduling and control). The limited time available between equipment availability and Venus conjunction necessitated extremely close control and scheduling of the installation and test activities. Accordingly, a master flow diagram was generated which showed the over-all activity broken down into individual tasks. Each task, together with its required performance specifications and required completion date, was made the responsibility of a definite individual. Copies of this diagram were posted throughout the area and helped pinpoint tasks which were experiencing difficulty and which required additional help to meet their completion dates. The maximum period for the taking of experimental data was assured by the completion of installation and testing on schedule.

Preliminary tests. Prior to the start of equipment installation, a preliminary test of the radiometer was conducted in the vicinity of the 30-ft antenna. The purpose of this test was to determine any possible interference to its operation from the 100-kw transmitter feeding the 85-ft antenna. Recordings were made of the output of the radiometer at various positions of the 85-ft antenna. No interference was noted.

Equipment installation. Installation activities proceeded simultaneously in many areas. The instrumentation and test equipment for the experiment were set up in the control room of the 30-ft antenna hydromechanical building, while the radiometer was installed at the apex of the antenna quadripod. Extensive use was made of the helicopter in installing a transmitter and antenna on Tiefort Mountain to facilitate antenna pattern and focusing measurements. The south end of the main control building was set aside for the installation of the control console and servo control equipment. The hydraulic pumps and associated equipment took up most of the south room of the hydromechanical building. Three large antenna drive packages were placed in positions on the antenna structure. Two of these were installed in the antenna base structure to provide drive in azimuth, while the third provided drive in elevation. System data readouts were provided on both antenna axes, and television coverage was obtained through a camera mounted on the dish structure. Its associated monitor was in an equipment rack located in the main control room. Due to windy conditions at the site, considerable difficulty was experienced in adjusting and measuring the surface of the dish. Finally, communications were provided between the antenna, the hydromechanical building, the control building, and Tiefort Mountain. Communications were provided through the use of telephones, an intercom system, and portable radio equipment. A previously installed SDS 910 computer was cabled to the above facilities and an antenna drive program was generated to provide automatic tracking of the planet Venus.

Equipment tests. At the completion of each task, subsystem tests were conducted. Among the subsystems tested were the following:

(1) Data readout system test.

(2) Electrical, mechanical, and hydraulic servo tests.

(3) Television alignment tests.

(4) Tiefort equipment and experiment instrumentation tests.

(5) Star tracks and optical alignment tests.

After the above tests, the complete system was tested in the following manner:

(1) Focusing and antenna pattern determinations using Tiefort Mountain.

(2) Moon track.

(3) Preliminary Venus track.

Venus millimeter wave experiment. The scientific objective of the experiment was to determine the water content of the atmosphere of Venus. Accordingly, the radiometer was designed for a nominal frequency of 22 Gc ($\lambda \approx 13.5$ mm), the water absorption line. Extensive data was taken during the period commencing June 29, 1964, and terminating July 20, 1964. Fig. 20 shows the block diagram of the 22-Gc radiometer used. The data is currently being processed and analyzed by the JPL Lunar and Planetary Sciences Section.

1/4-scale AAS preparations.[1] At the conclusion of the millimeter wave experiment, the radiometer and test instrumentation (hydromechanical building and Tiefort Mountain) were removed. The 30-ft antenna was made ready for a series of tests and pattern measurements on the 1/4-scale AAS model feed. A model cone was installed on the dish with a hyperbolic reflector and its drive at the apex of the quadripod, thereby converting the antenna to a Cassegrain configuration. Pattern and other measurements are currently being taken using the SDS 910 computer to drive the antenna.

2. Venus Voice-Bounce Experiment

a. Introduction. The inferior conjunction of the planet Venus, which occurred in mid-June, 1964, offered a target for the 100-kw planetary radar with a predicted signal return great enough to suggest an experiment using relatively wide-band modulation. The predicted signal strength for June 19 was −157.2 dbm, based upon the reflectivity figure as determined during the previous conjunction of 1962. For an average system noise temperature of 30°C, the noise density was approximately −184 dbm/cps. The fact that a signal-to-noise ratio exceeding unity

[1]See Sect. VI-E of this report.

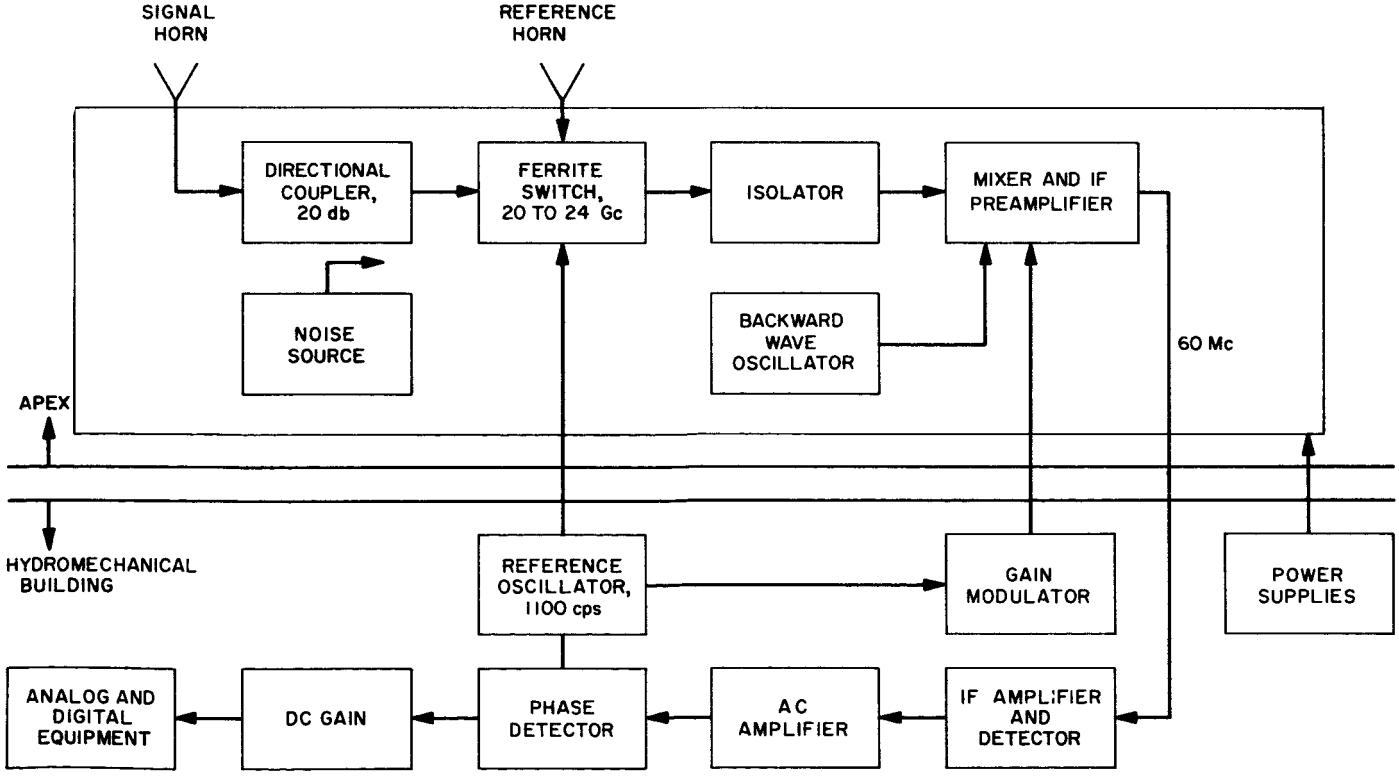

Fig. 20. 22-Gc radiometer block diagram

would be possible in a 100-cps noise bandwidth prompted consideration of time-scaled voice communication. For a frequency response of 2400 cps, the availability of 32:1 time expansion by means of a variable speed tape recorder set the channel bandwidth at 75 cps (single sideband AM) and 150 cps (double sideband FM). A limitation of this technique was related to the round-trip propagation time of 5 to 6 min. Due to the 32:1 time scaling, the real-time message would be limited in duration to about 10 sec since the transmit–receive cycle of the radar is necessarily limited to two round-trip times.

Although the predicted signal-to-noise ratios of 8 and 5 db [single sideband (SSB) and double sideband (DSB), respectively] were promising, four principal problems remained to be resolved:

(1) Subjective hearing thresholds in the presence of noise.

(2) Ability to operate the high-power transmitter in a linear AM mode with *average* voice-modulated power approaching 100 kw (Ref. 12).

(3) Choice of modulation system, SSB or DSB.

(4) Target distortion due to both phase and frequency variations of return from the total planet hemisphere. It was anticipated that gating (using planetary mapping modulation methods) would materially reduce the expected distortion at a cost of 3 to 6 db in signal return.

Early in the year a series of preliminary tests was conducted to obtain data on all but the last item, which, by necessity, was not resolved until the beginning of the actual experiment some 4 wk prior to conjunction. At that time the "signal-to-noise ratio" signal was down approximately 5.6 db from the peak values of 8 and 5 db determined above.

b. Preliminary tests and equipment description. The first laboratory test was used to gain subjective experience with general hearing thresholds in the presence of noise. A wide-band phase modulation system with variable constants throughout was assembled (Fig. 21). Several laboratory personnel individually evaluated optimum settings of modulation index and detector bandwidth versus several signal-to-noise ratios. A sample of the results is shown in Table 4.

The second in the series of laboratory experiments included the construction of a breadboard SSB transceiver, using existing laboratory equipment with a minimum of

Table 4. Wide-band phase modulation test results

Noise, mv	Signal, mv	Bandpass filter No. 1, cps		Loop adjuster setting	Bandpass filter No. 2, cps		Interpretation	Operator
		Low	High		Low	High		
100	50	250	10,000	2.15	0.02	1,000	Good	1
↓	↓	20	6,000	2.64	200	10,000	Good	2
↓	↓	40	1,500	2.00	300	1,500	Fair	3
↓	↓	55	1,500	0.7	480	650	Fair	4
100	50	200	20,000	2.87	200	580	Fair	5
50	50	No best	No best	No best	250	550	Good	1
↓	↓	↓	↓	3.9	340	290	Good	3
50	50	↓	↓	No best	340	2,400	Good	6

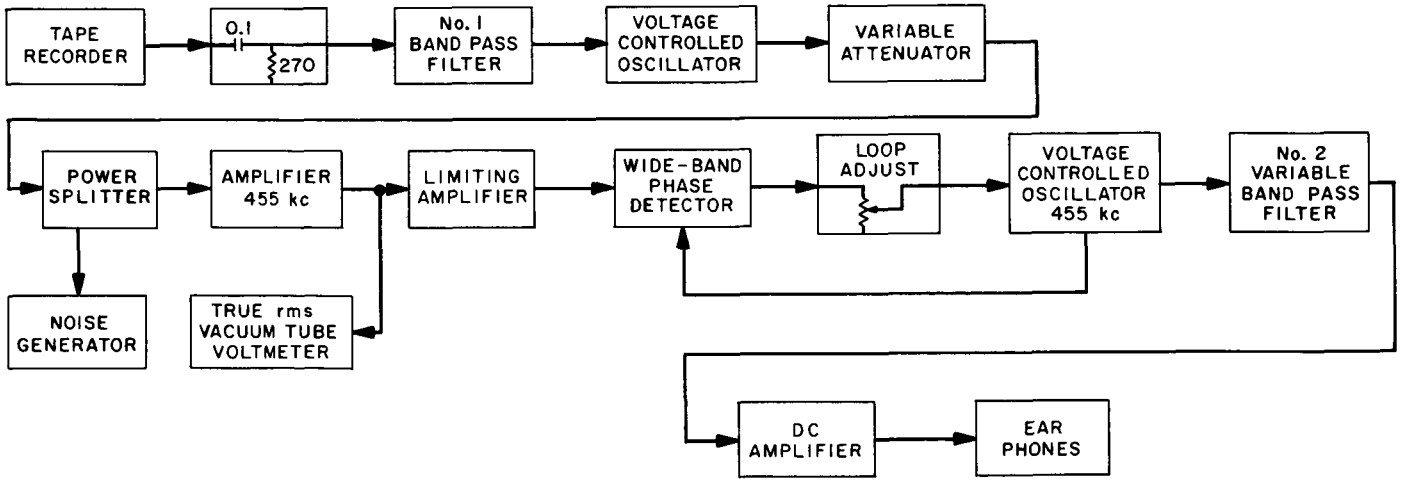

Fig. 21. Wide-band phase modulation system

modification, as shown in Fig. 22. This SSB system was then used for threshold tests in comparison with a narrow-band FM system.

The narrow-band FM system was assembled in a configuration closely resembling the planetary radar system at Goldstone (Fig. 23).

The third step in the experiment was the design of the audio system. The sound studio for Project Echo was used with a minor change. The fluorescent lights were disconnected since the transformers produced undesired background noise, and incandescent lights were installed. To further reduce the unwanted background audio, a noise-cancelling, controlled-reluctance microphone was used. This microphone (Shure Model 488 B) provided an additional 30-db attenuation of the background audio. The microphone signal was amplified by an audio preamplifier followed by a step attenuator. This was used to maintain optimum drive to the commercial automatic audio control amplifier, which assured maximum control of input audio levels and kept the output level as near constant as possible. A block diagram of the recording studio equipment is shown in Fig. 24.

The compression of the voice frequencies to accommodate receiver bandwidth was accomplished with an Ampex Model FR 100 tape recorder. The voice was recorded on Track 1 at a recording speed of 60 in./sec, then slowed down to 1⅞ in./sec for transmission, thus reducing the audio frequencies by 32 to 1. The received signal was then recorded at 1⅞ in./sec, and reproduced at a speed of 60 in./sec, restoring the audio frequencies to their original spectrum. A complete block diagram of the audio system is shown in Fig. 25. The FR 100 tape recorder is capable of a bandwidth from dc to 10 kc. The full frequency range was not required and, as the unused bandwidth recorded only noise, roll-off filters were installed. A closed-loop frequency response test was made on the completed FR 100 system, recording on Track 1

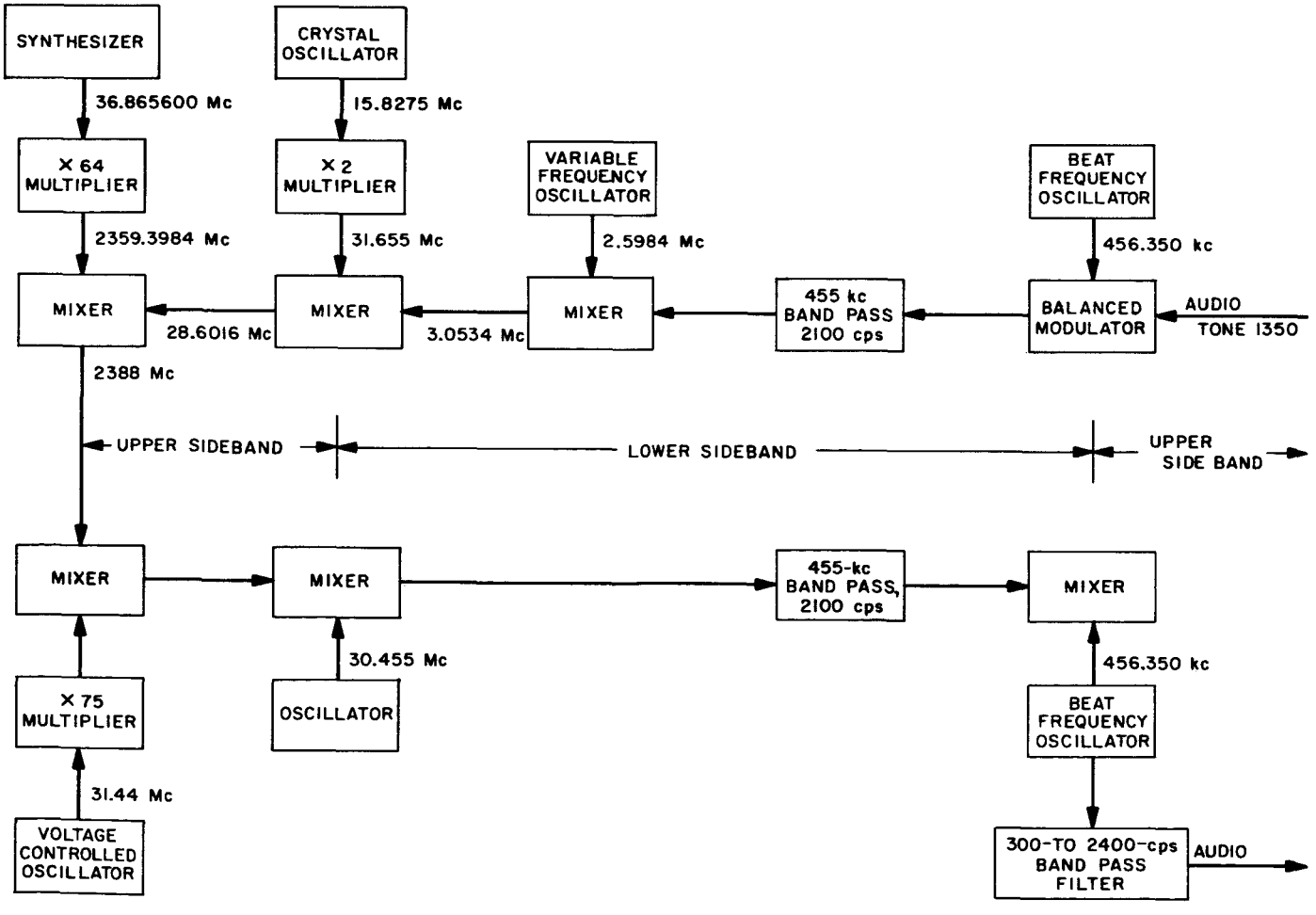

Fig. 22. Single sideband breadboard block diagram

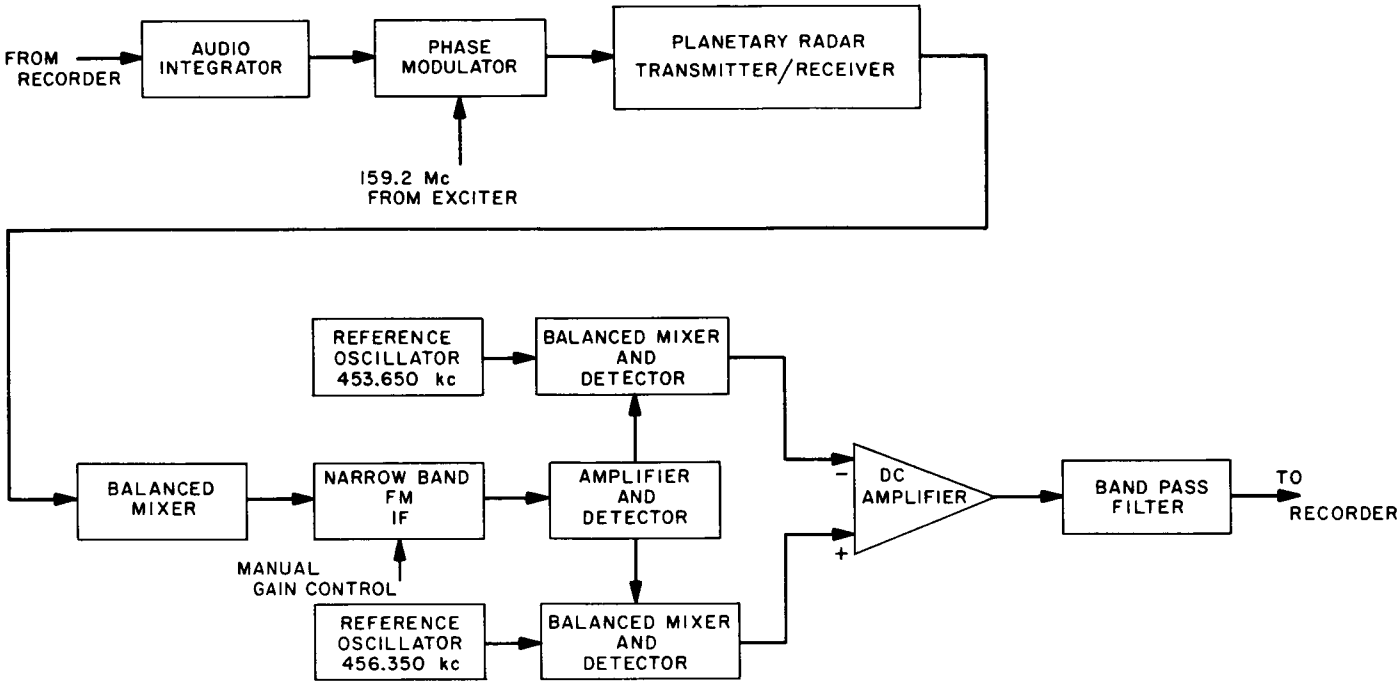

Fig. 23. Narrow-band FM block diagram

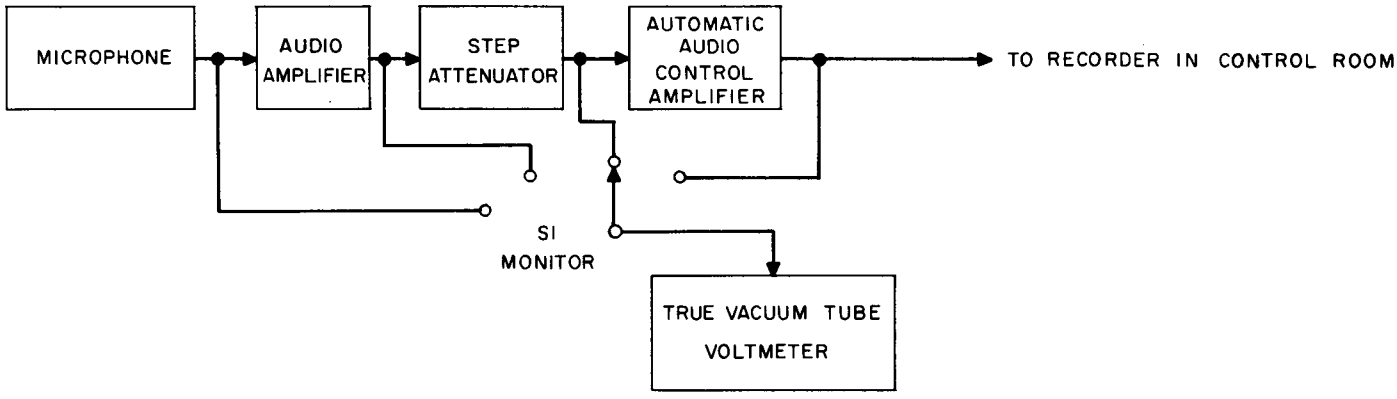

Fig. 24. Audio recording studio

at 60 in./sec, then transferring to Track 2 at 1⅞ in./sec. Replaying Track 2 at 60 in./sec produced the curve shown in Fig. 26.

The SSB system was constructed by modifying existing modules. A total system block diagram is shown in Fig. 27. The choice of upper sideband transmission was made in order to minimize synthesizer design problems. A double diode bridge modulator, with carefully matched components, provided a carrier suppression of from −62 to −72 db over the nominal range of signal level. To remove the unwanted sideband, a McCoy crystal filter was installed in a standard receiver IF amplifier. The 3-db response bandwidth was from 455.005 to 455.075 kc with carrier suppression of 20 db. The total carrier suppression then amounted to better than 80 db. The signal was then heterodyned to 30 Mc by means of balanced mixers; then, to assure maximum attenuation of reference frequencies, a narrow-band 30-Mc crystal filter was used. This 30-Mc signal was finally mixed to 2388 Mc using a balanced mixer, which was followed by a narrow-band cavity filter, which attenuated the 2358-Mc feedthrough by an additional 28 db over that of the balanced mixer. The final 2388-Mc signal out of the converter was a nominal −16

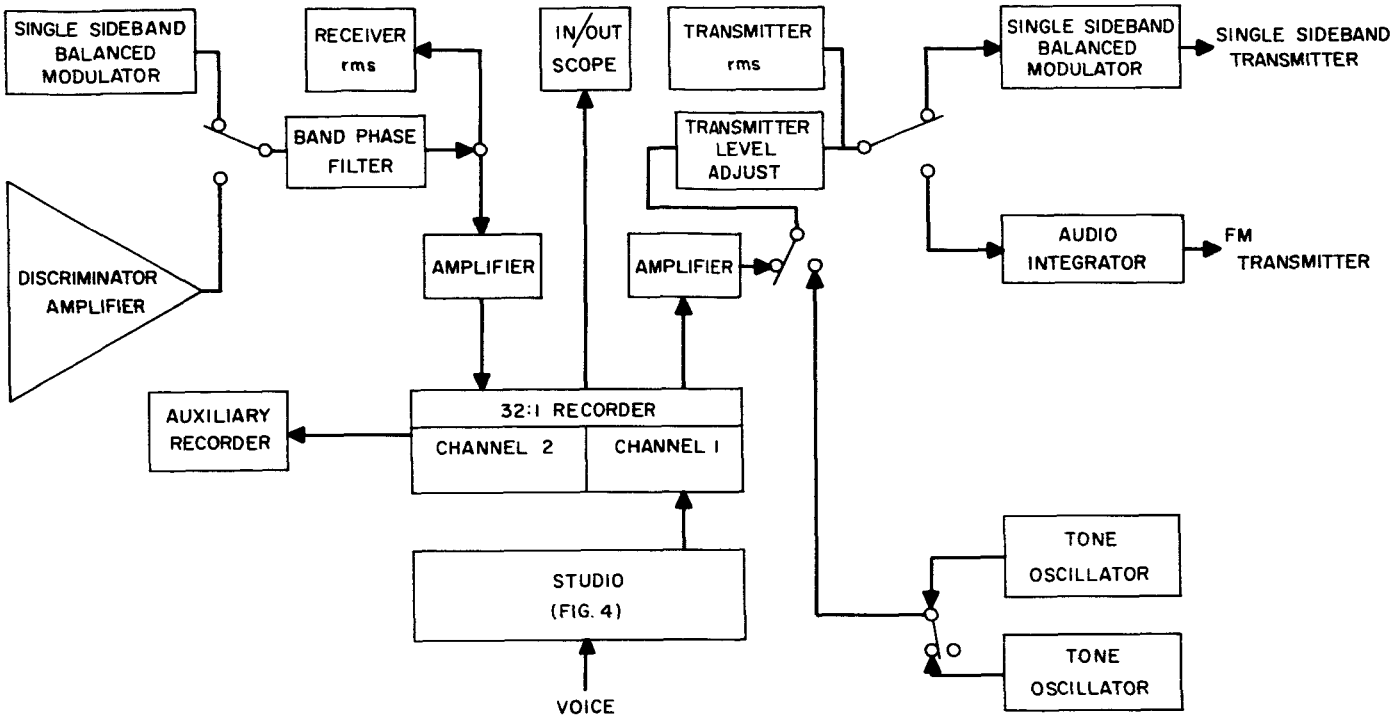

Fig. 25. Audio system block diagram

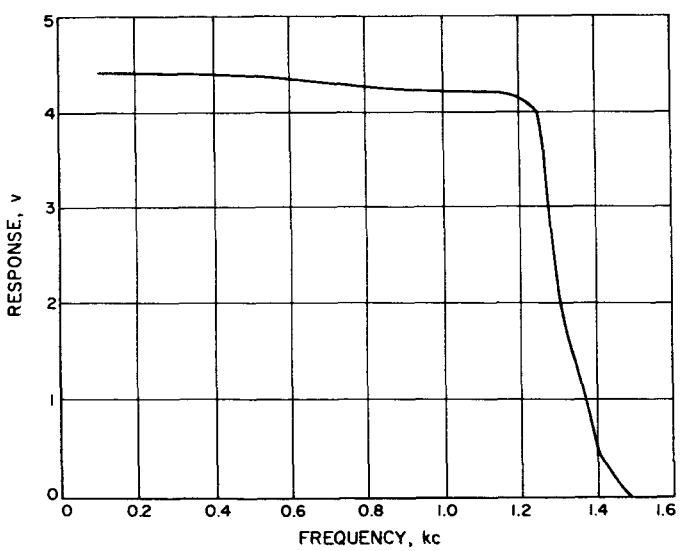

Fig. 26. Bandwidth FR 100 recorder curve

dbm. This was amplified by two traveling wave tube amplifiers (Ref. 12). Figs. 28 through 33 show general construction and installation of equipment.

c. Conduct of experiment. With the systems installed and testing completed, the Venus voice-bounce experiment proceeded. The first attempt to reflect SSB voice-modulated signals off Venus on May 21, 1964, with transmitter power averaging 80 kw, resulted in no intelligible return. The return spectrum was displayed using the AM total spectrum receiver. With a bandwidth of 200 cps, this provided a resolution of 2.5 cps. The second transmission was a single tone. When this first tone was received it was not audible; but an interesting feature occurred. On noting the AM spectrum display, the frequency was offset by 2.5 cps; and since this ephemeris error would be multiplied by 32 in the audio system, it was decided to offset the programmed local oscillator by the same amount in order to return to receiver band center. A sampling of AM spectrum returns is shown in Fig. 34.

The next attempt to reflect signals off Venus, which was on May 22, 1964, still using SSB signals, was a tone transmission. The experiment was changed from the tone transmission of the previous day in that at discrete time intervals the tone was alternately keyed off and the frequency shifted, with only two people forewarned. When the return was played back, everyone in the control room detected the tones. The same experiment was tried with the FM system, and again the tones were heard, with somewhat more clarity than the SSB transmission. Voice transmission was then tried with no success on the FM system; using the SSB system the return could be understood by those who had heard the message recorded, but it was not generally accepted as an intelligible return.

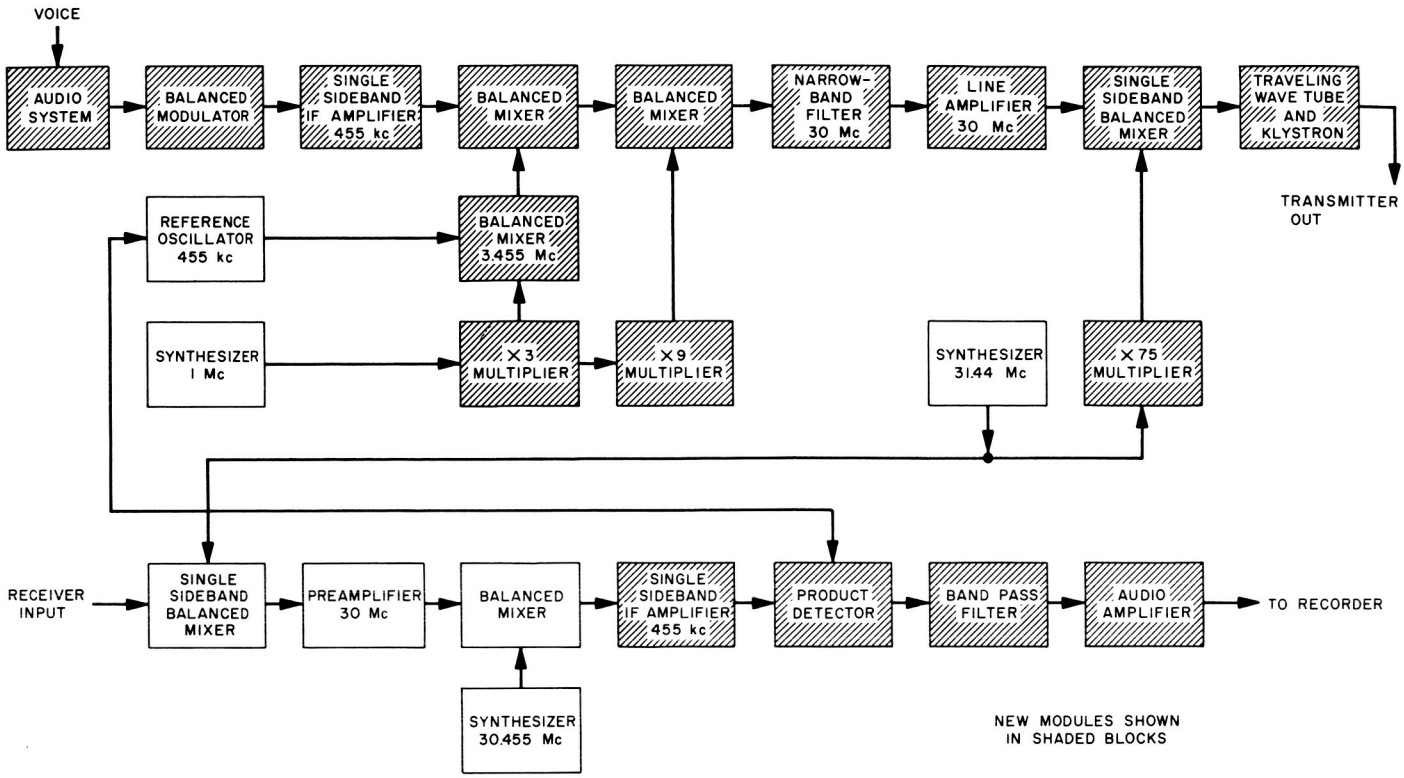

Fig. 27. Single sideband system block diagram

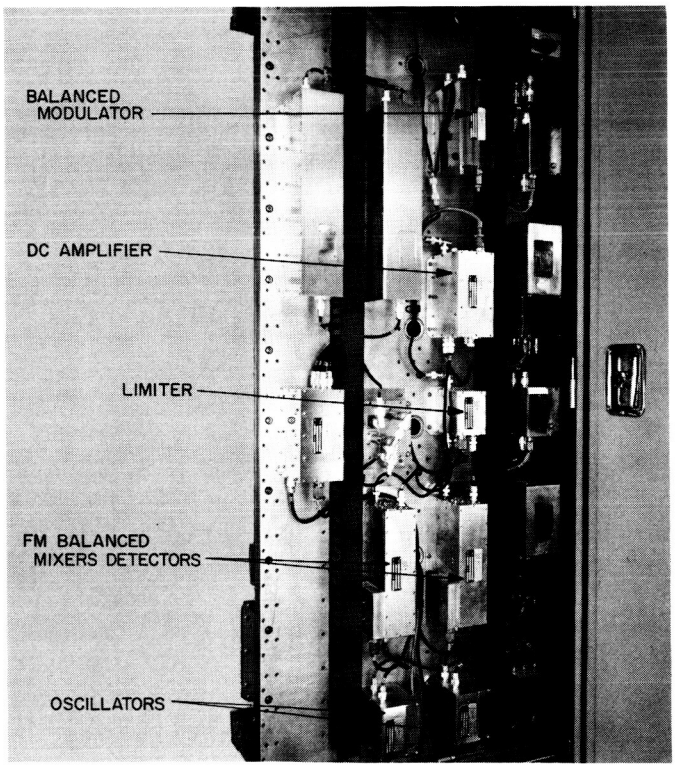

Fig. 28. Venus voice-bounce FM receiver units

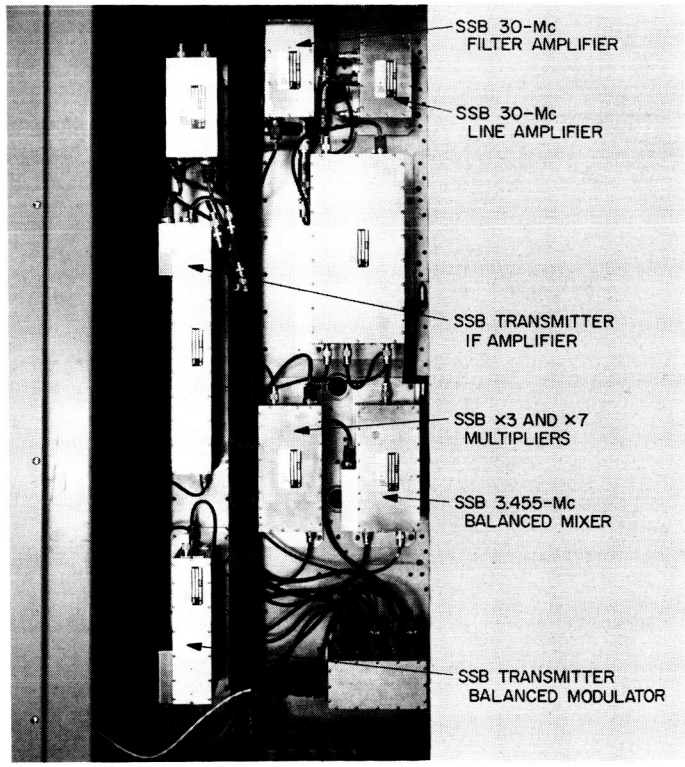

Fig. 29. Venus voice-bounce single sideband transmitter units

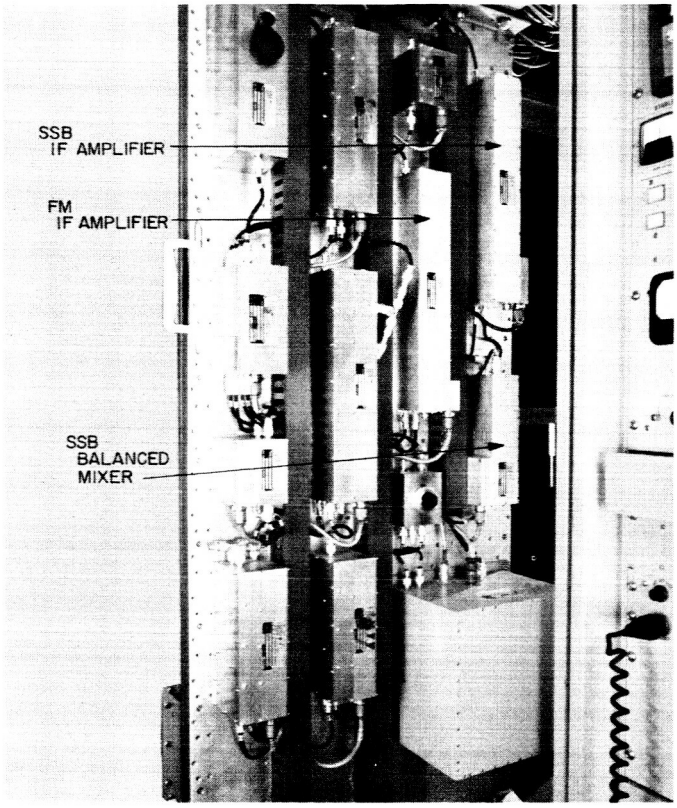

Fig. 30. Venus voice-bounce receiver units

Fig. 31. Venus voice-bounce 30- to 2388-Mc single sideband converter

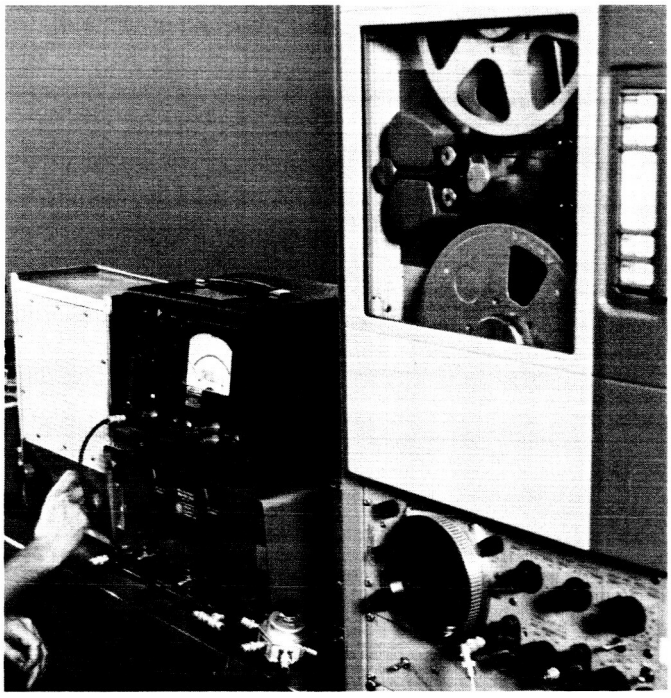

Fig. 32. Venus voice-bounce audio system

Fig. 33. Venus voice-bounce audio studio

A decision to try more transmitter power was made, and on the next attempts the beam voltage was increased from 32 to 42 kv with the average power held to 100 kw on the klystron forward power meter. The return was improved in understandability, as would be expected with a stronger signal. Tones were then transmitted, and the Mod III computer supplied range gating. The signal clarity of SSB was improved but no effect on the FM system was evident.

On June 7, 1964, SSB voice transmission was tried with the transmitter forward power meter averaging 90 kw. The first run was a complete success with everyone

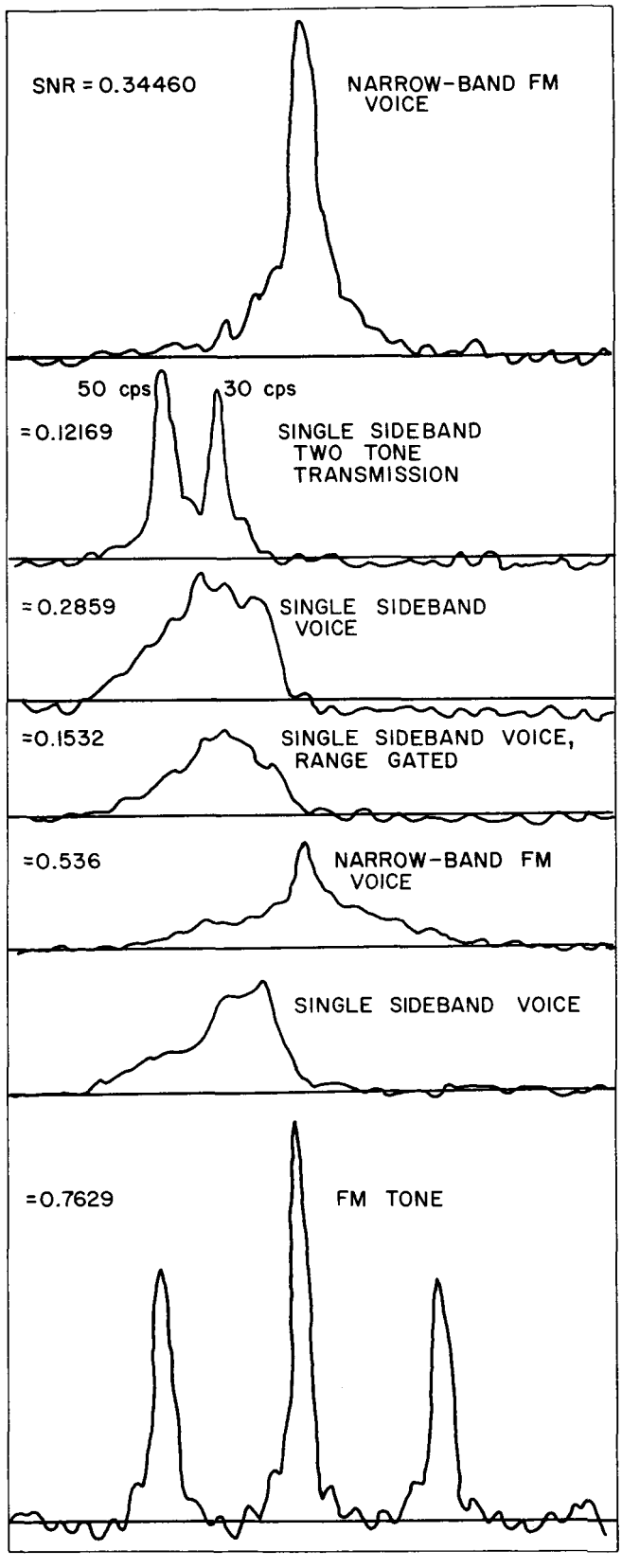

Fig. 34. Total spectrum returns

present acknowledging the exact message. The sound was much like a whisper masked by noise.

By performing several closed loop tests in which the output was severely limited, distortion due to limiting in the klystron was shown not to affect the intelligence to any great degree. (See transmitted waveform in Fig. 35.)

The results of May 22, 1964, indicated that range gating would improve this signal, and range gates of several different durations were tried in 0.5-msec steps from 4 to 0.5 msec. The 2.5-msec range gate provided the greatest improvement and the clarity was markedly improved. However, with the decrease in signal power, due to range gating, the noise became more objectionable than the whisper, and range gating was discontinued.

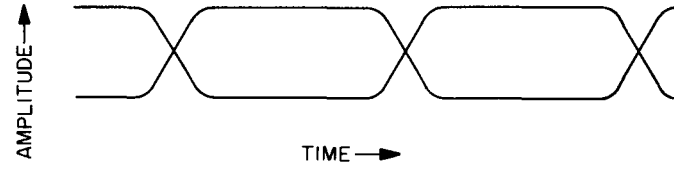

Fig. 35. Limiting of klystron power output

On subsequent transmissions, the programmed local oscillator offset from the ephemeris tape was changed in 0.5-cps steps with the result that a 2.5-cps offset was chosen as optimum. Further attempts were made to increase transmitter power with little success, since the klystron arced at higher levels of power. The voice-modulated FM system became a success 1 day before and 1 day after conjunction. The voice on the FM was not distorted as noted in the SSB returns and sounded like a weak but clear transmission; no further attempts were made to range gate the FM system.

Attempts were made to find an optimum voice for transmission. The voices of several Goldstone personnel and a professional announcer were recorded and transmitted. No consistent improvement was obtained over previous results.

The Venus voice-bounce experiment is considered a technical success in that the returned signals closely approximated the expected values. The quality of the recorded voice signals is very poor due to low signal-to-noise ratio; however, the signals are understandable to the majority of listeners. Valuable information on the implementation and operation of such a system was ob-

tained and the effect of the rotation of Venus on both FM and SSB signals was recorded. In addition, a new record for long distance transmission of voice signals was established with round-trip distances of 58 million miles covered. The results indicate that if at the next conjunction more transmitter power or a larger antenna or both are available, good voice-bounce signals should be possible.

3. High-Power, 100-kw S-Band Transmitter

a. Introduction. During this reporting period, the primary mission of the 100-kw S-band transmitter was radar observations of the 1964 opposition of Venus. At the end of each Cytherean day, the facility was used for checkout of the 100-kw *Mariner* transmitter sytem. The system was available for R&D work, improvements, maintenance, and testing from about 11 p.m. to 4 a.m.; new developments were necessarily limited.

No significant outages were experienced from April 28, 1964 until June 17, 1964, when the dc beam voltage to the klystron was increased in order to assure 100-kw average power output for amplitude, single sideband suppressed carrier, and modulated experiments. Both klystrons on hand (Serial Nos. 1 and 3) outgassed when tried in this service. In one tube the trouble was later resolved to be insufficient processing time at the factory. The system operated until July 29, 1964, when the new vendor-supplied filament supply was internally shorted and had to be replaced by a laboratory unit. On July 30, 1964, the high-voltage cable to the antenna shorted inside a conduit and was replaced. The following day the system was operable, but the klystron emission appeared to be limited. The experiment was ended as scheduled on July 30.

The reliability of the VA-858A klystrons since the installation of the system has been analyzed and is summarized in this article. A filament time delay unit was added to the system to reduce filament current surges during warmup. A 40-v instability in the high-voltage dc supply at 33-kv output is being studied. The overhead hoist for handling the solid-state rectifier in the transformer vault has been installed. Driver and control circuitry for the beam keyer has been developed.

b. 100-kw S-band klystron reliability. The 100-kw S-band planetary and lunar radar experiments began January 1, 1963, and were temporarily stopped August 1, 1964, following the 1964 Venus opposition. The entire operation was conducted with only two VA-858A 100-kw klystrons (Fig. 36) except for a period of 1 wk when a third tube was used. A review of the operating history of these tubes shows (Table 5) that tube failure was principally due to external causes, not a fault of the tubes, and to inadequate quality control by the tube manufacturer. The collector appears to be undersized for the planetary radar service; one tube failed because of a cracked collector. Collectors examined during other repairs exhibited localized, internal surface cracking. These klystrons were prototypes warranted for only 250-hr operating life; subsequent production tubes should perform better. The manufacturer is aware of his quality control problems, and negotiations are in process for an improved tube design with a larger collector and a shielded focus magnet. External failure causes have been corrected.

Klystron Serial No. 1 was repaired four times after failures. (Two of the failures occurred in the manufacturer's plant.) The total operating time on the body of the tube, which is the only original part left, is 2074 hr. The cathode assembly was transferred from Tube No. 3 to No. 1 after 1071 hr of filament operation and now has accumulated 2924 hr of operation. On the last day of the experiment, the cathode emission appeared to be limited.

Klystron No. 3 has not been operated as much as No. 1. The output cavity was damaged February 10, 1963, as a result of an improperly constructed focus magnet and has had high body current since; consequently, it has been used as a spare.

The causes of the external failures have been remedied. Most of these occurred during the site activation, while the system was still under the cognizance of the contractor. A 20-μ filter was installed in the cooling water line after a collector was damaged by Teflon plumber's tape plugging the water passages. The first arc detector had only one channel. Following the loss of a tube when an external waveguide arc caused a broken RF window, a two-channel arc detector was installed to provide redundancy. The original filament supply experienced arcing from the transformer and choke-to-ground because of insufficient insulation. One such arc damaged a tube filament. A new supply was procured with 55-kv insulation and no further arcing was noted. The focus magnets now have the coils cemented in place.

The principal weakness of the VA-858A klystron appears to be in the collector. The klystron is about 35% efficient; with 350 kw dissipated in the collector as heat. When the RF drive is removed from the tube and the dc beam voltage left on, the full 350 kw must be absorbed

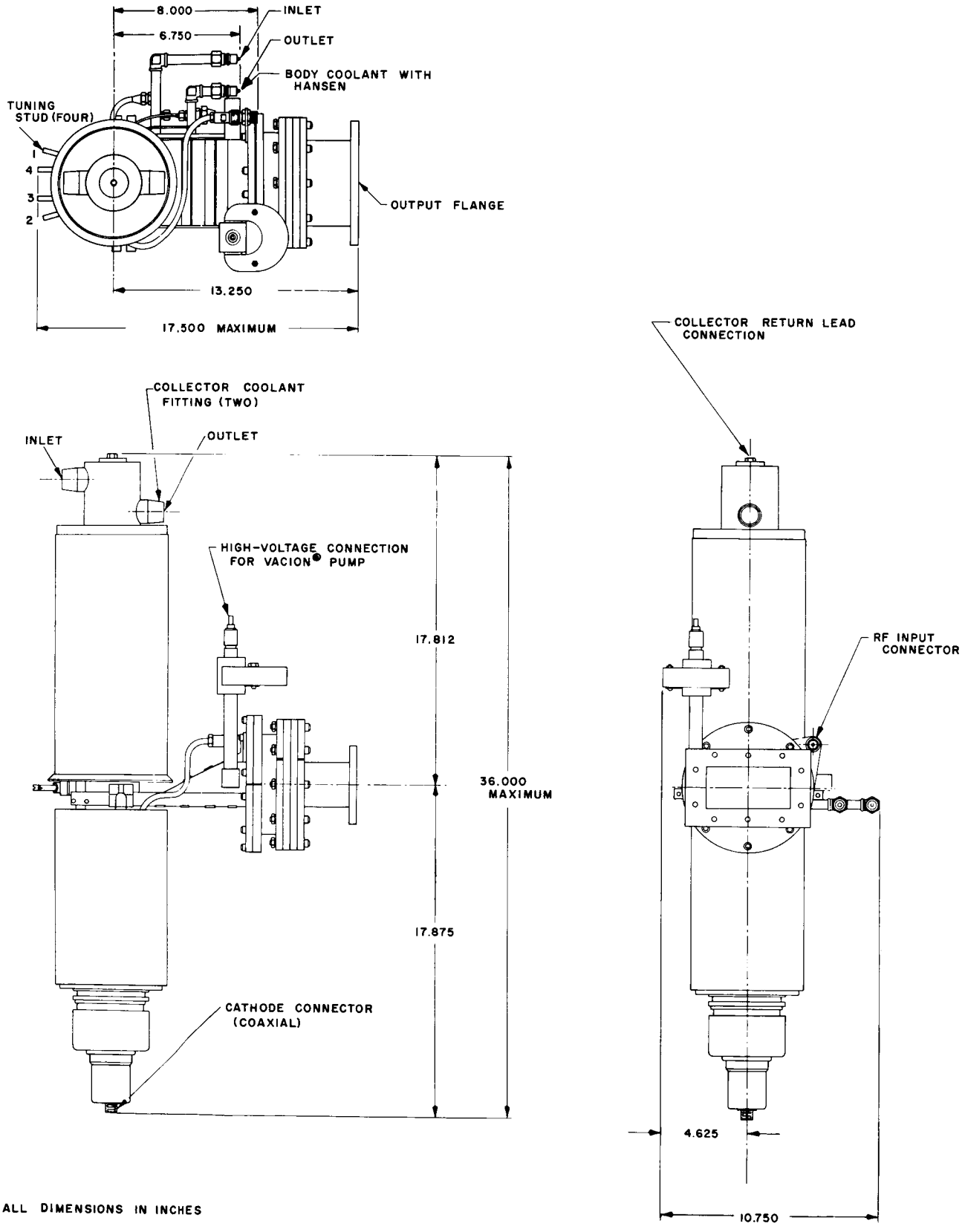

Fig. 36. Outline, VA-858 klystron

Table 5. Review of tube operation

Date	Tube Serial No.	Operating time on tube at GTS since last repair		Total operating time on tube parts (at GTS)					Condition	Failure responsibility	Remarks
		Filament hours	Beam hours	Collector	Body	Window	Cathode	Filament			
1/1/1963	1	—	—	—	—	—	—	—	Installed	—	Start experiment (system under contractor cognizance)
1/26/1963	1	206	85	85	85	85	85	206	Failed	External	Overheated collector due to plugged water channels from foreign material in transmitter cooling system (contractor cognizance)
1/26/1963	3	—	—	—	—	—	—	—	Installed	—	Water filter installed
2/5/1963	3	148	110	110	110	110	110	148	Failed	External	Broken RF window caused by waveguide arc not detected by inoperable arc detector (contractor cognizance)
2/10/1963	3	—	—	110	110	—0—	110	148	Installed	—	Repaired-broken window replaced
2/10/1963	3	—	—	110	110	—0—	110	148	Damaged	External	Loose coil in focus magnet deflected beam, damaging output cavity. Temporary repair by wedging coil (contractor cognizance)
3/18/1963	3	444	332	442	442	332	442	592	Operating	—	Mars experiment terminated, transmitter shipped to contractor for rework, repair of focus magnet and installation of dual channel arc detector
4/15/1963	3	444	332	442	442	332	442	592	Installed		Transmitter reinstalled at GTS (end of contractor cognizance)
9/11/1963	3	501	343	785	785	343	785	1093	Failed	External	Damaged filament, high-voltage arc-to-ground in filament supply; severe, localized collector cracking
9/11/1963	1	—	—	—0—	85	85	85	206	Installed	—	—
12/27/1963	1	1021	711	711	796	796	796	1227	Failed	External	Broken RF window while tube was delivering 178 kw in overload test
1/24/1964	3	—0—	—0—	—0—	785	343	—0—	—0—	Installed	—	Tube received from contractor, cathode and collector replaced
4/3/1964	3	1071	699	699	1484	1042	699	1071	Failed	Internal	Cracked collector work-hardened by beam impact
4/9/1964	5	—0—	—0—	—0—	—0—	—0—	—0—	—0—	Installed	—	New tube temporarily installed while awaiting repair of No. 1
4/16/1964	5	145	105	105	105	105	105	145	Failed	Internal	Poor braze joint in collector opened, water entered tube, cathode blew off
4/28/1964	1	—0—	—0—	711	796	—0—	699	1071	Installed	—	New window, reworked collector, cathode from No. 3[a]
6/17/1964	1	1082	752	1463	1548	752	1451	2153	Poor	Internal	Arcing and outgassing excessively for voice-bounce experiment
6/17/1964	3	—0—	—0—	—0—	1484	1042	—0—	—0—	Poor	Internal	New collector and cathode installed during repairs
6/17/1964	3	76	46	46	1530	1088	46	76	Installed	—	Severe outgassing and arcing; removed and returned to manufacturer
6/21/1964	1	1082	752	1463	1548	752	1451	2153	Installed	—	Reinstalled without repairs
7/31/1964	1	771	526	1989	2074	1278	1977	2924	Poor	Internal	System operable but cathode emission appears limited, end of 1964 Venus radar experiment

[a]Tube No. 1 was repaired March 6, 1964, and placed on test at the manufacturer's plant. The tube failed March 8, 1964: foreign material left inside tube carbonized. The window was removed and foreign material removed and tube resealed. On April 16, 1964, beam voltage was applied to the tube, and the cathode seal cracked from carbon deposits across the insulator. The tube was recleaned and the cathode from Tube No. 3 was installed in place of the cracked cathode. The tube continued to arc and outgas until removed from the test stand and shipped to JPL April 26, 1964.

in the collector. Furthermore, with drive, the beam is dispersed in the collector; without drive, the beam is not dispersed as much and is concentrated on the end of the collector. The alternate heating and cooling of the thick copper collector, as the drive is keyed on and off, eventually causes work-hardening and cracking of the interior surface at the upper end. Most of the collectors examined also had an elliptical spot of deteriorated metal on one side, near the bottom, where the beam enters. This seems to be due to some anomaly in the magnetic focus circuit which causes beam deflection. The collectors were originally fabricated in pieces and brazed together. After a failure of one of the brazed joints allowed cooling water to leak inside the klystron, the collectors were machined from solid copper.

c. Klystron filament delay unit. The tungsten filament of the Varian VA-858 100-kw klystron operates at approximately 10.5 v and 10 amp. The present operating practice during klystron turn-on is to apply the full 10.5-v power supply potential to the cold filament, and since the resistance change of tungsten from the ambient temperature to operating temperature is approximately 9 to 1, a turn-on current as high as 90 amp would be expected. The step-down filament transformer provides some limiting through its leakage inductance; however, the present system allows the klystron filament surge-current to be twice the amount specified by the manufacturer. This can shorten the life of the klystron filament and place an unwarranted strain on the filament supply.

To limit this turn-on surge current, the time delay unit (Fig. 37) has been built in the laboratory. The filament transformer primary voltage is limited to 70% of the nominal value during a 2-min warmup period. In case of a current interruption, the unit will automatically recycle to the start position. A schematic of the time delay unit is shown in Fig. 38.

This installation is expected to increase klystron life and is part of the continuing program to upgrade the performance and reliability of the 100-kw transmitter.

d. Transmitter power stability. Recent observations of the transmitter power output have revealed periodic variations in amplitude, which decreases and increases in a random manner over the course of a day's operation. The power variations were directly related to high-voltage variations caused by the power supply. Periodic power variations of ½ kw were often recorded (Fig. 39).

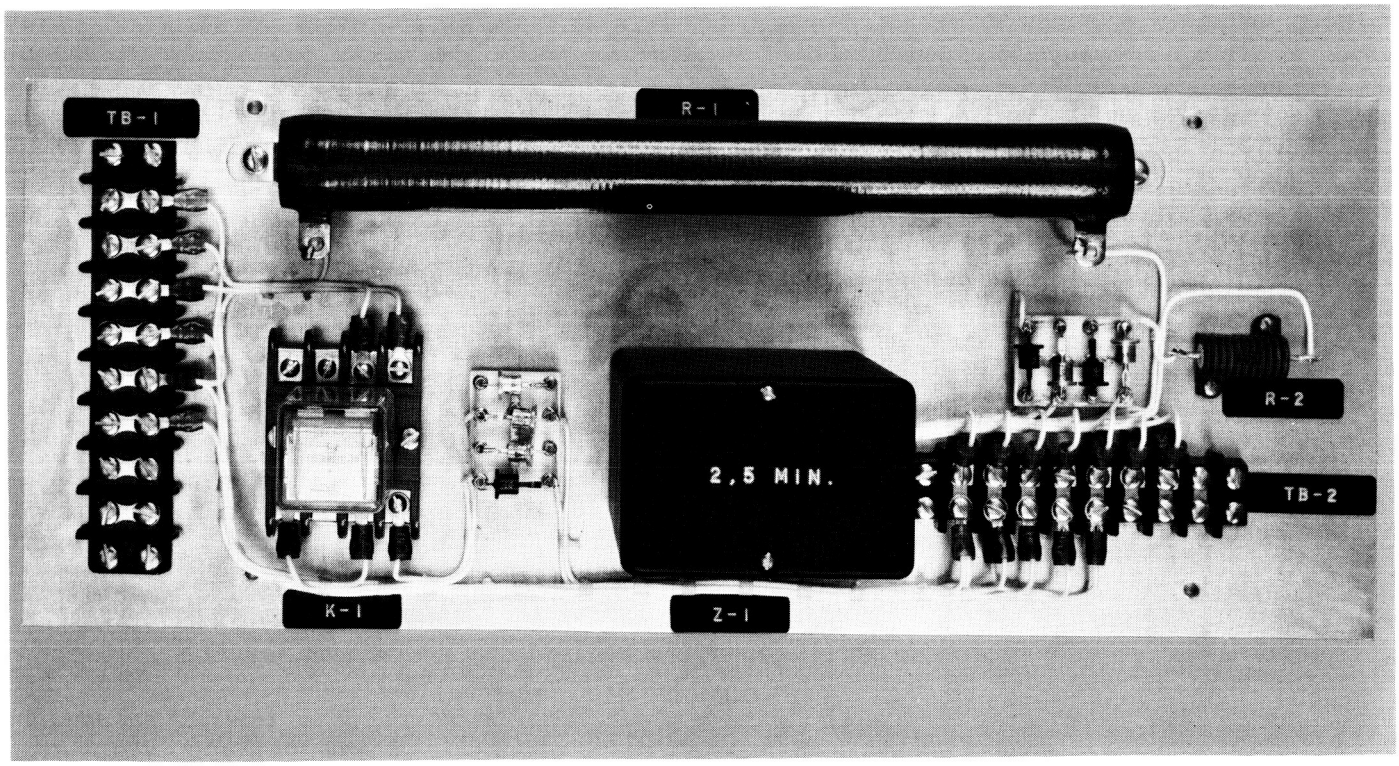

Fig. 37. Filament time delay unit

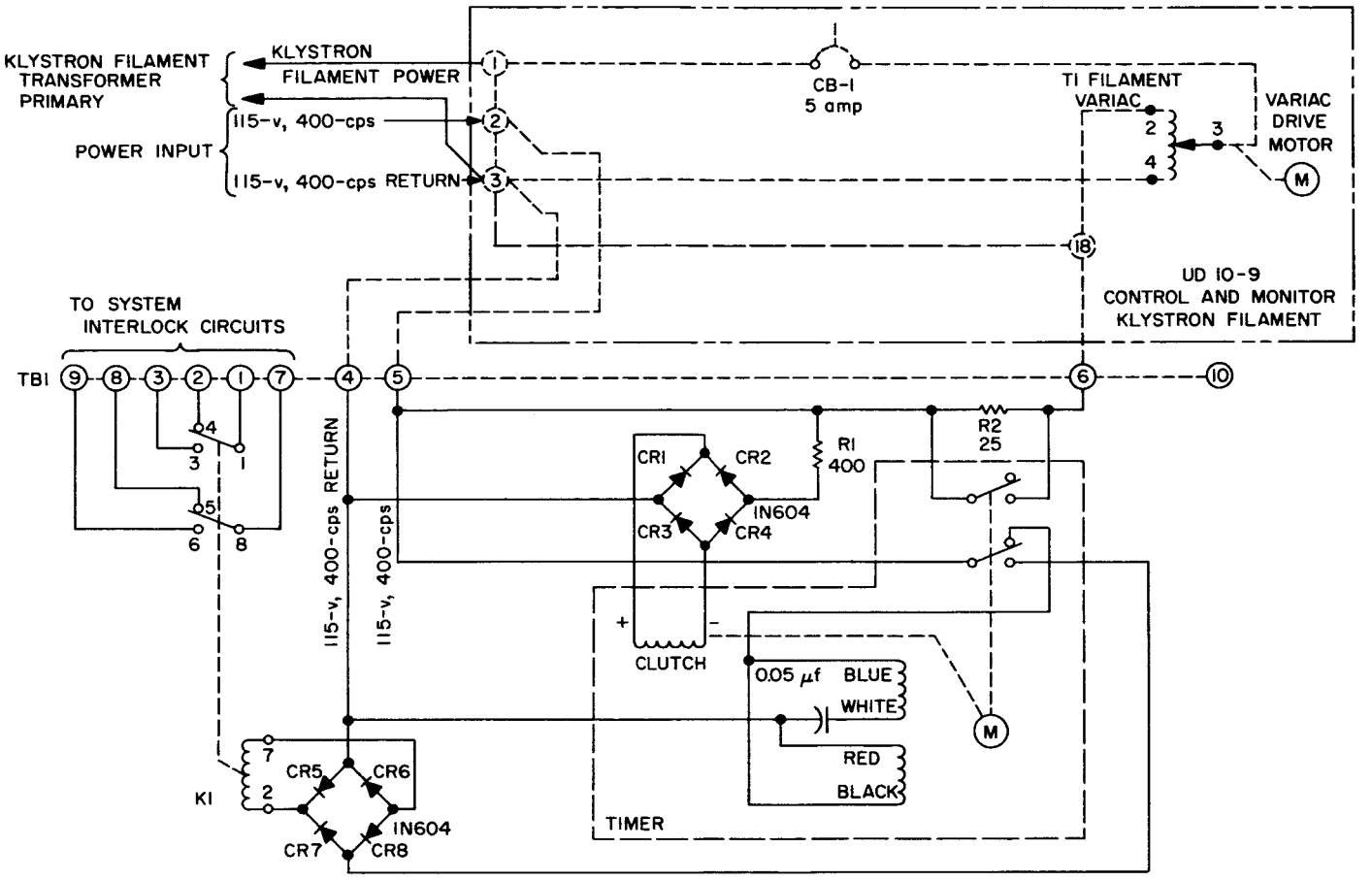

Fig. 38. Klystron filament time delay unit

The Venus 100-kw transmitter power supply uses a synchronous 60-cps motor to drive a 400-cps generator (Fig. 40, block diagram). The three-phase output of this generator is applied, through three vacuum switches, to the three-phase delta-wye high-voltage power transformer. The output of the transformer is rectified by a full-wave, three-phase bridge rectifier composed of 12 water-cooled vacuum tubes. The rectified dc passes through an L-C filter composed of a 1-henry choke and a 0.42-μf capacitor. The filtered, negative, high-voltage dc output is then applied to the cathode of the power klystron.

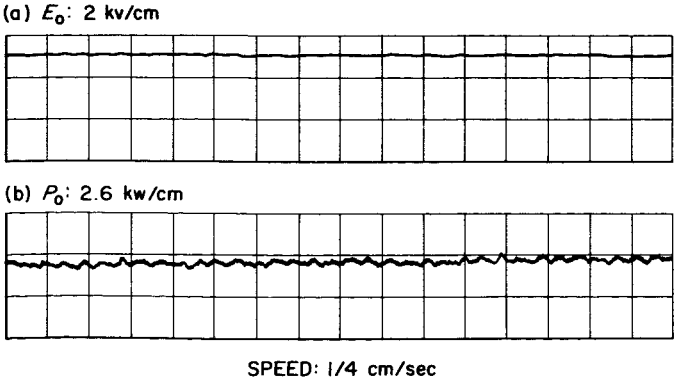

Fig. 39. Graphic recording: (a) power supply voltage and (b) RF power output

A sample of the dc output voltage is obtained through the use of a high-voltage dropping resistor. This sample voltage, 1/500 of the dc filtered output voltage, is sent to the input of an electronic differential amplifier. The output of this differential amplifier is applied to the signal-input field winding of an amplidyne system. The amplidyne is then used to control and excite the field of the main 400-cps generator. In this manner, the dc output voltage is compared with a fixed dc voltage in the electronic differential amplifier and, by means of this closed control loop, the dc output is regulated.

The response of the feedback regulator loop is quite slow, in the order of a second or more, due to the L-C high-voltage filter and the field inductance of the main 400-cps generator. Therefore, the electronic regulator system cannot remove fast variations from the output; but it can maintain a close control over the average dc voltage level.

The variations in the dc output voltage, compared with the main 400-cps generator field current, can be seen in Fig. 41. Here the electronic control is in use with the signal field of the amplidyne switched to the electronic field control output. The periodic variations are evident in the dc output voltage. The amplitude is approximately 40 v (peak-to-peak) at a beam voltage of 31 kv. The period is 3.6 sec and the high-frequency ripple superimposed on the low frequency variations is a 10-v (peak), 3.3-cps wave. Small deviations in the field current (in the reverse direction) can be seen as the automatic circuit attempts to make a correction. The ripple on the field current, running at a nominal current of 28 amp, is an 8-cps wave of 75-ma (peak) amplitude.

The variations in the dc output voltage compared with the main 400-cps generator field current, when operating in the manual-field condition, is shown in Fig. 42. Here the signal field of the amplidyne is switched to a potentiometer connected across a fixed 125-v dc voltage. The high-voltage dc output variations are larger (up to 100 v peak-to-peak) and the period of the variations is long (up to 17 sec in duration). There are several large transients that appear in the output voltage with no electronic correction to suppress them. (See Fig. 42, asterisked-marked points on curves.) The field current of the main 400-cps generator still contains some variations (in the reverse direction) reflecting the change in dc voltage. The sudden transient in the output voltage also shows up as a transient in the main generator field current.

The conclusions to be drawn are that the electronic regulator, although quite slow in acting, does reduce the amplitude of the variations in the high-voltage dc output. In addition, the transients are reduced and the average dc voltage is maintained constant over long periods of time. When the power supply is switched to manual control, current is supplied to the amplidyne signal field from a fixed dc source instead of from the electronic feedback path. The output variations are larger and serious transients occur. The period of the voltage variations is about four times as long and, most important, the variations in output voltage are still reflected in changes in the main 400-cps generator field current.

The results of these measurements, while not eliminating the main 400-cps generator as a trouble source, point to the amplidyne exciter system as the source of trouble. Future investigations of this problem will include a resistance load test of the amplidyne output and the excitation of the main 400-cps generator field with an external dc power source.

e. Solid-state rectifier hoist. The new solid-state, high-voltage rectifier, designed to replace the vacuum tube rectifiers in the 100-kw S-band transmitter, has been previously discussed (Ref. 13).

The installation and servicing of the solid-state rectifier has required the construction of an overhead hoist system. This system has been built and installed in the Venus transmitter power supply vault. The two hand-operated chain hoists are attached to each of two overhead I-beams. The tracked hoist trolleys are free to move along the overhead beams and permit the movement of the rectifier assembly from the operating position to the servicing position. This permits the inspection and service of the rectifier to be accomplished in the limited space of the power supply vault. Fig. 43(a) shows the rectifier and rectifier tank assembly hoisted up to the ceiling of the vault preparatory to traversing the I-beams to the operating position. Fig. 43(b) provides a view of the rectifier and tank assembly in the operating position. Fig. 43(c) illustrates the rectifier components and attached lid, after removal from the rectifier tank, in the servicing position.

It is mandatory that inspection and test of the solid-state rectifier be done in this enclosed space. Serious damage to the rectifier components and contamination of the oil in the rectifier tank would result if the outside climatic elements of moisture and dust were to come into contact with the rectifier assembly whenever it is removed from its oil-filled tank.

f. Lunar beam-switch driver. The desirability of removing the power klystron beam voltage during the receive period of a lunar mapping radar experiment has been previously discussed (Ref. 12). A considerable increase in signal-to-noise ratio and no klystron power limitation are the desirable results of this beam-keying technique. The equipment required to accomplish this task will now be described (Figs. 44 and 45).

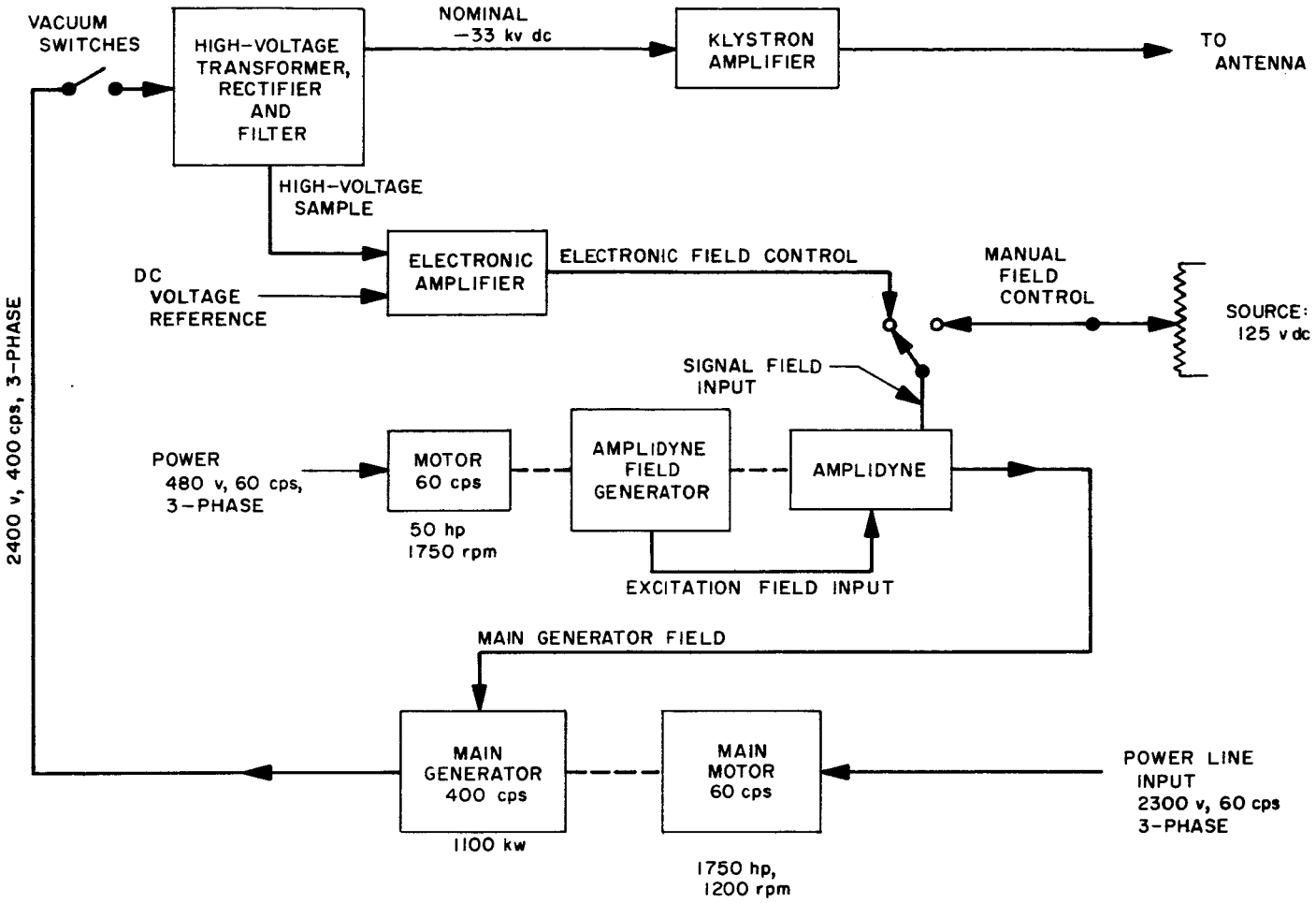

Fig. 40. 100-kw power supply system

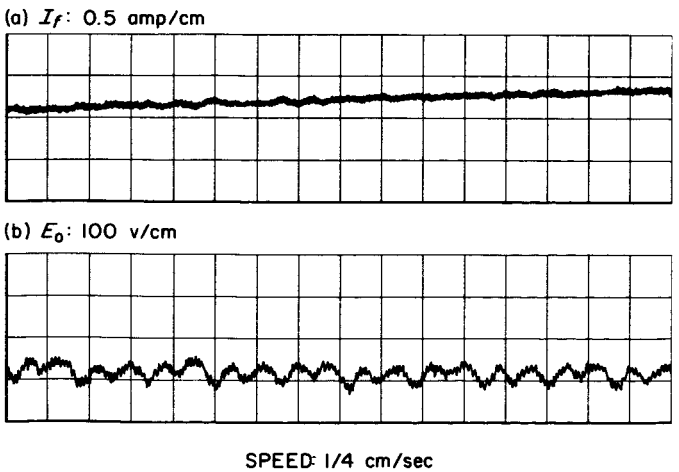

Fig. 41. Graphic recording, automatic field operation: (a) main generator field current and (b) high-voltage dc output

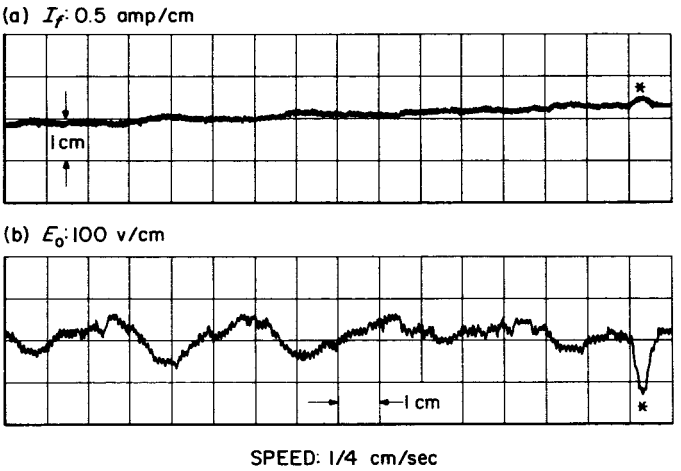

Fig. 42. Graphic recording, manual field operation: (a) main generator field current and (b) high-voltage dc output

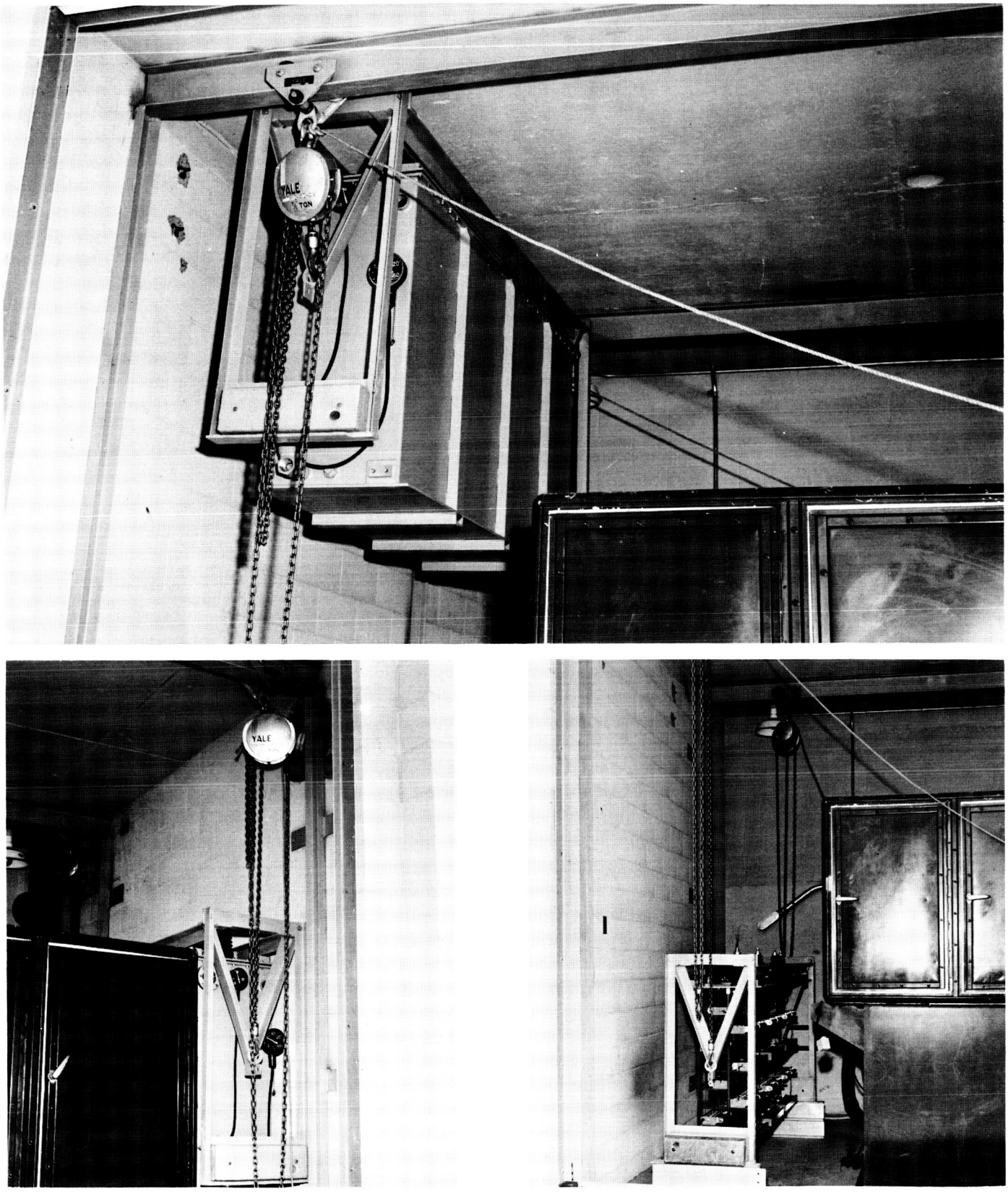

Fig. 43. Rectifier hoist

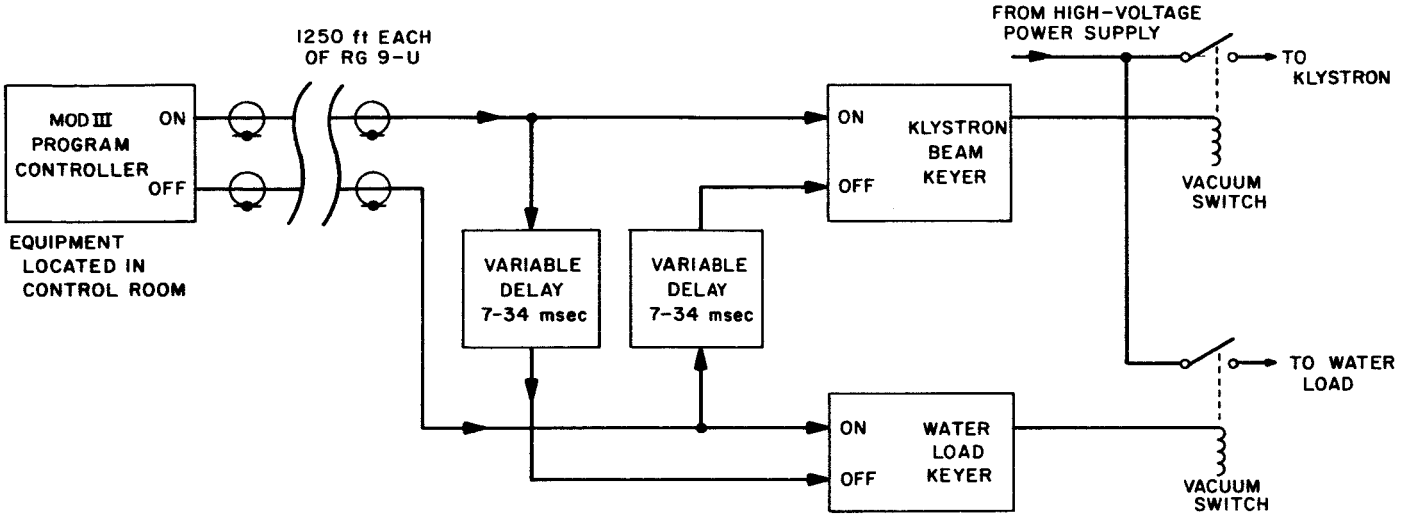

Fig. 44. Lunar beam-switch driver block diagram

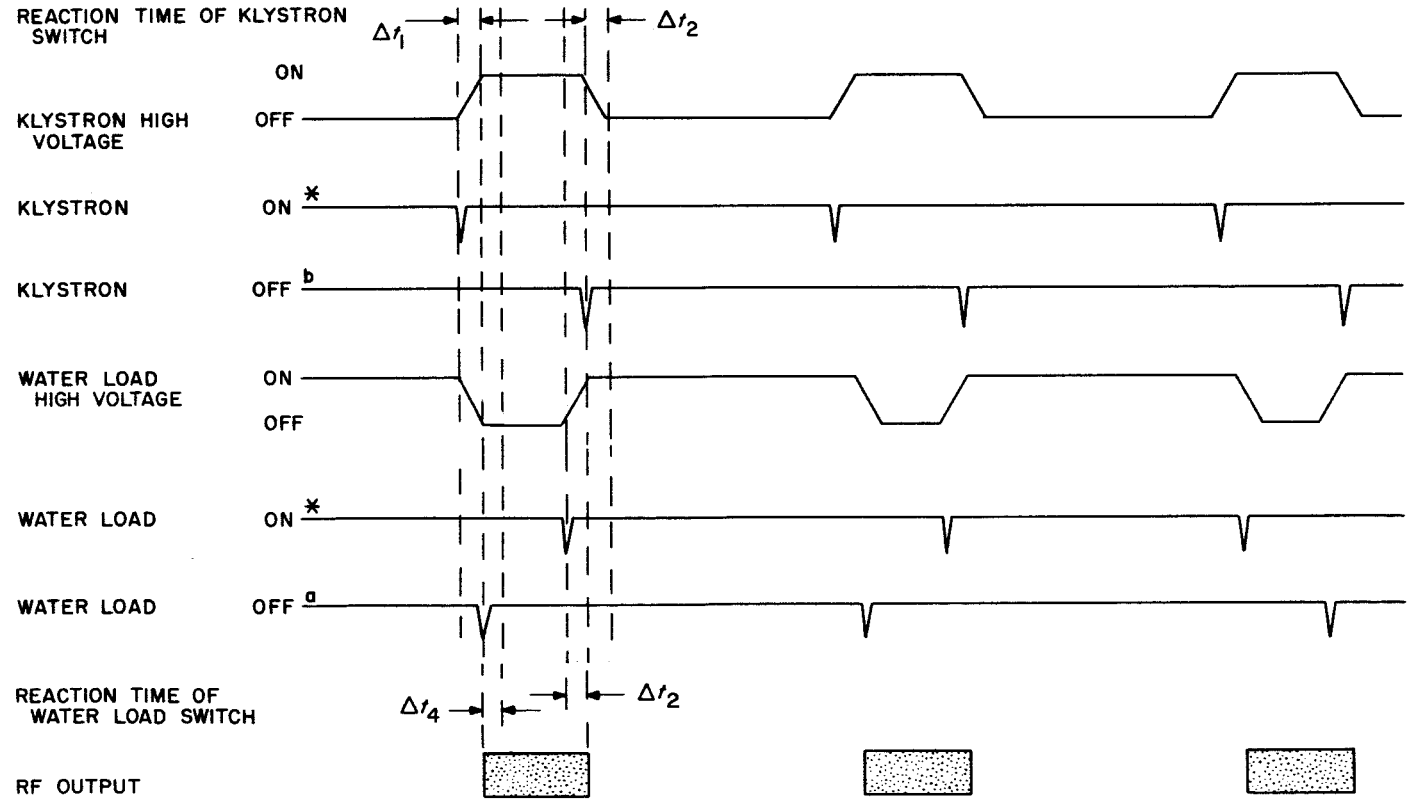

* PULSES DIRECT FROM COMPUTER

a. PULSES DELAYED FROM KLYSTRON *ON* PULSE (NOMINAL 16 msec)

b. PULSES DELAYED FROM WATER LOAD *ON* PULSE (NOMINAL 16 msec)

Δt_1 *ON*– SWITCHING DELAY
Δt_2 *OFF*–SWITCHING DELAY
} KLYSTRON BEAM SWITCH

Δt_3 *ON*–SWITCHING DELAY
Δt_4 *OFF*–SWITCHING DELAY
} WATER LOAD BEAM SWITCH

$$\Delta t_1 \approx \Delta t_2, \approx \Delta t_3, \approx \Delta t_4 \approx 16 \text{ msec}$$

Fig. 45. Lunar beam-switch driver, waveforms

The beam keying of the power klystron in the 100-kw S-band transmitter requires two high-voltage vacuum switches (Ref. 12). One vacuum switch provides a dc path from the high-voltage dc power supply to the klystron. The other vacuum switch provides a dc path from the power supply to the dc water load. These switches are opened and closed 180 deg out of phase with respect to each other so that the power supply loading is maintained and serious transients are avoided.

The initiation of the switching action is originated by the Mod III stored program controller in the Venus control room. This device transmits a pulse from its *on-command* cable connector to command the application of the klystron beam voltage. A second pulse, approximately 2 sec later, is transmitted from the *off command* cable connector to command the de-energizing of the klystron beam voltage and the application of power supply voltage to the dc water load. Thus, two cables, approximately 1250 ft long, connect the transmitter beam switches with the Mod III controller.

The Mod III controller generates 7-v, 5-μsec-long, negative pulses and directs them into the 1250-ft interconnecting coaxial cables. These cables are terminated in 50 Ω at the transmitter. The *on-command* pulse is directed to the *on-terminal* of the klystron beam keyer chassis. This unit accepts this computer pulse and energizes the vacuum switch which applies power to the klystron. A variable-delay chassis accepts this same *on-command* computer pulse. The pulse is delayed an appropriate amount and sent to the *off-terminal* of the dc water load beam keyer chassis. This unit then opens the vacuum switch which removes the dc water load from the high-voltage dc power supply. The variable delay unit is necessary to maintain a load on the high-voltage dc power supply at all times in spite of the time lost in physically closing and opening the vacuum switches. Fig. 45 shows the closing time of the klystron vacuum switch Δt_1. The opening action of the dc water load switch is initiated, as shown, shortly after the klystron vacuum switch is closed. This delay, $\Delta t_1 + e$, is supplied by the variable delay unit.

The *off-command* pulse from the computer performs a similar function in reverse. The *off-command* pulse is directed to the *on-terminal* of the dc water load keyer chassis. This unit accepts the computer pulse and closes the vacuum switch connecting the power supply to the dc water load. A second variable delay chassis accepts this same *off-command* computer pulse. This pulse is then delayed an appropriate amount and sent to the *off-terminal* of the klystron keyer chassis. This unit then opens the vacuum switch which removes the klystron from the high-voltage dc power supply. This second variable time delay unit is also necessary to maintain a load on the high-voltage dc power supply at all times. Fig. 45 shows the closing time of the dc water load switch Δt_3. The opening of the klystron vacuum switch is initiated, as shown, shortly after the dc water load switch is closed. This delay, $\Delta t_3 + e$, is supplied by the second variable delay unit.

The reaction times of the vacuum switches Δt_1 and Δt_2 for the *on* and *off* switching time of the klystron beam switch and Δt_3 and Δt_4 for the *on* and *off* switching time of the dc water load beam switch, are all about 16 msec. The variations in switching time are compensated for by the delay units to assure a load on the high-voltage dc power supply at all times.

Fig. 46 illustrates the circuit for the klystron and dc water load beam keyer chassis. The negative 7-v on-pulse enters the chassis at J1. This pulse triggers the keying and isolation amplifier Q2. This unit provides a positive pulse at the base of Q4, which causes the bistable multivibrator, Q3 and Q4, to change state so that Q3 is nonconducting. The positive potential at the collector of Q3 is sent through the emitter–follower Q5 and ultimately keys on the silicon controlled rectifier Q7. Q7 conducts and causes the stored energy of C1 to quickly actuate the vacuum switch solenoid. The solenoid plunger then closes the external high-voltage dc path in about 16 msec. The momentary current through the vacuum switch is over ten times the normal pull-in current. This provides a speedup action which greatly shortens the pull-in time from the unassisted 60-msec figure.

The negative 7-v off-pulse enters the chassis at J2. This pulse triggers the keying and isolation amplifier Q1. This unit then provides a positive pulse to trigger the bistable multivibrator, Q3 and Q4, at the base of Q3. The multivibrator changes state so that Q4 is now nonconducting. The positive potential on the collector of Q4 is sent to the emitter–follower Q6. The output of Q6 momentarily keys on the silicon controlled rectifier Q8. Q8, through its large anode-capacitor C2, momentarily drops the anode of Q7, the conducting silicon controlled rectifier, below ground potential. Q7 ceases conduction and the vacuum switch solenoid releases the vacuum switch plunger. The external dc high-voltage path is opened in about 16 msec.

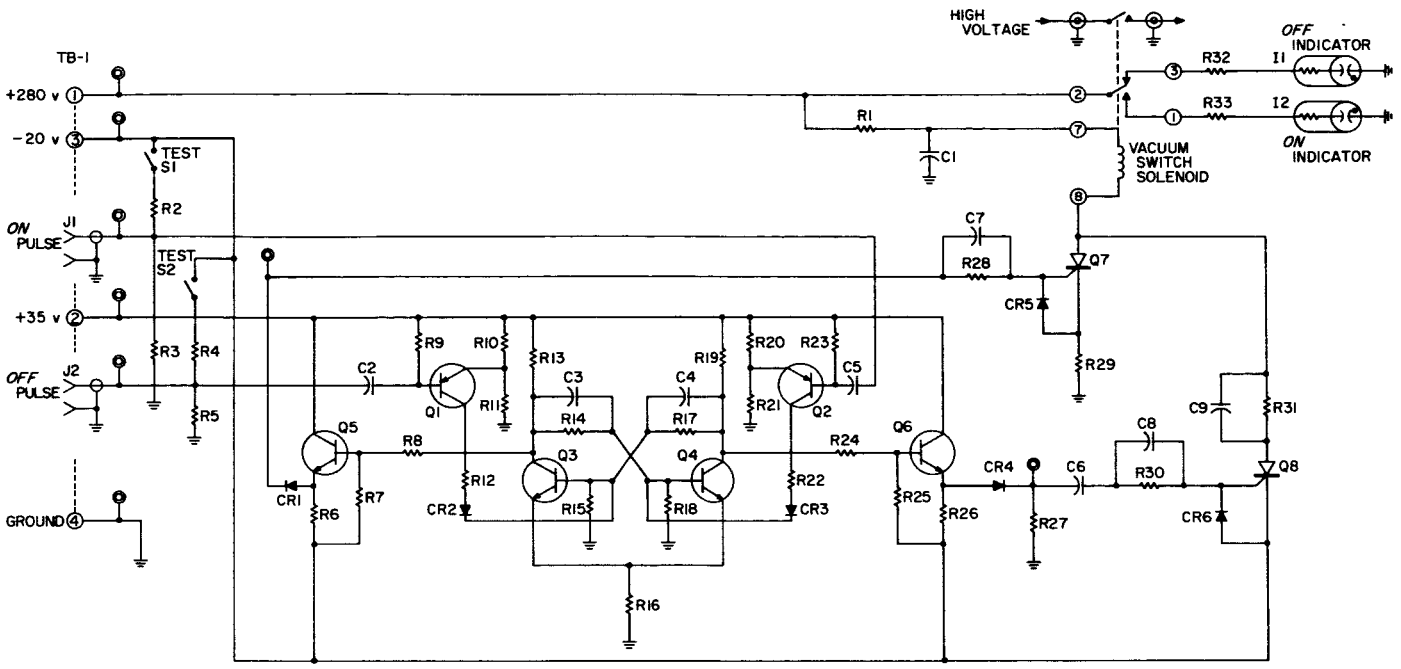

Fig. 46. Vacuum switch keyer

The pulse delay unit is shown in Fig. 47. A negative 7-v pulse is applied to the chassis at J1. The pulse is coupled to the base of the normally conducting side of the monostable multivibrator Q2. Q2 is cut off and Q3 is quickly turned on. Q2 is held off by virtue of the drop in the collector potential of Q3 and the time constant composed of R1, R2, R3, R4, and C1. When C1 has sufficiently discharged, Q2 again conducts. The negative wave in the collector circuit of Q2 is differentiated and applied to the output emitter–follower Q1. Q1 supplies the appropriate negative pulse at J2 for driving the particular off-channel of a keyer chassis to which it is connected.

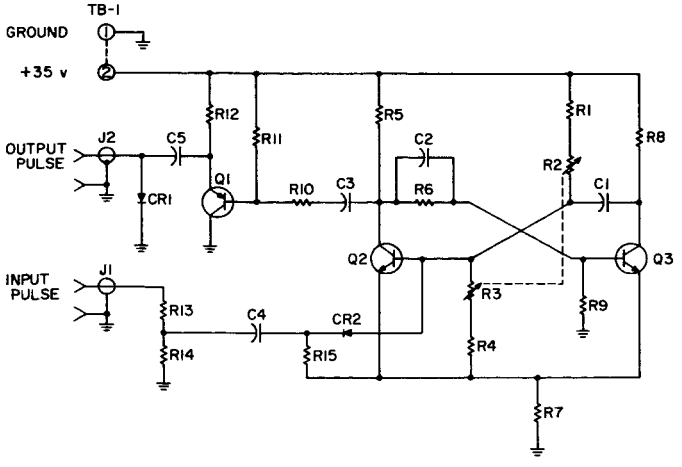

Fig. 47. Pulse delay unit

The lunar beam-switching units described herein provide the means of connecting the computer command pulses to the klystron beam switch and the dc water load switch. The electronic units are completely solid-state. In addition to operating the vacuum switches, these units provide a speedup of the switch closings and ensure minimum voltage transients by providing a constant load on the high-voltage dc power supply.

4. Calibration of Venus Site Antenna for Ranging

a. Introduction. The development of an ultra-precise lunar radar system (Ref. 14) indicated the need for a more accurate survey of the Venus site antenna–collimation tower system. This article presents some of the findings of this survey.

b. General discussion. The *station postion* is defined as that point on the antenna structure lying at the intersection of the azimuth axis and the horizontal plane passing through the elevation axis (Fig. 48). The distance from this point to the elevation axis is labeled a; the distance between the elevation axis and the *geometric* boresight is b'; and the distance from this point to the antenna vertex is c'. It should be pointed out that the *geometric* boresight is not necessarily the RF boresight. Hence, it is necessary to define virtual distances b and c: b is the

distance from the elevation axis to the RF boresight, and c is the distance from this point to the vertex of the dish. We *assume* that the RF boresight passes through the vertex of the antenna structure.

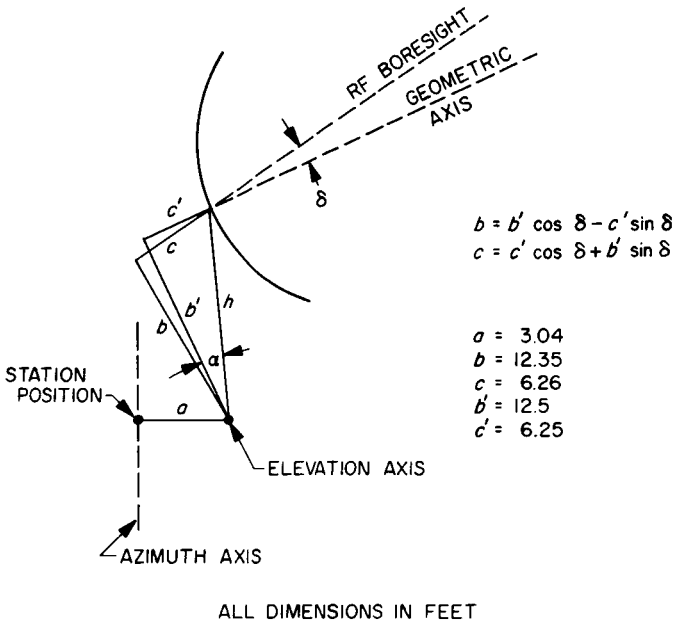

Fig. 48. Antenna configuration showing geometric and RF boresight parameters

Fig. 49 then shows the pertinent distances and angles during calibration. Only the RF boresight is shown in Fig. 49, and the distances display the effective calibration parameters.

The true distance D from the station location to a target at a point P, shown in Fig. 50, is a function of the measured elevation angle θ and the measured distance d from the vertex of the 85-ft antenna to the target, and is given by

$$D = \{a^2 + b^2 + (c + d)^2 + 2a\,[(c + d)\cos\theta - b\sin\theta]\}^{1/2}.$$

The true elevation angle ϕ is

$$\phi = \theta + \sin^{-1}\left(\frac{b - a\sin\theta}{d}\right).$$

Under calibration conditions, the distance d_{cal} is measured for a known value of D, and ϕ, or an equivalent θ.

$$d_{cal} = -c - a\cos\theta_{cal} + [D_{cal}^2 - (b - a\sin\theta_{cal})^2]^{1/2}.$$

The radar measures a time of flight $t(d)$ corresponding to a distance d

$$d = \frac{1}{2}c\,[t(d) - \varepsilon],$$

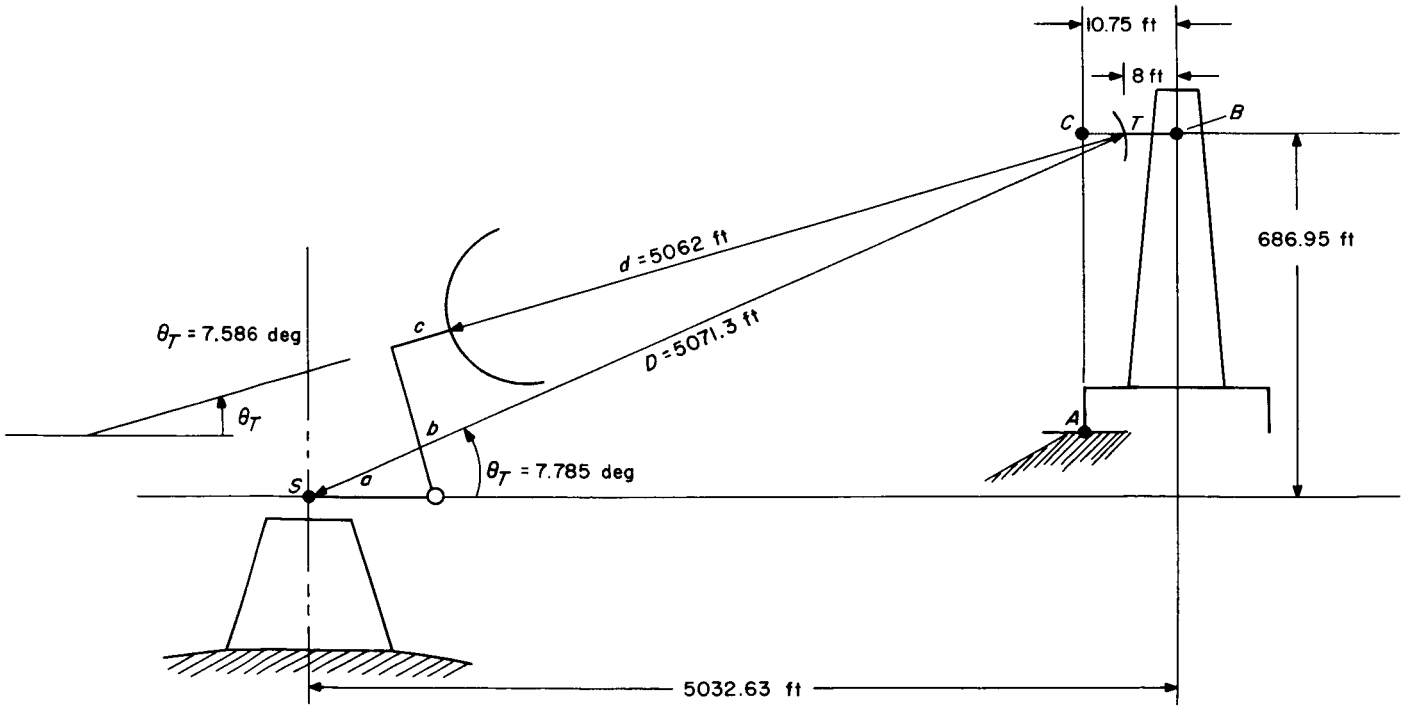

Fig. 49. Antenna while pointed at collimation tower

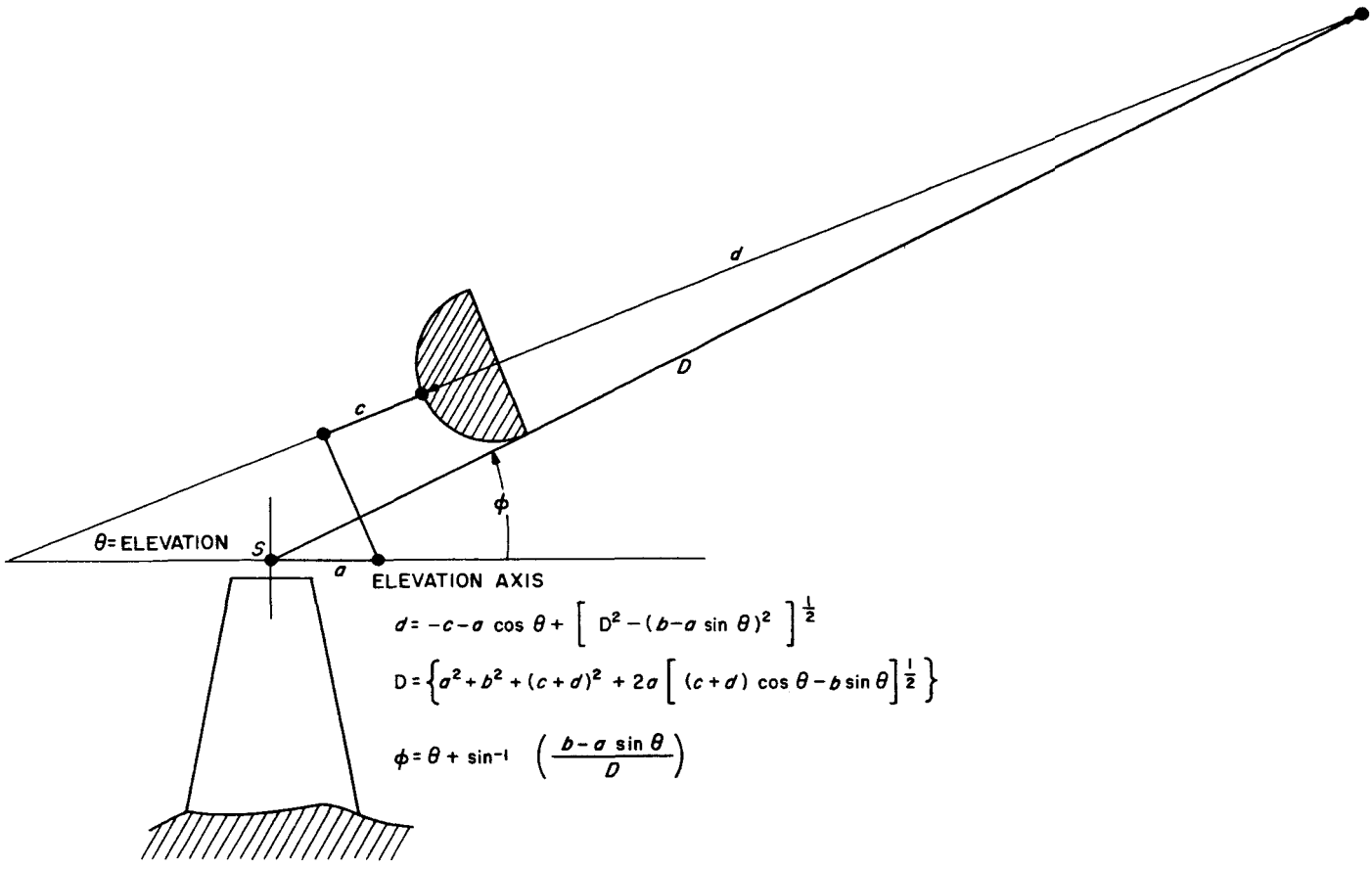

Fig. 50. Parallax and distance variation as a function of elevation angle

where ε is the error due to fixed delays in the system. We wish to calibrate ε. Then

$$\varepsilon = \frac{2d}{c} - t(d).$$

This ε is constant, so can be found by calibration:

$$\varepsilon = \frac{2d_{cal}}{c} - t(d_{cal}).$$

c. Calibration values. The measured values of a, b', and c' on the antenna are

$$a = 3.042 \text{ ft}$$

$$b' = 12.5 \text{ ft}$$

$$c' = 6.250 \text{ ft}.$$

The survey provided distances from the station location to the following points (Fig. 49):

(1) Point B: line of centers, collimation tower and target antenna axis; $D_B = 5079.3$ ft.

(2) Point C: plomb-line projection above surveyed "Point A" through target antenna axis; $D_C = 5068.6$ ft.

(3) Point T: center of target antenna; $D_T = 5071.3$ ft.

The station elevation angles ϕ to these points were also surveyed

(1) Point B: $\phi_B = 7.773$ deg.

(2) Point C: $\phi_C = 7.789$ deg.

(3) Point T: $\phi_T = 7.785$ deg.

The measured RF-boresight elevation to the target antenna is

$$\theta_T = 7.586 \text{ deg}.$$

d. Calibration of the lunar radar (two-antenna) system. The lunar radar makes use of a 6-ft auxiliary antenna mounted on the apex, 42 ft from the face (Fig. 51). The distance from the auxiliary to the target antenna is 5020 ft, or 1524.7 m. Using the radar, the auxiliary-to-target distance was measured during the first lunar experiments (Ref. 14, p. 43). The figure obtained by this method was 1528.5 m. The difference, about 4 m, is the

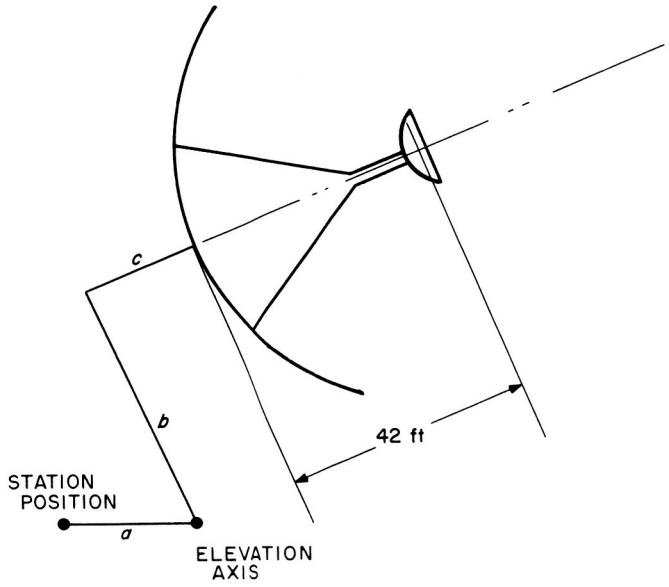

Fig. 51. Placement of auxiliary antenna in the lunar radar system (S-band)

present calibration uncertainty for point targets using the lunar radar system, in high signal-to-noise ratios.

The time-of-flight to the collimation tower is 10.74 μsec. Hence, the value of ε is -0.45 ± 0.01 μsec.

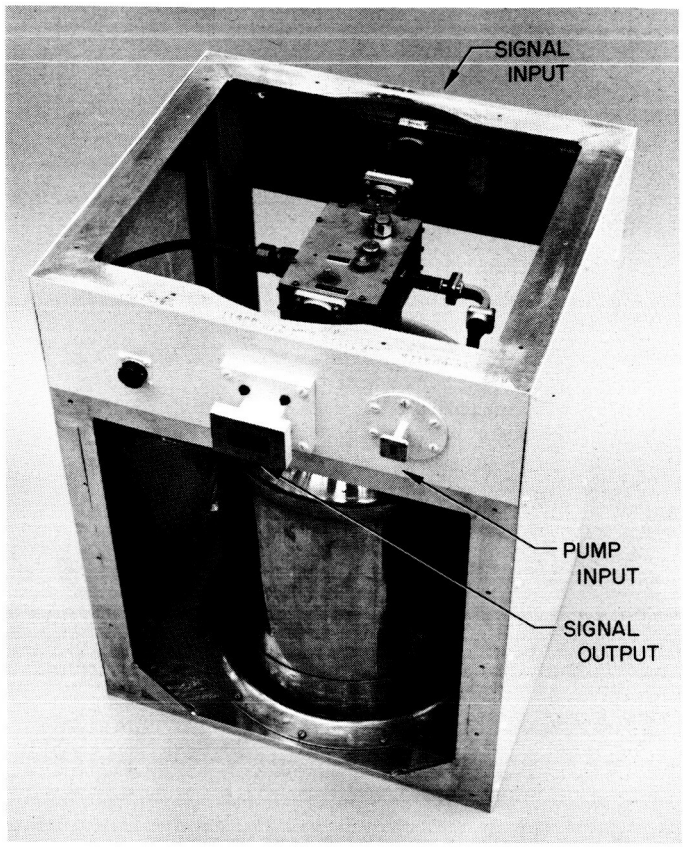

Fig. 52. Packaged H-band maser amplifier shown with some panels removed

C. Experimental X-Band Lunar/Planetary Radar Project

1. Maser and Instrumentation

a. Summary. An 8448-Mc maser was purchased from Hughes Research Laboratories, Malibu, California. The maser will be used in a low-noise radiometer/radar astronomy receiver for advanced communication systems and components experiments on the 30-ft antenna at the Goldstone Venus site. The maser capabilities were evaluated at JPL; measurements of bandwidth, gain, gain stability, input impedance match, and noise–temperature were made.

b. Recent work. The complete Dewar-mounted maser assembly is shown in Fig. 52 installed in a welded aluminum mounting frame. This frame will be installed in the antenna cage on a 30-deg, wedge-shaped bracket. The wedge will support the maser at a 30-deg angle when the antenna is at zenith to reduce the maximum tilting angle of the maser when the antenna is pointed at the horizon. The aluminum panels on the frame provide additional RF shielding from the transmitter.

The maser pump package is shown in Fig. 53. A crystal detector with calibrating attenuator is used to provide pump power monitor at the control panel.

The monitor receiver package is shown in Fig. 54. This receiver has a balanced crystal mixer and a 30-Mc IF amplifier. Crystal current can be monitored through a removable plug on the receiver top. The single channel equivalent noise temperature is about 1000°K.

The repackaged maser control panel is shown in Fig. 55. Remote readout at the maser amplifier is provided for reading liquid helium level.

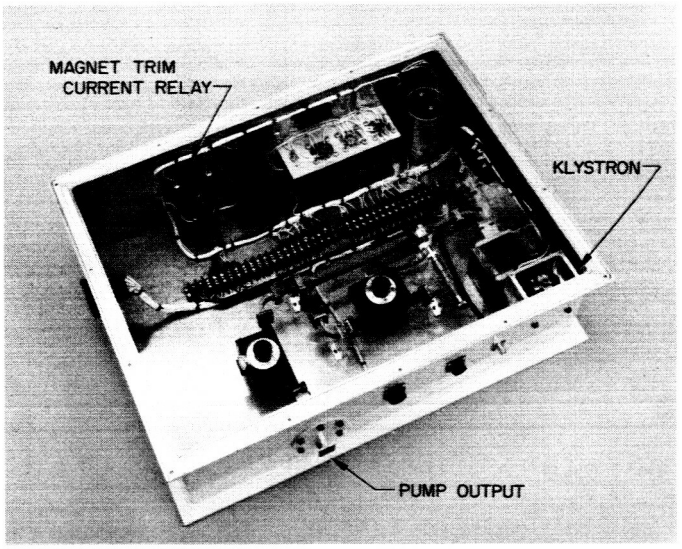

Fig. 53. Maser pump package with top removed

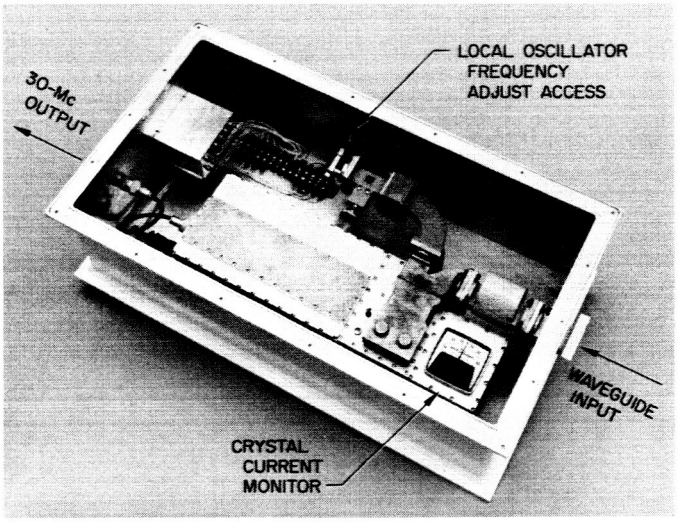

Fig. 54. Monitor receiver with top removed

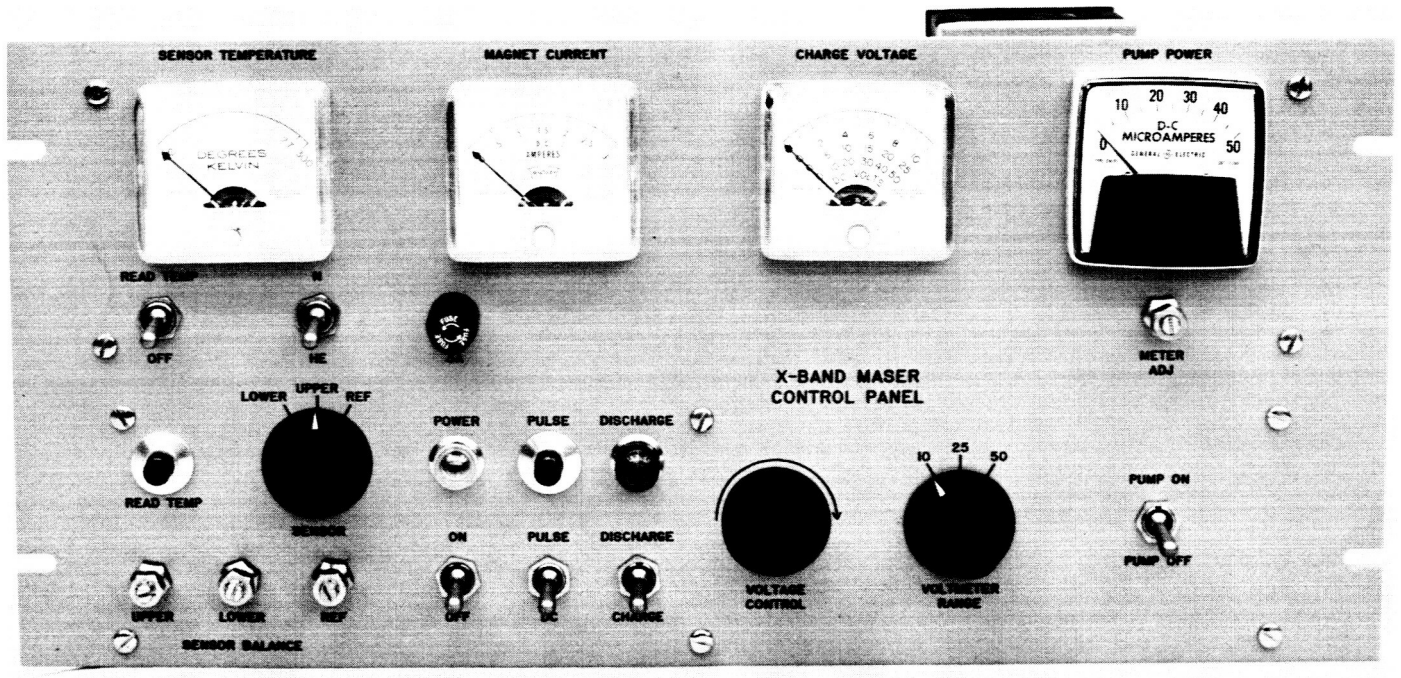

Fig. 55. Repackaged maser control panel

Fig. 56 shows the 10-liter Linde Dewar Model CD-206 which will be used to transfer liquid helium from the large 25-liter storage Dewars to the maser on the antenna. The transfer Dewar weighs about 30 lb when filled with liquid helium. Fig. 57 shows the evaporation rate of the transfer Dewar for a first fill (precooled for 24 hr with liquid nitrogen) and the second fill. A liquid helium level of 14 in. corresponds to 10 liters. The anticipated scheme of operation is to first fill the transfer Dewar with 10 liters of liquid helium. Filling the maser from the transfer Dewar should leave about 2 liters, enough to keep the transfer Dewar cold until refilling 24 hr later.

Fig. 56. 10-liter Linde transfer Dewar Model CD-206

The complete maser system will be checked out in the laboratory before installation on the antenna.

2. Transmitter

a. Introduction. Construction of the X-band 8.448-Gc lunar radar transmitter is nearing completion. The transmitter has been wired and most of the components have been installed. The antenna-mounted control and monitor cabinet is complete except for the exciter. The traveling-wave-tube buffer amplifier is almost completely wired. Ground-mounted control panels have been assembled and wired, and the auxiliary control cabinet is being wired.

Present plans call for the remote controls for the X-band exciter and transmitter equipment to be housed in the control room in the 100-kw S-band exciter cabinets (Ref. 15). Space was made available by the recent relocation of the S-band frequency synthesizer equipment from these cabinets to the central frequency synthesizer.

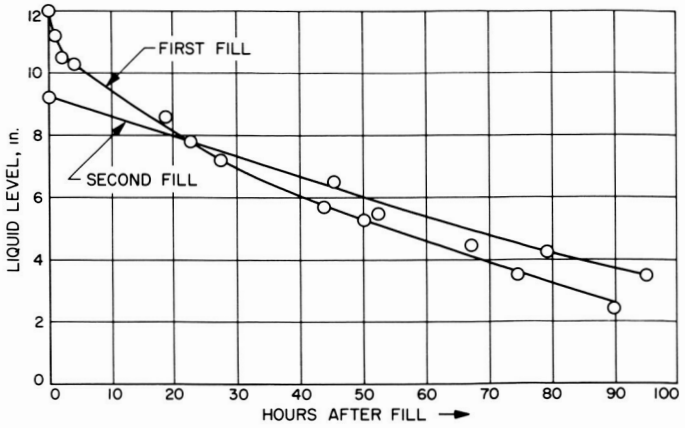

Fig. 57. Liquid helium evaporation rate in Linde transfer Dewar Model CD-206

After completion and before installation in the 30-ft antenna, the transmitter will be tested at full output power (8 kw) in the high-voltage equipment room near the antenna at the Venus site. The RF water load will be used to absorb the output power during the tests.

A block diagram of the RF equipment to be located in the antenna is presented (Fig. 58). Filament controls and protective circuitry are discussed in this article.

b. Description. The transmitter, as described in Ref. 16, is actually a hybrid system using new antenna-mounted equipment and the existing 10-kw S-band power supply. The block diagram (Fig. 58) shows the RF equipment installed in the antenna along with expected power levels. During transmitter shutdown, the system incorporates a convenient method of directing approximately 1 to 2 mw of exciter power out of the antenna feedhorn via the output waveguide. A waveguide switch is used in this klystron drive chain to direct approximately 4 w of exciter power into the 33-db reflected power, directional coupler. This exciter power may be used for making phase jitter measurements, antenna gain measurements, or other experiments requiring phase and frequency stable signals at low power.

c. Filament controls. A new control panel (Fig. 59) has been built to replace the controls that were formally located in the antenna on the old 10-kw S-band transmitter. While most of the controls are conventional in design, new features include filament controls and interlock circuitry that will help prevent klystron filament damage through operator error. The new features are discussed in the following paragraphs.

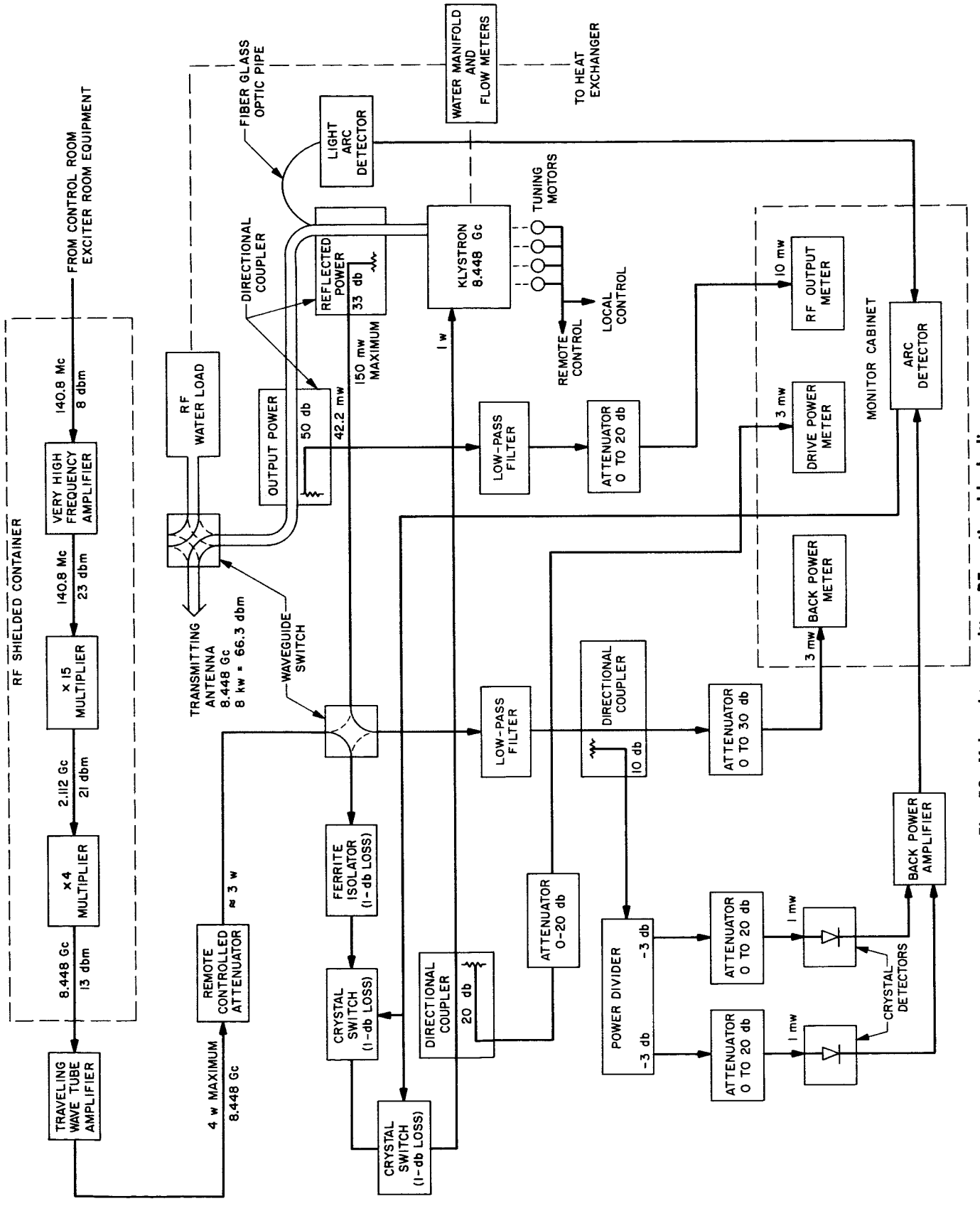

Fig. 58. X-band transmitter: RF section block diagram

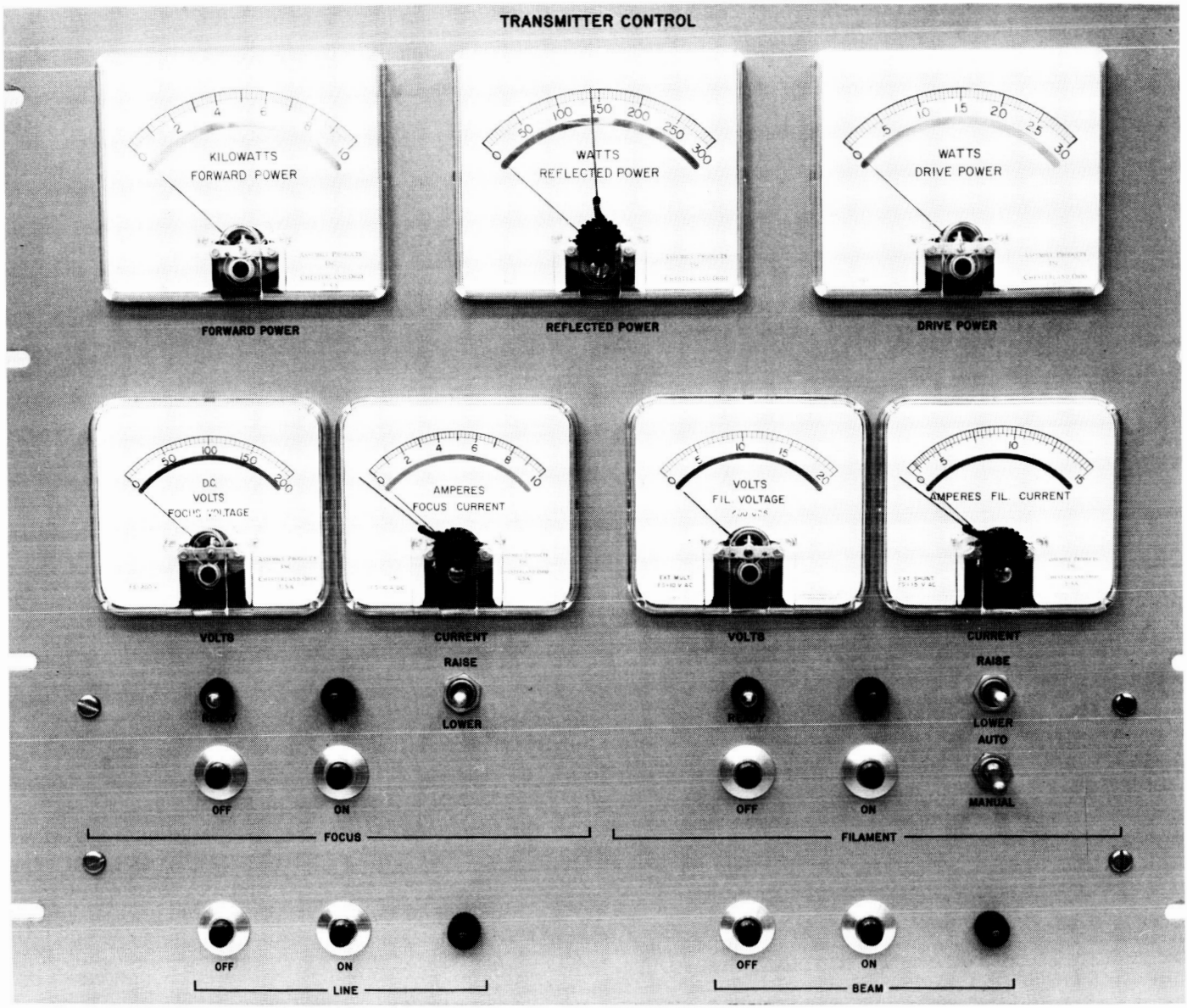

Fig. 59. Transmitter control panel

Time delay. Inadequate filament warmup time materially reduces klystron life. Proper filament warmup will be ensured by a time delay that prevents application of klystron beam voltage until 5 min after filament turn on.

Automatic/manual raise mode. The filament voltage may be applied in either a manual or automatic mode. In the manual raise mode, the operator raises or lowers the filament voltage and current to the proper level by a switch on the control panel. The switch controls a motor-driven variable transformer which adjusts the filament transformer's primary voltage. In the automatic filament raise mode, the motor-driven variable transformer automatically raises the filament voltage to a predetermined voltage set on a meter latching relay.

Surge current protection. Controls will prevent thermal shocks from damaging the klystron filament during warmup. In either the automatic or manual filament raise mode, the filament voltage is automatically turned off and the variable transformer is driven to its lowest point after the initial system turn-on. Filament current surges are also limited to less than 8 amp by using a slow-speed drive on the adjustable transformer; approximately 1 min is required to bring the filament voltage and current up to the operating values.

3. Beam Voltage Keyer, 8.448-Gc Lunar Radar

a. Introduction. The beam voltage keyer (see Ref. 17 for a description) has been assembled and wired, and will be installed at the Venus site, Goldstone, during the next reporting period. The control panels have been fabricated and are ready for wiring. The switching logic and relay drivers developed for the 85-ft Lunar Program will be used initially to operate the beam keyer. Fig. 60(a) and (b) shows the keyer.

b. Transmitter pulse-fall time characteristics. It was previously reported (Ref. 17) that the hydrogen thyratron crowbar could be used to improve the fall time of the dc high-voltage pulse by rapid discharge of the energy stored in the 200-ft cable connecting the power supply and klystron. In the 1964 Lunar Radar Project the transmitter keying rate will be 1.3 sec on and 3.5 sec off. It can be shown that the fall time of the beam voltage pulse due only to the discharge through the klystron will be fast enough so as not to require the thyratron. Klystrons approximately obey Child's law for a space charge limited diode:

$$I = \rho V^{3/2}$$

where I = the klystron current, V = the beam voltage of the klystron, and ρ = the perveance of the klystron (a constant primarily dependent on the tube geometry). From the published data on the tube, at 17.5-kv beam voltage, the beam current is 1.8 amp.

$$\rho = \frac{I}{v^{3/2}} = \frac{1.8}{(1.75 \times 10^4)^{3/2}} \simeq 0.8 \times 10^{-6}$$

After the vacuum switch has opened to disconnect the high-voltage power supply from the klystron, the beam

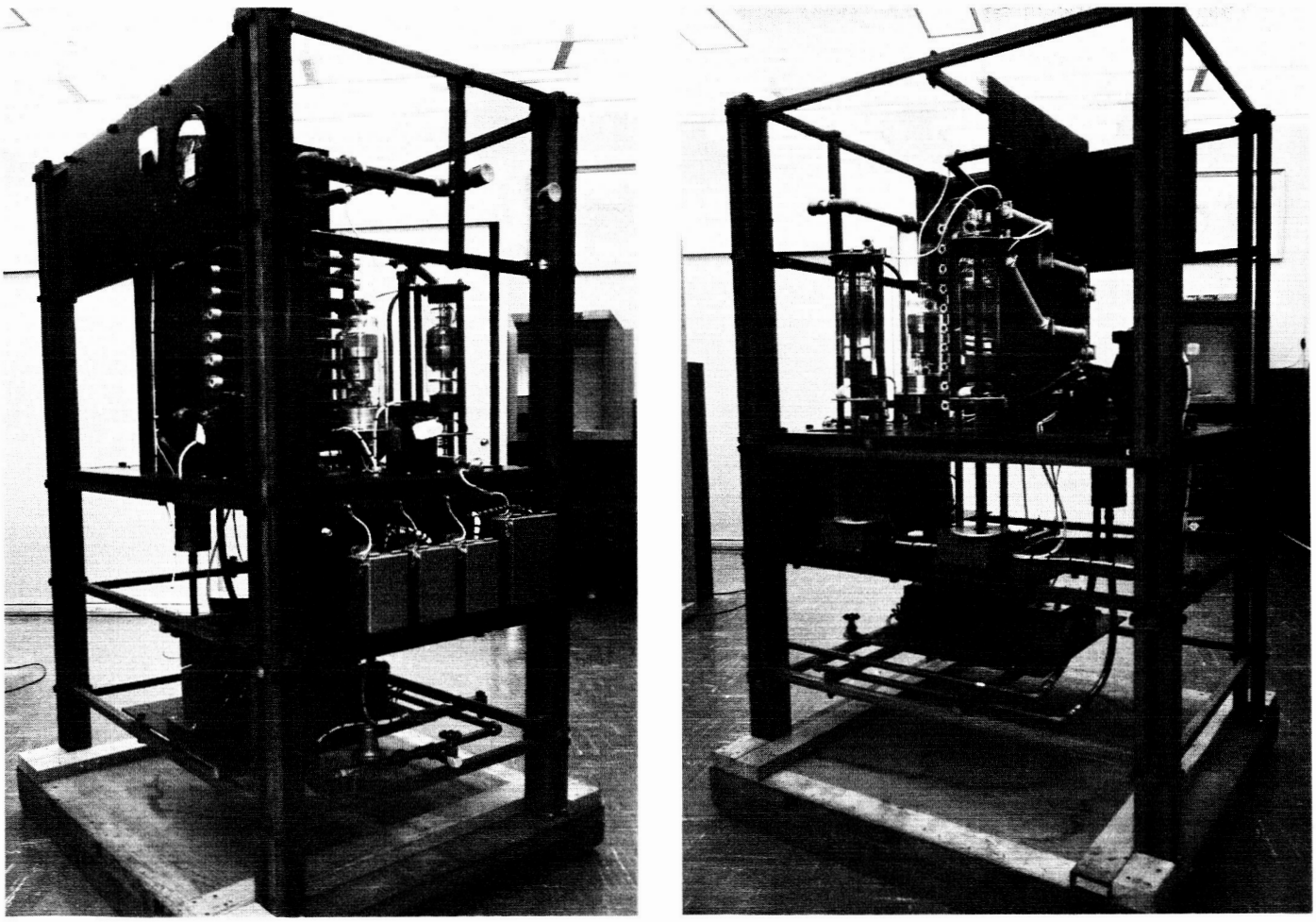

Fig. 60. X-band lunar radar beam keyer: (a) front view and (b) rear view

voltage will consist of the stored energy in the capacitance of the connecting cable, and the instantaneous current in the klystron will be:

$$-i_c = \rho v^{3/2}$$

$$-c\frac{dv}{dt} = \rho v^{3/2}$$

$$\int_{t_1}^{t_2} dt = \int_{v_1}^{v_2} -\frac{c}{\rho}\frac{dv}{v^{3/2}}$$

$$t_2 - t_1 = \frac{2c}{\rho}\left(\frac{1}{v_2^{1/2}} - \frac{1}{v_1^{1/2}}\right)$$

where v = the instantaneous beam voltage at time t, and c = capacitance of the line = 10^4 pf. Let

$$v_1 = 0.9V_0 = 0.9\,(17.5 \times 10^3) = 15.75 \times 10^3 \text{ v}$$

$$v_2 = 0.1V_0 = 0.1\,(17.5 \times 10^3) = 1.75 \times 10^3 \text{ v}$$

$$t_2 - t_1 = \frac{2 \times 10^{-8}}{0.8 \times 10^{-6}}\left(\frac{1}{(1.75 \times 10^3)^{1/2}} - \frac{1}{(15.75 \times 10^3)^{1/2}}\right)$$

where $t_2 - t_1 = 0.398$ msec, which is the time for beam voltage to fall from 90% to 10%. This time is not significant when compared to the pulse duration time of 1.3 sec. Should the keying rate be increased until the decay time is objectional, the hydrogen thyration can be connected to accelerate the discharge.

4. X-Band Lunar Radar (Receiver)

a. Introduction. The new equipment required for the S- to X-band conversion of the Mod IV receiver has been assembled and is undergoing module and subassembly testing. This includes the X-band to 30-Mc converter (Fig. 61), receiver antenna power supply, solid-state frequency multipliers and modulators (Refs. 18 and 19), and conversion of the control room portion of the Mod IV receiver (Ref. 18, Fig. 31).

b. 8448- to 30-Mc converter and power supply. The noise figure, conversion gain, and IF bandwidth of this unit have been tested using laboratory signal generators in lieu of frequency multiplier sources for signal and local oscillator inputs. Results are: noise figure, 8.0 db; conversion gain, 41.5 db; and 3-db IF bandwidth, 8.8 Mc. Complete evaluation, including long-term stability, awaits availability of multiplier components now undergoing individual tests.

This unit will be powered by a spare power supply assembly from Mod IV, housed in an antenna box designed to be interchangeable with that on the 85-ft antenna, presently used with the S-band system.

c. Solid-state frequency multipliers and modulators. Presently, at least one module of each type (Ref. 18, Fig. 32) has been received from the supplier and has satisfactorily completed individual testing. These modules provide frequency multiplication and modulation for the X-band exciter, receiver local oscillator, and signal generator. As the hardware becomes available in complete chains, further temperature and phase stability tests will be performed. Performance specifications and results of testing and field evaluation will be reported in the future.

d. Control room modifications, Mod IV receiver. This phase of the conversion is well underway. Removal of the synthesizer modules to be used in the central frequency synthesizer has been completed; other temporary miscellaneous modules and cabling previously installed or those that have become obsolete in the planetary experiments have also been removed. The loop filter modifications and a test VCO at 35.075 Mc have been completed. This VCO, while not required by the operating block diagram, has been adjusted to the same transfer characteristics as the existing 31.44-Mc VCO in the main loop and will allow the receiver to function in a closed-loop manner without the programmed local oscillator.

In addition to previous planning, the wide-swing, vacuum-tube operational amplifiers associated with the AGC system and the ranging channel output have been eliminated, and will be replaced where required with solid-state amplifiers of the appropriate voltage output capability. Attention is being focused on cabling, mechanical and maintenance aspects of the modules and racks until the balance of the new equipment described is ready for installation.

e. Signal generator. Primarily, developments during this reporting period include packaging studies and design. A purchase order has been placed with a local microwave supplier to provide the waveguide assembly for incorporation as a unit in the generator.

By several revisions in packaging philosophy, the original size estimate of $40 \times 20 \times 20$ in. has been reduced to $37 \times 20 \times 14\frac{3}{4}$ in. Special attention to this feature is necessitated by flexibility of installation, including the likelihood of use in a Cassegrain cone. Present design calls for low-frequency RF modules through 140.8 Mc (including modulators) in one shielded enclosure, the

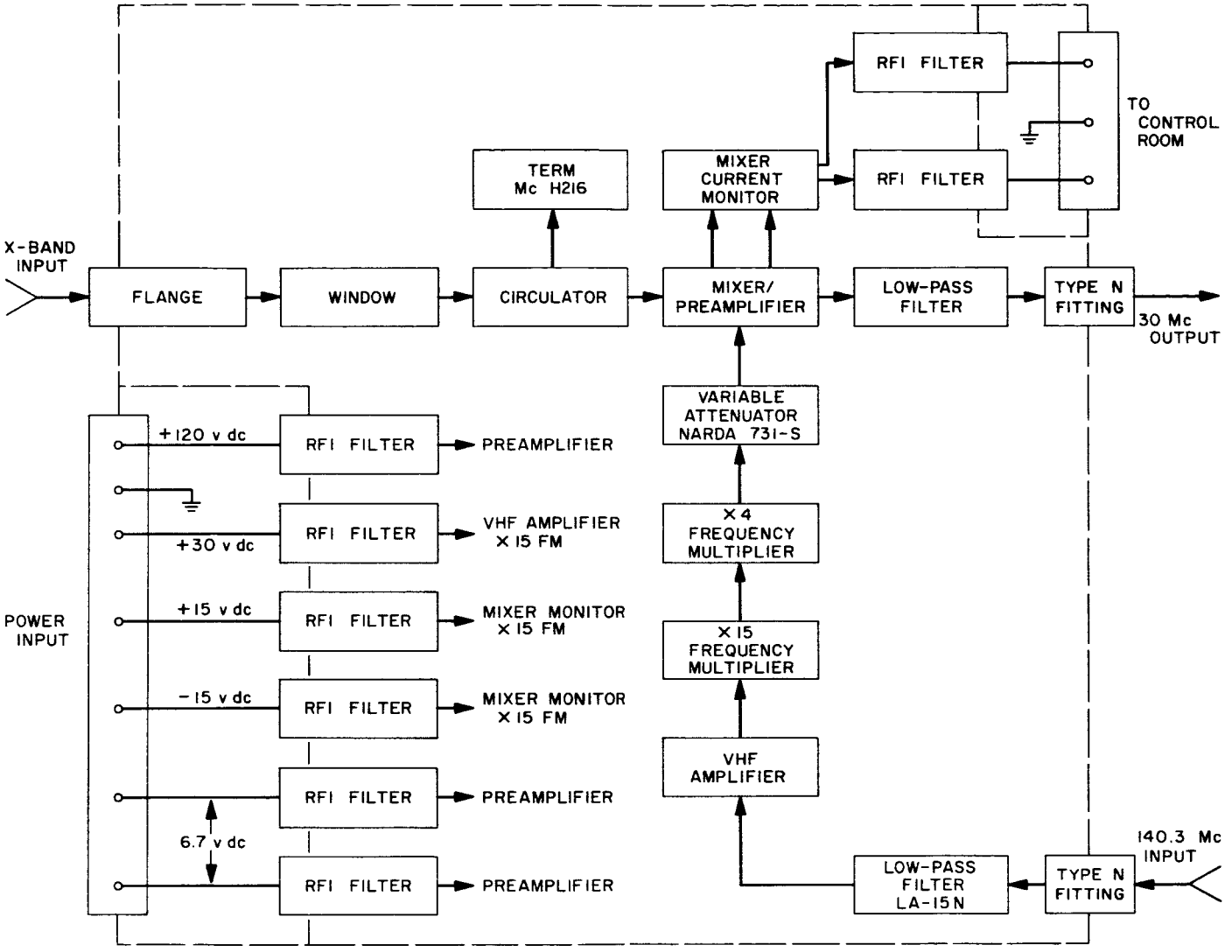

Fig. 61. 8448- to 30-Mc converter

remaining multipliers and waveguide components as a second shielded assembly, plus power meter, power supplies, etc., all enclosed in an RF and weatherproof outer case of the dimensions given.

5. S- and X-Band Interim Frequency Synthesizer

a. Introduction. The construction of the S- and X-band interim frequency synthesizer has been completed. The system will undergo system testing prior to shipment to the Venus site at Goldstone. Some modifications have been made to improve the reliability of system performance.

Previous reports on the interim frequency synthesizer were published in Refs. 20 and 21.

b. Recent work. Work on the system was completed as much as possible before August 1, 1964. All 18 modules that were to be built at the Laboratory or by outside contractors were fully tested and found to meet specifications. The power supplies and monitoring equipment were installed and ready for testing by August 1. The major portion of the coaxial and power cabling was contracted to an outside vendor. Delivery and installation of these cables were also accomplished on schedule.

After the station shutdown at the Venus site on August 2, 40 modules were stripped from the Mod IV exciter and receiver and shipped to the Laboratory. The rubidium frequency standard was also removed from the Mod IV exciter and returned to the Laboratory.

c. Modifications. The spare rubidium frequency standard has been returned to the manufacturer for a general rework and for installation of a transistorized lamp package. This modification should increase the reliability of the spare standard to the level of the previously modified standard used in the interim synthesizer.

The 10-kc, phase-locked loop (Ref. 20, Fig. 36) has been removed from the system. A divide-by-100 module from 1 Mc to 10 kc has been substituted for the loop. The divide-by-100 showed no increase in phase noise over the 10-kc loop, which had been troublesome in operation; this modification should greatly increase system reliability.

d. Conclusion. The system is being subjected to over-all system tests. Installation at the Venus site is expected to be completed by September 1. A final report on system specifications and performance will appear in a subsequent issue of *SPS*, Vol. III.

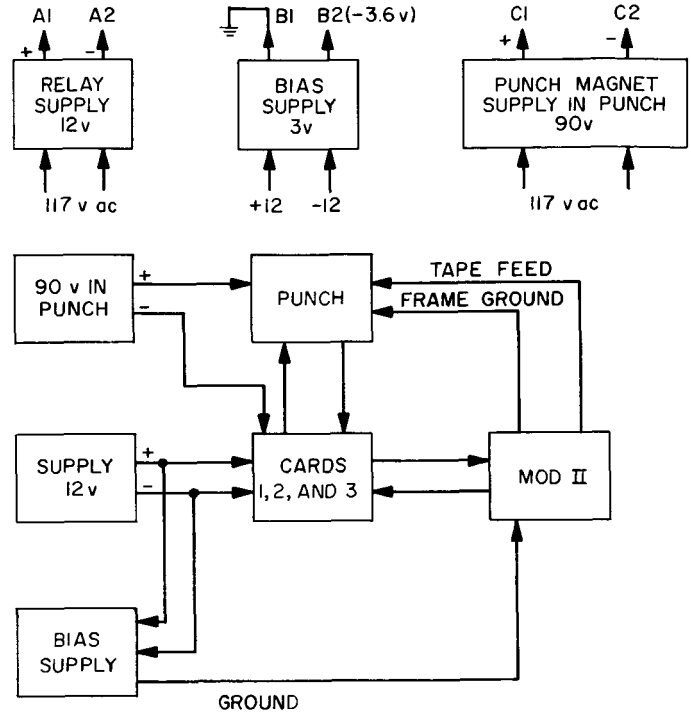

Fig. 62. Punch buffer unit block diagram

D. Equipment Development

1. Mod II Punch Buffer

a. Introduction. The connection of the paper tape punch to the Mod II Stored Program Controller (SPC) has been plagued for some time with problems of electrical noise. These problems manifested themselves both as noise in the punch and punch drive system and as noise in the remainder of the Mod II.

In order to correct this fault, the Mod III SPC was furnished with a relay buffer unit between the punch drive and the punch. This, coupled with a concerted effort in controlling ground loops and induction coupling paths, provided a more reliable punch unit for the Mod III SPC.

With 8 mo. of experience using the Mod III punch buffer, it was decided that the operation of the Mod II could be improved by the addition of a like unit to it.

b. Description of unit. The punch buffer unit consists of buffered transistor relay drivers driving mercury relays, which in turn drive the solenoids of the punch.

Fig. 62 is a block diagram of the punch buffer unit. As can be seen from the diagram, each system (logic, relay buffer, and punch) is arranged to keep the circulating currents contained entirely within the system where they are generated.

The unit was constructed on a 19-in. rack panel. The relays and drivers were mounted on Vector 16-pin circuit boards and the wiring was done on the mating connectors. The power supply for the driver amplifiers was also mounted on the panel. The cards are accessible from the front of the panel.

c. Description of cards. Five driver-amplifiers and relays are mounted on each card. Four of the relays are operable only through the amplifiers. The fifth is also operable by direct connection to its coil. This allows a contact closure in the punch unit to operate a relay for feedback signals. The operation of the feedback relay does not use the amplifier because of the noise level in the punch circuits.

Figs. 63 and 64 show in more detail the card configuration and circuit.

d. Results. There has been a marked improvement in the reliability of the punch due to the modification. Errors

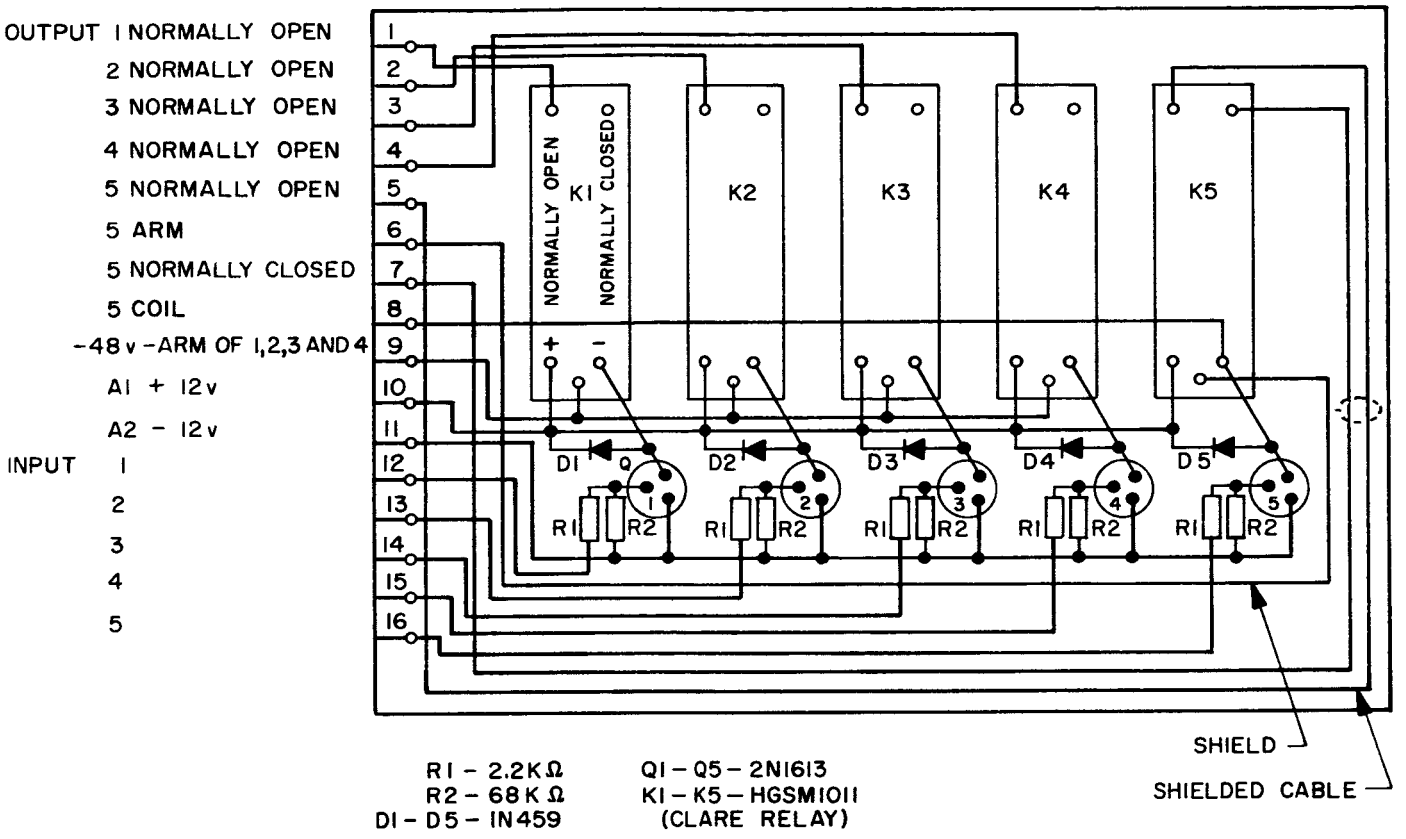

Fig. 63. Card layout

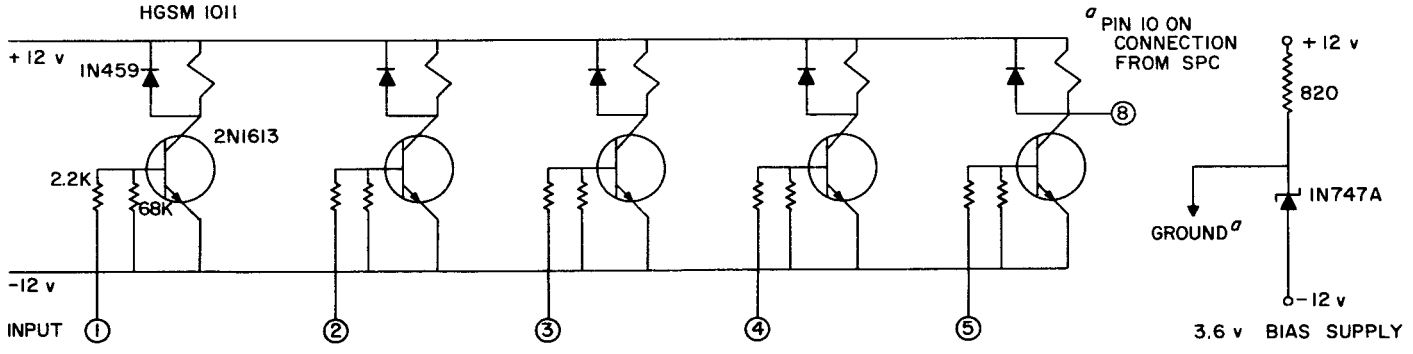

Fig. 64. Card schematic

were occurring at a rate of 1 per 3632 characters before the change. Errors are now occurring less than 1 per 2 rolls (1000 ft) of tape (132,000 characters per roll). While this level of operations is still below that desired, it is a significant improvement in the operation.

Work is still being done to reduce the electrical noise of the Mod II as a whole in an effort to improve the total operation of the Mod II as well as the punch.

2. *Frequency Dividers Using Synchronized Oscillators*

a. Introduction. Previous frequency dividers for generation of coherent submultiple reference frequencies used either phase-locked loops (Ref. 22) or parametric dividers (Ref. 23). Parametric dividers have the advantages of greater bandwidth and less complexity; however, it is difficult to design them to operate at output frequencies below about 50 kc because of the general lack of Hi-Q

components in this frequency range and of high capacity varactors. Synchronized oscillators appear to be applicable to frequency division at these lower frequencies.

b. Description of synchronized oscillator and evaluation. A synchronized oscillator frequency divider was designed to divide by 100 from 1 Mc to 10 kc. This choice of frequencies was made to permit direct comparison with the divide-by-100 phase-locked divider used in the interim central frequency synthesizer (Ref. 24). A schematic diagram of this divider is shown in Fig. 65.

The first stage in this unit is an amplifier/limiter which isolates the input line from the first divider and presents a constant drive voltage to the first divider. This stage is followed by three cascaded dividers which divide-by-five, -five, and -four, respectively. The last two stages serve to isolate the output line from the last divider, to produce a constant amplitude output, and to produce the required output level at low distortion.

The individual divider oscillators are separated by slightly over-coupled, double-tuned circuits to isolate them, and to achieve some bandwidth improvement. Each oscillator is operated with Class C bias to achieve a fail-safe mode of operation. No output is produced unless the input signal is present and within the lock-in range of the oscillators. The operating bandwidth of the unit is 3% ($\pm$15 kc at the 1-Mc input).

The phase noise introduced by this unit was compared with the noise of the previous phase-locked divider used in the interim central frequency synthesizer. In each case, the output frequency (10 kc) was multiplied by 16 to 160 kc and subtracted from 32 Mc to produce 31.84 Mc. A cleanup loop of $2B_1 = 3$ cps was used to measure the phase noise. The residual noise in the loop due to oscillator noise and the synthesis process was 0.075 deg rms. The additional noises due to the 10-kc sources were both undetectable as compared to this noise level; the only conclusion that could be drawn from this test was that the phase noise on the output of the divider was, after multiplication by 16, much less than 0.075 rms, i.e.,

$$16\Phi_N << 0.075 \text{ deg rms}$$

$$\Phi_N << 0.0047 \text{ deg rms.}$$

c. Conclusion. Since the phase-noise contribution due to the synchronized oscillator frequency divider is negligible and since it is much simpler and presumably more reliable, the unit is being installed in the interim central frequency synthesizer in lieu of the previously used phase-locked divider.

3. 1.0-Mc Hi-Q Crystal Filter

a. Introduction. The 1.0-Mc crystal filter was designed and constructed to fulfill the need of a $\pm$1.0-cycle passband at 1.0 Mc. A rubidium vapor frequency standard has an output of 1.0 Mc and is followed by the 1.0-Mc crystal filter to eliminate any spurious signals, noise, or harmonics.

b. Scope. The 1.0-Mc crystal filter consists of a +13-dbm input amplifier/limiter stage, the Hi-Q crystal, and one amplifier/limiter output stage which delivers +10 dbm into 50 Ω (Fig. 66).

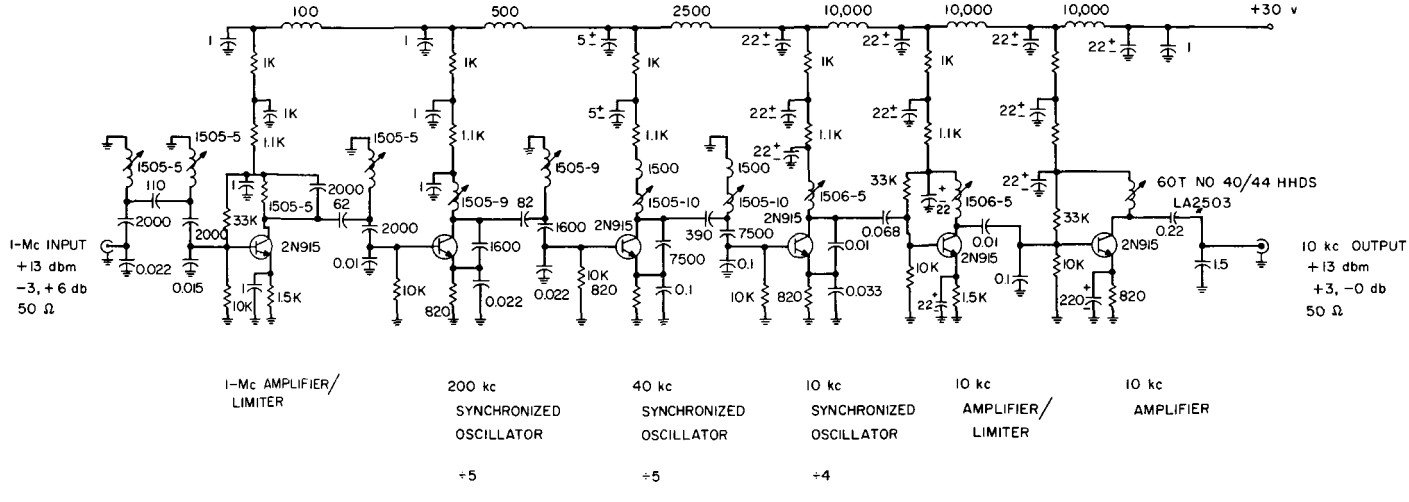

Fig. 65. Divide-by-100 frequency divider (1 Mc to 10 kc)

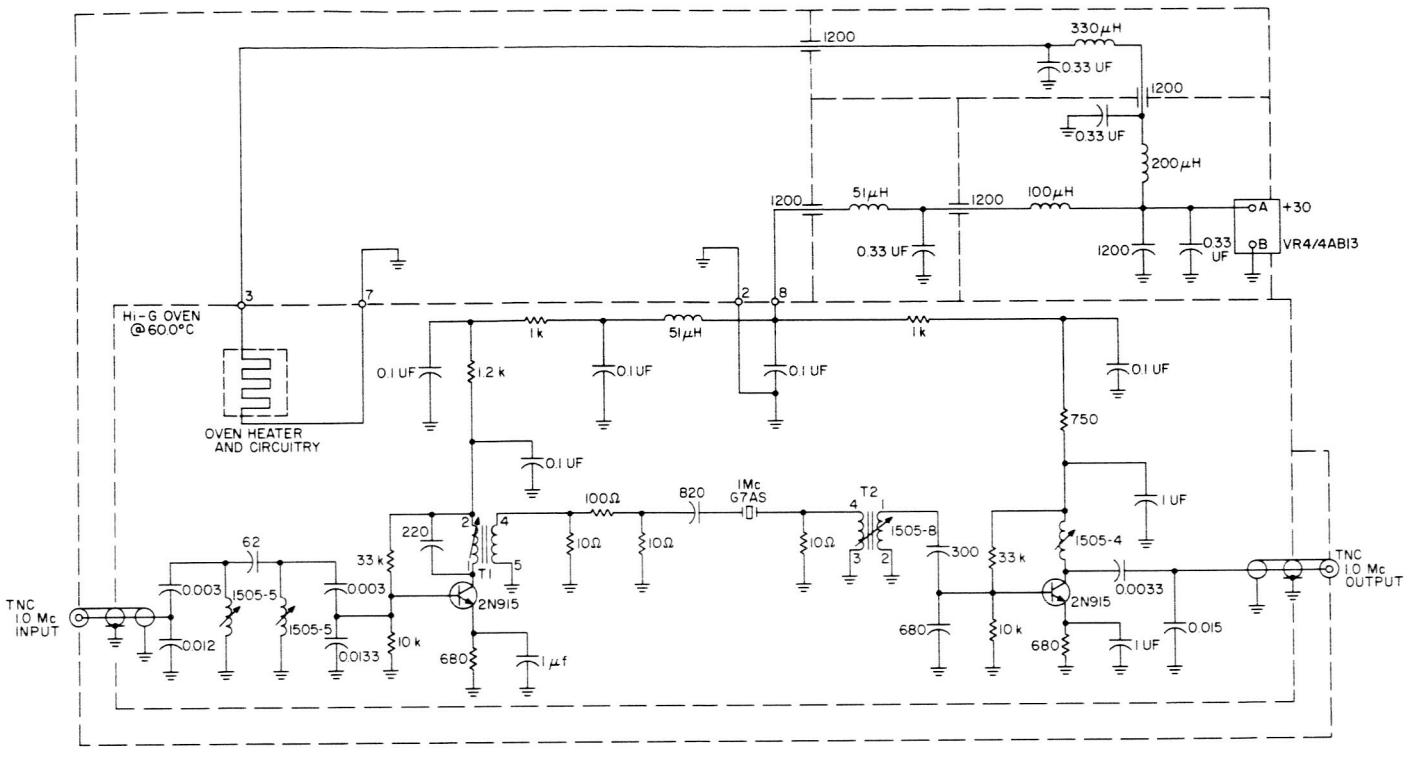

Fig. 66. 1.0-Mc Hi-Q crystal filter interim central frequency synthesizer system

The crystal and associated circuitry are within a proportional control oven at 60°C and are completely solid state [Fig. 67(a) and (b)]. At this temperature, the crystal has a Q of 1,000,000.

The mechanical configuration is the gold-plated cavity type of RF module design conforming with existing hardware [Fig. 67(a)].

The crystal bandwidth characteristic is shown in Fig. 68, in which the symmetry of the curve and the absence of spurious signals can be noted. The ±3-db bandwidth points have a frequency spread of +1.29 and −1.20 cycles at the center frequency of 999,999.6 cps.

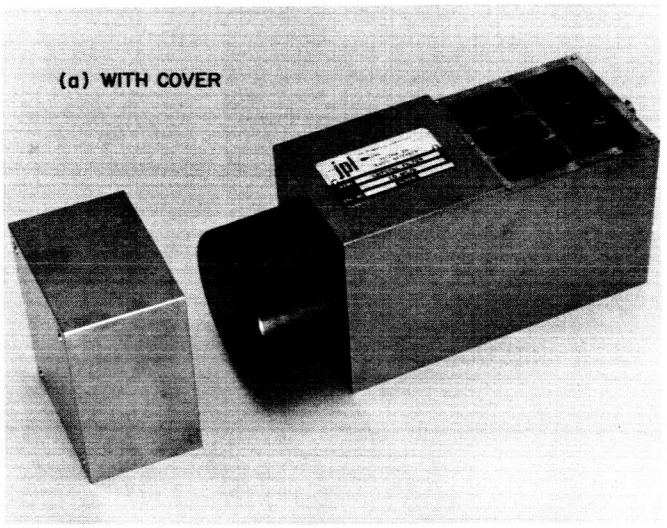

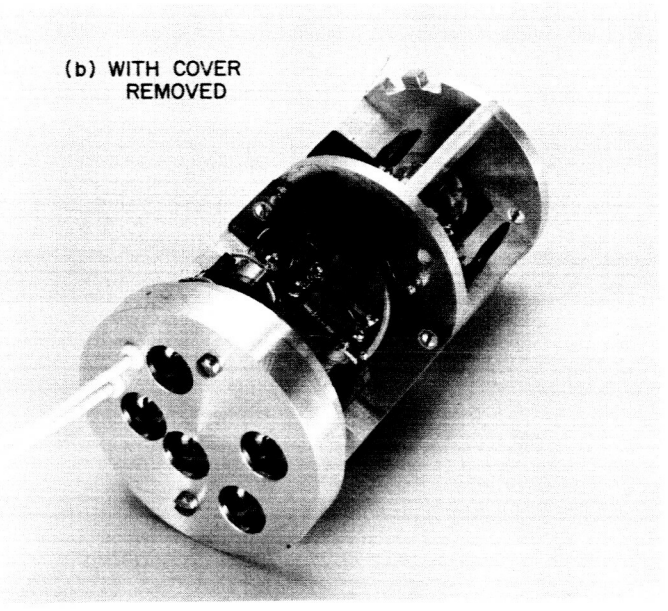

Fig. 67. 1.0-Mc Hi-Q crystal filter: (a) with cover and (b) with cover removed

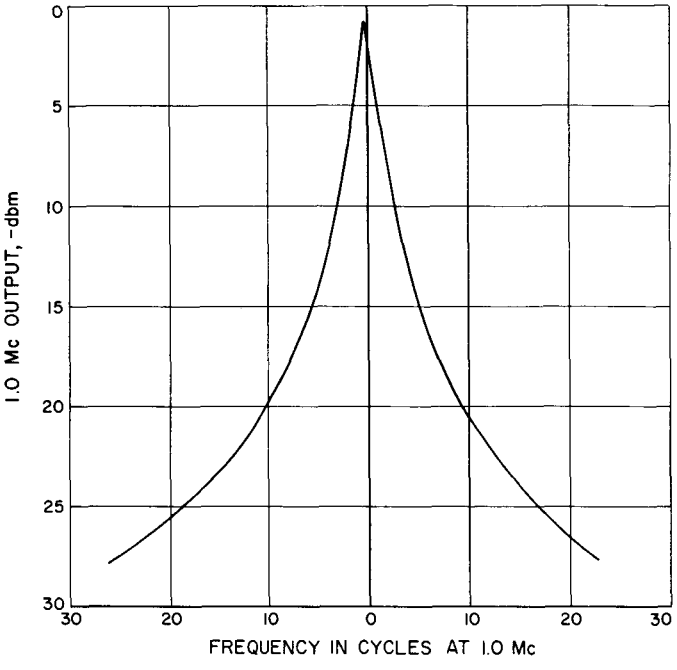

Fig. 68. Crystal filter passband

The limiting characteristics are shown in Fig. 69, and the output power versus power supply is shown in Fig. 70. Total dc power drain is 5.66 w.

An RF leakage test was conducted on the power lines, TNC connectors, and mechanical junctions and was not found to be greater than 0.6 μv.

c. Conclusion. The 1.0-Mc Hi-Q crystal filter will be used in the interim central frequency synthesizer (Ref. 25) as part of the S- and X-band lunar and planetary radar system at the Venus site, Goldstone, California.

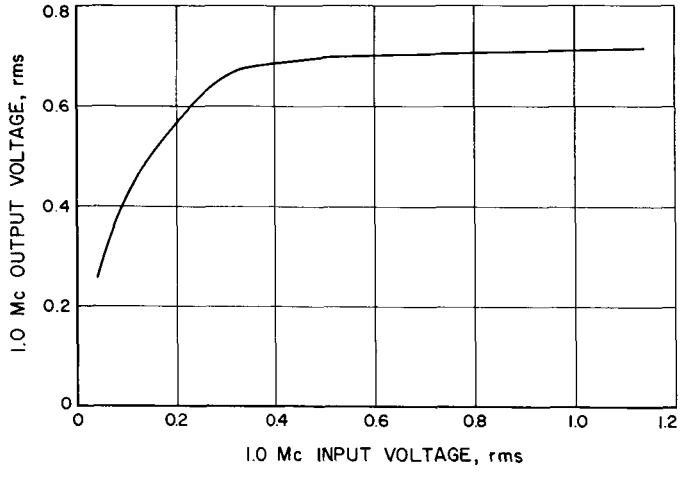

Fig. 69. Limiting characteristics

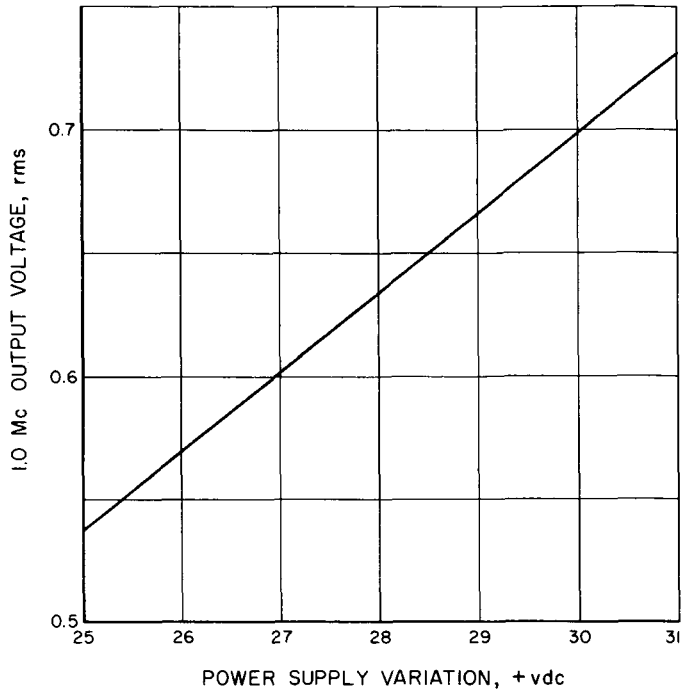

Fig. 70. Power supply versus output voltage

E. Coding Systems

1. Construction of Random Pulse Generator

a. Summary. This article describes the construction and testing of the random pulse generator whose design was considered in Ref. 26. This machine produces outputs, or pulses, depending on the last 7 bits from a length 36 maximal-length shift register generator. Initially, this machine will be used to generate data for the quantile data compression system (Ref. 27) and noise for the punctured-cyclic coder–decoder (Ref. 28). It was built using the new line of digital circuit modules being developed at JPL (Ref. 29), and occupies only one block of hardware, exclusive of counters and power supplies.

b. Review. First, the principles of operation of the random pulse generator are considered. What is desired is a machine which produces an output train of pulses in which not only is the average density of pulses a variable, but also the conditional probability of a pulse at a given time given a short segment of the previous pulse history. In effect, what was desired was the ability to

produce trains of pulses with a variable autocorrelation function. Ref. 30 discusses a less flexible pulse generator.

Such variability is useful in many contexts. For example, as a noise generator, various autocorrelation functions of the pulse train correspond to various colorings of Gaussian noise. When the colored noise is quantized along with the signal, the resulting errors, which correspond to pulses, have varying autocorrelation functions. In particular, a large positive autocorrelation function corresponds to bursts of errors.

As an artificial data source, the conditional probability of a pulse, given that a pulse has occurred, depends on the type of particle counter used, when pulses are considered as being particles counted. For example, *counters of Type I* have the property that the occurrence of a pulse at a given bit time inhibits the occurrence of a pulse for a specific number of bit times thereafter. This corresponds to a "dead time" in the counter. All of the options discussed are available with the random pulse generator.

"Pulses" are produced by word detection on words of length 7 or less in a stream of "pseudo-random" digits. A most convenient source of such digit streams are the so-called *maximal-length shift register generators* (Ref. 31), which generate digits by a linear recurrence implemented through a shift register. The shift register considered here corresponds to the primitive polynomial $x^{36} + x^{11} + 1$. That is, the recursion is $a_{n+36} = a_{n+11} + a_n$, addition being mod 2. Since this polynomial is known to be primitive (Ref. 32), the period of any sequence generated by any initial condition (other than the all *zero* state) is $2^{36} - 1$, which is over 19 hr at the 1-Mc rate being used.

Now that the incoming bit stream has been described, attention can be focused on the methods of word detection used to test whether a pulse is to be produced.

*c. **Pulse production.*** Basically, there are five (nondisjoint) options available to the pulse generator used to define pulse occurrence. These options, A through E, correspond to the control panel positions shown on Fig. 71; however, only three are statistically distinct.

Option A produces a pulse for each $1 \rightarrow 0$ transition. No inhibition occurs after a pulse. This option is mainly useful in system test and checkout, since the same statistics can be obtained under both Options B and D. (The other options do not directly test for $1 \rightarrow 0$ transitions.)

Option B requires the user to select a *window* of length 7. A *window* is defined as a tuple of *zeros, ones,* and *x*'s, an *x* corresponding to "don't care." A pulse is produced whenever the window occurs in the sequence; however, a user can inhibit a pulse occurrence up to $l - 1 \leq 6$ bits after a pulse by setting the *inhibit number* l (as a binary number in three *cumulator capacity switches*).

Windows of length less than 7 can be acquired by merely calling the extra positions "don't cares." If the inhibit number now equals the word length, the output process is called a *renewal process* (Refs. 33, 34), a special kind of output for counters of Type I.

Option C outputs a pulse when the cumulator has counted up to l *ones*, $1 \leq l \leq 7$. There is no inhibition. Option C is not duplicable in any other position.

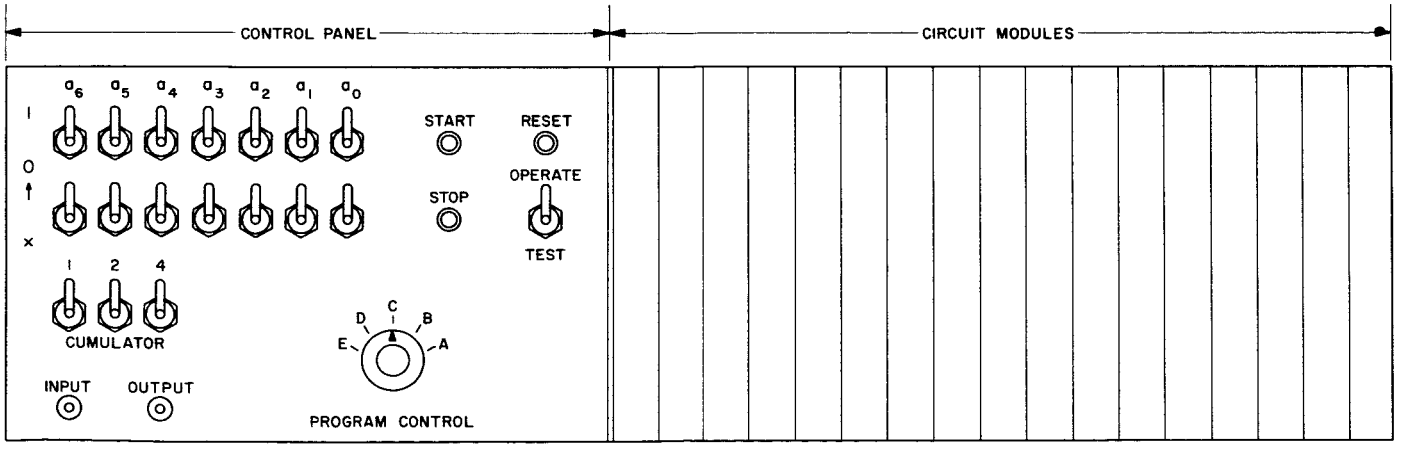

Fig. 71. Panel of generator

Option D is the same as Option B with the cumulator capacity switches set to $l = 1$ (no inhibition).

Option E allows windows to be chosen, but the search for a pulse is on consecutive non-overlapping blocks of words of length l, where l is chosen by the cumulator switches. This feature is known as *strobing*. Option E is not reproducible in any other option.

Observe that Options B, C, D, E agree when l is set to be equal to 1 and the window is chosen; then, every occurrence of a *one* produces a pulse, and every pulse is produced only in this way.

Fig. 72 illustrates Options B, D, E, with arrows indicating bit times at which pulses are looked for. One should especially note when reading this part of this article how the various options are so easily obtainable with a few switches.

d. Experiments. The first experiment was done to check the periodicity of the shift-register generator. An 8-decimal-digit counter was connected to count the 1-Mc shift pulses for a full cycle. Also connected to the pulse-counting control flip-flop was a pen recorder. After reset of all units the test setup was manually started. It automatically stopped (detecting the first repeat of the initial condition) after approximately 19 hr, 5 min, as determined by from the pen recorder. The 8-digit counter read 19476735. Now $2^{36} - 1 = 68719\ 476735$, so $(2^{36} - 1)$ μsec = 19 hr, 5 min, 19.476735 sec. Thus, the period is $2^{36} - 1$, as required for a maximal-length shift-register generator.

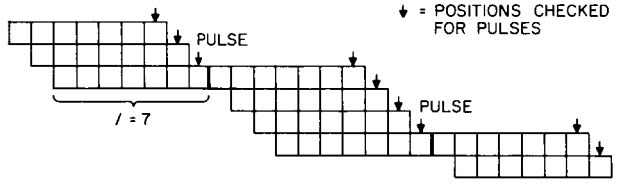

OPTION *B* (RENEWAL; WINDOW OF LENGTH 7)

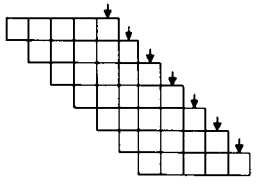

OPTION *D* (OVERLAPPING, OR *B* WITH $l = 1$; WINDOW OF LENGTH 5)

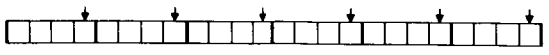

OPTION *E* (STROBED; WINDOW OF LENGTH 4)

Fig. 72. Window patterns

Some statistical experiments were performed to ensure that the control switches were properly wired, and to illustrate the types of experiment performable. More detailed experiments will be reported in *SPS 37-29*, Vol. IV.

Table 6 indicates the experiments performed, the expected results from a truly random source given in Ref. 34, and the results obtained in the experiment. Each experiment ran for 1,000,000 bit times of the generator, i.e., for 1 sec. The first column gives the control option, the second the window used, the third the number of pulses expected according to Ref. 34, and the fourth the number of pulses counted. In each case, the deviation of actual from expected was well within the standard errors given in Ref. 34. Thus, the pulse generator is working as desired.

e. Operation. In addition to the selector switch that selects the option for the method of producing pulses, the following controls are used in the operation:

START — The start push button will impress a "true" condition at the set control of control flip-flop C_1. System clock will then synchronize the start. With C_1 set, shift clock to the main shift register, as well as the cumulator, is provided.

STOP — The stop push button provides collector reset of control flip-flop C_1.

RESET — The reset push button will preset the main register to the 00 · · · 0001 initial condition; diode isolated collector reset is used. In the normal position of the reset push button, the preset-bus is via an inverter used as the reset trigger for control flip-flop C_1.

Table 6. Statistical experiments

Option	Window	Expected	Observed
Renewal (Option B with $l = 7$)	1110111	7,042	7,082
	111X111	10,250	10,165
	1111111	3,938	3,948
Cumulated ones (Option C)	Three	71,429	71,399
	Seven	166,667	166,600
Strobed (Option E)	0010111	1,117	1,127
	0X101X1	4,464	4,478
Overlapping (Option D)	1111111	7,813	7,781
	X01XX11	62,500	62,680

TEST/OPERATE The test switch changes the input to the main register from $a_0 + a_{11}$ to a_0, which means that instead of a full cycle being $2^{36} - 1$ clock pulses, the cycle is only 36 clock pulses, and that the beginning and end of the 36-clock pulse cycle are determined by the condition of the main register at the instant the test switch is switched from OPERATE to TEST.

f. Additions and modifications. A modification will be included to permit counting the number of 2, 3, 4, 5, 6 consecutive pulses in the output that are "bracketed" by no pulses at both ends. This feature is useful in monitoring burst error patterns. Another modification will include automatic change of the cumulator capacity for every other sample for the purpose of deriving a bimodal histogram. The quantile system needs to be tested with these bimodal histograms (Ref. 35).

A scanning and paper tape punch device will be added to the generator so that the result of consecutive experiments of the same type can be recorded for later processing to determine the mean and variance distributions, and to prepare histograms of the experiment.

When the quantile system and the punctured-cyclic coder have been built, the random pulse generator (Fig. 73) will be used both as a data and noise source. No modifications to the pulse generator are necessary for this operation, but the other two systems will have to be slowed down in certain experiments so that the data and noise source is operating as if the pulses were occurring synchronously with the other two systems. For example, if noise for the coder with error probability $\frac{1}{128}$ is desired, then disjoint blocks of seven *ones* could be used to define a pulse (Option E); however, the coder should operate at $\frac{1}{7}$ megacycle so that "pulses" mean "errors in a given code bit." Joint synchronous operation of the two machines would not, however, be necessary.

2. Experiment in Teletype Coding

a. Summary. An effort to establish an error-correcting coding system for use on inter-DSN teletype lines is reported. Since error statistics must be obtained, a computer program is being written which will accomplish

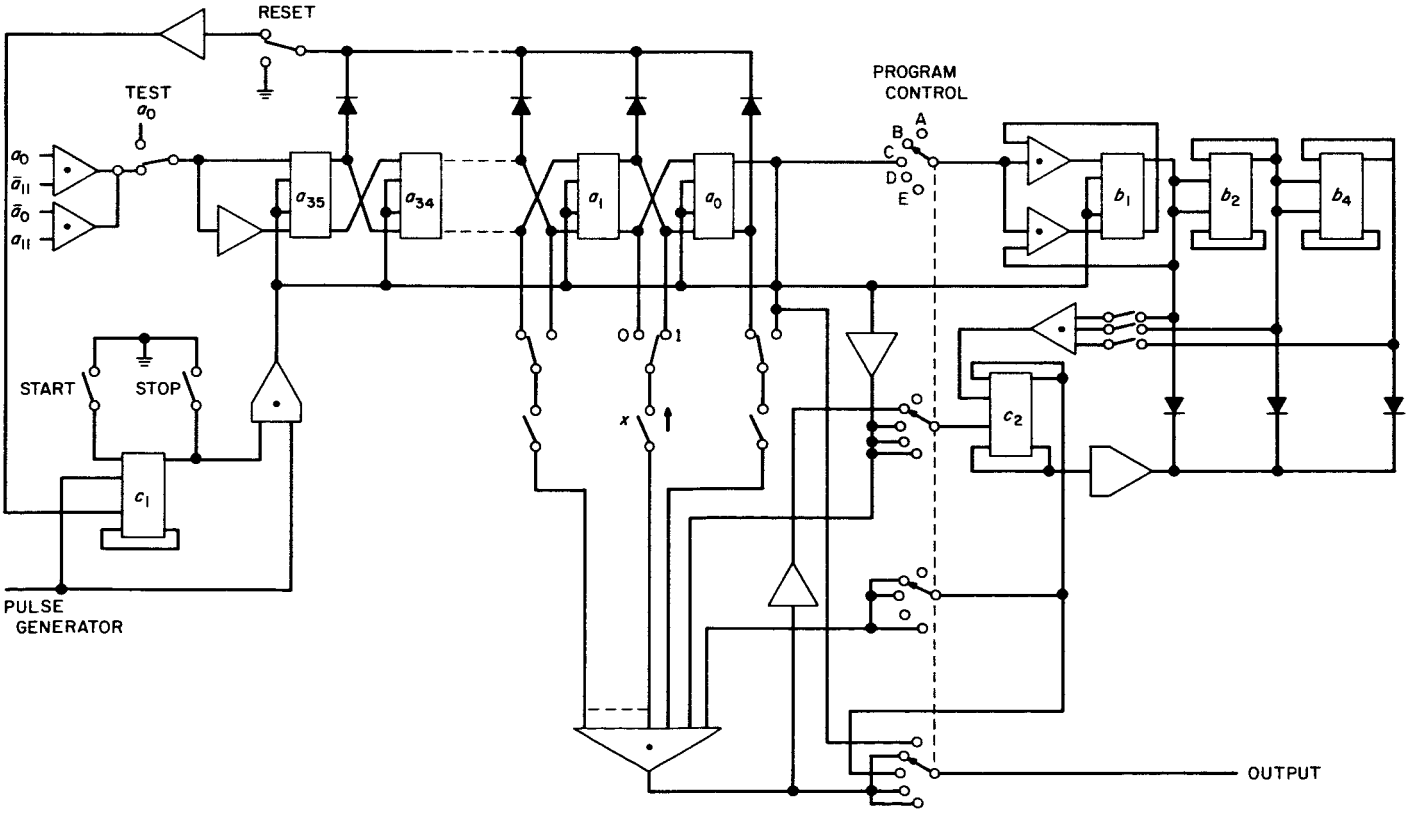

Fig. 73. Random pulse generator

this function. The code to be used is the (62, 17) code over the 32-element field (Ref. 36) previously developed at JPL. By computer, encoding is easy; however, the difficulty is in decoding up to the full capability of 10 errors in real-time. Preliminary calculations show, however, that with improved decoding theory (Ref. 37) recently developed at JPL, decoding can be done in less than one word time with present machines.

b. Introduction. As described in Ref. 36, the teletype format consists of words of length 63, with one symbol of the word being a synchronization symbol not at the disposal of the code designer. Each teletype symbol is a 5-binary-bit symbol, i.e., there are 32 teletype symbols. Thus, at the coder's disposal are 310 binary bits, or 62 symbols over a 32-letter alphabet.

In Ref. 36, a code over a 32-letter alphabet was described for use on teletype lines. This code has 17 information symbols and 45 check symbols; thus, the rate is 0.274. A low rate on teletype is acceptable if the error rate is reduced, since teletype lines are used to transmit commands from the SFOF to the DSIF sites for transmission to the spacecraft, and errors must be avoided. Furthermore, the rate at which these commands are generated is compatible with this reduction information rate.

The 32 symbols used in Ref. 36 are the 32 elements of the field $GF(2^5)$. Use of this field allows each teletype symbol to be encoded as a unit into a field element. The (62, 17) code will correct all combinations of 10 (or fewer) teletype letter errors in the word of length 62. These 10 errors are errors in the teletype symbols, not just in the binary symbols. Ref. 36 showed that if the input error probability per teletype symbol is 0.02 (considered a high error probability), the output information symbol-error probability when the (62, 17) code is used is $< 10^{-8}$. Thus, this code is ideal for the application envisioned.

c. Obtaining channel statistics. Before a particular code is adopted, however, more certain data on error probabilities must be obtained; previous data were obtained partly by oral communication. To this end, an SDS 910 computer at the Goldstone Tracking Station is being programmed to gather these data.

A binary test message of length 16,303 ($= 2^{14} - 1$) will be generated by the machine as a maximal-length linear shift-register sequence (Ref. 38) from a length 14 shift register. Since there are 25 binary bits of teletype per second, this message will occupy about 11 min of time. The plan is to send this binary message around a closed loop through the various DSIF Stations and back to Goldstone. An error-checking program is also being written which will compare the original test message with the received word to check for errors. Single binary symbol errors will be counted, as well as bursts of more than one error in a row. When these statistics have been gathered, the performance of teletype channels under the (62, 17) code can be predicted as in Ref. 36.

d. Encoding the (62, 17). Encoding on the 910 is easy, and merely requires setting up a shift register in the machine, as was done in Part ***b*** of this article to generate the binary test word. Since the 920 has *shift* and Mod 2 *add* commands, the programming job is especially easy. As explained in Ref. 36, each of the 17 teletype information letters is decomposed into 5 binary bits, resulting in 5 binary words of length 17. An additional "0" symbol is added as an 18th teletype letter. Each of these 5 binary words is expanded to length 62 by running them through the same shift register in series. The teletype letters are then formed from these 5 binary words of length 63 and the extra "0" symbol is deleted before transmission. Thus, the $GF(2^5)$-word of length 62, whose first 17 letters are the original teletype letters, is acquired. The word is now ready for transmission.

e. Decoding. The encoding described can trivially be performed in real-time; as is usual in coding theory, it is the decoding which presents a problem. In fact, it is the complexity of the decoding procedures previously used that has prevented a more rapid spread of error-correcting coding.

As mentioned, there are 25 binary bits of teletype per second; i.e., there are 5 teletype symbols per second. Thus, one teletype word of length 63 (including the synchronization symbol) takes 12.6 sec. In order to have a real-time system, then, the decoding must be done in $<$ 12.6 sec while the next word is being received; furthermore, the less time taken the better.

Recent advances in decoding theory (Refs. 37, 39, 40) have enabled the decoding to be done with the 910 in real-time. The difficulty with older techniques has been that to correct up to 10 errors, the full capability of the (62, 17) code, requires the performance of time-consuming algebraic operations on the entire word. The recent advances in decoding theory have vastly simplified the algebraic nature of the operation to be performed.

To describe the decoding procedure in more detail, it must first be pointed out that the (62, 17) code being used is shortened from a length 63 Bose–Chaudhuri code (Ref. 41), and that the decoding procedure employs quite heavily the theory of finite fields; however, this algebra mod 2 is easy to program because of the command structure of the 910.

The part of this decoding program already written corrects up to 4 errors and uses 1200 instructions. It is estimated that to correct up to 10 errors using the improved decoding techniques will take 7000 instructions (and no loops). Since each instruction takes about 50 μsec, the decoding procedure will take about 0.35 sec, a highly desirable result. Previous methods could take more than 100 times as long, and would not be real-time. Although nonreal-time is acceptable for these experiments, it is not acceptable in actual operation.

The code will first be used in the closed-loop operation (described in Part *b* of this article) to demonstrate the low error probabilities attainable, and to demonstrate the decoding procedure being developed. Since there will be a real-time system, however, the same programs can immediately be used in the actual system operation.

f. Flow diagram of decoding procedure. In this section, the flow diagram of the decoding procedure being programmed is given (Fig. 74), from which can be derived an idea of the type of programming involved. A more mathematical treatment will be given in subsequent issues of *SPS*, Vol. IV.

The disecting of the decoding procedure is now considered, relying heavily on Refs. 37, 40, and 42. The recursion polynomial for the (63, 18) code, taken from (Ref. 36), is

$$\sum_{i \in I} x^i,$$

where I is the set of powers

$$I = \{18, 16, 11, 9, 8, 7, 5, 3, 2, 0\}.$$

The extra "0" symbol put in at the encoder was deleted before transmission, but is put back in as "0" after transmission, before using the decoding program.

The basic idea is to test whether no errors have been made, then 1 error, $\cdots$, then 9 errors. If these tests all fail, then 10 errors are assumed and an attempt made to correct them. If the procedure works, then 10 errors were made—the error vector also being acquired by the decoding procedure. If the procedure fails all of the tests of "0" through 9 errors and the correction procedure for 10 errors does not work, more than 10 errors have occurred, and the occurrence of error is merely detected. If one of the tests for 1 through 9 errors passes, the error vector is then determined and added to the received word to get the correct word.

The test for "0" errors is to run the received word (after inserting the extra "0" information symbol) through the shift register corresponding to recursion polynomial

$$\sum_{i \in I} x^i,$$

and check for all zeros. The test for t errors, $1 \leq t \leq 9$, assuming the test for $t-1$ errors failed, is to evaluate a certain $(t+1) \times (t+1)$ determinant over the 32-element field to ascertain whether the value is "0." If so, then t errors were made, and the error vector is determined as in Refs. 37 and 38 by straightforward algebra over the 32-element field. Fig. 74 illustrates the process, using notation from Ref. 37.

To find the error vector once t errors have been determined, $1 \leq t \leq 9$, the last row of the $(t+1) \times (t+1)$ determinant used in checking for t errors is replaced in turn by the rows:

(1) $S_{21}\, S_{20}\, S_{19}, \cdots, S_{21-t+1}$

(2) $S_{23}\, S_{22}\, S_{21}, \cdots, S_{23-t+1}$

(3) $S_{27}\, S_{26}\, S_{25}, \cdots, S_{27-t+1}$

(4) $S_{31}\, S_{30}\, S_{27}, \cdots, S_{21-t+1}$,

and the values S_{21}, S_{23}, S_{27}, S_{31} are solved for. (The 10-error case is special and will be discussed in *SPS* 37-29, Vol. IV.) In an effort to recover the values c_0, c_1, c_5, c_9, c_{21} (of previous *Summaries*) which were used in the encoding of the message, use is made of the equation

$$c_0' = c_0 + t$$

$$c_1' = c_1 + S_{62} = c_1 + (S_{31})^2$$

$$c_5' = c_5 + S_{58} = c_5 + (S_{29})^2 = c_5 + (S_{23})^8$$

$$c_9' = c_9 + S_{54} = c_9 + (S_{27})^2$$

$$c_{21}' = c_{21} + S_{42} = c_{21} + (S_{21})^2.$$

Compute $S^2{}_{21}$, $S^8{}_{23}$, $S^2{}_{27}$, $S^2{}_{31}$, and then solve for c_0, c_1, c_5, c_7, c_{21}. By substituting $c_0, c_1, c_5, c_9, c_{21}$ in the encoder, the

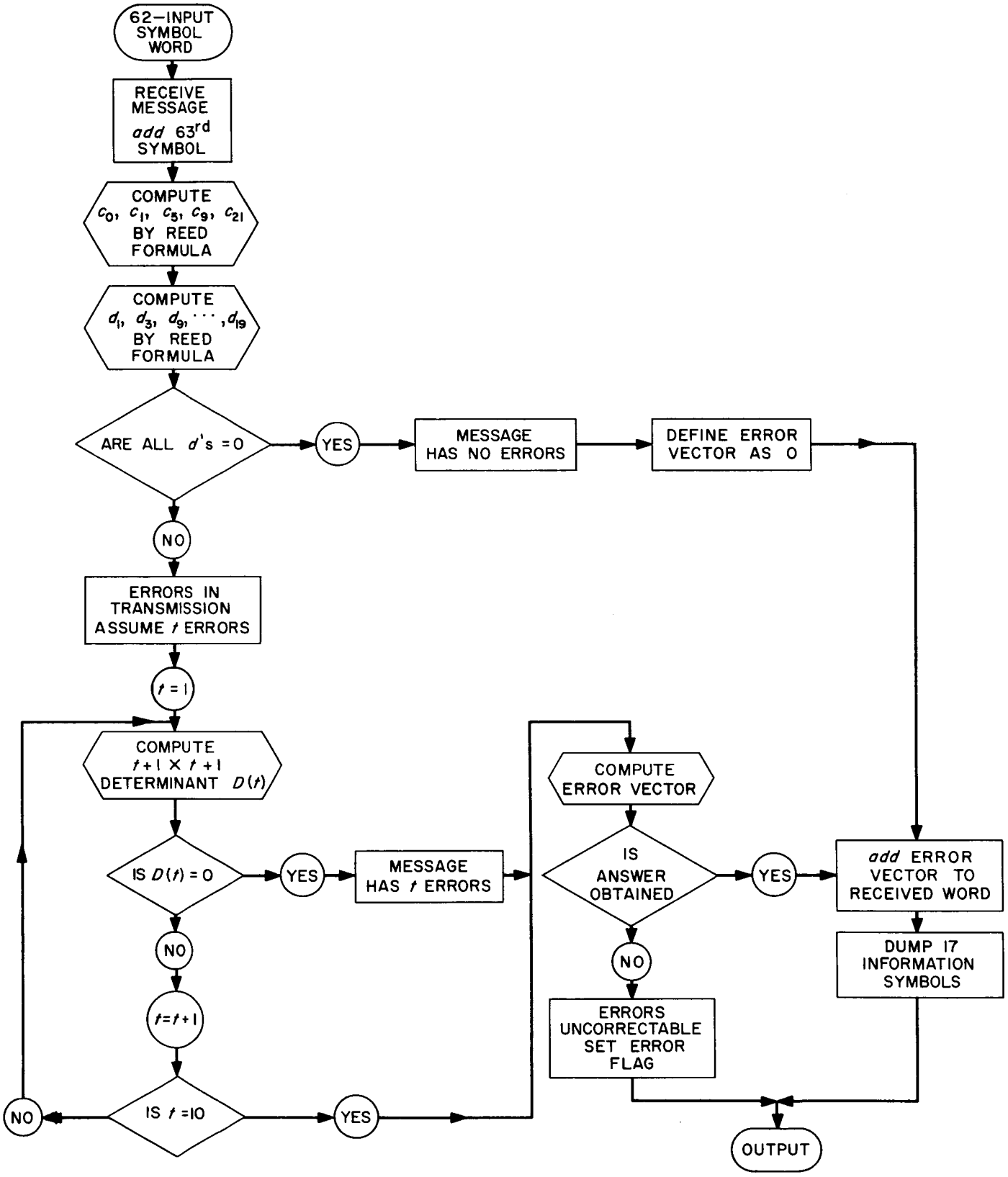

Fig. 74. The decoding program

corrected message with error-vector removed can be obtained.

Determinants to be evaluated in order to find the number t of errors made in transmission are:

$$t = 1\text{: } D(2) = \begin{vmatrix} S_1 & 1 \\ S_3 & S_2 \end{vmatrix} = S_1S_2 \oplus S_3 \text{ (addition is mod 2}$$
$$= S_1^3 \oplus S_3 \,(S_{2j} = S_j^2);$$

$$t = 2\text{: } D(3) = \begin{vmatrix} S_1 & 1 & 0 \\ S_3 & S_2 & S_1 \\ S_5 & S_4 & S_3 \end{vmatrix} = S_3\,D(2) \oplus S_4S_1S_1 \oplus S_5S_1$$
$$= S_3\,D(2) \oplus S_1^6 \oplus S_1S_5;$$

$$t = 3\text{: } D(4) = \begin{vmatrix} S_1 & 1 & 0 & 0 \\ S_3 & S_2 & S_1 & 1 \\ S_5 & S_4 & S_3 & S_2 \\ S_7 & S_6 & S_5 & S_4 \end{vmatrix} = S_4\,D(3) \oplus S_5S_1S_2S_2$$
$$\oplus\, S_5S_5 \oplus S_5S_4S_1$$
$$\oplus\, S_5S_3S_2 \oplus S_6S_1S_1S_2$$
$$\oplus\, S_6S_1S_3 \oplus S_7S_1S_2$$
$$\oplus\, S_7S_3$$
$$= S_1^4\,D(3) \oplus S_1^5S_5 \oplus S_5^2$$
$$\oplus\, S_1^5S_5 \oplus S_1^2S_3S_5$$
$$\oplus\, S_1^4S_3^2 \oplus S_1S^3$$
$$\oplus\, S_1^3S_7 \oplus S_3S_7$$
$$= S_1^4\,D(3)$$
$$\oplus\, S_5^2 \oplus S_1^2S_3S_5 \oplus S_1S_3^3$$
$$\oplus\, S_1^3S_7 \oplus S_3S_7, \oplus S_1^4S_3^2$$

etc., foi higher t These formulas are much simpler than the equation-substituting algebra used, for example, in Ref. 41.

The method of "table look-up" can also be used for these computations. Each S_j is equal to some power of β e.g., $S_1 = \beta^i$, $S_3 = \beta^k$, then $S_1\,S_3 = \beta^{j+k}$. The table look-up is used in the following manner:

In Table 7, S_j is associated with the power of β to which it corresponds. Adding the power of β that corresponds to S_i and S_j (as real numbers), the power of β that corresponds to $S_i\,S_j$ is obtained. In the inverse table would be the inverse set of relationships which is in Table 7, i.e., with each power of β is associated the elements S_j to which is corresponds.

Table 7. Lookup

Vector	Power of β	Vector	Power of β
1	0	33	5
2	1	34	11
3	6	35	25
4	2	36	31
5	12	37	34
6	7	38	47
7	26	39	17
8	3	40	23
9	32	41	15
10	13	42	51
11	35	43	53
12	8	44	44
13	48	45	37
14	27	46	40
15	18	47	55
16	4	48	61
17	24	49	10
18	33	50	30
19	16	51	46
20	14	52	22
21	52	53	50
22	36	54	43
23	54	55	39
24	9	56	60
25	45	57	29
26	49	58	21
27	38	59	42
28	28	60	59
29	41	61	20
30	19	62	58
31	56	63	57
32	62		

References

1. "Precision Drive System for 30-ft Antenna," *SPS 37-28*, Vol. III, p. 46, Jet Propulsion Laboratory, Pasadena, California, July 31, 1964.
2. "Antenna Instrumentation," *SPS 37-20*, Vol. III, pp. 31–34, Jet Propulsion Laboratory, Pasadena, California, March 31, 1963.
3. "Antenna Instrumentation," *SPS 37-27*, Vol. III, p. 54, Jet Propulsion Laboratory, Pasadena, California, May 31, 1964.
4. "Antenna Instrumentation," *SPS 37-24*, Vol. III, pp. 33 and 39–43, Jet Propulsion Laboratory, Pasadena, California, November 30, 1963.
5. Seidel, B., "Simultaneous Lobing Radiometric Tracking System," *SPS 37-26*, Vol. IV, pp. 216–220, Jet Propulsion Laboratory, Pasadena, California, March 31, 1964.
6. "Simultaneous Lobing Radiometric Tracking System," *SPS 37-27*, Vol. III, pp. 57–61, Jet Propulsion Laboratory, Pasadena, California, May 31, 1964.
7. "Simultaneous Lobing Radiometric Tracking System," *SPS 37-28*, Vol. III, pp. 48–51, Jet Propulsion Laboratory, Pasadena, California, July 31, 1964.
8. "STAIR Instrumentation Manual," *Lincoln Manual No. 48*, MIT Lincoln Laboratory, Lexington, Massachusetts.
9. Utku, S., and Barondess, S. M., "Computation of Weighted Root Mean Square of Path Length Changes Caused by the Deformations and Imperfections of Rotational Paraboloid Antennas," JPL Technical Memorandum No. 33-118, Jet Propulsion Laboratory, Pasadena, California, March 1, 1963.
10. "Instrumentation Setup for 85-ft Az–El Tests," *SPS 37-24*, Vol. III, p. 42, Jet Propulsion Laboratory, Pasadena, California, November 30, 1963.
11. "Venus Site Experimental Activities," *SPS 37-28*, Vol. III, pp. 51–55, Jet Propulsion Laboratory, Pasadena, California, July 31, 1964.
12. "100-kw S-band Transmitter," *SPS 37-28*, Vol. III, pp. 61–69, Jet Propulsion Laboratory, Pasadena, California, July 31, 1964.
13. "High-Power 100-kw S-Band Transmitter," *SPS 37-27*, Vol. III, pp. 69–70, Jet Propulsion Laboratory, Pasadena, California, May 31, 1964.
14. "A Range-Gated Lunar Radar Experiment," *SPS 37-25*, Vol. III, pp. 38–47, Jet Propulsion Laboratory, Pasadena, California, January 31, 1964.
15. "Mod IV Planetary Radar Exciter," *SPS 37-23*, Vol. III, pp. 44–46, Jet Propulsion Laboratory, Pasadena, California, September 30, 1963.
16. "X-Band Lunar Radar Transmitter," *SPS 37-27*, Vol. III, pp. 81–83, Jet Propulsion Laboratory, Pasadena, California, May 31, 1964.
17. "Beam Voltage Keyer, 8.448-Gc Lunar Radar," *SPS 37-27*, Vol. III, pp. 83–84, Jet Propulsion Laboratory, Pasadena, California, May 31, 1964.
18. "Multiplier Chains," *SPS 37-27*, Vol. III, pp. 86–89, Jet Propulsion Laboratory, Pasadena, California, May 31, 1964.

References (Cont'd)

19. "Multiplier Chains," *SPS 37-28*, Vol. III, pp. 75–77, Jet Propulsion Laboratory, Pasadena, California, July 31, 1964.

20. "S- and X-Band Interim Frequency Synthesizer," *SPS 37-27*, Vol. III, pp. 90–92, Jet Propulsion Laboratory, Pasadena, California, May 31, 1964.

21. "S- and X-Band Interim Frequency Synthesizer," *SPS 37-28*, Vol. III, p. 75, Jet Propulsion Laboratory, Pasadena, California, July 31, 1964.

22. "S- and X-Band Interim Frequency Synthesizer," *SPS 37-27*, Vol. III, pp. 90–92, Jet Propulsion Laboratory, Pasadena, California, May 31, 1964.

23. "RF Signal Generation and Control," *SPS 37-26*, Vol. III, pp. 57–59, Jet Propulsion Laboratory, Pasadena, California, March 31, 1964.

24. "S- and X-Band Interim Frequency Synthesizer," *SPS 37-27*, Vol. III, pp. 90–92, Jet Propulsion Laboratory, Pasadena, California, May 31, 1964.

25. "S- and X-Band Interim Frequency Synthesizer," *SPS 37-27*, Vol. III, p. 91, Jet Propulsion Laboratory, Pasadena, California, May 31, 1964.

26. "A Random Pulse Generator for Use as a Data and Noise Source," *SPS 37-27*, Vol. III, pp. 112–115, Jet Propulsion Laboratory, Pasadena, California, May 31, 1964.

27. "Design of a Quantile System for Data Compression of Space Telemetry," *SPS 37-27*, Vol. III, pp. 103–112, Jet Propulsion Laboratory, Pasadena, California, May 31, 1964.

28. "Design of Punctured-Cyclic Coder–Decoder," *SPS 37-27*, Vol. III, pp. 97–103, Jet Propulsion Laboratory, Pasadena, California, May 31, 1964.

29. "Evaluation of Digital Circuit Modules Procured Under JPL-Owned Design," *SPS 37-27*, Vol. III, pp. 123–127, Jet Propulsion Laboratory, Pasadena, California, May 31, 1964.

30. Ericksen, B. K., and Schmidt, J. D., "Random Pulse Generator Tests Circuits, Encodes Messages," *Modern Digital Circuits*, pp. 276–279, Samuel Weber, Editor, McGraw-Hill, New York, N. Y., 1964.

31. Baumert, L., Easterling, M., Golomb, S. W., and Viterbi, A., Technical Report No. 32-67, Chapter II, Jet Propulsion Laboratory, Pasadena, California, December 29, 1961.

32. Golomb, S. W., Welch, L. R., and Hales, A. W., "On the Factorization of Trinomials Over *GF*(2)," Technical Memorandum No. 20-189, Jet Propulsion Laboratory, Pasadena, California, July 12, 1959.

33. Feller, W., "An Introduction to Probability and Iits Applications," Chapter IX, John Wiley & Sons, Inc., New York, N. Y., 1957.

34. Posner, E. C., "Statistics of Data Sources," *SPS 37-18*, Vol. IV, pp. 225–229, Jet Propulsion Laboratory, Pasadena, California, December 31, 1962.

35. Eisenberger, I., "Genesis of Bimodal Distributions," *SPS 37-18*, Vol. IV, pp. 178–180, Jet Propulsion Laboratory, Pasadena, California, December 31, 1962.

References (Cont'd)

36. Posner, E. C., and Solomon, G., "A Code Over the 32 Element Field for Use on Interstation Teletype Channels," *SPS 37-26*, Vol. IV, pp. 223–225, Jet Propulsion Laboratory, Pasadena, California, April 30, 1964.

37. Solomon, G., "A New Decoding Procedure for Bose–Chaudhuri Codes," *SPS 37-27*, Vol. IV, pp. 190–193, Jet Propulsion Laboratory, Pasadena, California, June 30, 1964.

38. Baumert, L., Easterling, M., Golomb, S. W., and Viterbi, A., "Coding Theory and Its Application to Communication Systems," Technical Report No. 32-67, Chapter II, Jet Propulsion Laboratory, Pasadena, California, December 29, 1961.

39. Mattson, H. F., and Solomon, G., "A New Treatment of Bose–Chaudhuri Codes," *Journal of the Society for Industrial and Applied Mathematics*, Vol. 4, 1961.

40. Solomon, G., "Improved Decoding for a Class of BC-Codes," *SPS 37-29*, Vol. IV (to be published).

41. Peterson, W. W., "Error-Correcting Codes," John Wiley & Sons, Inc., New York, N. Y., 1961.

42. Solomon, G., and Fredricksen, H., "Real-Time BC-Decoding," *SPS 37-29*, Vol. IV (to be published).

VI. Advanced Antenna System

A. Introduction

A 210-ft-diameter Advanced Antenna System (AAS) is being designed and constructed for the Mars site of the Goldstone Tracking Station. This AAS is designed specifically for deep space communications and will be integrated with related systems and equipment at the Goldstone Station of the Deep Space Instrumentation Facility (DSIF).

The work progress on the AAS Project has been reported regularly in this *SPS*. Since the last reporting, the major work effort has been in the detail design of the structural components of the antenna and assuring the over-all system integration. Most of the structural components are now in either manufacturing planning or in fabrication at various subcontractor locations.

The over-all project continues generally on schedule with the various component areas maintaining a satisfactory pace in relation to the schedule. Based upon current evaluation, no slippage in the end date for project completion is anticipated.

B. Supporting Studies

Work continues on the Precision Data System (master equatorial) which will serve as the primary pointing reference for the antenna system. A discussion of the master equatorial preliminary design analysis was contained in Ref. 1. Work on the experimental mount for the Precision

Data System is in progress, and actions to accomplish fabrication and installation of the intermediate reference structure, optical boresight mount, and Precision Data System astrodome have been initiated. The astrodome will be mounted atop the completed reinforced concrete instrument tower which extends from its independent foundation through the center of the antenna pedestal.

Development and planning activities for inter- and intra-site communications facilities, ancillary instrumentation for test and measurement of antenna components, and the DSIF station equipment necessary to provide the receiving capability of the antenna system continue at JPL.

C. Construction and Fabrication Progress

Fig. 1 is a combined photograph and line drawing depicting the constructed antenna pedestal in relation to future construction. The line drawing is approximately to scale for comparison purposes. A cross-sectional detail drawing and brief description of the major components of the AAS were included in Ref. 1.

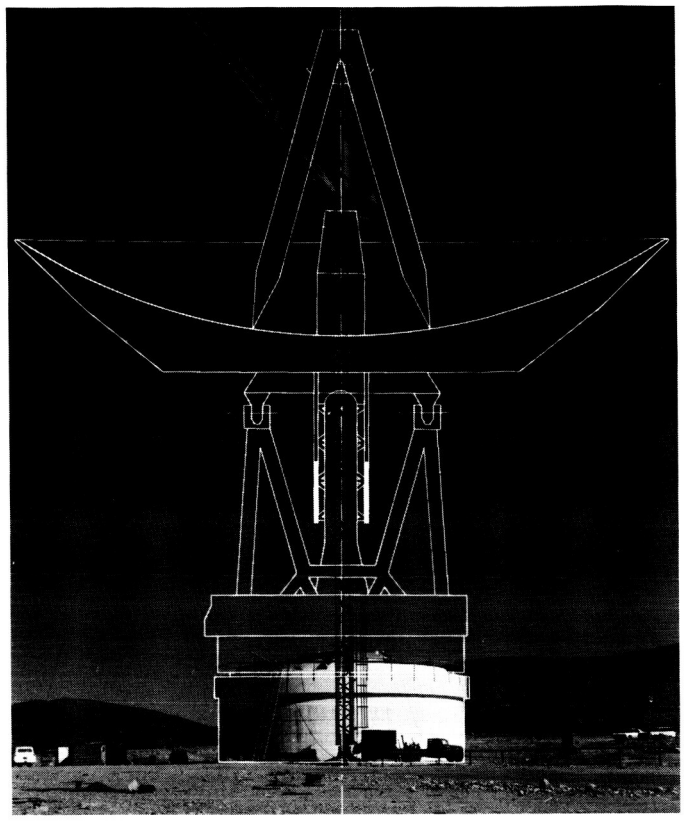

Fig. 1. Combined photograph and line drawing of the AAS

Fig. 2 depicts the Mars site construction layout and on-site progress as of June 12, 1964. By August 1, the on-site facility A&E construction was nearing completion. Work continues within the pedestal where two floors of working space are provided for the future operating crews. Partitions and stairs are under construction, along with the installation of plumbing, electrical and air conditioning facilities.

The placement of metal components on the massive foundation pedestal has begun. Azimuth motion elements consisting of the azimuth bull gear, azimuth radial bearing runner, and hydrostatic thrust bearing runner have been delivered to the Mars site and placed in their designed locations on the antenna pedestal.

A pintle sweep arm alignment tool (Fig. 3) has been installed on the AAS for use in installation and alignment of pedestal components such as the azimuth bull gear, azimuth radial bearing, and hydrostatic thrust bearing runner. The tool is approximately 40 ft long by 7 ft high and weighs about 2 tons. The azimuth radial bearing runner and wear strip have been lowered into position on the reinforced concrete radial bearing collar. The weight of the runner and wear strip is approximately 20 tons. The runner is composed of four segments and is 30 ft in diameter. The wear strip is composed of 10 segments.

The construction of other on-site facilities has been completed, including the pump house, cooling tower basin, and diesel generator building. The diesel generator equipment, which will provide late construction power and be the primary source of operating power for the antenna, has been delivered to the Mars site. Installation and checkout of the generator equipment are in progress. The installation of the cooling tower will begin in October of this year.

The generator building will house three Caterpillar 500-kva diesel motor generator units and associated switch gear. Two 12,000-gal fuel tanks are buried immediately south of the building. For reliability, a redundant pump system is provided. The building itself is located 345 ft southeast of the AAS pedestal. Six underground ducts are installed between the pedestal and generator building which carry utility, electronic, communications, and spare cabling.

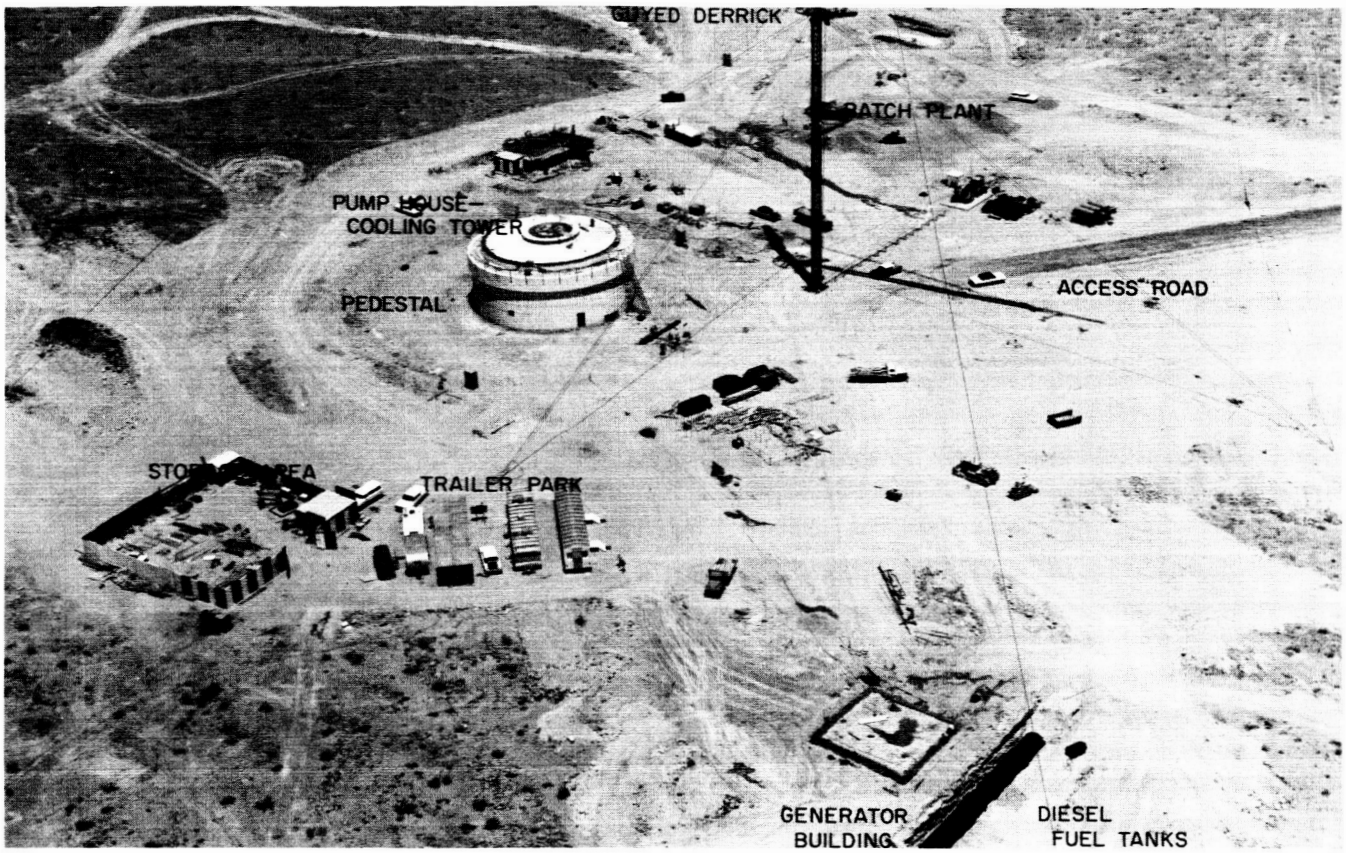

Fig. 2. Mars site layout and on-site progress as of June 12, 1964

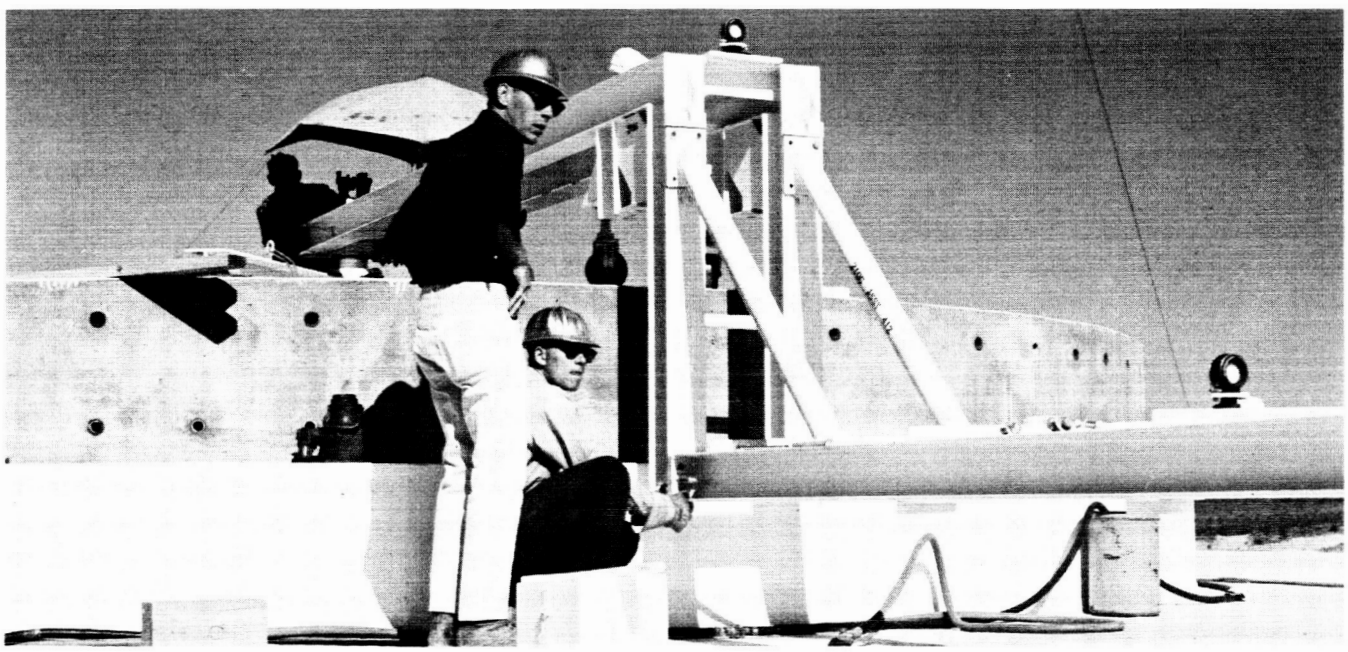

Fig. 3. AAS pintle sweep arm alignment tool

D. Azimuth Gears

The following is a more detailed discussion of the AAS azimuth gears and drives augmenting the brief description of the major components of the AAS in Ref. 1.

1. Summary

The design effort on the AAS azimuth gears and drives is now essentially complete. Components are now being manufactured, and installation on the antenna has begun. The detail design and fabrication is being accomplished by Philadelphia Gear Corporation, King of Prussia, Pennsylvania, under subcontract to Rohr Corporation.

The function of the drive system is to convert electrical and hydraulic servo signals to antenna rotation. The rotation of the antenna structure about the azimuth axis is accomplished by four azimuth gear reducers attached to and rotating with the alidade. Pinions on the output shaft of the reducers mesh with a fixed azimuth bull gear. A single reducer is mounted at each of the two front alidade legs, and two reducers are mounted at the rear alidade leg (Fig. 4).

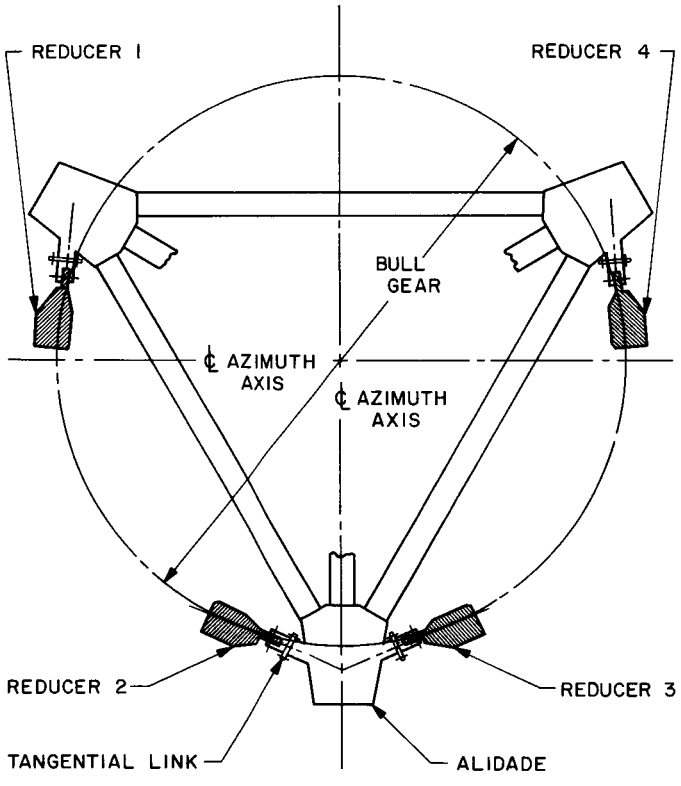

Fig. 4. Plan view AAS azimuth drive

2. Azimuth Bull Gear

The azimuth bull gear consists of 26 segments bolted and doweled to a steel sole plate (Fig. 5). The sole plate is of an "H" cross section and is mounted on anchor bolts atop the pedestal. The sole plate is similarly made up of 26 segments, each of which is approximately 100 in. long. Fig. 6(a) shows the sole plates being installed. The joint between individual gear segments occurs at the center of a sole plate segment. Subsequent to the final alignment of the bull gear, the sole plate will be grouted in place as indicated in Fig. 5.

The bull gear is a 70-ft-pitch-diameter spur gear, L-shaped in cross section, with the toothed vertical leg of 4140 steel welded to a 1020 steel horizontal mounting plate. Fig. 6(b) shows the gear rough aligned on the sole plate prior to grouting in place. The teeth are 3½-in. cir-

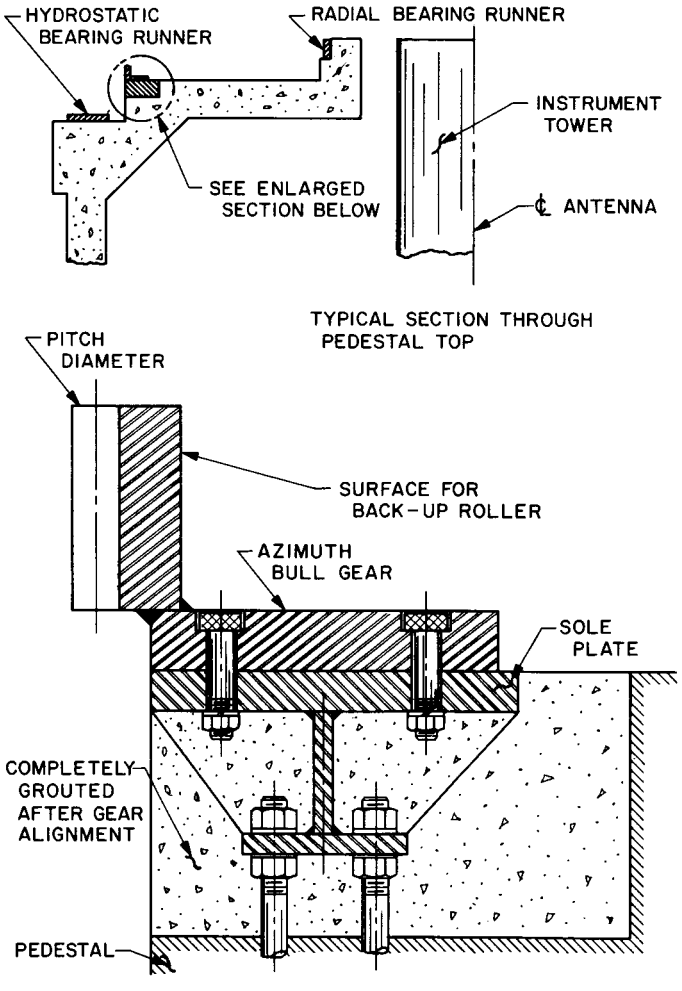

Fig. 5. AAS azimuth bull gear

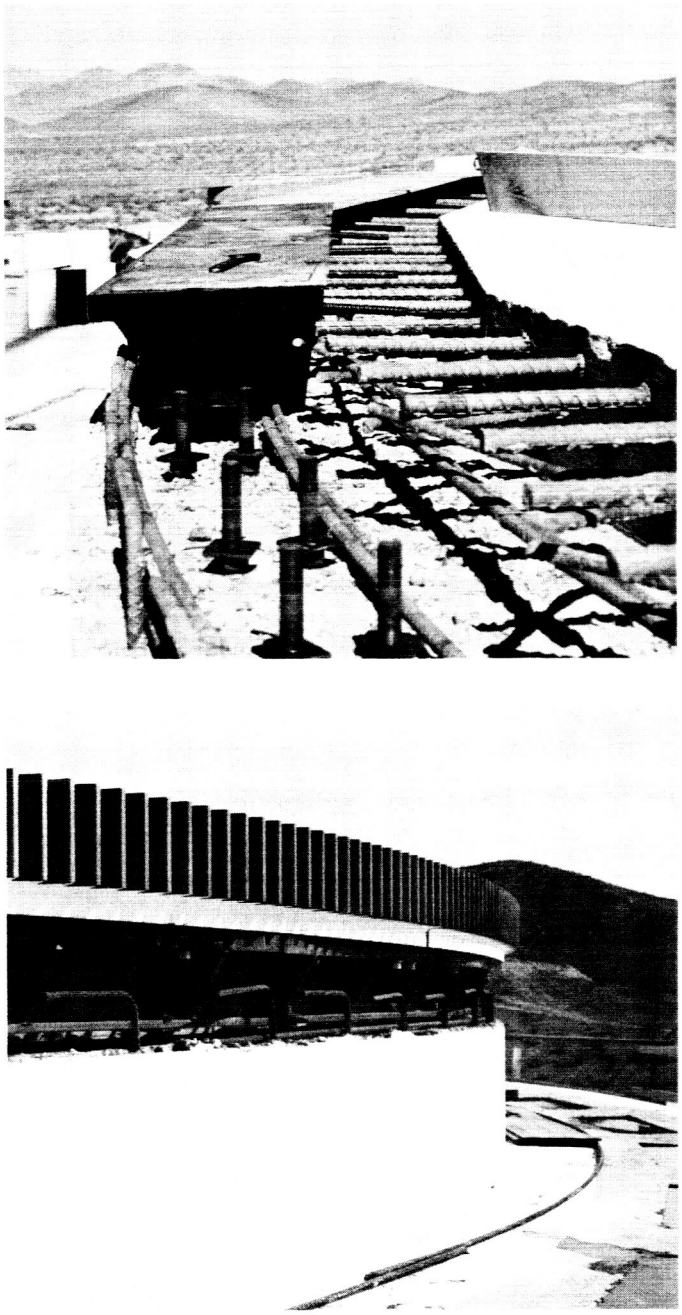

Fig. 6. Azimuth bull gear sole plate: (a) being installed on concrete pedestal and (b) prior to final alignment and grouting

cular pitch, 25-deg pressure angle, 9¾-in. face width and hardened to 245 to 285 BHN.

3. Reducer Mounting

To achieve the requisite gear reducer stiffness and to provide proper final gear mesh alignment, the four azimuth gear reducers are mounted with a linkage and backup roller arrangement. The reducer is restrained tangentially by means of a tangential link connection to a hard point on the alidade (Figs. 4 and 7). Radial restraint is accomplished by a backup roller integral with the reducer housing and rolling on a machined surface on the back of the vertical leg of the bull gear (Figs. 5, 7, and 8). The tangential link connection to the reducer has a spherical joint to allow the roller and the reducer to follow variations in the bull gear (Fig. 7). The tangential component of the tooth loading is taken directly into the alidade by simple tension or compression. The gear separating force is taken by the backup roller through its supporting bearings into the housing. A portion of the dead weight of the reducer is supported by hangers suspended from the alidade structure (Figs. 7 and 8).

4. Reducers

Each of the four reducer assemblies consist of a welded steel housing; a four-stage gear reduction exclusive of the final pinion-to-gear mesh; associated shafts, bearings, and seals; final drive pinion and backup roller; and an integral pressure lubrication system. Each reducer has provisions for mounting hydraulic motors, a hydraulic-release spring-set brake and a tachometer. These components are part of the servo system (Fig. 8). The total weight of an assembly is approximately 22,000 lb.

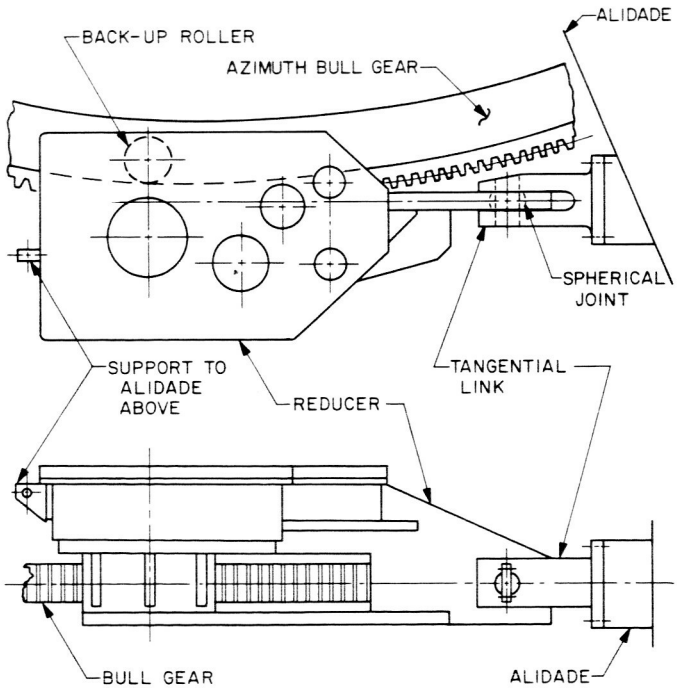

Fig. 7. AAS azimuth drive reducer

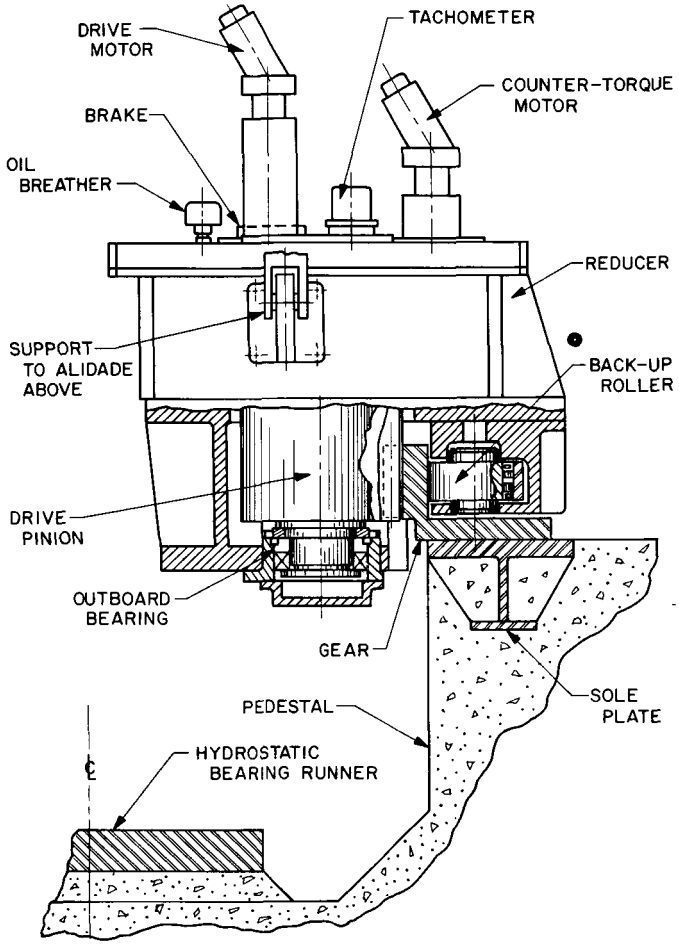

Fig. 8. Section through azimuth reducer showing backup roller

The first two meshes in the reducer are helical gearing, while the final two meshes and the pinion-to-bull-gear are spur gearing. The pressure angle in all gearing is 25 deg. The ratio within the reducer is 610 to 1 which, in combination with the final pinion-to-bull gear ratio of 47+ to 1, makes the total ratio from motor to antenna axis 28,724 to 1. The output pinion is integral with the low-speed shaft of the reducer, and has 16 teeth, 17.8-in.-pitch-diameter, hardened to 285 to 325 BHN. The backup roller is 12 in. in diameter, 5½ in. wide, manufactured of 4320 steel and case-hardened to 55 to 60 Rc.

Maximum reducer output torque is 71,000 ft-lb, and occurs with the antenna reflector at the horizon in a 70-mph wind. Strength and wear ratings of the gearing have been calculated according to the American Gear Manufacturers Association standards. The calculated life of the gearing exceeds the 22,000-hr (10 yr at 25% usage) requirement of the antenna specification.

Lubrication within the reducers is supplied by a force feed pressure system. The system has two pumps for redundancy and, in the event of a failure of a pump, the system is switched to a standby pump.

5. Countertorque System

A countertorque system is employed to eliminate backlash in the antenna drive system (Fig. 9). There are four gear reducers, each having a drive motor and a countertorque motor on the input shaft, and a single output pinion. The drive motor is shown at "D," and the countertorque motor is shown as "CT" in Fig. 9. The four drive motors are connected in parallel to a common servo valve. The countertorque motors are connected in series to a pressure regulating valve which provides a constant pressure across these motors, and hence a constant torque output. The countertorque motors are piped so that two provide continuous clockwise torque, while the other two provide continuous counter-clockwise torque. Two reducers oppose each other with the constant torque from the countertorque motors. As shown in Fig. 9, Reducer 1 opposes Reducer 2, and Reducer 3 opposes Reducer 4, as indicated by the arrows.

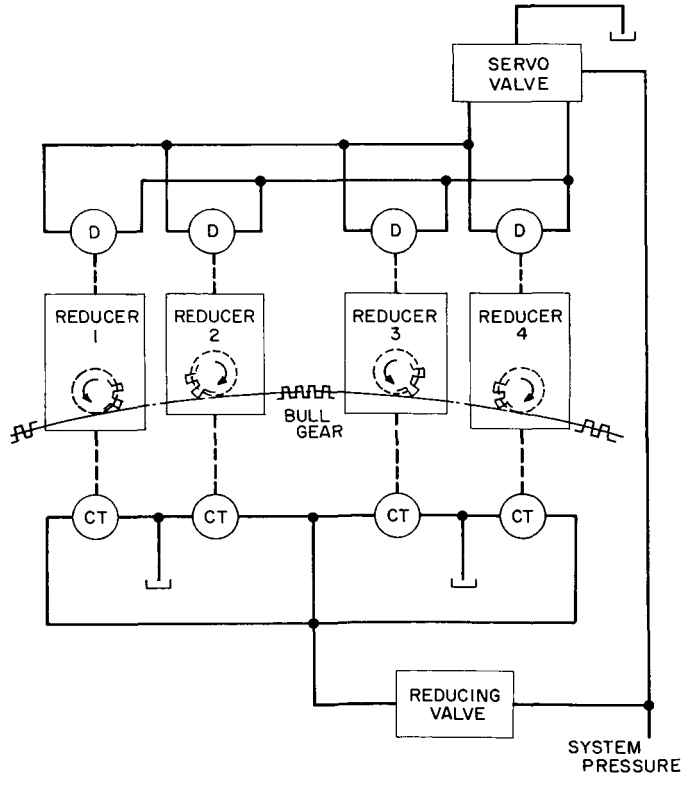

Fig. 9 AAS countertorque system

For the condition of no external load on the antenna, the drive motors produce no torque, and the only contributors to torque are the "CT" motors. The output of the opposed reducers is balanced, and there is no net torque on the axis.

With the application of external loads on the antenna, all drive motors drive in the same direction, sharing the load. Two of the "CT" motors are also driving in this direction and add driving torque. The two remaining "CT" motors are dragging (acting as pumps) and absorbing torque. The torque on the antenna axis is thus equal to the torque from four "D" motors plus the torque from the two "CT" motors aiding, less the torque from the two dragging "CT" motors.

For most operating wind torques, the dragging "CT" motors exert more torque than their companion "D" motors; hence, their reducer output pinions will oppose the driving motion. The driving pinions bear on one side of the gear teeth, and the dragging pinions bear on the opposite side.

If the direction of the antenna rotation is reversed, the dragging pinions and the driving pinions exchange roles simply by the reversal of the driving motors, and there is no lost motion due to backlash.

For very high axis torque, the drive motors overcome the "CT" motors, and all four pinions assist motion. In this case, the anti-backlash feature is lost.

E. 1/7-Scale Model Feed

a. Summary. Preparations have been completed for the first series of K_u-band scale model studies of the feeds for the 210-ft AAS. The K_u-band Mesa Antenna Range, used for amplitude and phase primary patterns of the feeds, is temporarily shut down while operations shift to the Goldstone 30-ft antenna.

Two scaled feeds, a dual mode horn and a simultaneous lobing (monopulse) configuration, have been evaluated. Each feed was investigated with and without the AAS scale hyperboloidal subreflector, and with and without the beamshaping flange. A portion of the measured data on the monopulse configuration is presented.

b. Recent work. The objective of the K_u-band scale model studies is to simulate AAS angle tracking feed performance with the Goldstone 30-ft reflector. As described in Refs. 1 and 2, the JPL precision machined monopulse assembly, operating in the K_u-band (16,330 Mc), is intended to simulate the performance of an available S-band feed—the SCM (S-band Cassegrain Monopulse)—a DSIF feed presently under development. As shown in Fig. 10, the JPL scale feed consists of a linearly polarized bridge assembly and a pyramidal horn. This feed utilized the TE_{10} mode for the sum channel radiation pattern, the resultant of the TE_{11} and TM_{11} modes for the E-plane error channel, and the TE_{20} mode for the H-plane error channel. The theory and results of the S-band DSIF feed are available in Ref. 3.

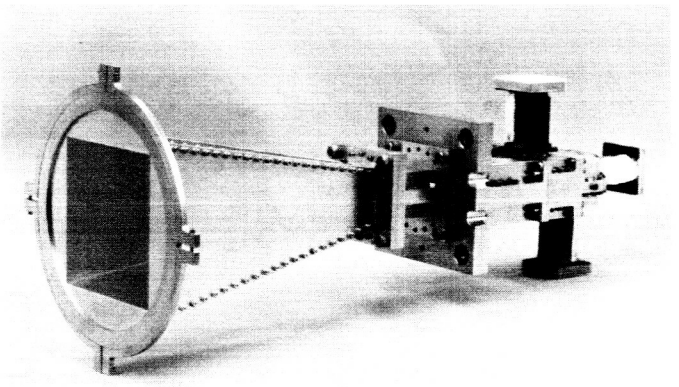

Fig. 10. 16,330-Mc monopulse feed

The radiation patterns for the JPL model, taken at the scaled frequency on the Mesa Antenna Range, are presented in Figs. 11 and 12 for the feed alone. As can be seen by referring to the S-band patterns (Ref. 3), the simulated performance is entirely acceptable.

Of particular interest in Figs. 12(a) and 12(b) are the boresight null depths, which are approximately 55 and 58 db for the E- and H-planes, respectively. Null depths of this order indicate that a very high degree of mechanical symmetry was achieved during both construction of the individual parts and assembly of the waveguides.

Phase-front patterns obtained for the feed alone also simulate the S-band performance of the SCM. Table 1 compares the Hughes Aircraft Company data (scaled from S- to K_u-band) with that of the JPL K_u-band. The JPL data represent interpolations believed to be accurate to ± 0.25 in. The Hughes data are available in Ref. 3.

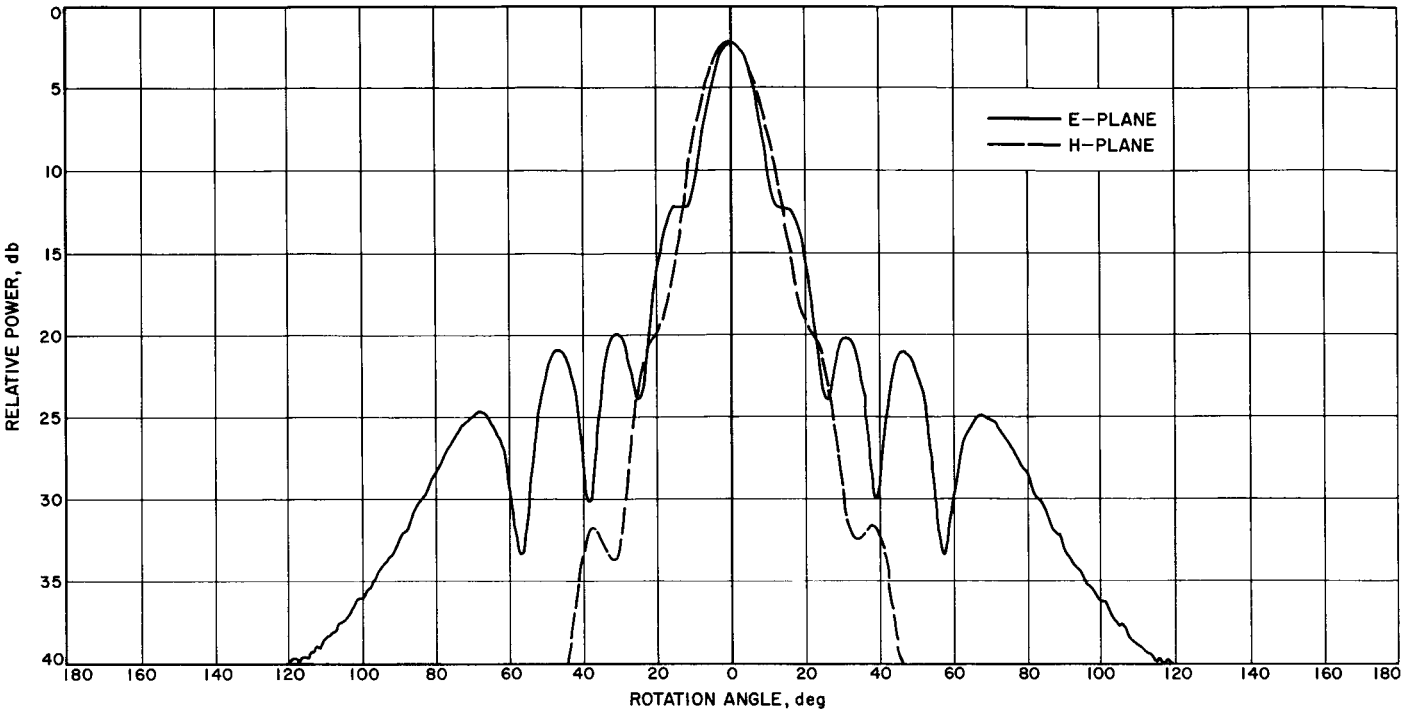

Fig. 11. 16,330-Mc monopulse feed sum channel: (a) E-plane and (b) H-plane

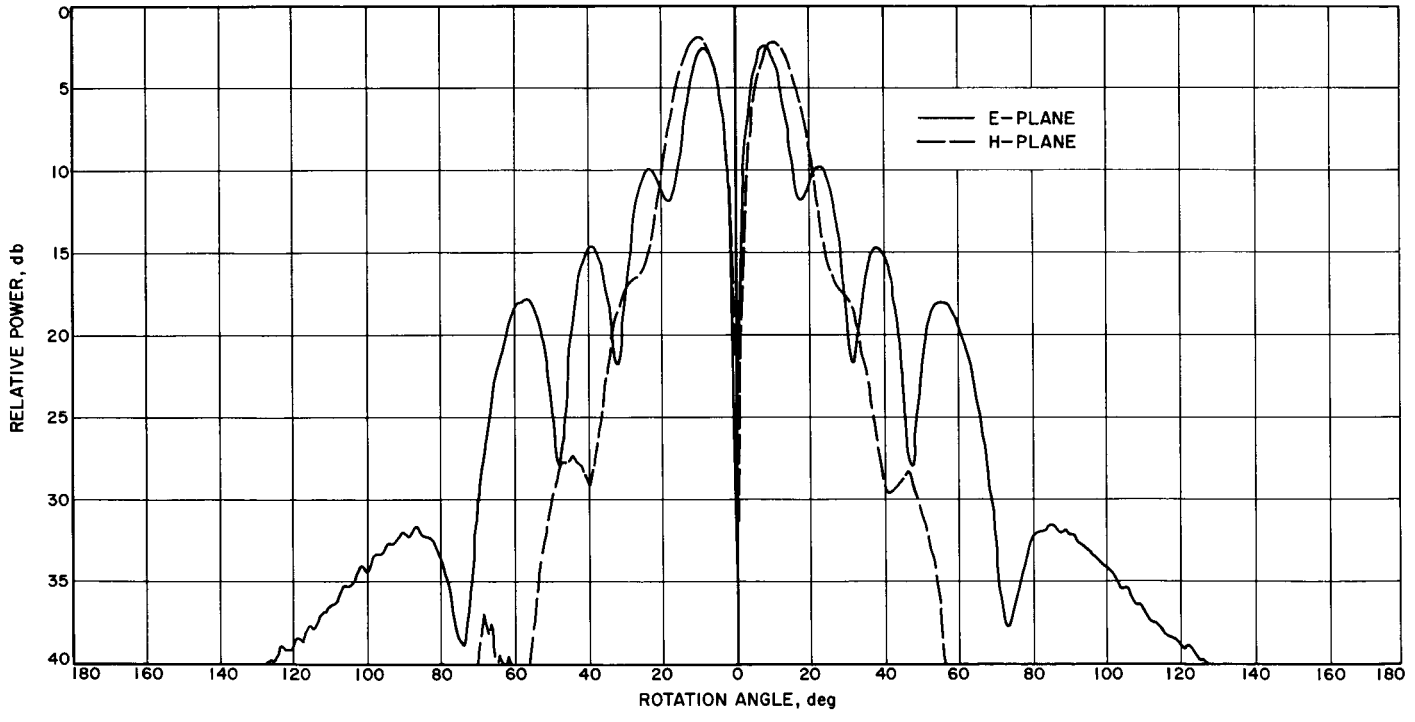

Fig. 12. 16,330-Mc monopulse feed error channels: (a) E-plane and (b) H-plane

Figs. 13 and 14 are the subreflector-scattered field patterns of the JPL model, taken with the AAS scale subreflector with the beamshaping flange attached.

An improved model of the DSIF S-band Cassegrain monopulse feed exists. As described in Ref. 4, the initiation of additional propagating modes within the feedhorn,

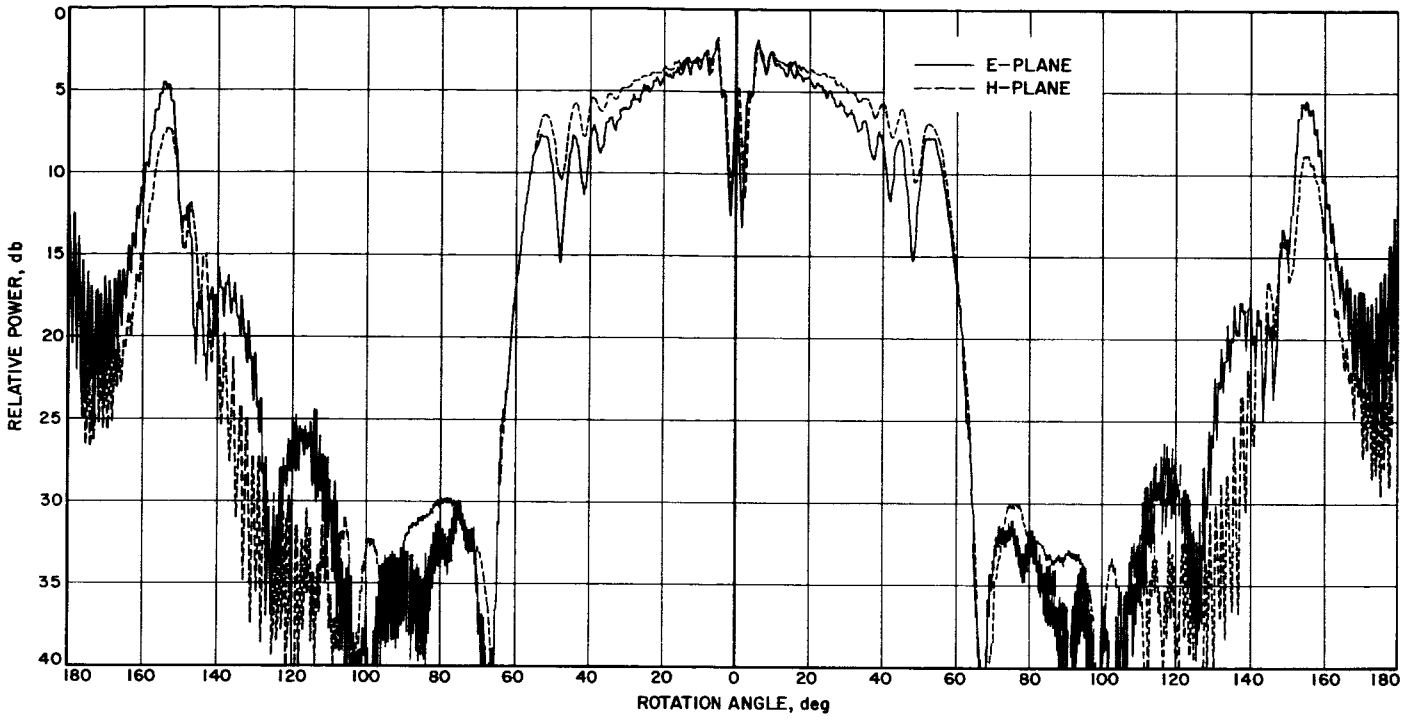

Fig. 13. 16,330-Mc Cassegrain monopulse sum channel: (a) E-plane and (b) H-plane

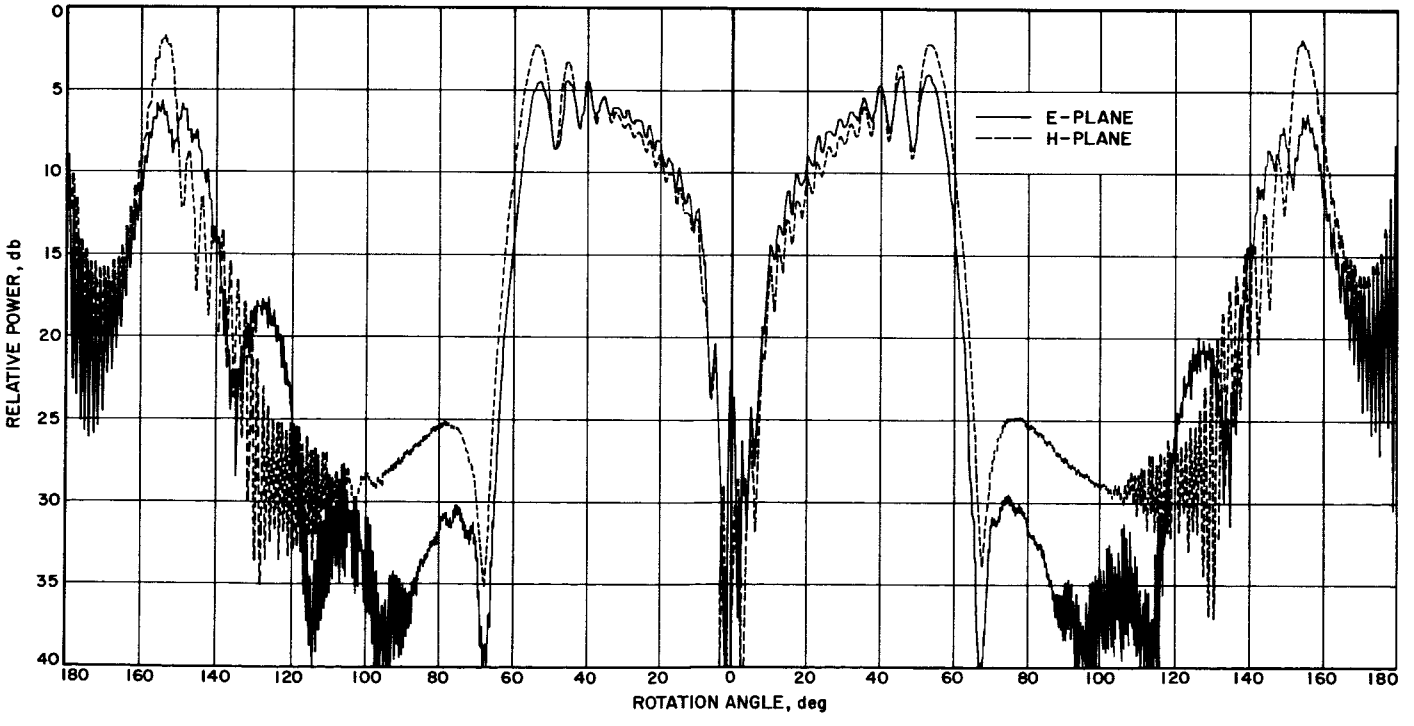

Fig. 14. 16,330-Mc Cassegrain monopulse error channels: (a) E-plane and (b) H-plane

properly phased at the aperture, results in sidelobe suppression. The improved feedhorn utilizes the TE_{12}, TM_{12}, and TE_{30} modes, in addition to those used in the earlier version. Because the JPL scale assembly is linearly polarized, certain circular polarization phasing requirements are removed; it is easy to obtain the enhanced

sidelobe-suppressed action with the model monopulse. Accordingly, a model of the S-band horn throat region is being fabricated to obtain the improved performance for the 210-ft scale model feed.

The listening feed, a straightforward scale model of previous dual-mode conical horns of circular cross-section, has been evaluated. The horn alone exhibits radiation patterns identical to lower frequency horns previously investigated. The subreflector-scattered patterns exhibit desirable characteristics, near-uniform illumination with equal E- and H-plane beamwidths over the region of the paraboloid surface, and rapid cutoff near the paraboloid edge. The near-uniform illumination and rapid cutoff are attributable to the relatively large (diameter $\simeq 50\ \lambda$) hyperboloid.

Table 1. Phase centers, inches behind aperture

Channel	DSIF-SCM feed data scaled	JPL feed 16,330 Mc
E-plane sum	4.8	4.5
H-plane sum	2.7	3.0
E-plane error	1.6	2.0
H-plane error	0.9	1.0

References

1. "Advanced Antenna System," *SPS 37-26*, Vol. III, pp. 67–72, Jet Propulsion Laboratory, Pasadena, California, March 31, 1964.
2. "1/3-Scale Model Feed for AAS," *SPS 37-28*, Vol. III, pp. 93–94, Jet Propulsion Laboratory, Pasadena, California, July 31, 1964.
3. "DSIF S-Band Cassegrain Monopulse Monthly Progress Report. Final Report Phase V" (JPL Reorder No. 62-519), Hughes Aircraft Company, Culver City, California, August 13, 1962.
4. "Final Report for Modification of DSIF SCM Feeds" (JPL Reorder No. 64-52), Hughes Aircraft Company, Culver City, California, January 11, 1964.